The Study of Tribological Phenomena using Linear and Nonlinear Ultrasound

Saeid Taghizadeh

Supervisors: Prof. R. Dwyer-Joyce and Dr G. Manson

Doctor of Philosophy

The University of Sheffield

Faculty of Engineering

Department of Mechanical Engineering

Submission Date

May 2024

Acknowledgements

The author would like to acknowledge the financial support of the Engineering and Physical Sciences Research Council for funding this research through RDJ's fellowship on Tribo-Acoustic Sensors EP/N016483/1 and the Centre for Doctoral Training in Integrated Tribology EP/L01629X/1. The author also would like to acknowledge the guidance and inspiration given by Prof. Rob Dwyer-Joyce and Dr G. Manson throughout this project.

Abstract

Tribology is the science of friction, lubrication, and wear. A single surface or a contact created by multiple parts can be studied in tribology. The contact is either dry or lubricated. In addition, lubricants can be studied for their viscosities, degradation or film thickness when used. When two solid surfaces come into contact, the asperity peaks touch, and the real contact area is substantially less than the nominal contact area. Applying pressure to the surfaces causes a small approach of the mean lines of their roughness. The interfacial stiffness (per unit area) is then defined as the rate of change in contact pressure with the approach of the mean lines of the roughness of the contacting surfaces. If the real contact area is low, then a low nominal contact pressure is all that is required to deflect the asperities. Increasing the nominal contact pressure brings more asperities into contact, making the interface stiffer; hence, the interfacial stiffness is a nonlinear variable. Interfacial stiffness is important in tribology because it affects machine element deflection, wear and friction since stiffer interfaces tend to have less deflection. Machining accuracy, for example, depends on the stiffness of the joints in the machine tool assembly.

Lubricants have a significant impact on energy consumption and the level of environmental pollution. As lubricants circulate in an engine or machinery, they become degraded. Various sources of lubricant degradation include oxidation, water, soot, wear debris and other contaminations. The two approaches for lubricant drain times are hours/rotation/mileage operation of the engine or machinery and degradation monitoring.

In the current study, high-power ultrasonic waves have been used in two ways. First, to explain the nonlinear stiffness of dry contacts and, second, the nonlinear behaviour of lubricants as they degrade. The nonlinearity due to longitudinal ultrasonic waves was investigated both analytically and numerically. The reason for the peak of the amplitude of

nonlinearity was investigated as it was not sufficiently studied in the previous research. The effect of frequency and the amplitude of excitation and the mechanical properties of the contacting surfaces on the amplitude of fundamental frequency and second-order harmonic was studied. The effect of consecutive loading/unloading cycles and surface roughness on nonlinear interfacial stiffness was experimentally investigated.

Nomenclature

A	Amplitude of incident wave (V)
a	Radius of piezoelectric transducer (m)
A_1	Amplitude of particle displacement of fundamental frequency (V or m)
A_2	Amplitude of particle displacement of second-order harmonic (V or m)
c	Speed of sound ($m.s^{-1}$)
c_0	Linear (small-signal) sound speed of liquid lubricants at ambient pressure ($m.s^{-1}$)
E	Elastic modulus (Pa)
E^*	Effective Elastic modulus (Pa)
p	Sound pressure (Pa)
h	Rough surface mean line separation (surface separation) variation with time (m)
p_0	Amplitude of pressure of incident ultrasonic wave (Pa)
h_0	Equilibrium separation of the rough surface mean line (m)
p_1	Amplitude of pressure of fundamental frequency (Pa)
K_1	Linear interfacial stiffness ($Pa.m^{-1}$)
p_2	Amplitude of pressure of second-order harmonic (Pa)
K_2	Second order nonlinear interfacial stiffness ($Pa.m^{-2}$)
r	Cylindrical coordinate variable (m)

p	Total nominal contact pressure (summation of the sound pressure and externally applied pressure)(Pa)
t	Time (s)
Z	Acoustic impedance (Pas/m)
p_0	Nominal externally applied contact pressure (Pa)
z	Propagation direction (m)
R	Reflection coefficient
Z_n	Distance from the ultrasonic source in the near field where the wavefronts are planar (m)
Z_n^{em}	Empirical value for Z_n (m)
Z_r	Near filed or Rayleigh distance (m)
r	average radius of curvature of the summits (m)
Y	Relative surface approach (m)
Γ	standard deviation of the asperity heights (m)
γ	Second order nonlinear parameter for reflected ultrasound (V^{-1}) or (m^{-1})
u	Particle velocity ($m.s^{-1}$)
α	Embedding parameter
δ_1	Voltage to amplitude (meter) conversion at fundamental frequency($m.V^{-1}$)
β	Nonlinear coefficient
δ_2	Voltage to amplitude (meter) conversion at second order harmonic($m.V^{-1}$)
δ	Sound diffusivity ($m^2.s^{-1}$)
η	density of summits per unit area (m^{-2}
$\delta\dot{}1$	Meter to voltage conversion of fundamental frequency (m/V)
ρ	Density of the media ($kg.m^{-3}$)

$\delta\dot{}2$	Meter to voltage conversion of second harmonic (m/V)
ω	Angular frequency $(rad.s^{-1})$
μ	Shear viscosity $(Pa.s)$
μ_B	Bulk viscosity $(Pa.s)$
ρ_0	Ambient density of liquid lubricant (s)
τ	Retarded time (s)
ω_0	Angular frequency of incident ultrasonic wave $(rad.s^{-1})$
ω_1	Fundamental angular frequency $(rad.s^{-1})$
ω_2	second-order harmonic angular frequency $(rad.s^{-1})$

Contents

List of Figures

Chapter 1

Introduction

1.1 Statement of the Problem

Tribology is the science of wear, friction and lubrication of contacting surfaces [7]. Tribology plays a significant part in energy consumption and the environment. Mechanisms that are well-designed and monitored in terms of tribology can cause less environmental damage. Numerous methods and techniques, such as Digital Image Correlation (DIC) and tribometers, can be used to measure tribological parameters online and offline. Despite their advantages, some are only laboratory-based methods, while others might be offline techniques or damage the sample during the analysis. Ultrasound has been used in different disciplines, such as medicine and engineering. It is a non-destructive method that is used for online engineering monitoring. In tribology, it has been used to measure the thickness of the oil film [8], the measurement of viscosity [9] and the stiffness of contact [10]. In most studies, the linear behaviour of ultrasound has been investigated [6, 8, 11–18], and less attention has been paid to the nonlinear behaviour of ultrasound.

In the current study, the nonlinear behaviour of ultrasound was used in:

1. solid-solid interface to measure the nonlinear contact interface
2. liquid lubricant to detect the contamination and degradation

Analytical and numerical models were employed to analyse the mechanism of nonlinearity for both the solid-solid interface and other liquid lubricants. Different parameters that affect these nonlinearities were also studied. Then, the contact acoustic nonlinearity (CAN) and nonlinearity in the liquid lubricant were measured experimentally.

1.2 Aims and objectives

The aim of the current study is to explore how the nonlinear behaviour of ultrasound can be used to measure the features of tribological contacts. It is used in two applications: to develop an ultrasonic method to experimentally measure the nonlinear normal interfacial stiffness in the pitch-catch through reflection mode and to detect liquid lubricant contamination and degradation. To achieve the aim, several objectives are set:

1. Use analytical and numerical models (finite different method FDM) to study the behaviour of high-power ultrasound for solid-solid interface.
2. Investigate the effect of incident amplitude, frequency, material and contact pressure on nonlinearity generated at the solid-solid interface and in the liquid lubricant.
3. Investigate the effect of surface roughness on the nonlinearity generated in solid-solid contact.
4. Develop an experimental approach using a laser Doppler vibrometer to convert the unit of ultrasonic waves from voltage to metre.
5. Apply an experimental approach to measure the nonlinear normal interfacial stiffness.
6. Investigate the effect of elastic and plastic deformation of asperities on nonlinear normal interfacial stiffness.
7. Study the effect of different couplant gels on the reflected ultrasound waves.
8. Apply an experimental approach to measure the nonlinear coefficient in liquid lubricants.
9. Investigate the relationship between the nonlinear coefficient, the degradation of the lubricant and the viscosity.

1.3 Thesis Layout

In Chapter 2, the background of tribology is briefly discussed. The features of surface topography, viscosity, methods for polishing and grinding solid surfaces and methods for measuring viscosity are presented.

In Chapter 3, the background of ultrasound, different ultrasonic modes, ultrasonic properties, reflected and transmitted ultrasonic waves are presented.

In Chapter 4, a literature review of the current study is presented.

In Chapter 5, an analytical model and numerical analysis based on FDM for contact acoustic nonlinearity are used. The accuracy of the models is compared. Different parameters and factors, such as excitation amplitude, frequency and materials affecting higher-order harmonics, are also studied.

In Chapter 6, experimental setup and signal processing for the contact acoustic nonlinearity are presented. The effect of amplified signals and couplant gels on the ultrasonic waves and nonlinearity is investigated. This chapter shows the surface profile and roughness of the sample before the loading and the loading apparatus. Finally, the effect of the different functions for signal processing is determined.

Chapter 7 is devoted to linear and nonlinear normal interfacial stiffness using the longitudinal behaviour of ultrasound. In this chapter, the experimental measurements are then validated using numerical differentiation.

In Chapter 8, the effect of elastic and plastic deformation and surface roughness on nonlinear normal interfacial stiffness is studied. Two pairs with different surface roughnesses, varying from rough to smooth roughness, are analysed to do this. It is shown how consecutive loading/unloading affects the nonlinear normal interfacial stiffness.

In Chapter 9, an analytical analysis of the nonlinear behaviour of longitudinal ultrasound in a liquid lubricant is used. These analyses are then used to study the effect of viscosity, density, amplitude and frequency on ultrasound of higher-order harmonics.

In Chapter 10, the experimental setup for measuring the nonlinearity in the liquid lubricant is presented. Different common fresh liquid lubricants and their contaminated ones are used. In addition, a real degraded liquid lubricant is studied. Here, voltage-to-length unit conversion is needed.

In Chapter 11, the nonlinearity in distilled water is measured because the value is known to show the precision of the experiment. Finally, this nonlinearity is used to detect degradation and contamination of liquid lubricants.

Chapter 12 is a general discussion and the conclusion of the thesis.

1.4 Novelty of the Work

The novelty of this thesis is as follows:

1. Experimentally measured second-order nonlinear normal interfacial stiffness with pitch-catch through reflection. In previous studies, the researchers measured the interfacial stiffness using the pitch-catch through transmission where the emitter and receiver are placed on either side of the interface. However, this method is impractical in most engineering structures (for example, an engine) when only one side is accessible. Although Li [4] used pitch-catch through reflection with shear transducers to measure friction, in the current study, the pitch-catch through reflection is used to measure interfacial stiffness with longitudinal transducers.

2. Validation of second-order nonlinear normal interfacial stiffness. Biwa et al. [15] proposed the second-order nonlinear normal interfacial stiffness. Two nonlinear differential equations were proposed here and an experimental test was completed to validate them. The results were published in [2].

3. The mechanism of contact acoustic nonlinearity as the nominal contact pressure increases. Although analytical and numerical analyses have been previously proposed (which were also used in this thesis), the behaviour of the higher-order harmonics as the nominal contact pressure increases was unknown. In the current study, different factors, parameters, and materials were used to study the mechanism of CAN.

4. Elastic-plastic asperity deformation during consecutive loading/unloading cycles for second-order interfacial stiffness. Other researchers have studied asperity deformation and its effects on linear ultrasound. In the thesis, the effect

of elastic-plastic deformation on CAN and the second-order interfacial stiffness during loading/unloading was studied.

5. Effect of surface roughness on second-order interfacial stiffness.
   The effect of surface roughness has also been studied for linear ultrasound. In this thesis, different levels of surface roughness were studied to investigate their impact on CAN and second-order interfacial stiffness.

6. Online measurement of lubricant degradation and contamination using the nonlinear behaviour of ultrasonic waves. In the current study, the nonlinear behaviour of ultrasound in liquid lubricants was used to detect their contamination and degradation. Despite most available methods, which are offline or lab-based, the technique proposed here is an online method.

Chapter 2

Background on Tribology

This chapter defines dry tribological contact, lubricants and the factors and parameters characterising them. The methods, techniques, equipment, and machines used for preparation and measurement are also briefly introduced.

2.1 Tribological contact

In dry contact, solid surfaces are in contact without lubricants (Figure 2.1b). However, in a lubricated contact, a lubricant film in solid or fluid occurs between the solid surfaces. Depending on the thickness of the lubricant film, this contact is divided into the boundary (Figure 2.1c), mixed (Figure 2.1d), HL (hydrodynamic lubrication) or EHL (elastohydrodynamic lubrication) regimes (Figure 2.1e). In dry contact, there is no lubricant between the solid surfaces. When the contact is lubricated, but the solid surfaces are still in contact (owing to surface roughness), the contact is partially supported with the solids and lubricant. This contact is called the boundary regime. As the lubricant film in the contact becomes thicker, the portion of the solid surfaces in contact becomes smaller, and the lubricant supports the contact with less solid surfaces. This is a mixed lubrication regime. When the contact is fully flooded, the content is either HL (for conformal contacting surfaces, such as a journal bearing and a shaft) or EHL (for nonconformal contacting surfaces, such as a rolling element bearing).

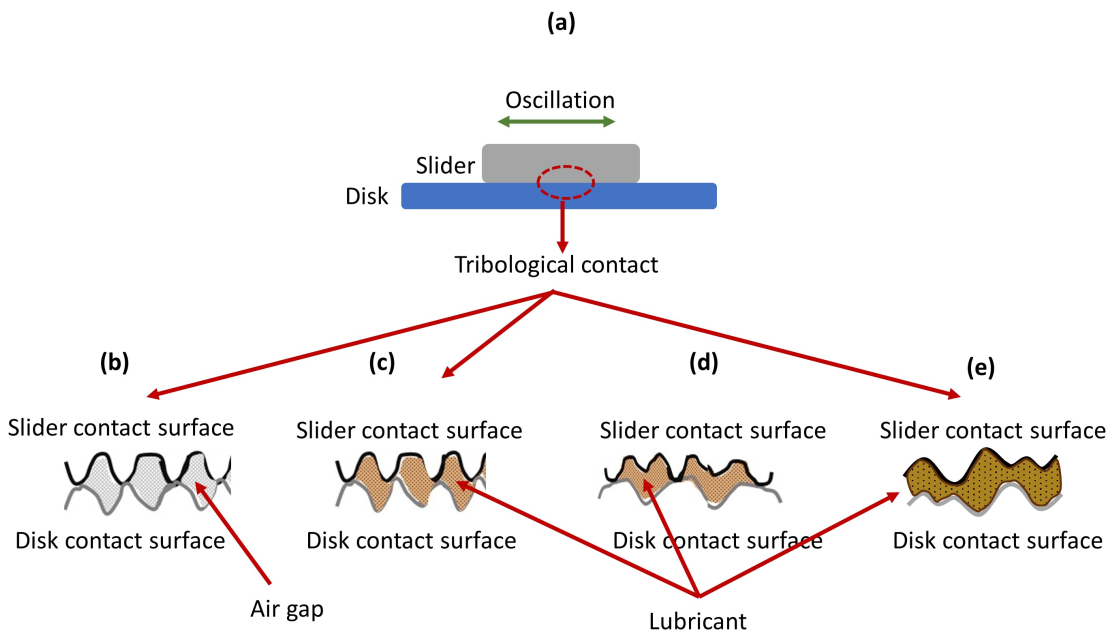

Figure 2.1: Tribological contact: (a) slider-disk under oscillation; (b) dry contact; (c) boundary lubrication regime; (d) mixed lubrication regime; (e) HL or EHL lubrication regime.

2.2 Surface topography

A surface texture or surface topography is a complex and random repetitive deviation of a surface from a nominally flat surface. It includes surface roughness, waviness, lay and flaw [19], as shown in Figure 2.2. The primary surface roughness includes waviness and roughness, as shown in Figure 2.2c.

2.2.1 Waviness and lay

Lay is the direction of the surface pattern (Figure 2.2b), and waviness is irregularities in which their wavelength is greater than the wavelength of surface roughness [19], as shown in Figure 2.2c. The waviness is caused by vibration, noise, heat treatment and deflection in the workpieces [19]. The surface roughness can be analysed and measured when the waviness is removed from the primary surface.

2.2.2 Surface roughness

Real engineering surfaces are not perfectly smooth. The surfaces are made of various defects and distortions and have a strong influence on wear and lubrication [7]. Surface roughness is a characteristic of surface topography that indicates that a real surface is

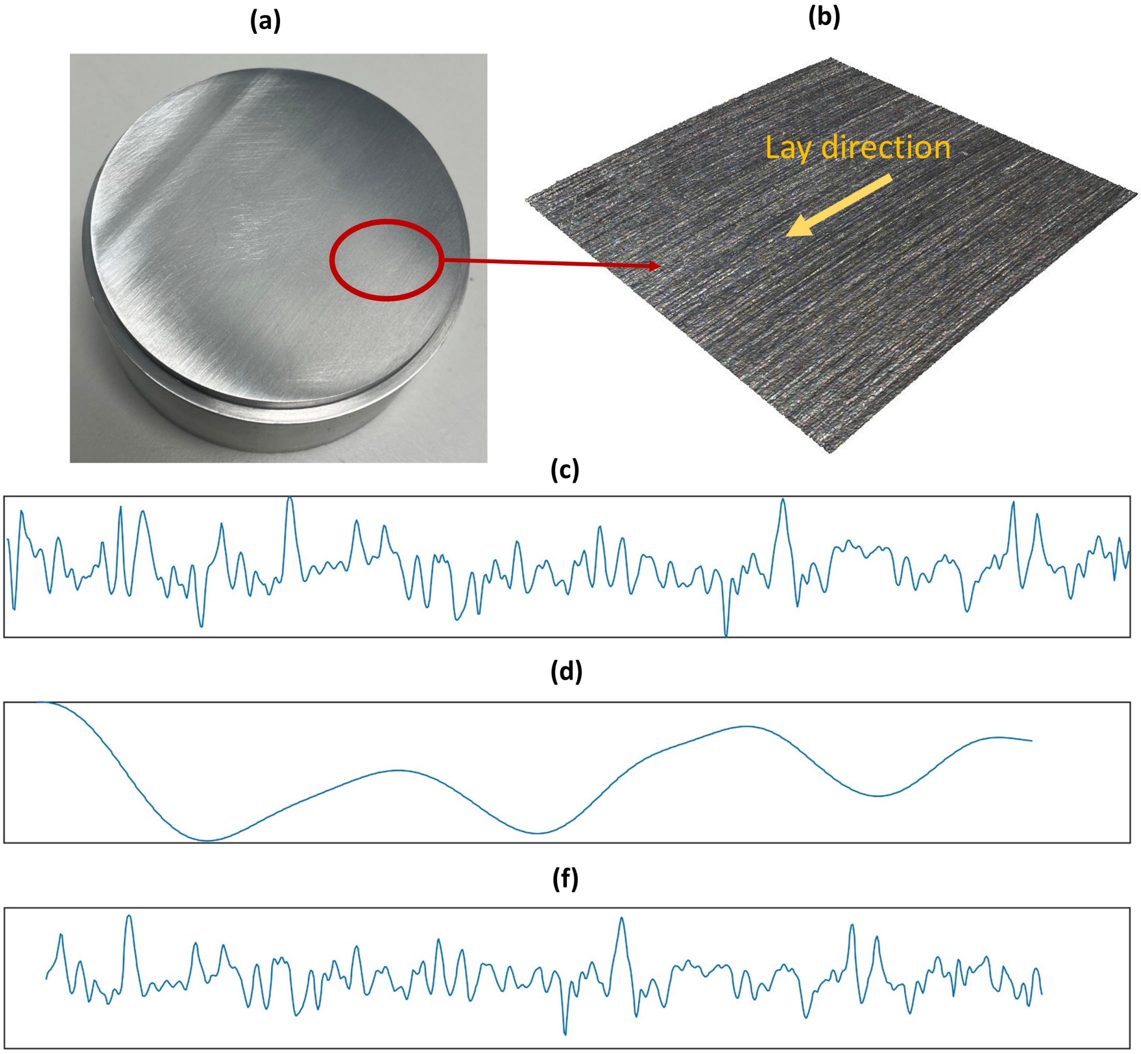

Figure 2.2: Surface topography scanned by a 3D optical profilometer: (a) real engineering surface; (b) lay direction; (c) primary surface (both waviness and surface roughness) ; (d) waviness; (f) surface roughness.

a series of peaks and valleys. These peaks and valleys are randomly distributed. The peaks of a two-dimensional surface profile are called asperity, while they are called summits in a surface map [19]. Two parameters are required to describe surface roughness: variation of height and distribution of height variation [7]. As these parameters are randomly varied, some statistical parameters are required to describe them [7]. Some statistical measurements describe the height variation of a surface, as shown in Figure 2.3. The centre-line average of height R_a, determines the average surface roughness of peaks and valleys, and for the finite size of a surface is given by

[7]:

$$R_a = \frac{1}{L}\int_0^L |z|dx \tag{2.1}$$

where L is the sampling length, x is the profile length axis and z is the height of the profile length along x. As seen in Eq. 2.1, R_a measures the magnitude of the height, and the nature of the peak or valley has no influence on the measured surface roughness. Therefore, one of its disadvantages is that R_a gives the same surface roughness despite the distribution of the peak and valley. To overcome this limitation, root-mean-square R_q is defined as [7]:

$$R_q = \sqrt{\frac{1}{L}\int_0^L z^2 dx} \tag{2.2}$$

The other surface roughness parameter is ten-point height R_z. This parameter averages the height of ten consecutive peaks and valleys within the sampling length and is given by [7]:

$$R_z = \frac{\sum_{i=1}^{5}|p_i| + \sum_{i=1}^{5}|v_i|}{5} \tag{2.3}$$

where p_i and v_i are the height of i^{th} peak and valley, respectively. Unlike R_a, the nature of the peak or valley influences the surface roughness measured by R_z.

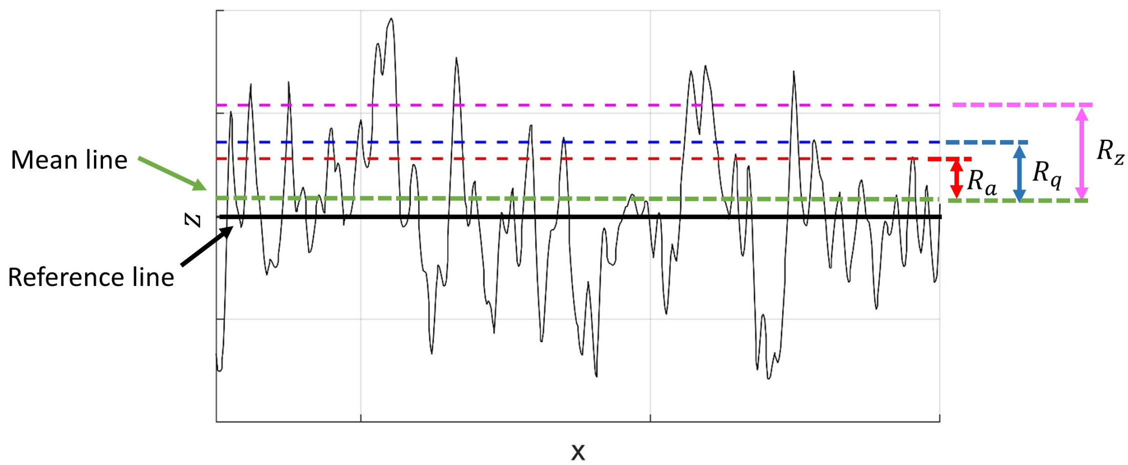

Figure 2.3: Surface roughness measured with a 3D optical profilometer of a real surface to show the different surface roughness parameters.

2.2.3 Grinding and polishing

When the surfaces come into contact, their asperities or summits create real contact. Real engineering surfaces are manufactured using a variety of methods and techniques. The surface finished by these methods is required to be ground and/or polished to achieve the desired surface roughness that fits their use. For the current study, EcoMet30 and AutoMet250 (as shown in Figure 2.4 were used to create surfaces with different roughness using silicon carbide papers from P180 to P2500 grit size.

(a) **(b)**

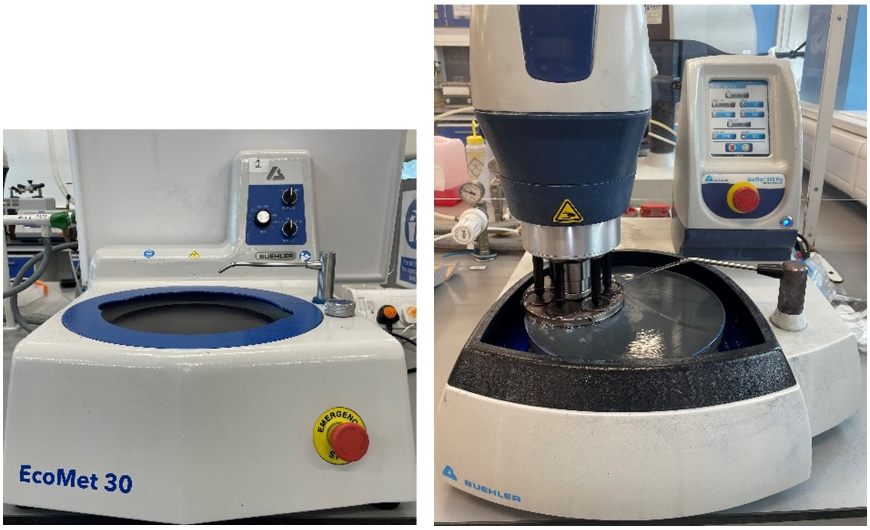

Figure 2.4: Grinding and polishing machines: (a) EcoMet30; (b) AutoMet250.

2.2.4 Surface profile measurement techniques

The surface roughness can be measured using machines based on contact or non-contact measurements. In a contact-type surface roughness instrument (as shown in Figure 2.5a), a stylus tip comes into direct contact with the surface of the sample. As the stylus moves along a desired direction, the vertical direction records the height of the surface profile with a finite sampling frequency. These profilometers are suitable for line measurement (2D measurement) and are transparent and opaque. However, the size of the tip of the stylus limits the roughness scale of the surface.

A 3D optical roughness measurement device (Alicona Infinite SL) is a non-contact and non-destructive surface roughness instrument, as shown in Figure 2.5b. These profilometers emit light to the desired surface and capture reflected light from the surface. The reflected light is compared to the reference light, and the difference is used to measure the height of the surface's peaks and valleys.

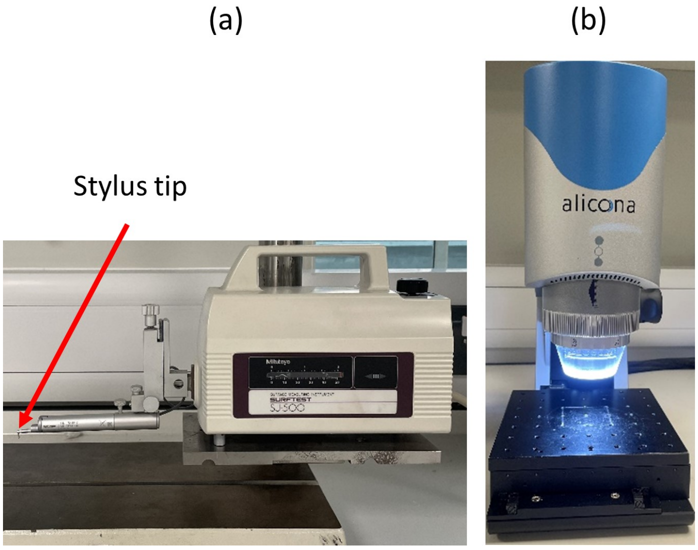

Figure 2.5: Surface roughness measurements instruments: (a) contact-type (Mitutoyo SJ-500P); (b) non-contact type (Alicona Infinite SL).

One of the standards used to measure surface roughness is ISO 4288, as shown in Table 2.1. For example, when the surface roughness is between 0.1 and 2.0, the measurement length must be 4 mm. In this standard, both surface roughness instruments shown in Figure 2.5 are used.

Table 2.1: Standard ISO 4288 for surface roughness measurement.

Non-periodic profiles $R_a(\mu m)$	Cutoff length $\lambda_c(mm)$	Evaluation length $I_n(mm)$
< 0.2	0.08	0.40
0.02< R_a <0.1	0.25	1.25
0.1< R_a <2.0	0.80	4.00
2.0< R_a <10	2.50	12.5
10< R_a <80	8.00	40.0

2.3 Lubricant

Lubricants are used mainly to control friction and wear [7]. One of the main aspects of the quality of a lubricant is its resistance to degradation [7].

2.3.1 Viscosity

Viscosity is one of the fundamental parameters of any lubricant and is defined as the resistance of a fluid to motion or deformation under shear stress or sliding. When a tangential force is applied to the surface of a fluid, the particles slide against each other. This sliding generates internal friction, which is known as viscosity [1]. Figure 2.6 shows two plates separated by a fluid with thickness L. The shear rate of the

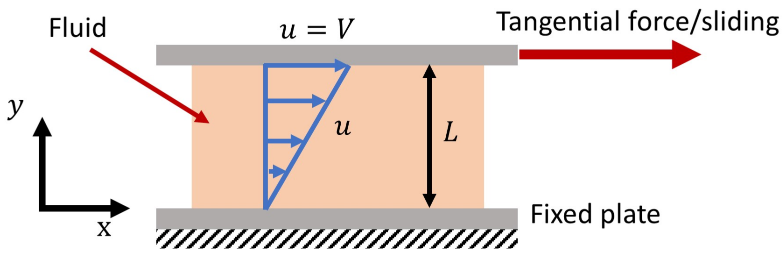

Figure 2.6: Schematic of Newtonian viscosity model.

fluid is given by:

$$\dot{\gamma} = \frac{du}{dy} \tag{2.4}$$

where du is the velocity of the upper plate, and dy is the fluid film thickness. The shear stress is determined by:

$$\tau = \frac{F}{A} \tag{2.5}$$

where F is the tangential force and A is the area of the upper plate in contact with the fluid. According to Newton's law of viscosity, a Newtonian fluid is a fluid when the shear rate and shear stress are linearly proportional:

$$\tau = \eta\dot{\gamma} \tag{2.6}$$

η is constant for Newtonian fluid and is called dynamic viscosity in the unit of Ns/m^2. Distilled water and acetone are examples of Newtonian fluids. The fluid is called non-Newtonian when the shear stress and shear rate are not linearly proportional. The viscosity of the non-Newtonian fluid varies as the shear rate changes; therefore, at each shear rate, Eq. 2.6 should be used to determine the dynamic viscosity of the fluid. Figure 2.7 shows the shear stress and viscosity of Newtonian and non-Newtonian fluids against the shear rate. A Bingham fluid behaves as a solid material at low shear stress; however, as the shear stress exceeds the yield stress, it becomes fluid [1]. An example of a Bingham fluid is toothpaste [1]. Shear thinning fluids are those whose viscosity decreases as shear stress increases, such as an engine oil [1]. Shear thickening fluids behave in a way opposite to the shear thinning fluids [1].

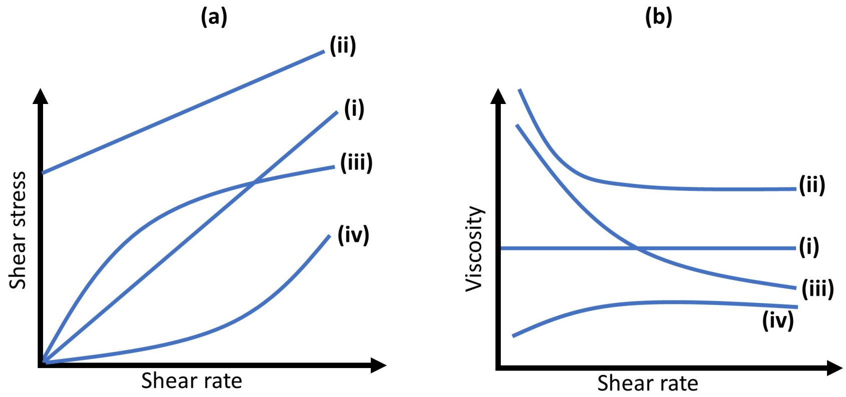

Figure 2.7: Behaviour of Newtonian and non-Newtonian fluids against shear rate adapted from [1]: (a) shear stress ; (b) viscosity; (i) Newtonian fluid; (ii) Bingham fluid; (iii) shear thinning fluid; (iv) shear thickening fluid.

2.3.2 Viscosity measurement techniques

There are different instruments to measure dynamic viscosity, such as rotational viscometers (Figure 2.8a). Rotational viscometers can measure the viscosity of Newtonian and non-Newtonian fluids. The two common types of these viscometers are parallel plates and cone-on-plate viscometers, as shown in Figures 2.8b and 2.8c. The parallel plates are suitable for measuring the viscosity of Newtonian fluids, while the cone-on-plate is used for non-Newtonian fluids.

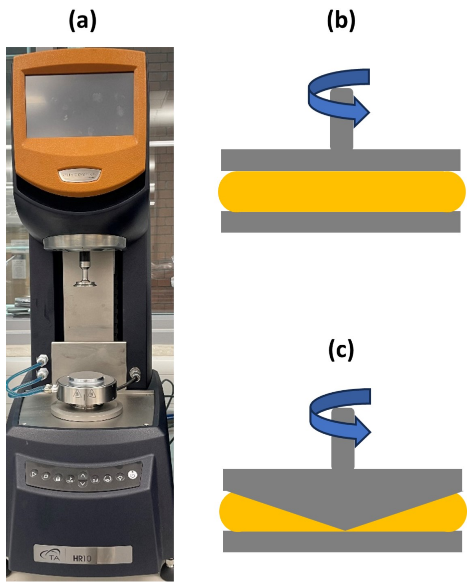

Figure 2.8: Rotational viscometer: (a) TA Instruments rheometer HR 10; (b) parallel plates; (c) cone-on-plate.

Chapter 3

Background of Ultrasound

This chapter briefly presents the background of ultrasound, its modes and the techniques required for the current work. It describes how ultrasound propagates in a medium and discusses the factors and parameters that affect ultrasonic waves.

3.1 Ultrasonic plane waves

Ultrasound is a mechanical wave propagating in a medium at a frequency between 20 KHz and 1 GHz. In this frequency range, particles of the medium oscillate around the equilibrium position (an unperturbed medium without ultrasound). Mechanical energy is transferred to neighbouring particles and the ultrasonic waves propagate in the medium. Ultrasonic waves are propagated in a solid or fluid medium in different wavefronts, such as plane waves. Plane waves are the waves where the wavefronts are parallel [20].

3.1.1 Longitudinal wave

In the longitudinal wave (or primary wave), the particles oscillate about their equilibrium state along the direction of wave propagation, as shown in Figure 3.1. A longitudinal wave consists of two parts: rarefaction and compression. As the wave propagates, the compression part pushes the particles toward each other. The rarefaction (tensile) part separates particles. The wavelength is the distance that contains both the rarefaction and compression parts. Longitudinal waves are capable of propagating in solids and fluids.

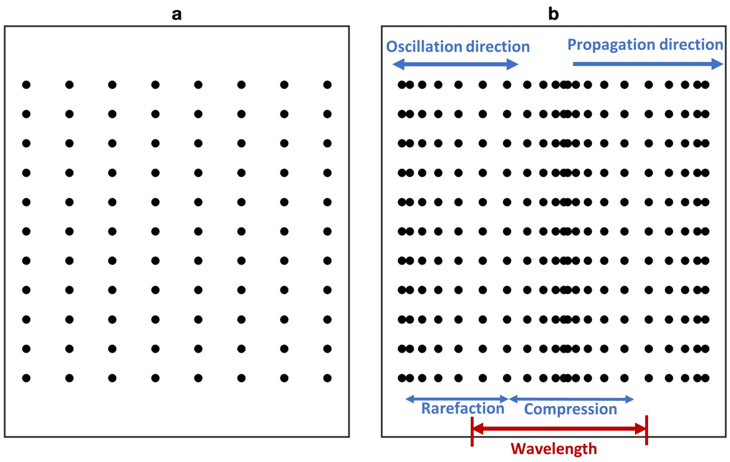

Figure 3.1: Schematic diagram of particles of a medium at: (a) equilibrium (unperturbed or in the absence of ultrasound); (b) longitudinal wave propagation.

3.2 Speed of sound

Sound is a mechanical wave and travels by oscillating particles in a medium. It depends on the density, elastic modulus or shear modulus (for solids) or bulk modulus (for fluids) of the medium based on the propagation modes. The speed of sound for longitudinal waves in solids is given by [21]:

$$c_l = \sqrt{\frac{E(1-\nu)}{(1+\nu)(1-2\nu)\rho}} \tag{3.1}$$

where E is the elastic modulus (the resistance of materials to elastic deformation), ν is the Poisson's ratio, and ρ is the density of the solid. The speed of sound (Eq. 3.1) in one dimension propagating parallel to the main axis of the transducer can be given as [22]:

$$c_l = \sqrt{\frac{E}{\rho}} \tag{3.2}$$

The speed of sound for fluid is given by:

$$c_0 = \sqrt{\frac{B}{\rho}} \tag{3.3}$$

where B is the bulk modulus. The speed of sound is also influenced by the temperature and stress of the medium in which it propagates. However, it is independent of the frequency of the sound waves.

Time-of-flight (TOF) is a technique that can measure the speed of sound in a medium. The distance of the ultrasonic waves travelling in a medium is known, and the time of the sound from the sound source and a receiver (a microphone or a transducer) is also known. The speed of sound is then determined by:

$$c = \frac{L}{t} \tag{3.4}$$

where L is the travelled distance and t is the time of travel. Table 3.1 shows the speed of sound of some materials at room temperature.

Table 3.1: Speed of sound in longitudinal and shear modes of engineering material at room temperature [23, 24].

Medium	Longitudinal velocity (m/s)	Shear velocity (m/s)
Aluminium	6420	3040
Mild steel	5900	3200
Distilled water	1498	-
PAO 40	1484	-

3.3 Acoustic impedance

The resistance of a medium to ultrasound propagation is called acoustic impedance Z. Acoustic resistance is a function of material properties and the speed of sound. For solids, the acoustic impedance is a real value and is given by:

$$Z = \rho c \tag{3.5}$$

where ρ is the density of the solid. It is seen from Table 3.2 that the acoustic impedance in solids is significantly greater than in fluids.

Table 3.2: Acoustic impedance of solids and fluids at room temperature [23, 24].

Medium	Density ρ (kg/m^3)	Acoustic impedance Z (MPas/m)
Aluminium	2700	17.33
Stainless steel	7850	45.45
Distilled water	998	1.49
PAO 40	850	1.26

3.4 Attenuation

As sound waves propagate in a medium, their energy is reduced. This reduction is called attenuation. The sources of sound attenuation are friction absorption and scattering [25, 26]. Absorption occurs as the sound energy is reduced to overcome internal friction and converted to heat [24]. When an ultrasonic beam incident a flaw, crack, grain of a medium or imperfect contact between two solids, it reflects in all directions due to the acoustic impedance mismatch of the air and the medium (for the crack, flaw and imperfect contact), called scattering. If the wavelength of the ultrasonic waves is 10^{-3} to 10^{-2} of the wavelength, the scattering is negligible [25]. If the size of the gap at the interface (caused by the rough interface of the solid-solid contact) is compatible with the ultrasonic waves, scattering occurs [10, 13]. Chapters 6 and 9 discuss ultrasonic attenuation for linear and nonlinear ultrasound in solid and liquid lubricants.

3.5 Diffraction

When a sound beam passes around the edge of an object, the tips of cracks or through an ultrasonic transducer, it bends or spreads, which is called diffraction [26, 27]. The wavefronts in the regions near the ultrasonic source are planar [28]. As waves propagate further from the interface, they become spherical, known as beam spreading [28]. The spread of the beam is also called diffraction [28, 22]. For consistency with other nonlinear ultrasound resources in fluids, this definition is used in this study for the nonlinear behaviour of ultrasound in liquid lubricants (Chapters 9-11).

3.6 Reflected and transmitted ultrasonic waves

Figure 3.2 shows two perfectly bonded media at the interface. An ultrasonic source generates an ultrasonic wave called incident wave f. Part of the ultrasonic wave is reflected G, and part of it is transmitted H. The reflection coefficient is defined as the ratio of the reflected waves to the incident waves and is given by [12]:

$$R = \frac{Z_2 - Z_1}{Z_1 + Z_2} \tag{3.6}$$

where Z_1 and Z_2 are the acoustic impedances of medium 1 and 2, respectively. As the contact is perfectly bonded and the incident wave hits the interface perpendicularly, the loss of ultrasonic energy in Eq. 3.6 is not considered [12, 25]. The continuity of pressure and displacement must be satisfied at the boundary of the perfect contact [24]. Therefore, the relationship between the reflected and transmitted ultrasonic energy is $1 + R = T$ [24].

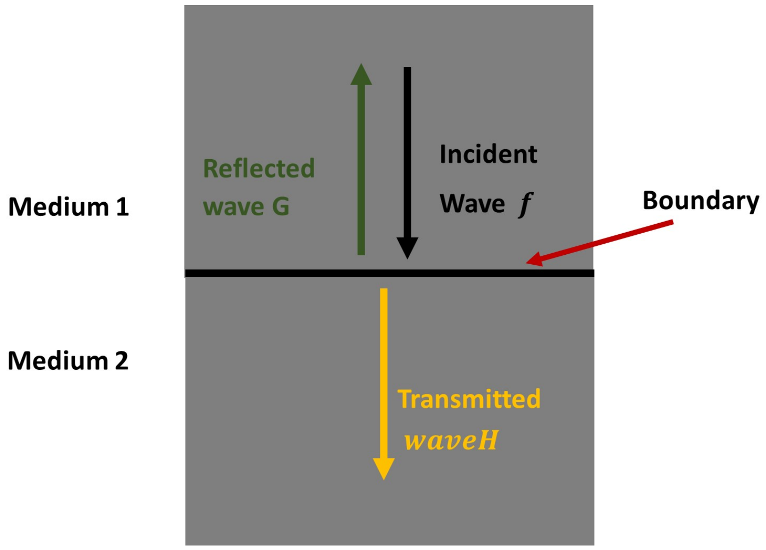

Figure 3.2: Schematic diagram of incident (f), reflected (G) and transmitted (H) ultrasonic waves at the interface.

Chapter 4

Literature Review

This chapter discusses a literature study of interfacial stiffness, oil degradation detection and monitoring and ultrasound as a measurement method. It mentions the gap between previous studies and links this thesis's novelties to the gaps.

4.1 Linear and nonlinear normal interfacial stiffness

When two solid surfaces come into contact, it is the asperity peaks that touch, and the real contact area is substantially less than the nominal contact area [10]. Applying pressure to the surfaces causes a small approach of the mean lines of their roughness. The interfacial stiffness (per unit area) is then defined as the rate of change in contact pressure with the approach of the mean lines of the roughness of the contact surfaces [29]. A low nominal contact pressure is required to deflect the asperities if the real contact area is low. Increasing the nominal contact pressure brings more asperities into contact, and the interface becomes stiffer; hence, the stiffness of the interface is a nonlinear variable. Interfacial stiffness is important in tribology because it affects machine element deflection, wear and friction since stiffer interfaces tend to have less deflection. Machining precision, for example, depends on the stiffness of the joints in the machine tool assembly [29].

Several studies have focused on the interfacial stiffness of rough contact from both theoretical and experimental perspectives. An early example from Mindlin [30] provided a theoretical model for the elastic contact of a smooth curved surface. Later, Greenwood and Williamson [31] presented a statistical model (GW model) for the relation between the contact area of the rough elastic mating surfaces and the applied pressure. The model is limited by two assumptions: first, asperities are treated as a distribution of hemispherical capped peaks, and secondly, the peaks are treated as independent such that the deformation of one peak does not affect its neighbours. The relationship between the contact area and the applied pressure is also presented by models such as the Whitehouse-Archard-Onion (WAO) model [32, 33] and the Buh-Gibson-Thomas (BGT) model [34]. These models have been widely used to predict contact stiffness. Campana et al. [35] used Mindlin's theory to measure the stiffness ratio of stationary contacts.

Digital image correlation (DIC) [36, 37, 11] has been used to measure joint stiffness. In this method, a series of images are taken before and during loading from the interface and surrounding area. The comparison of the images shows the relative displacement. A plot of the applied load measured with a load cell is created against the relative surface displacement; the gradient gives the contact interface. Although it has advantages such as full field capability and high resolution, the main limitation is that a surface near the contacting surfaces must be accessible for the camera to capture images. In many elements of engineering machinery, optical access is limited, limiting the application of DIC outside a laboratory setting. Another method is to measure the displacement of the interface directly under the applied load. Chikate et al. [38] measured the displacement of a smooth surface directly using strain gauges and spring-loaded pins. For example, Handzel-Powierza et al. [39] used a tensometric bridge to measure the applied load and an indicator sensor to measure the surface approach. They compared their results to theoretical predictions from the GW model in the range of elastic deformation for quasi-isotropic surfaces. However, this technique is restricted to low contact stiffness (1 GPa/μm) [40].

Measurement of contact stiffness from the resonance frequency of a structure is also possible. This contact frequency method uses a relationship between the contact stiffness and the natural frequency of the mating surfaces [41]. One of the disadvantages of this method is the need for vibration response equations of the experimental tools [42]. The approach used here, also a vibrational method, is through the reflection or transmission of ultrasound [6, 8, 11–15]. The ultrasound technique has the advantage of being non-invasive and non-destructive, and it can measure on the surface inside a machine where desired surfaces are inaccessible. Reflection and transmission coefficients are the proportion of an incident wave reflected from or transmitted through the interface. The reflection coefficient depends on the amount of solid contact. The acoustic impedance of air is significantly small compared to that of solid materials, so the air gap at the interface causes more incident energy to reflect. Increasing the nominal contact pressure leads to an increase in the number of asperities in contact.

Therefore, less incident energy is reflected and more energy is transmitted [8]. Kendal and Tabor [43] and Tattersall [12] used a spring model, where the interface is treated as a distributed stiffness, to demonstrate that the reflection coefficient of an imperfect contact (incomplete contact) is dependent on the interfacial stiffness.

The authors have studied both normal and tangential interfacial stiffness in the linear regime using longitudinal or transverse polarised ultrasound, respectively [6, 8, 11–18]. Elastic and plastic rough surface contact models have been used to predict interface stiffness compared to ultrasonic measurement [40, 44, 45]. Krolikowski et al. [40, 44] presented a spring-damper model in a parallel configuration to address the effect of ultrasound attenuation. However, the results were still far beyond those predicted by the GW model. Rokhlin et al. [46] modelled the interface as a layer of equivalent materials such as viscoelastic materials. Their study is accurate in cases where the Poisson's ratio of the layer model is known. The principle has been modified by Du et al. [47], Xiao et al. [48] and Sun et al. [42].

These studies have been based on the linear response of an interface to an ultrasonic wave. The pressures generated by the wave and the resulting deflections are usually minimal, so the process is elastic and reversible. However, in recent years, there have been several studies based on higher-power ultrasound that cause nonlinear behaviour. The nonlinear behaviour may originate from the material itself, as the stress-strain relationship of the medium exceeds the yield strength (nonlinear elasticity). Alternatively, the interface may also be a source of nonlinearity. If the wave is of sufficient power, it can cause the opening and closing of the air gaps, which can lead to the generation of higher harmonics in the reflected/transmitted waves. This is known as contact acoustic nonlinearity (CAN) [49–51]. In Section 5.2, a description of the generation of higher harmonics (mechanics of CAN) is given.

Richardson [52] studied one-dimensional nonlinear wave propagation through identical contacting materials by considering the concept of CAN. He defined an analytical relation between the incident wave and the relative surface approach of the interface. Biwa et al. [53] used Richardson's findings to propose a nonlinear nominal contact pressure-relative surface approach relationship using a polynomial Taylor series to define linear and nonlinear normal interfacial stiffnesses using the reflection coefficient. nonlinear normal interfacial stiffness is important when a high-power ultrasound is used to define the interface. The wave distorts the interface, so a linear model can no longer describe the response of the interface. In previous studies, only transmission methods had been used to measure nonlinear normal interfacial stiffness. This method is impractical in most engineering structures, such as an engine with only one accessible side. In addition, the accuracy of the technique has not been validated. In the current study, the pitch-catch through reflection addresses this limitation, and the model is investigated for its accuracy.

4.2 Detection of oil degradation and contamination

Lubricants have a significant impact on energy consumption and the level of environmental pollution [54]. As lubricants circulate in an engine or machinery, they become degraded. There are various sources of degradation of the lubricant, such as oxidation, water contamination, soot, wear debris, and other particle contamination [55, 56]. The two approaches for lubricant drain times are hours/rotation/mile of engine or machinery operation and degradation monitoring [57].

Lubricant degradation monitoring is divided into offline and online approaches. In the offline method, a lubricant sample is collected from the machine and sent to the laboratory for examination. Although the results are accurate and well-detailed, measurement is not undertaken in the real-time run. Therefore, the results may be less relevant to the operation of real machinery [58]. This disadvantage is addressed by using online degradation monitoring, where the lubricant condition is continuously monitored as the machinery operates. The monitoring of lubricant degradation (both offline and online) is categorised into four main groups [55]: electrical or magnetic techniques [59–62]; chemical methods [63]; optical methods [64, 65]; and physical methods. Measurement of the variation of the dielectric constant is one of the electrical and magnetic methods to monitor oil degradation [62, 66, 67]. In this method, special capacitors are used. When the lubricant is placed between the poles, the dielectric constant is measured and compared to fresh oil [55]. The variation of the dielectric constant is used to measure oil oxidation, water contamination, and wear debris [55]. The main disadvantage of using electrical and magnetic techniques is that any failure in the electrical circuit, such as the resistance of the poles, gives less accurate results. The chemical methods are based on measuring the total acid number and flash temperature [63]. This method is an offline method. Fourier Transform Infrared (FTIR) spectroscopy [68, 69] is an optical method based on the absorption/transmission of optical radiation [54]. The molecular bonds of the lubricants can absorb infrared radiation at different frequencies [54]. The FTIR spectroscopy is used to measure carbon black content, water and, in particular, oxidation in a degraded lubricant [54, 70–72]. Some of the molecules have similar functional groups, such as water, glycol and phenol, which makes the FTIR spectroscopy results less accurate [54]. This limitation may be improved by using the concept of near infrared radiation (IR) in an engine [54, 73, 74]. However, prior knowledge of the wavenumber of functional groups of the oil is required, which makes the FTIR spectroscopy method more complicated.

Oxidation, wear debris, water, particle contamination and other sources of degradation affect the viscosity of lubricants [58]. Likewise, a change in viscosity during machinery operation can accelerate the degradation of the lubricants. For example, as the viscosity becomes thinner, the lubricant film thickness between the journal bearing and the crankshaft decreases. This viscosity thinning increases the metal-metal contact and consequently increases the level of wear debris in the lubricants. Therefore, the viscosity variation of a lubricant can be measured to detect lubricant degradation. This delays damage and failure in mechanical engineering operating systems. Most physical techniques used in lubricant degradation monitoring are based on viscosity measurements. The conventional methods to measure the viscosity of lubricants are capillary, falling body and rotational viscometers. These viscometers provide accurate results and are mainly used in laboratories (offline methods). Although there are some in-situ viscometers, such as oscillatory [75, 76], they are either unable to measure the viscosity of non-Newtonian or provide a less accurate measurement [77]. These methods are also limited to a low shear rate [77]. Ultrasonic viscometers [78–82] are conventional techniques for online viscosity measurement.

Ultrasound is a non-invasive and non-destructive method. It has a wide range of applications in mechanical engineering, such as measurements of contact stiffness [2, 10, 14, 53, 83], oil film thickness [84–88], and viscosity [9, 81, 89]. Mason et al. [90] investigated whether rapidly sheared liquids exhibit a shear elastic effect and viscosity. They related the reflection coefficient to the shear acoustic impedance of the liquid. Roth et al.[91] introduced the first ultrasonic viscometer fabricated with a piezoelectric element to generate shear ultrasonic waves. Cohen-Tenoudji et al. [92] used shear mode ultrasound to measure the dynamic viscosity of a thermal curing resin. They bonded a shear piezoelectric element to a copper buffer. The reflection coefficient was used to measure the dynamic viscosity of the resin. All the methods presented by [90–92] used analogue signal analysis, which is time consuming [93]. Alig et al. [93] used a single-frequency pulse burst system to generate shear ultrasonic waves for the experimental setup proposed by Mason et al. [90]. Greenwood et al. [94] used both longitudinal and shear ultrasonic waves to measure the viscosity of water, the water-sugar solution and silicon oil. The main disadvantage of using the solid-lubricant interface to measure viscosity is the relatively small difference in the reflection coefficient of the viscous liquid. It was also shown in [95]. Greenwood et al. [94] used the sixth reflected signal from a solid-liquid interface to improve this limitation. However, this makes the measurement less accurate. Ju et al. [80] used two longitudinal immersion transducers to empirically measure the mineral oil's shear viscosity. The error of their results was between 8.8 % and 12.5 %. In addition to this uncertainty, they had to use a reference oil and voltage to sound pressure for the experiment, which made the experiment more complicated.

These studies have been based on the linear behaviour of ultrasound. In the linear behaviour of ultrasound, a low amplitude of ultrasound is generated by a piezoelectric element. The generated mono-frequency ultrasonic waves propagate in the liquid lubricant and are either reflected from a boundary or captured by a receiver. The captured signals have the same frequency as the incident waves. When high-power ultrasonic signals are generated in a liquid lubricant, they distort, and higher-order harmonics are generated. This behaviour is called the nonlinear behaviour of ultrasound. In Sections 9.1 and 9.2, a description of the nonlinear ultrasound mechanism is described. There have been many studies on the nonlinear behaviour of ultrasound to measure fluid nonlinearity [28, 96–98]. However, none of the studies used this nonlinear behaviour for online lubricant degradation monitoring, which is proposed in this study.

Chapter 5

Analytical and Numerical Analysis of Nonlinear Behavior of Ultrasound at Contact of Solids

When high-power ultrasonic waves are incident on an imperfect contact, the reflected or transmitted waves are distorted. These distortions appear as higher-order harmonics in the frequency domain of the waves and are called contact acoustic nonlinearity (CAN). The current chapter aims to use the analytical and numerical models for CAN to understand its mechanism and the parameters that influence it. In addition, the accuracy of the analytical and numerical models is investigated.

The high-power ultrasonic waves and the applied load here do not cause geometry nonlinearity because they do not cause large geometric deformations. Therefore, only material and contact nonlinearities are considerable.

5.1 Ultrasonic waves reflected and transmitted from contact

The equations used in this chapter follow [52]. Consider two linear elastic media in contact subjected to a one-dimensional elastic longitudinal ultrasonic wave (Figure 5.1). The direction of ultrasound propagation is through the thickness of the medium, defined as the x-axis. The origin of the x-axis is the point of first contact of the surfaces. The mean roughness lines above and below the interface are X_- and X_+, respectively (Figure 5.1a). The separation (mean gap) between the two surfaces under zero load is then given by $(X_+ - X_-)$. When there is no elastic wave, the surfaces are in static equilibrium under a nominal contact pressure p_0 that causes an equilibrium separation h_0 (Figures 5.1b and 5.1c). When an elastic wave passes through the

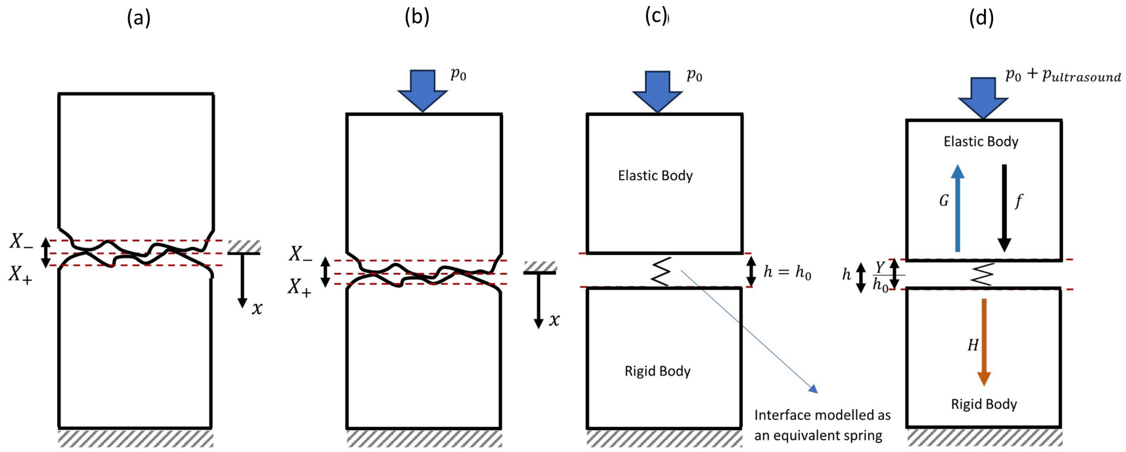

Figure 5.1: Schematic diagram of the asperity junctions and ultrasonic wave propagation through the media adapted from [2]: (a) aluminium blocks and asperity contact in the absence of normal load; (b) origin and direction of the positive propagation axis; (c) contacting surfaces in the absence of elastic wave under static equilibrium; (d) relative surface approach and surface separation due to propagating elastic wave.

interface of surface separation, $h(t)$ is cyclically reduced, and then the equilibrium value is increased by h_0. The relative surface approach $Y(t)$ is defined as the difference between the separation variation with time $h(t)$ and the equilibrium separation h_0, $(Y(t) = h(t) - h0)$. In the absence of an elastic wave, the relative surface approach $Y(t)$ is zero. The sign of the relative surface approach $Y(t)$ is opposite to the direction of loading/unloading by the wave. During the loading process by the elastic wave, the relative surface approach $Y(t)$ is negative, whereas during the unloading process, it is positive. To clearly illustrate the relative approach of the surfaces (assuming that the lower body is fixed and the upper moving), the upper body is considered to be rigid and flat, while the lower body is elastic and rough (Figure 5.1c).

The elastic wave pressure superimposed on the nominal contact pressure p_0 generates a relative surface approach $Y(t)$, which varies over time (shown in Figure 5.1d). Increasing the nominal contact pressure p_0 decreases the separation of the surfaces.

The equations described in this section follow the method presented in [2, 52, 53]. The equation of the interface subjected to a one-dimensional longitudinal ultrasonic wave is given by:

$$\rho \frac{\partial^2 u}{\partial t^2} = \frac{\partial \sigma}{\partial x} \tag{5.1}$$

The stress-displacement relation is given by:

$$\sigma(x,t) + p_0 = E \frac{\partial u}{\partial x} \tag{5.2}$$

where E is the elastic modulus considering the longitudinal direction only, ρ is the density of the media, $\sigma(x,t)$ is the normal stress generated by the ultrasonic wave and p_0, $u(x,t)$ is the displacement of the ultrasonic wave and p_0 is the nominal contact pressure. It should be noted that the contact pressure is either nominal or real. The real contact pressure is the ratio of the applied load to the real contact area, while the nominal contact pressure is the ratio of the applied load to the cross-sectional area. The real contact area is where the asperities of the contacting surfaces are in touch. This area is smaller than the nominal contact area. The general solution of Eq. 5.1 results in the displacement of each side of the interface:

$$\begin{cases} u(x,t) = f(x-ct) + G(x+ct) \quad ; \quad x < X_- \\ \\ u(x,t) = H(x-ct) \quad ; \quad x > X_+ \end{cases} \tag{5.3}$$

where $u(x,t)$ is the total displacement of the interface, c is the speed of sound in the media (Eq. 3.2), t is time of flight (TOF) of ultrasound, $f(x-ct)$ is the incident wave, $G(x+ct)$ and $H(x-ct)$ are the reflected and transmitted wave, respectively. The upper and lower media displacement is $x < X_-$ and $x > X_+$, respectively. The boundary condition at the interface is defined by:

$$\sigma(X_+,t) = \sigma(X_-,t) = -p(h(t)) \quad ; \quad p(h_0) = p_0 \tag{5.4}$$

where $h(t)$ is the rough surface mean line separation (surface separation) variation with time (as the ultrasonic waves are incident on the interface, the interface moves with time in one dimension in the direction of the ultrasonic wave propagation) and h_0 is the separation under static equilibrium ρ_0 in the absence of the elastic wave (as shown in Figure 5.1). A negative sign pressure term indicates compression at the interface. Substituting Eq. 5.4 into Eq. 5.2 gives:

$$\begin{cases} \frac{\partial u(X_-,t)}{\partial x} = \frac{-1}{E} p(h(t)) + \frac{1}{E} p_0 \\ \\ \frac{\partial u(X_+,t)}{\partial x} = \frac{-1}{E} p(h(t)) + \frac{1}{E} p_0 \end{cases} \tag{5.5}$$

The relative surface approach $Y(t)$ of the mating surfaces is defined as the difference in the wave displacement $u(x,t)$ of both sides of the interface (Figure 5.1d):

$$Y(t) = u(X_+,t) - u(X_-,t) = h(t) - h_0 \tag{5.6}$$

Eq. 5.6 shows that the relative surface approach $Y(t)$ can be used instead of the surface separation $h(t)$. The translational motion of the interface is defined by:

$$X(t) = \frac{u(X_+,t) + u(X_-,t)}{2} \tag{5.7}$$

The interface displacement is considered to be excited by the incident wave only [52]:

$$X(t) = f(x - ct) \tag{5.8}$$

The ultrasonic waves propagate in space at different times. Therefore, two independent variables, x for space and t for time, are required. The argument $(x - ct)$ is used for the incident and transmitted waves as they are forward-travelling. In contrast, the argument $(x + ct)$ is used for the reflected wave from the interface as it is backward-travelling and is in the opposite direction to the incident wave. Differentiation of Eq.s 5.6 and 5.8 with respect to time gives:

$$\dot{X}(t) = -c\frac{\partial f(x - ct)}{\partial(x - ct)} \tag{5.9}$$

where dots denote the differentiation with respect to time.

$$\dot{Y} = c\left[-\frac{\partial H(X_+ - ct)}{\partial(X_+ - ct} + \frac{\partial f(X_- - ct)}{\partial(X_- - ct)} - \frac{\partial G(X_- + ct)}{\partial(X_- + ct)}\right] \tag{5.10}$$

Eq. 5.10 is expressed in terms of incident, reflected, and transmitted ultrasonic waves; it is necessary to reduce this in terms of only the incident wave and nominal contact pressure. To do this Eq. 5.3 is differentiated with respect to x:

$$\begin{cases} \frac{\partial u(X_-,t)}{\partial x} = \frac{\partial f(X_- - ct)}{\partial(X_- - ct)} + \frac{\partial G(X_- + ct)}{\partial(X_- + ct)} \\ \frac{\partial u(X_+,t)}{\partial x} = \frac{\partial H(X_+ - ct)}{\partial(X_+ - ct)} \end{cases} \tag{5.11}$$

Rearranging Eq. 5.11 to make the reflected and transmitted waves the subject gives:

$$\begin{cases} \frac{\partial G(X_- + ct)}{\partial(X_- + ct)} = \frac{\partial u(X_-,t)}{\partial x} - \frac{\partial f(X_- - ct)}{\partial(X_- - ct)} \\ \frac{\partial H(X_+ - ct)}{\partial(X_+ - ct)} = \frac{\partial u(X_+,t)}{\partial x} \end{cases} \tag{5.12}$$

Substituting Eq. 5.5 into Eq. 5.12 gives:

$$\begin{cases} \frac{\partial G(X_- + ct)}{\partial(X_- + ct)} = -\frac{1}{E}p(h(t)) + \frac{1}{E}p_0 + \frac{\partial f(X_- - ct)}{\partial(X_- - ct)} \\ \frac{\partial H(X_+ - ct)}{\partial(X_+ - ct)} = -\frac{1}{E}p(h(t)) + \frac{1}{E}p_0 \end{cases} \tag{5.13}$$

Substituting Eq. 5.13 into Eq. 5.10 gives:

$$\dot{Y} = 2c\frac{\partial f(X_- - ct)}{\partial(X_- - ct)} + \frac{2}{\rho c}\{p(h_0 + Y) - p_0\} \tag{5.14}$$

Eq. 5.14 is a first-order differential equation describing the relative surface approach regarding of the incident wave and the nominal contact pressure $p(h_0 + Y)$. Solving this differential equation results in an equation for the relative separation of the interface. Eq. 5.14 can be written in terms of surface separation $h(t)$:

$$\dot{h} = 2c\frac{\partial f(X_{-} - ct)}{\partial(X_{-} - ct)} + \frac{2}{\rho c}\{p(h) - p_0\} \tag{5.15}$$

The reflected ultrasonic wave is now defined in terms of the relative surface approach. Eqs. 5.5 and 5.6 give the relationship between the relative surface approach $Y(t)$ and translational motion of the contact interface X:

$$u(X_{-}, t) = X(t) - \frac{1}{2}Y(t) \tag{5.16}$$

Substituting Eq. 5.3 (for $x < X_{-}$) and Eq. 5.7 into Eq. 5.15 gives:

$$G(x + ct) = -\frac{1}{2}Y\left(t + \frac{x - X_{-}}{c}\right) \tag{5.17}$$

It can be seen from Eq. 5.17 that the reflected ultrasonic wave $G(x+ct)$ is expressed only in terms of the relative surface approach. The negative sign of the reflected wave indicates propagation in the opposite direction to the incident wave through the upper body. Eq. 5.17 gives the reflected waves from the interface. As mentioned in Section 5.1, the contact is assumed to be flat (perfect contact). Therefore, the ultrasonic waves $G(x + ct)$ are reflected from the entire contact area. The amplitude of the reflection is then substituted into Eqs. 7.12 and 7.15 to determine the reflection coefficients R and γ. The reflection coefficients R and γ are then substituted into Eqs. 7.14 and 7.16 to determine the linear and nonlinear normal interfacial stiffness.

5.2 Contact acoustic nonlinearity (CAN)

5.2.1 Analytical approach

The same approach is presented in [2, 52]. An interface consists of asperity contacts and air gaps. In the regions of the interface with the air gap, there is no contact between the surfaces (Figure 5.2a). The approach of the two surfaces depends on the magnitude of the applied pressure [99]. The applied pressure is the sum of the externally applied pressure and the pressure applied by the incident wave. A longitudinal incident cosinusoidal wave with an angular frequency w and amplitude A strikes the interface at time t_0:

$$f(x - ct) = A\,cos\left\{\frac{\omega}{c}(x - X_{-} - ct)\right\} \tag{5.18}$$

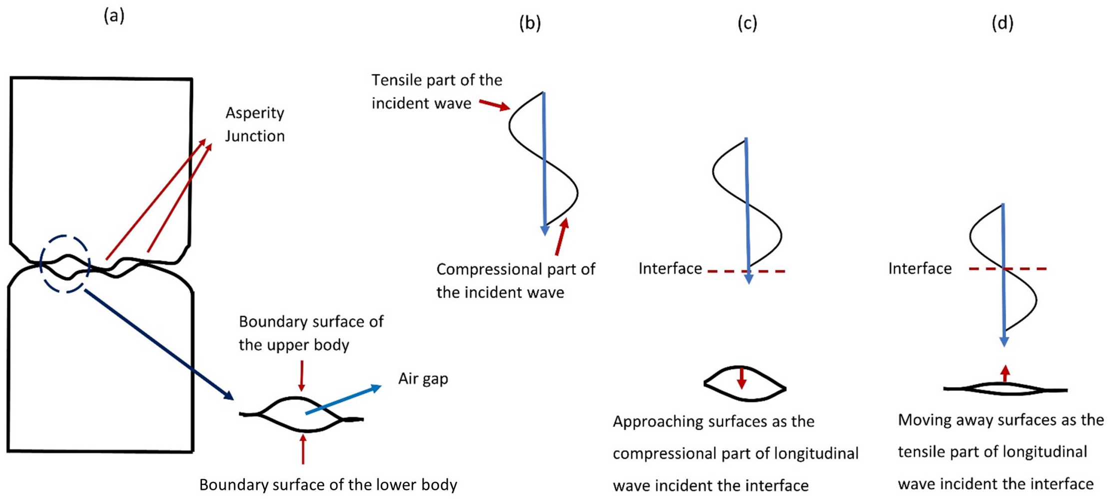

Figure 5.2: Schematic diagram of higher harmonic generation at an imperfect interface adapted from [2, 3]: (a) rough surface interface modelled as an array of gaps; (b) incidents ultrasonic wave interacts with the interface; (c) approaching surfaces; (d) being apart surfaces.

Substituting Eq. 5.18 into Eq. 5.15 at the interface gives:

$$\dot{h} = -2A\omega\ sin\omega t + \frac{2}{\rho c}\{p(h) - p_0\} \tag{5.19}$$

It is assumed that at time $t_0 = 0$, the gap is closed and remains closed until just before time t_1. For the sake of derivation, the gap is assumed to be fully closed; in reality, even under high pressure, there will be air gaps and the contact is not fully closed. Therefore, the gap separation h, velocity of gap separation $\dot{h}$, and relative surface separation Y are zero, subsequently, the initial surface separation h_0 is zero. When the gap is open at time t_1, the pressure at the interface is zero, so the boundary condition in Eq. 5.4 is:

$$\sigma(X_+, t) = \sigma(X_-, t) = -p(h(t)) = 0 \tag{5.20}$$

Substituting Eq. 5.20 into Eq. 5.19 gives time t_1:

$$sin\omega t_1 + \frac{p_0}{\rho c A\omega} = 0 \tag{5.21}$$

Eq. 5.21 is a nonlinear equation and in the present work, it is solved by the Newton-Raphson method. The gap remains open until time t_2. Integration of Eq. 5.19 with respect to time and substituting Eq. 5.20 in the interval $[t_1, t_2]$ gives an opening interval:

$$h(t) - h(t_1) = 2A\{cos\omega t - cos\omega t_1\} - \frac{2}{\rho c}p_0(t - t_1) \quad ; \quad t_1 \le t \le t_2 \tag{5.22}$$

Hence, at time t_2 the gap is just about to be closed; the right-hand side of Eq. 5.22 is zero. Time t_2 can be found using the Newton-Raphson method:

$$cos\omega t_2 - \frac{p_0}{\rho c A} t_2 - cos\omega t_1 + \frac{p_0}{\rho c A} t_1 = 0 \tag{5.23}$$

The gap remains closed until time t_3. The opening-closing gap transition is repeated periodically:

$$h(t) = \begin{cases} h(t_{2n}) \quad ; \quad t_{2n} \le t < t_1 + nT \\ \\ h(t_{2n}) + 2A\{cos\omega t - cos\omega(t_1 + nT)\} - \frac{2}{\rho c} p_0 (t - t_1 - nT); t_1 + nT \le t < t_2 + nT \end{cases} \tag{5.24}$$

where $n = 0, 1, 2, ...$ and T is the period of the incident wave.

A single incident longitudinal ultrasound wave cycle consists of two parts, causing tension and compression (Figure 5.2b). Figure 5.3 shows the surface separation at the interface of aluminium blocks subjected to a longitudinal wave with the centre frequency 2 MHz and amplitude 20 nm. The gap is initially assumed to be closed at time $t_0 = 0$. It is seen from Figure 5.3a that when the compression part of the wave reaches the interface (corresponding to zero to the point **a** on the incident wave), the applied pressure is large enough to keep the gap closed in the interval $[t_0,\ t_1]$ (also see Figure 5.2c). As the wave passes (corresponding to part of the wave between points a and b on the incident wave), the applied pressure is reduced so that the surfaces of the gap are open at time t_1 and are pulled apart away from the mean position (also see Figure 5.2d). After that, the applied pressure increases (corresponding to part of the wave between points b and c on the incident wave) and presses the surfaces of the gap closer together.

In the time interval $[t_2,\ t_3]$ the gap is closed as the applied pressure increases (corresponding to a part of the wave between points c and d in the incident wave). The opening-closing gap transition is repeated periodically. Figure 5.3b shows solid-solid contact and solid–air contact. The time domain signals presented in Figures 5.3b and 5.3c were converted to the frequency domain using the Fast Fourier Transform (FFT). It is seen that the surface of a solid-air contact freely moves; therefore, no higher harmonic is generated. However, higher harmonics are generated (both even and odd) in solid-solid contact (Figure 5.3d). Figure 5.3c shows the effect of nominal contact pressure on the opening and closing of the gap at the interface. It is seen that the higher nominal contact pressure closes the gap for a longer period, and the surfaces are less separated.

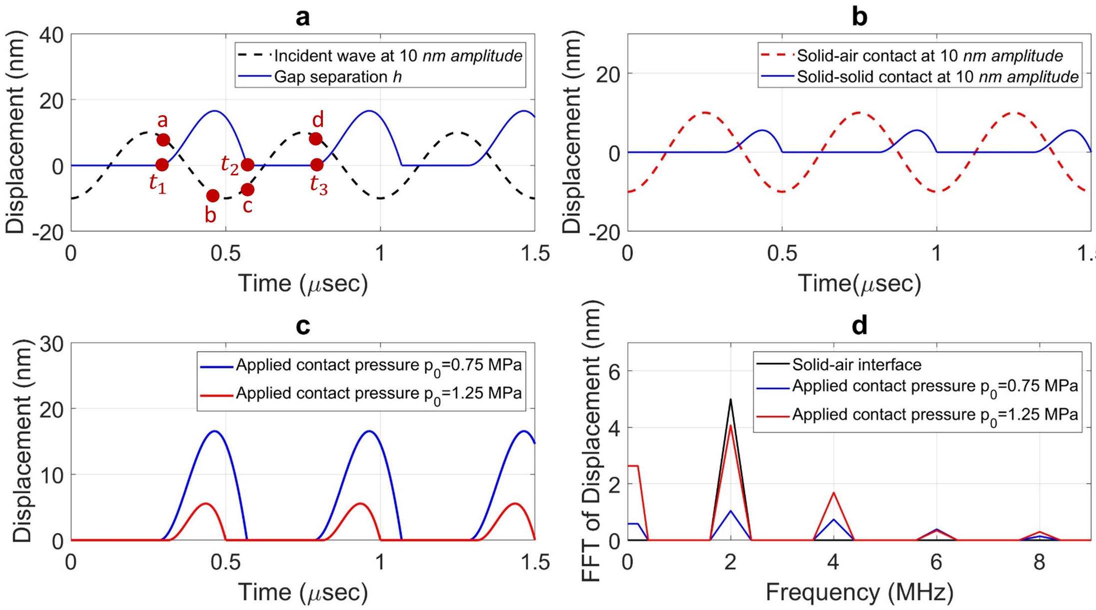

Figure 5.3: A theoretical approach for contact acoustic nonlinearity (CAN) at incident wave with amplitude of 10 nm: (a) comparison between incident wave and gap separation h in time domain; (b) comparison between reflected wave from solid-air contact (reference signal) and solid-solid contact at 0.75 MPa in time domain; (c) effect of nominal contact pressure on reflected wave from solid-solid contact at 0.75 MPa and 1.25 MPa in time domain; (d) frequency spectrum comparison of reflected waves from solid-air, and solid-solid contact at 0.75 MPa and 1.2 MPa in frequency domain.

5.2.2 Numerical approach

This section uses the same approach presented in [100] to simulate ultrasonic wave propagation in a solid medium and the effect of different parameters, such as the amplitude and frequency of excitations and the material properties of the media on the reflected ultrasonic waves. The propagation of ultrasonic waves in a solid medium can be numerically analysed using finite difference methods (FDM). In finite difference methods, the medium in which the ultrasonic waves propagate is discretised in both the space and the time domains, as shown in Figure 5.4. FDM is mainly based on explicit or implicit approaches. The explicit approaches solve the system's state at a later time using its state at the current time. However, the implicit methods use the later and current state of the system to solve desired equations. The implicit and explicit methods can be used for the study of ultrasonic waves. However, explicit methods are recommended for high contact nonlinearity. One of the most simple explicit FDM is based on the centre difference for both space and time with

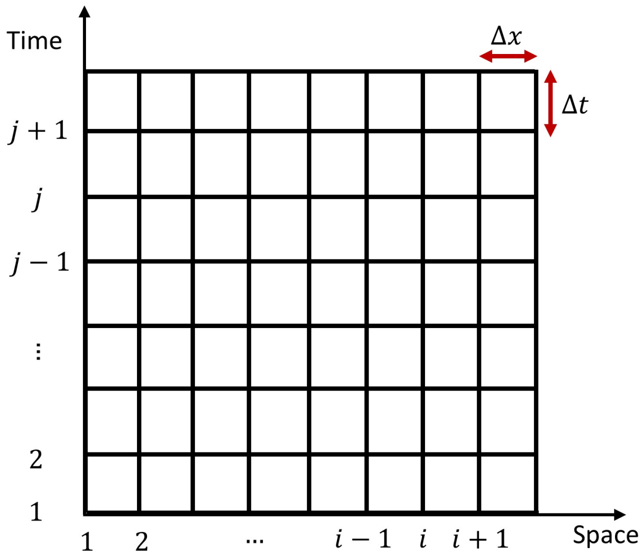

Figure 5.4: Schematic diagram of space and time discretisation for the one-dimensional system.

the subscript i and the superscript j, respectively. The wave equation in terms of displacement is derived by substituting into Eq. 5.2 into Eq. 5.1:

$$\frac{\partial^2 u}{\partial t^2} = c^2 \frac{\partial^2 u}{\partial x^2} \tag{5.25}$$

where c is the speed of sound in the medium. The discretised wave equation is given by:

$$\frac{u_i^{j-1} - 2u_i^j + u_i^{j+1}}{\Delta t^2} = c^2 \frac{u_{i-1}^j - 2u_i^j + u_{i+1}^j}{\Delta x^2} \tag{5.26}$$

where Δx and Δt are the step sizes in the space and time domains, respectively. The displacement of the next nodes in the ultrasonic wave in the space is given by:

$$u_i^{j+1} = \Lambda^2 \left(u_{i-1}^j - 2u_i^j + u_{i+1}^j \right) - u_i^{j-1} + 2u_i^j \tag{5.27}$$

where

$$\Lambda = c \frac{\Delta t}{\Delta x} \tag{5.28}$$

A numerical solution is stable if the error at each increment becomes smaller. Courant et al. [101] showed that the numerical solution is stable for Λ (also called the Courant-Friedrichs-Lewy (CFL) condition) smaller than 1. The derivative of Eq.5.3 for $x < X_{-}$ gives the particle velocity in the medium (as there is only one medium on the left side of the contract, for the sake of simplicity of following the equations, the variable X_{-} is replaced by x):

$$\frac{\partial u(x,t)}{\partial t} = c \left[-\frac{\partial f(x-ct)}{\partial (x-ct)} + \frac{\partial G(x+ct)}{\partial (x+ct)} \right] \tag{5.29}$$

Substituting Eq.5.12 into Eq.5.29 to eliminate the terms containing the reflected ultrasonic waves:

$$\frac{\partial u(x,t)}{\partial t} = c\left[-2\frac{\partial f(x-ct)}{\partial(x-ct)} + \frac{\partial u(x,t)}{\partial x}\right] \tag{5.30}$$

In the current study, only the reflected waves are used. Therefore, to simplify the numerical analysis, the waves propagated in the medium are considered a semi-infinite elastic medium, and the other contacting part is assumed to be a rigid body [100]. In this manner, the deformation of both surfaces is assumed to apply to the elastic body. Figure 5.1 is adapted to Figure 5.5). The contact is assumed to be frictionless [52, 100]. An ultrasonic source is bounded at the back face of the medium at $x = 0$ and the interface at the origin $x = L$. The ultrasonic source $F(t)$ generates particle

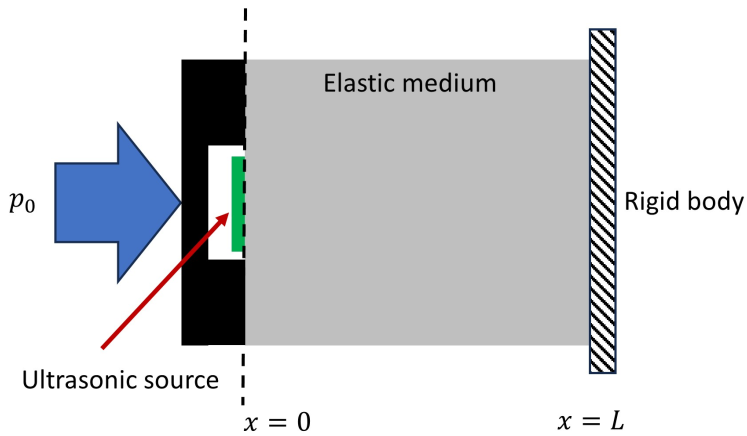

Figure 5.5: Schematic diagram of a one-dimensional elastic medium in contact with a rigid body.

velocity at $x = 0$, which is the derivative of the incident ultrasonic wave with respect to time [100]:

$$F(t) = -c\frac{\partial f(x-ct)}{\partial(x-ct)}|_{x=0} \tag{5.31}$$

To derive an equation of ultrasonic waves in a solid medium with a source $F(t)$, Eq.5.31 is substituted into Eq.5.30:

$$\frac{1}{2}\left[\frac{\partial u(x,t)}{\partial t} - c\frac{\partial u(x,t)}{\partial x}\right] = F(t) \tag{5.32}$$

It should be noted that Eq.5.26 cannot be used at the boundary conditions, and it is valid only in the range of $i \in [i+1, \frac{L}{\Delta x} - 1]$. At the boundary with nodes $i = 1$, Eq.5.26 requires node u_0^j that is not in the medium. Likewise, at the end of the medium ($x = L$) where the node is $i = \frac{L}{\Delta x}$, Eq. 5.26 requires $u^j_{\frac{L}{\Delta x}+1}$. This node is also outside the boundaries. To address this limitation, the second-order upwind scheme is used [100]. By applying the second-order upwind scheme in Eq. 5.32:

$$\frac{1}{2}\left[\frac{u_1^{j+1}-u_1^j}{\Delta t}-c\frac{-3u_1^j+4u_2^j-u_3^j}{2\Delta x}\right]=F(t) \tag{5.33}$$

To find the displacement of the nodes at the boundary $x = 0$ and at a later time $j + 1$, Eq.5.33 is rearranged as:

$$u_1^{j+1}=u_1^j+\Lambda\left(-\frac{3}{2}u_1^j+2u_2^j-\frac{1}{2}u_3^j\right)+2F(t)\Delta t \tag{5.34}$$

The contact condition must be considered for the nodes at the interface $x = L$. The contact is either closed or open.

i. Closed interface

When the contact is closed, the particle displacement at the interface is zero $u_i^j = 0$ (for $i = \frac{L}{\Delta x}$). The normal stress (due to the ultrasonic stress) at the interface is given by using the second-order upwind scheme:

$$\begin{cases} \sigma_i^j = \frac{E}{2\Delta x}\left(3u_i^j + u_{i-2}^j - 4u_{i-1}^j\right) \\ \\ u_i^{j+1} = u_i^j \end{cases} \tag{5.35}$$

The contact remains closed until the normal stress generated by the ultrasonic source at contact becomes less than the static pressure applied by an external load p_0 ($p_0 < 0$ for compression).

ii. Open interface

The contact is open when the total normal stress generated by the ultrasound is less than the static pressure applied by the external load p_0. The particle displacement at the interface is given by using the second-order upwind scheme and the normal stress of the interface:

$$u_i^j=\frac{1}{3}\left(-\frac{2}{E}\sigma_i^j\Delta x+4u_{i-1}^j-u_{i-2}^j\right) \tag{5.36}$$

5.2.3 Numerical analysis procedure

Figure 5.6 shows the numerical procedure of the reflected ultrasonic waves from a perfect and frictionless contact. In the numerical analysis presented here, the roughness

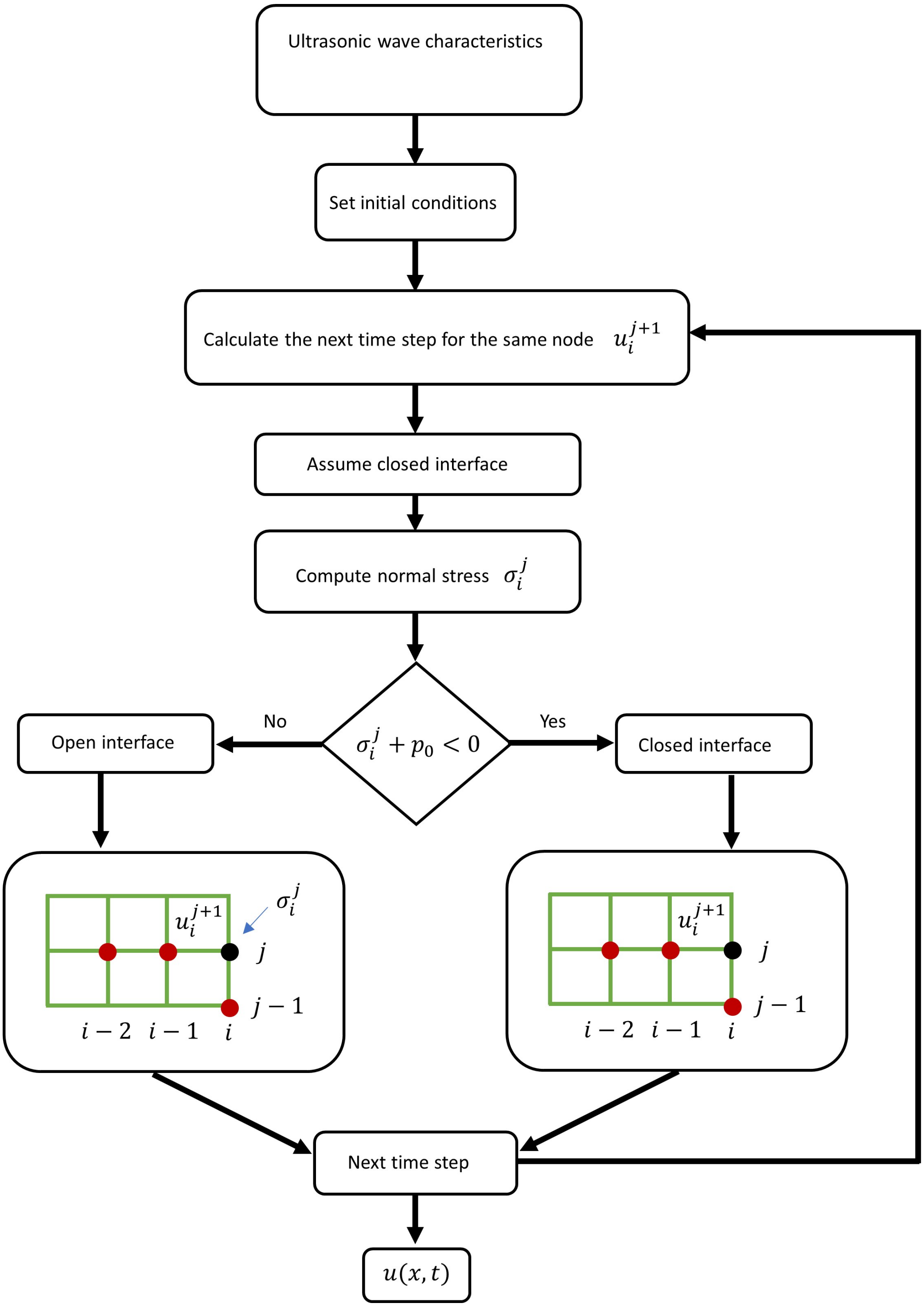

Figure 5.6: Schematic diagram of a numerical procedure of reflected ultrasonic waves adapted from [4].

and topography of the surface are ignored and the contact is assumed to be perfect. The contact is initially assumed to be closed. The displacement and normal stress of the particles at the boundary $x = 0$, where the ultrasonic source is placed, for the entire analysis time are defined (u_i^j and σ_i^j for $i \in [1, \frac{L}{\Delta x} + 1]$ and $j \in [1, \frac{t}{dt} + 1]$ using Eqs. 5.34 and 5.35. It should be noted that at the node $i = 1$ and for all time, the Eq. 5.35 is multiplied by -1 as the nodes are on the right side of the first element. When $\sigma_i^j + p_0$ at the interface ($i = \frac{L}{\Delta x} + 1$) is positive, the contact is open. Eq. E5.35 computes the normal stress generated by ultrasound at the interface. The particle displacement at the interface u_i^j is then determined by Eq. 5.36. u_i^j is substituted into Eq. 5.27 to compute the displacement of the node before the interface for the later time u_{i-1}^{j+1}. The contact remains open until $\sigma_i^j \leq p_0$. When $\sigma_i^j > p_0$, the contact is closed and the displacement of the node at the interface becomes zero $u_i^j = 0$. This is substituted in Eq.5.27 to compute the particle displacement of the node before the interface for all time u_{i-1}^{j+1}. The displacement of the nodes at the interface is determined by Eq. 5.35. The particle displacement of the interface is then substituted in Eq. 5.27 to compute the reflected waves from the interface towards $x = 0$ (see Appendices A and B for the MATLAB script).

5.2.4 Numerical results and discussion

To illustrate CAN with the numerical analysis in solid elastic medium, an aluminium alloy ($Al6082 - T6$) and longitudinal ultrasonic waves with parameters and properties listed in Table 5.1 were considered. Figure 5.7 shows the propagation of the longitudinal ultrasonic wave in a solid medium and the reflection of the interface. Ul-

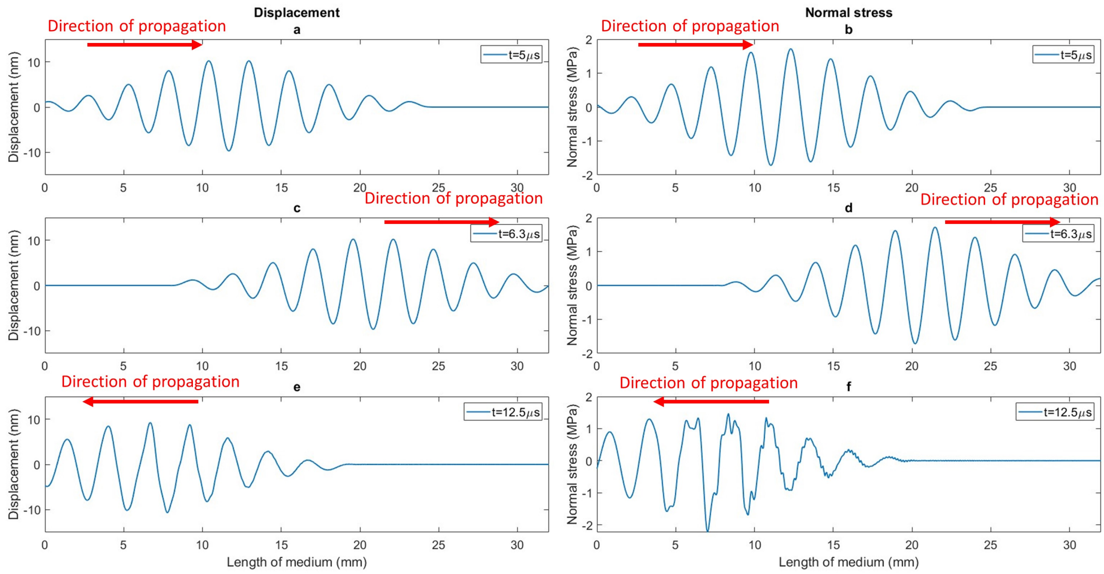

Figure 5.7: Numerical analysis of CAN as ultrasonic waves propagating in an elastic medium and reflect from the interface: (a,c,e) displacement; (b,d,f) normal stress.

Table 5.1

Parameters and Properties	Values
Waveform	sine wave
Density ρ	2700 kg/m^3
Λ (Eq. 5.28)	0.509
External load p_0	1 MPa
Speed of sound c	5092 m/s
Elastic modulus E	70 GPa
Time increment size Δt	1 ns
Space increment size Δx	10 μm
Frequency of excitation f_0	2 MHz
Amplitude of excitation A_0	5 nm
Number of tone burst cycles	10

trasonic waves were generated at $x = 0$ and propagated in the elastic medium. There is no distortion in displacement and normal stress waves before the incident at the interface, as shown in Figures 5.7 a-d. However, if the solid medium were an elastic nonlinear material, they would distort as the waves propagated from the source to the interface. When waves incident on the interface, they are reflected. The portion of reflection depends on the extent of the real contact area. If the contact is perfect (the nominal and real contact areas are equal), no ultrasonic energy is reflected, and all is transmitted to the second medium. However, the second body is considered rigid in this section, and all the amplitude is reflected as shown in Figures 5.7 e-f. These waves are propagated backward in the medium and are captured by a transducer.

To illustrate the effect of contact on the reflected waves, first, consider the ultrasonic waves incident of a solid-air interface with a peak frequency of 2 MHz and two different amplitudes of excitation of 5 nm and 35 nm, respectively. The waves were emitted at $x = 0$ and captured at the same point. The TOF for the medium with the parameters and characteristics listed in Table 5.1 is almost 12.5 μsec. Due to the difference in the acoustic impedance at the interface (the acoustic impedance of the air is negligible compared to Al 6082-$T6$), the waves were fully reflected (Figure 5.8). When the incidence waves reach the interface, they move the interface without resistance. Therefore, the waves were reflected without any distortion. However, only the phase of the reflected waves is changed (Figure 5.8). The effect of attenuation

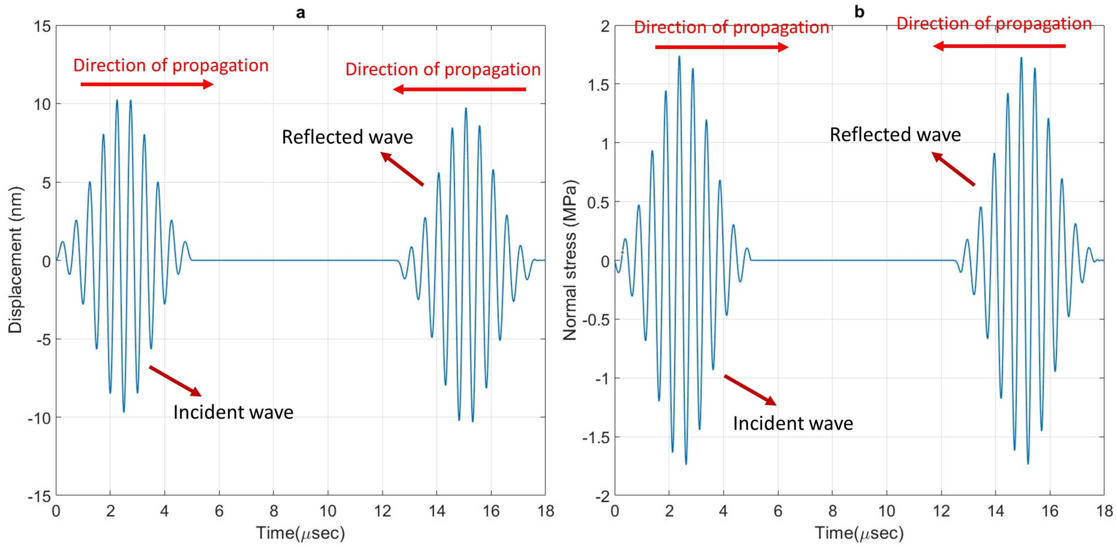

Figure 5.8: Ultrasonic wave propagation in linear elastic medium and reflect from solid-air interface: (a) displacement; (b) normal stress.

(absorption) is neglected (for the sake of simplicity) in the numerical analysis. Therefore, the amplitude of the reflected waves is the same as that of the incident waves. It can be seen in Figure 5.9 that despite the increase in the amplitude of excitation, there is no distortion in the reflections. Figure 5.9b shows the frequency domains (FFT) of the incident and reflected waves from the interface at different excitation amplitudes. It is seen that the waves from the interface are reflected at the same frequency as the incident waves, which indicates that there is no distortion (neither material nor contact nonlinearities in the medium and the interface).

Figure 5.10 shows the time and frequency domains of the initial excitation from the source, the propagated waves between the source and the interface, and the reflected waves from the interface. The frequency domain of the incident wave shows that the wave generated by the ultrasonic source is a mono-frequency wave that contains only the excitation frequency which is called the fundamental frequency (Figure 5.10d). The ultrasonic wave in the linear elastic medium from the ultrasonic source to just before the interface is also propagated with the fundamental frequency, as shown in Figure 5.10e. However, the reflected waves from the interface are distorted as a result of the opening and closing mechanism of the interface, as the waves incident the interface. This distortion is seen as higher-order harmonics (2^{nd}, 3^{rd}, etc.) as shown in Figure 5.10f.

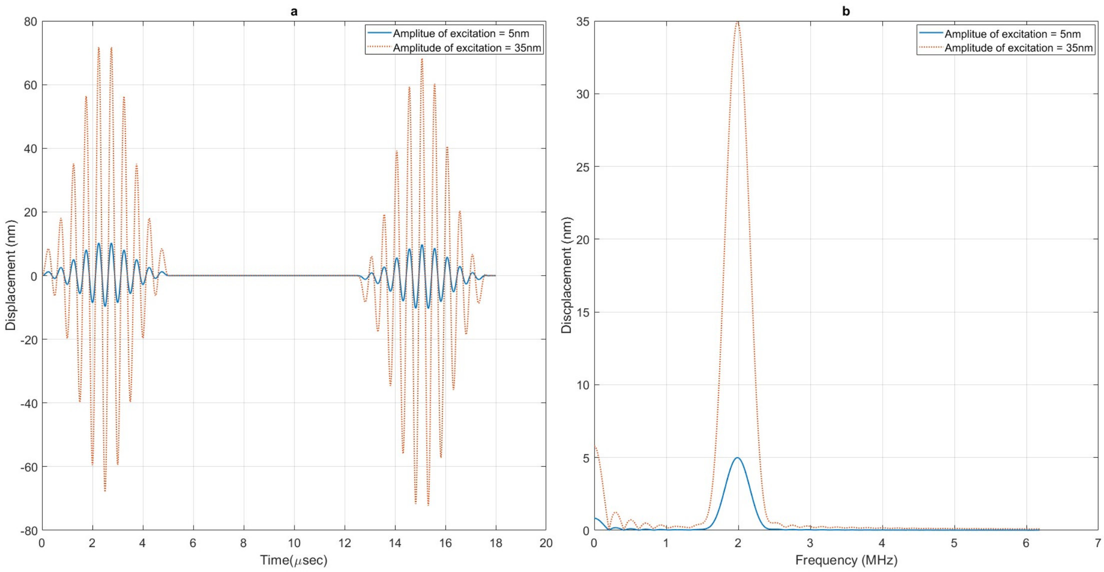

Figure 5.9: Ultrasonic wave propagation in linear elastic medium and reflection from solid-air interface at the excitation amplitudes of 5 nm and 35 nm: (a) time domain; (b) frequency domain.

Let us study the effect of different external loading, excitation conditions, and materials of the medium on the CAN.

i. Effect of excitation amplitude

Ultrasonic waves with a peak frequency of 2 MHz at three different excitation amplitudes of 5 nm, 7.5 nm, and 10 nm, respectively, were excited by the ultrasonic source. The applied load was increased for every amplitude from 0 to 10 MPa with a step of 0.15 MPa. The reflected waves from the interface were captured at $x = 0$. The FFT of the displacement is shown in Figure 5.11a. It is seen in Figure 5.11a that the amplitude of the second-order harmonic A_2 is zero when the applied load (nominal contact pressure) is zero. This indicates that there is no material nonlinearity. In addition, at this load, the surfaces are not in contact, so there is also no contact nonlinearity. Figure 5.11b shows that as the amplitude of excitation increases, the particle displacement and the normal stress generated by the ultrasonic source increase, as shown in Figure 5.11b. The nonlinearity of the contact (the amplitude of the second-order harmonic A_2) excited at 5 nm increases from 0 to $\approx$ 0.87 MPa and decreases to 0 at 3 MPa. At this excitation amplitude, the normal stress generated by the ultrasonic source is 0.87 MPa (Figure 5.11b); therefore, when the applied load (nominal contact pressure) is less than 0.87 MPa, the particle displacement at the

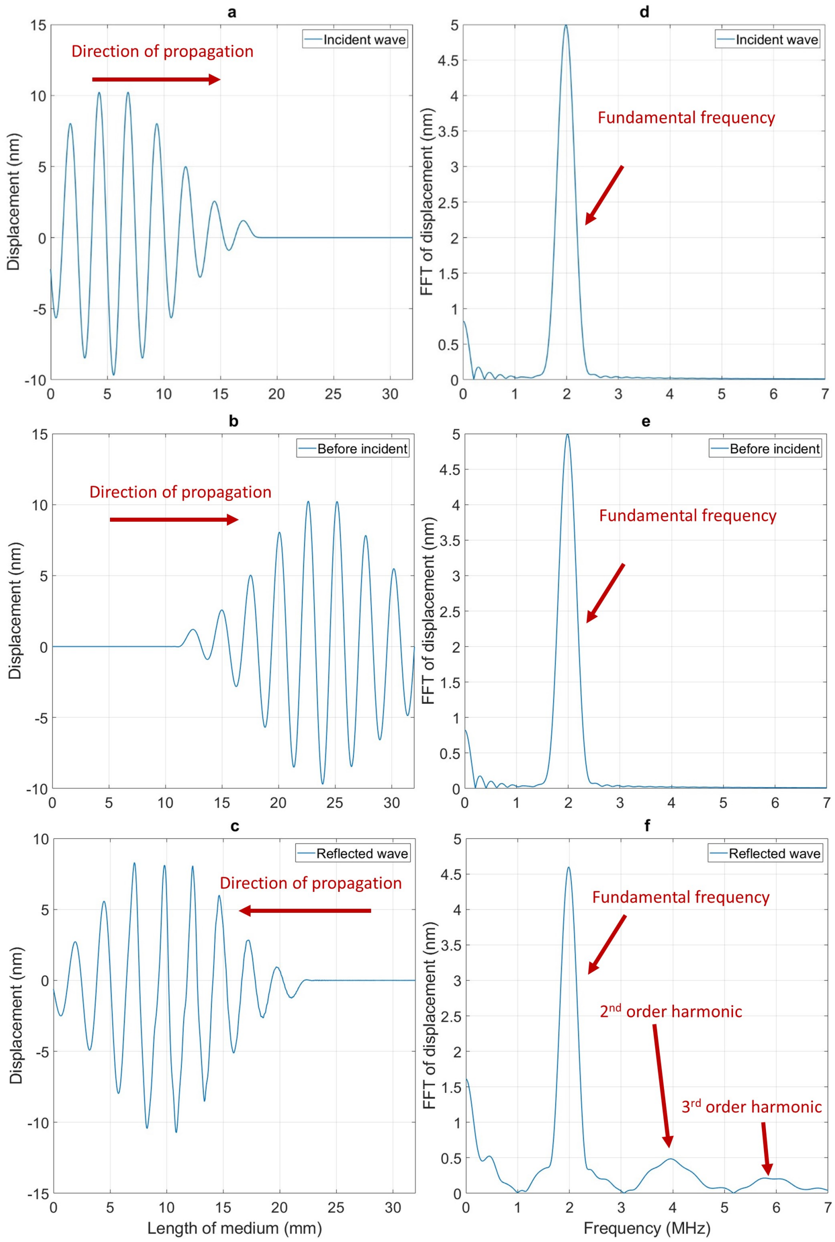

Figure 5.10: Incident and reflected ultrasonic waves from a solid-solid contact: (a-c) time domain; (d-f) frequency domain.

interface increases. The interface remains open for a longer time, and the nonlinearity of the contact increases. When the nominal contact pressure increases the normal stress generated by ultrasound (larger than 0.87 MPa), the normal stress can open the interface for a shorter time. Eventually, at the nominal contact pressure 3 MPa, the normal stress is less than the applied load, and the contact remains closed, making $A_2 = 0$. This trend is also true for the amplitude of excitation 7.5 nm and 10 nm where the normal stress generated by ultrasound is 1.3 MPa and 1.75 MPa, respec-

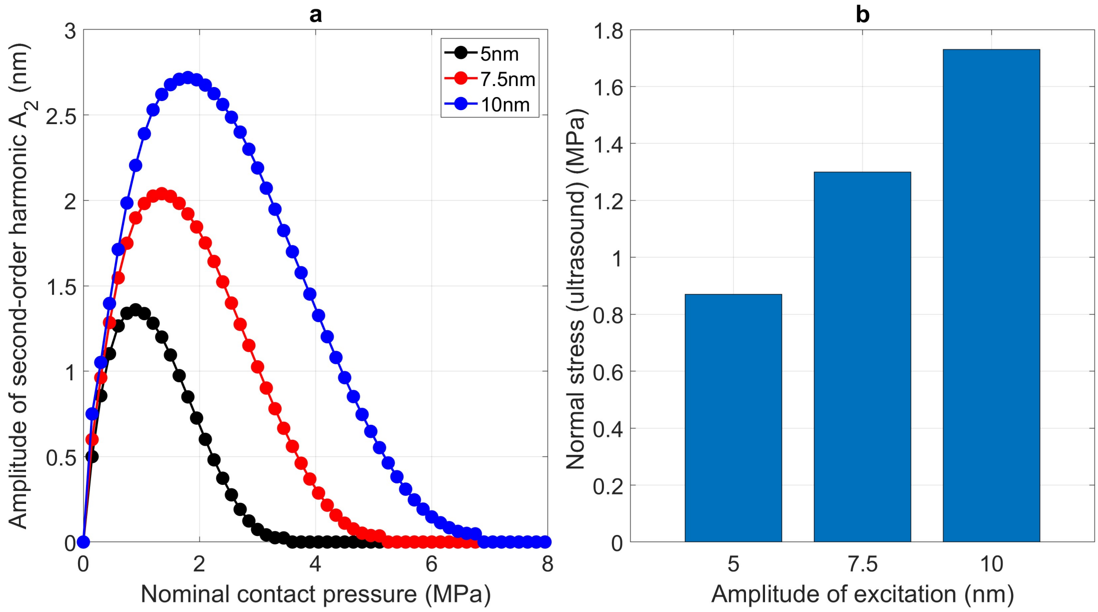

Figure 5.11: Variation of: (a) the amplitude of the second-order harmonic against the applied load; (b) normal stress generated by ultrasound at different excitation amplitudes.

tively. A_2 for the amplitude of excitation 7.5 nm increases from 0 to 1.3 MPa and then decreases as the nominal contact pressure becomes larger than 1.3 MPa. The contact nonlinearity for the higher amplitude of excitation becomes 0 at the larger nominal contact pressure, while, for excitation at 10 nm, the nonlinearity becomes 0 at 7 MPa nominal contact pressure.

ii. Effect of material properties of the medium

It is necessary to study how the contact acoustic nonlinearity varies for different metal-metal contacts. Figure 5.12 shows that the maximum amplitude of the second-order harmonic A_2 occurs at the normal stress generated by ultrasound. For example, for the amplitude of excitation 5 nm, the normal stress for brass and stainless steel is 2.54 MPa and 1.79 MPa, respectively (Figure 5.12a), where the peak of A_2 is. This behaviour is also true for the excitation of 7.5 nm and 10 nm as shown in Figures 5.12b and c. The value of the amplitude of the second-order harmonic A_2 is related to the contact stiffness of the mating surfaces, which is discussed in Chapters 6-8. The maximum normal stress generated by ultrasound for the material used (shown in Figure 5.12d) is significantly lower than their yield strength. For instance, the yield strength of stainless steel is approximately 165 MPa (for ASTM A283 Grade A), while the maximum normal stress generated by ultrasound for the amplitude of excitation

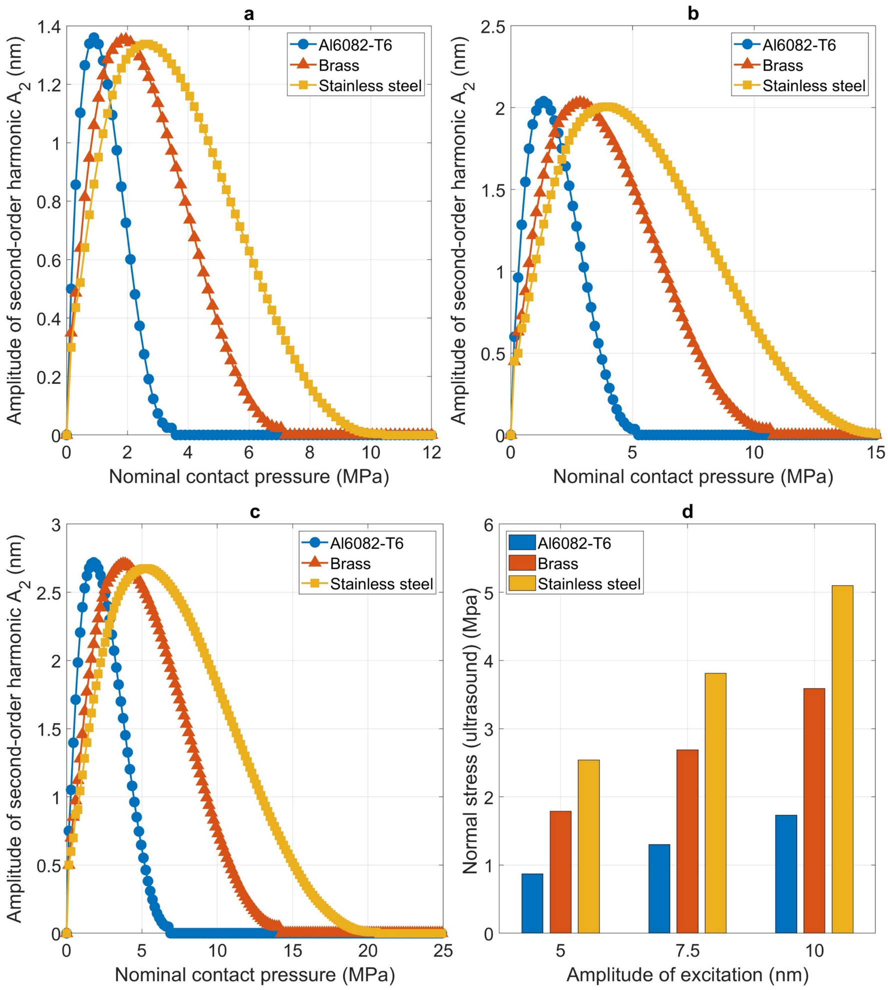

Figure 5.12: Variation of A_2 in different contacting surfaces of *Al* 6082-*T*6, stainless steel and brass with amplitude of excitation of: (a) 5 *nm*; (b) 7.5 *nm*, (c) 10 *nm*; and (d) their normal stress generated by ultrasound.

of 10 *nm* is 5.1 MPa. This indicates that when high-power ultrasonic waves (with 10 *nm* displacement amplitudes) are propagated in a solid medium, the medium is in the linear elastic limit.

iii. Effect of excitation frequency

One of the main concerns about using ultrasound is the decision-making on the frequency of the ultrasonic source (transducer). Although the frequency range is between 20 KHz and 1 GHz, the frequency selection can be based on some parameters such as the application, the medium of propagation and operating conditions. To study their differences, Figure 5.13 shows the incident waves in a solid-air interface at three different excitation frequencies: 0.5 MHz, 2 MHz and 5 MHz. An Al 6082-T6 medium with 32 mm length is not long enough for the ultrasonic waves with 0.5 MHz frequency and a five-tone burst cycle to extract and generate (Figure 5.13a). However, waves with frequencies 2 MHz and 5 MHz can be generated and propagated without interfering (shown in Figures 5.13b and c).

One of the disadvantages of using higher frequencies may be their attenuations. The higher the frequency, the smaller the thickness of the piezoelement, which generates less ultrasonic energy than the thicker transducers made from the same materials. However, this effect is not considered for numerical analysis.

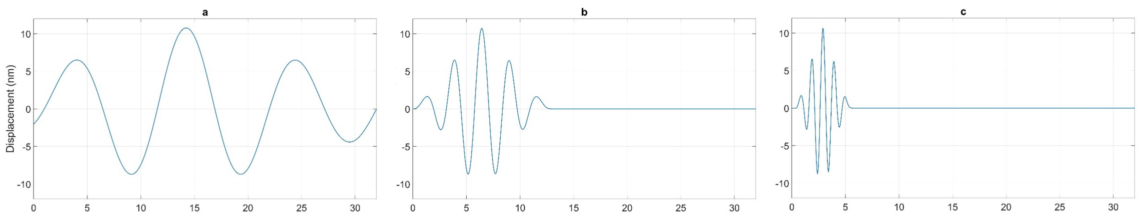

Figure 5.13: Incident ultrasonic waves with an amplitude of excitation 0.1 m/s in a 32 mm length of Al 6082-T6 and frequency: (a) 0.5 MHz; (b) 2 MHz; (c) 5 MHz.

In Figure 5.14 it is seen that (ignoring the effect of attenuation) as the centre frequency of excitation increased from 2 MHz to 5 MHz, the maximum amplitude of the second-order harmonic occurred at a higher contact pressure. This is because the stress generated by ultrasound with the centre frequency of 5 MHz was higher than at 2 MHz, as shown in Figure 5.14d.

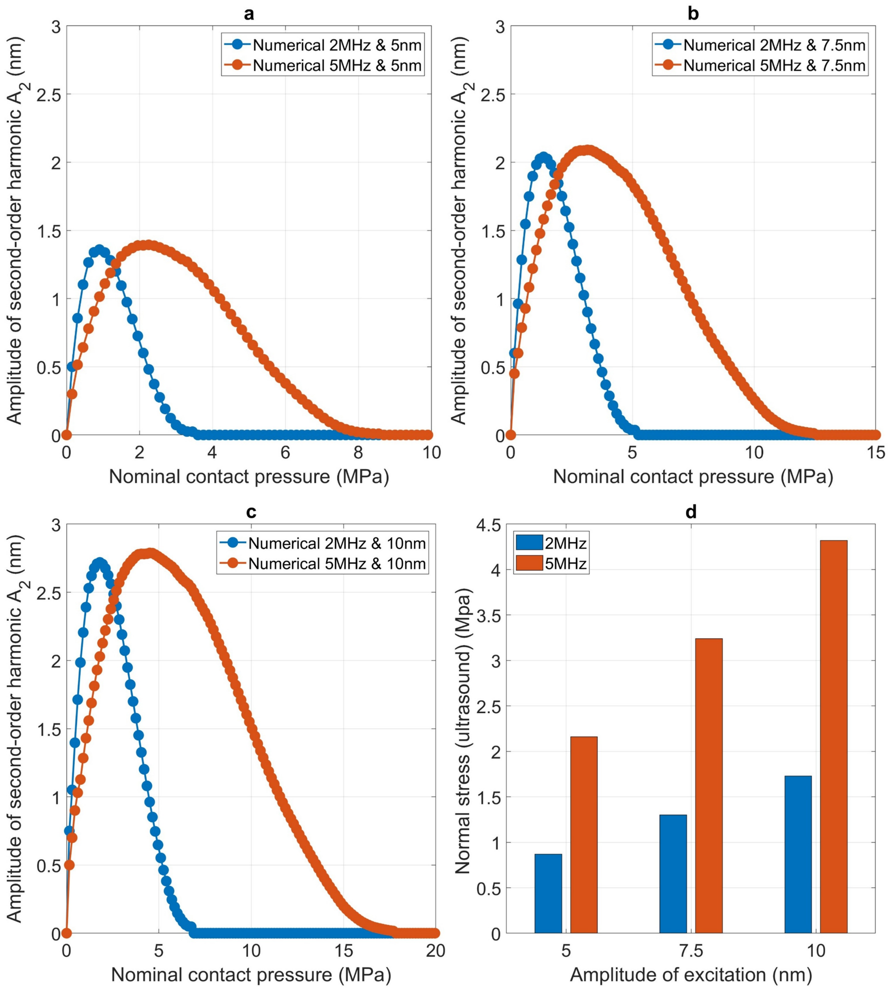

Figure 5.14: Comparison between A_2 with excitation frequencies of 2 MHz and 5 MHz at the amplitude of excitation: (a) 5 nm; (b) 7.5 nm; (c) 10 nm; and (d) their normal stress generated by ultrasound.

5.2.5 Analytical and numerical comparison

Figures 5.15 and 5.16 compare the amplitude of second-order harmonics A_2 determined with the analytical and numerical models at the centre frequencies of 2 MHz and 5 MHz. It is seen that regardless of the frequency and the amplitude of excitation, the analytical model is less accurate compared to the numeric ones.

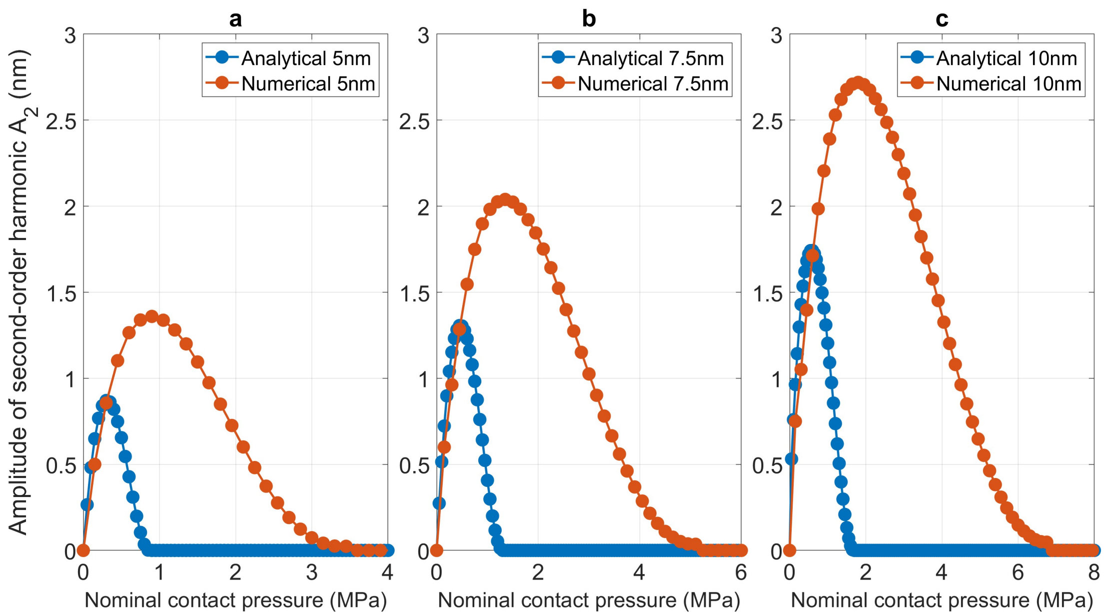

Figure 5.15: Numerical and analytical comparison of A_2 at excitation frequency of 2 MHz and amplitude of: (a) 5 nm; (b) 7.5 nm; and (c) 10 nm.

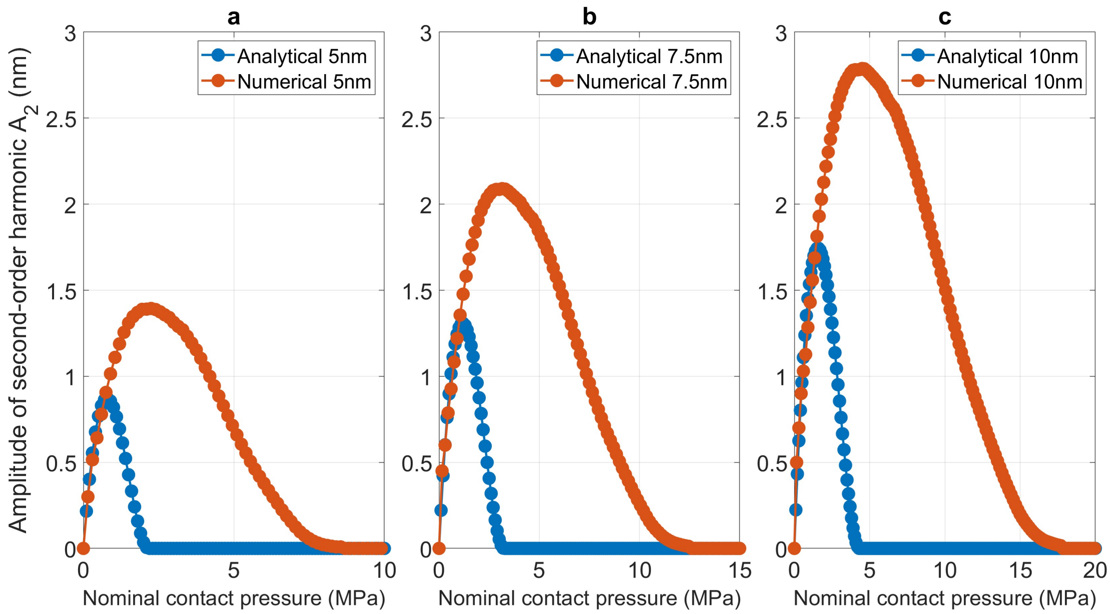

Figure 5.16: Numerical and analytical comparison of A_2 at excitation frequency of 5 MHz and amplitude of: (a) 5 nm; (b) 7.5 nm; and (c) 10 nm.

5.3 Conclusion

In this chapter, analytical and numerical models were used to derive equations that model the propagation of ultrasonic waves in a solid medium and reflected from a solid-air and solid-solid interfaces. The analytical model used the Newton-Raphson method, while the numerical model was based on an explicit FDM. When high-power ultrasonic waves are incident on the solid-solid interface, they open and close it. This distorts the reflected waveform from the interface and is called contact acoustic nonlinearity (CAN), which appears as higher-order harmonics (multiples of fundamental frequency) in the frequency domain. Ultrasonic waves with the centre frequency of 2 MHz and different amplitudes of 5 nm and 35 nm were incident on a solid-air interface. The reflected waves in the time domain of the interface were not distorted, and their frequency domain showed only the fundamental frequency (the frequency of excitation), which indicates the linear response of the contact. Even when the excitation amplitude increased from 5 nm to 35 nm, there was no higher-order harmonic. Therefore, there was no CAN.

In both analytical and numerical models, different material properties, excitation frequency and amplitude were used to study the effect of these parameters on CAN. The numerical model gave more accurate results than the analytical one, since it is based on an explicit method. However, more studies are required to find the sources of this difference. For both models, the effect of attenuation and surface roughness was ignored for simplicity. The amplitude of second-order harmonic A_2 increased from 0 until the contact pressure was equal to the stress generated by the ultrasound waves. For example, when ultrasonic waves with the centre frequency of 2 MHz and amplitude of excitation of 5 nm were incident on the solid-solid contact of Al6082-T6, A_2 increased from 0 to 0.87 MPa, which is equal to the ultrasound stress at this frequency and amplitude of excitation. A_2 decreased to 0 as the contact pressure increased to more than 0.87 MPa. For the higher excitation amplitudes of 7.5 nm and 10 nm, the maximum of A_2 increased to 1.3 MPa and 1.75 MPa (equal to their ultrasonic stress).

Ultrasonic waves with a higher excitation frequency were also seen to generate higher ultrasonic stress, ignoring the effect of ultrasound attenuation. Therefore, the peak of A_2 occurred at the higher contact pressure. For example, when ultrasonic waves with the centre frequency of 5 MHz and amplitude of excitation of 5 nm were incident on the solid-solid contact of Al6082-T6, the maximum A_2 was at 2.16 MPa. However, the maximum of A_2 was at 0.87 MPa for the centre frequency of 2 MHz.

This chapter also showed that the maximum amplitude of A_2 is dependent on the stiffness and density of the interface materials. The peak of A_2 occurred at a higher contact pressure in stainless steel than in Brass and Al6082-T6, respectively.

Chapter 6

Experimental Setup and Signal Processing for Contact Acoustic Nonlinearity

This chapter describes techniques and tools to experimentally measure nonlinear longitudinal ultrasonic waves from an imperfect contact. Different parameters, such as the amplitude of excitation and the couplant gel, are investigated. Ultrasonic waves are captured in the voltage unit. To determine the second-order interfacial stiffness K_2, the second-order nonlinear coefficient γ must be in a length unit (here in a unit of metres). A laser Doppler vibrometer was used here to convert the captured ultrasonic waves from the voltage to the metre. Finally, different signal processing methods, such as windowing, were applied to the recorded data to select the most accurate and appropriate method.

6.1 Introduction

The contact acoustic nonlinearity (CAN) generated by the longitudinal ultrasonic waves has been measured using the pitch-catch through reflection technique, as shown in Figure 6.7b [49, 53]. In this technique, the emitter and receiver are placed on either side of the interface. The emitter generates the ultrasonic signal. The waves propagate through the first medium and incident at the interface. The ultrasonic waves are partly reflected and partly transmitted. The transmitted waves are captured by the receiver in the pitch-catch through transmission mode. This method is not practical in engineering structures and mechanisms where only one surface is accessible. For example, when the piston-liner contact is required to study, the receiver cannot be placed on the other side of the engine block since other parts are also in the engine, and it is not possible to distinguish the signals that are related to the piston-liner contact. One of the novelties of the current study is to measure the amplitude of the second-order nonlinear normal interface. To do this, the amplitude of the fundamental frequency and second-order harmonic were measured using the pitch-catch through reflection method where both the emitter and receiver are placed on the same side of the contact (as shown in Figure 6.7b).

6.2 Loading apparatus

Compressive load to some contacts was applied using a loading machine (Tinius Olsen 25ST), as shown in Figure 6.1. The specimens (upper and lower bodies) were placed in the machine such that the ground surfaces created an imperfect interface. The machine was equipped with a load cell and was programmed using a tabulated spreadsheet by the user. To apply quasi-static loads, the speed of the loading part was considered significantly slow at 0.05 mm/s. The load was set from 0 to 10 MPa with a step size of 0.25 MPa. To protect the transducers (which were placed on the back face of the upper specimen and shown in Figure 6.13), a spacer was placed between the samples and the upper body.

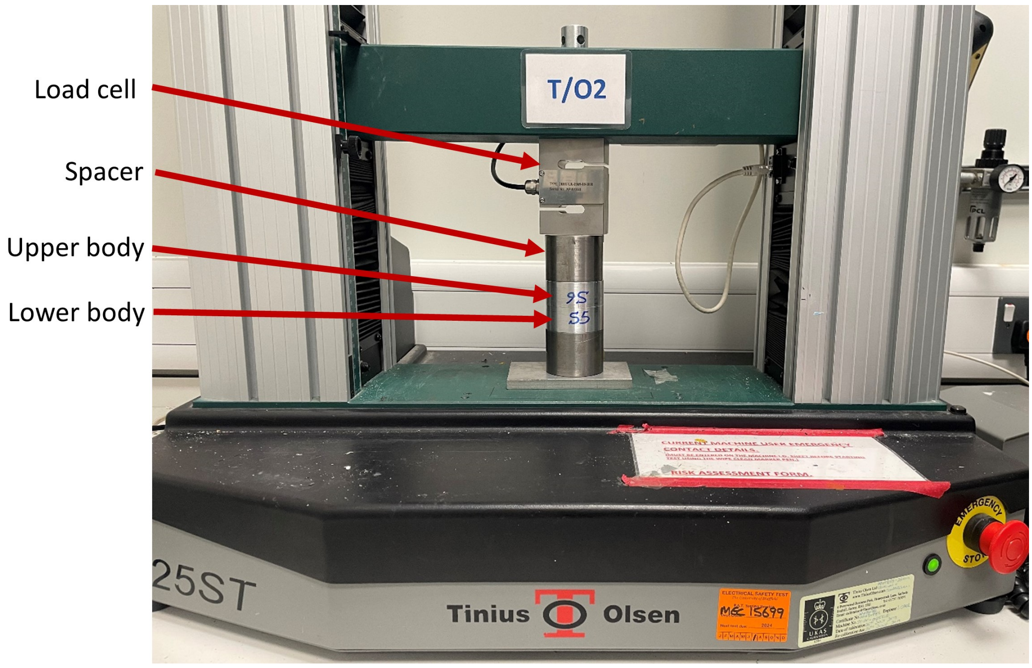

Figure 6.1: Loading machine (Tinius Olsen 25ST) to apply compression load.

6.3 Specimens

In the current study, aluminium alloys *Al* 6082-*T*6 were used due to their wide range of applications in engineering. Four *Al* 6082-*T*6 cylinders of diameter 59 *mm* and thickness 32 *mm* were ground and polished with silicon carbide papers (grit size P1200 for samples S1 and S2 and grit size P2500 for samples S9 and S10) as shown in Figure 6.2. A 3D optical profilometer (Alicona Infinite SL) was used to measure

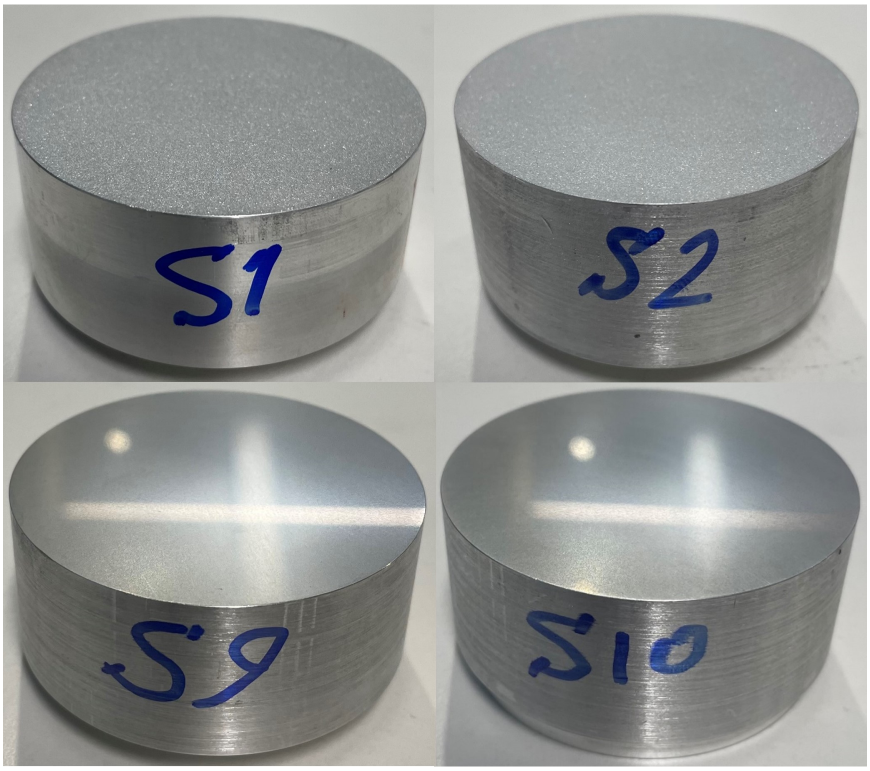

Figure 6.2: Ground and polished samples used in the current study.

the surface topography and roughness. Table 6.1 shows the filtered surface roughness (without waviness) of the samples prior to the first loading.

Table 6.1: Surface roughness of the samples before loading.

Samples	$R_a(\mu m)$	$R_q(\mu m)$	$R_z(\mu m)$
S_1	3.707	5.000	34.711
S_2	4.063	6.047	35.672
S_9	0.455	0.588	3.148
S_{10}	0.495	0.640	3.453

6.4 Ultrasonic measurement setup

Figure 6.3 illustrates the experimental setup that was used to measure the ultrasonic waves from a solid-air interface and solid-solid contact (Chapters 7 and 8) and a liquid lubricant (Chapters 10 and 11).

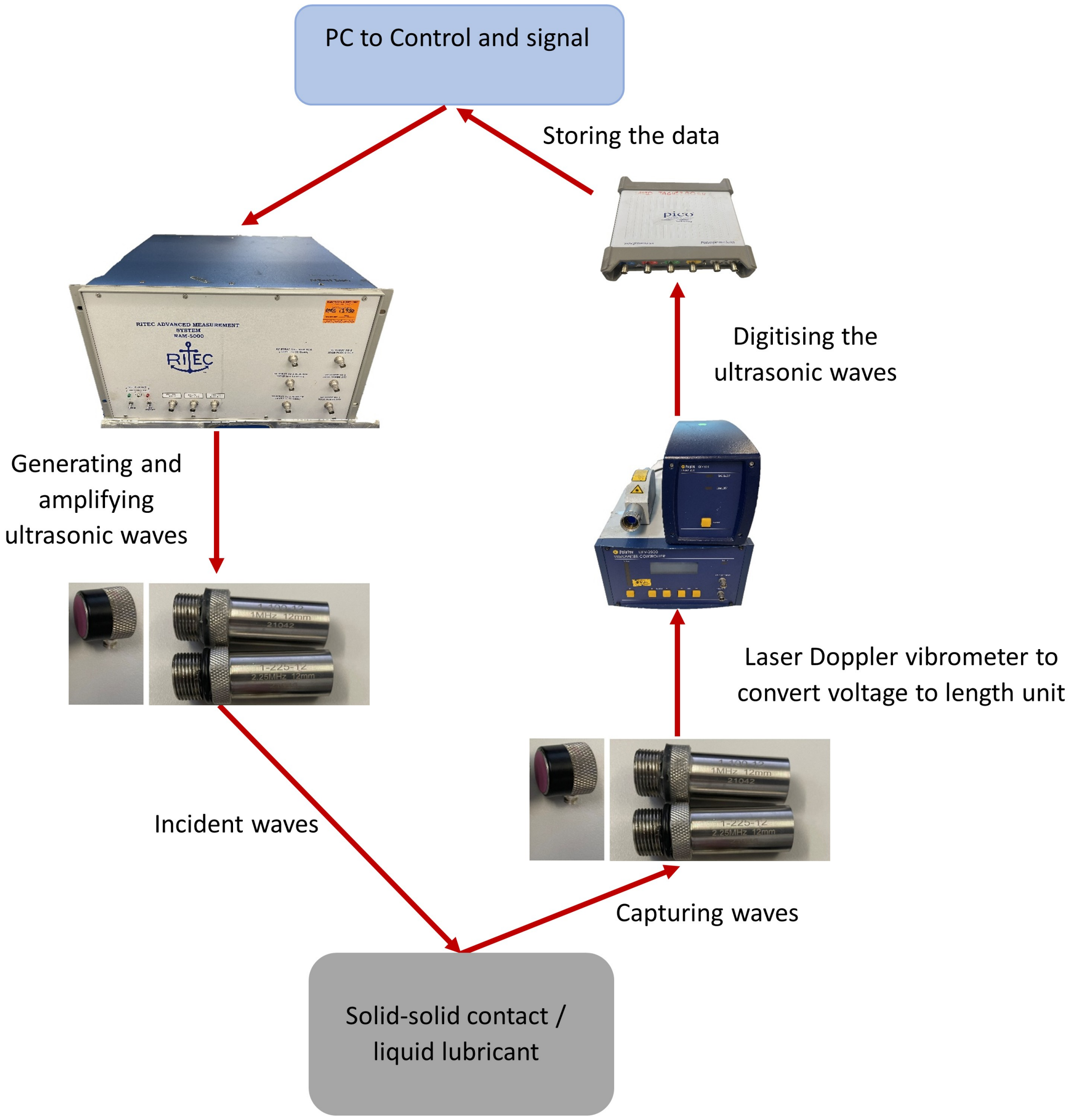

Figure 6.3: Schematic diagram of ultrasonic measurement setup.

As seen in Figure 6.3, the ultrasonic waves were first generated and amplified with the amplifier. The amplified signals were incident on the solid medium (Chapters 7 and 8 for CAN) or in the liquid lubricant (Chapters 10 and 11) to determine contamination and degradation of the lubricant. The reflected signals from the solid-solid interface or transmitted in the lubricant were captured with the second transducer.

The captured signals are in units of voltage. To measure the second-order interfacial stiffness K_2 (in Chapters 7 and 8) and the nonlinear coefficient β, the voltage must be converted to the length unit. This conversion was done with a laser Doppler vibrometer (as shown in Sections 6.12 and 6.16). Then, the captured signals were digitised with an ultrasonic digitiser and stored on a PC for signal processing. The tools required for these measurements are explained as follows.

6.5 Piezoelectric element

When pressure is applied to piezoelectric materials, they generate an electrical charge. This is called the direct piezoelectric effect. Some piezoelectric materials are capable of converting an electrical charge to deformation. This effect is known as the inverse piezoelectric effect. One of the most common piezoelectric materials for generating ultrasound is lead-zirconate-titanate (PZT), which can have a direct and inverse piezoelectric effect [102].

6.6 Ultrasonic transducers

Ultrasonic transducers are excited at their peak frequency (or resonant frequency) in order to generate the maximum ultrasonic energy. Figure 6.4 shows a schematic diagram of a common ultrasonic transducer. The input voltages to the ultrasound excite the piezoelectric element (piezoelement) at a desired frequency. When the piezoelement vibrates, it generates undesired vibration. This vibration is dissipated using a backing. The backing is a high density damped material. An other main feature of the ultrasonic transducer shown in Figure 6.4 is the wear plate. This plate works as a protection against wear and a relatively harsh chemical environment. The wear plate also functions as a matching layer to overcome the acoustic impedance between the piezoelement and the contacting surface of the medium.

The two main types of transducers are contact and immersion transducers, as shown in Figure 6.5. The contact transducers are used to contact the solid (Figure 6.5a). They are mainly manufactured to generate longitudinal or shear ultrasonic waves. The centre frequencies are between 0.1-100 MHz. If they are water-resistant and waterproof, they may also be used in liquids. Immersion transducers are made for longitudinal mode only and are suitable to dip in liquids. In the current study, contact and immersion transducers were used.

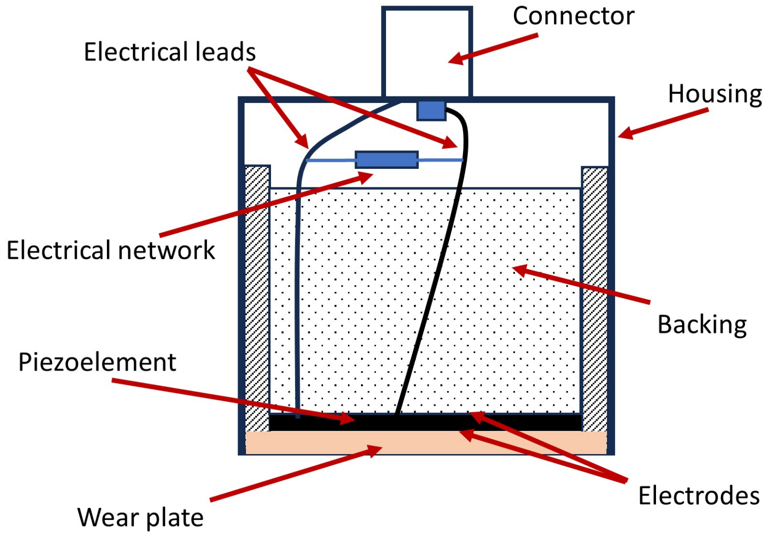

Figure 6.4: Schematic diagram of an ultrasonic transducer adapted from [5].

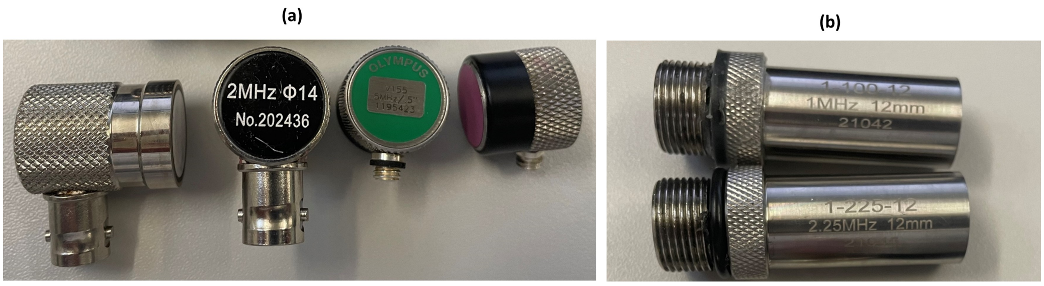

Figure 6.5: Ultrasonic transducers: (a) contact transducers; (b) immersion transducers.

6.7 Ultrasonic couplant

The contact transducers are required to be placed on the surface of a solid medium that ultrasonic waves are propagated through. The surfaces of the transducer and medium are rough, and there is an air gap at the interface, as shown in Figure 6.6. The air impedance is significantly smaller than the wear plate impedance of the transducer. Therefore, almost all of the ultrasonic energy is reflected back. To increase the transmission of ultrasonic energy, the air gap must be replaced by some couplants (as shown in Figure 6.6). There are different couplants in the form of liquid, gel or paste. The viscosity and the substance of the couplants are selected depending on the operating conditions, such as temperature, frequency and propagation mode. The common substances of the couplants are water, shear and longitudinal couplants. In the current study, a non-toxic and water-soluble gel with very high viscosity (Olym-

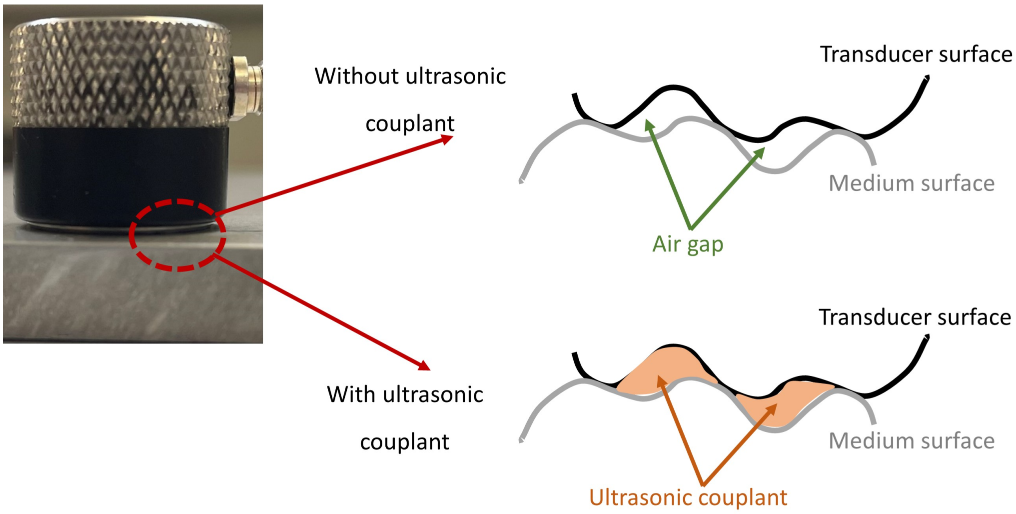

Figure 6.6: Transducer-medium contact with and without ultrasonic couplant.

pus SWC-2) was used as a couplant gel. In Section 6.13.4, the effect of different ultrasonic couplants on ultrasonic waves is discussed.

6.8 Ultrasonic measurement modes

There are two main modes to capture the ultrasonic waves, as shown in Figure 6.7. In a pulse-echo mode (Figure 6.7 a), a single transducer is used to generate and capture the reflected signal from a medium. In other words, the emitter and receiver are the same transducer. The second setup is a pitch-catch mode. In this setup, a transducer generates the ultrasonic waves (emitter) and a different transducer captures the ultrasonic waves (receiver). When the receiver captures the reflected waves, the configuration is called pitch-catch through reflection, as shown in Figure 6.7b. If the receiver captures the transmitted signals, the setup is known as pitch-catch through transmission (Figure 6.7c). In the current study, the pitch-catch through reflection was used for CAN, and the pitch-catch through transmission was used for lubricant degradation. When only one surface of a medium is accessible, the pitch-catch through reflection is used. For example, to measure oil film thickness between a liner and piston in an engine, as only one side of the engine block is accessible and the receiver cannot be placed inside the piston.

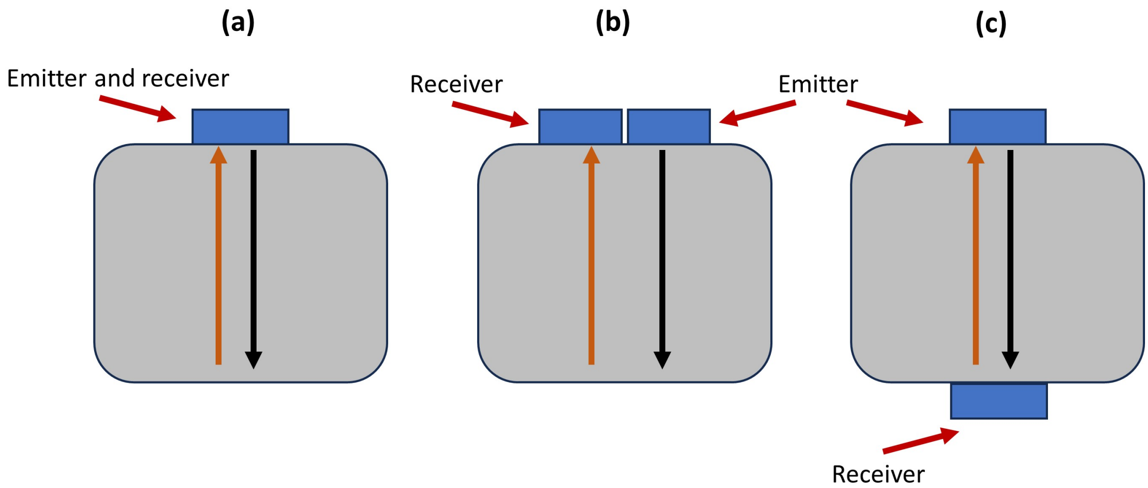

Figure 6.7: Ultrasonic measurement modes: (a) pulse-echo; (b) pitch-catch through reflection; (c) pitch-catch through transmission.

6.9 Ultrasound signal characteristics

The actual ultrasonic signals captured by a transducer are in the time domain (Figure 6.8a). They are characterised by centre frequency f_c, waveform duration and bandwidth. The centre frequency and bandwidth of the signals cannot be detected in the time domain. However, a frequency domain (Fast Fourier Transform (FFT) of the time domain signals) gives this information, as shown in Figure 6.8b. It is seen from Figure 6.8b that the peak of the amplitude of the ultrasonic wave is at the frequency 1.78 MHz. This frequency is called the peak frequency. The amplitude of the ultrasonic signal decreases as the frequency deviates from the peak frequency. For example, at frequencies 1.46 MHz and 2.05 MHz, the amplitude of the FFT decreases by -3 dB or 70%. The lower and upper frequencies at -3 dB (or any desired value, e.g., -6 dB) are known as lower f_l and upper f_u cut-off frequencies, respectively. The bandwidth frequency is defined as the difference between these cut-off frequencies. When using a transducer as an emitter or receiver, it is recommended that the peak frequency be in the bandwidth frequency. In other words, to use a transducer as a receiver, its peak frequency is suggested to be between 1.46 MHz and 2.05 MHz. The centre frequency is given by:

$$f_c = \frac{f_l + f_u}{2} \tag{6.1}$$

This indicates that the centre frequency is in the middle of the lower and upper cut-off frequencies. However, the peak frequency may be different from the centre frequency.

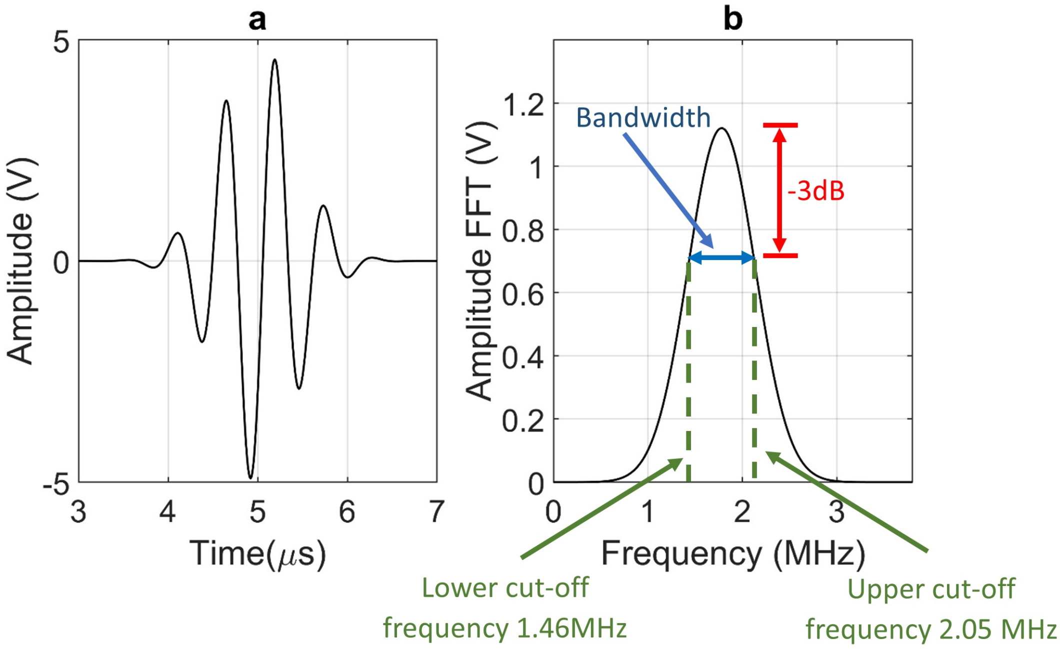

Figure 6.8: Ultrasonic signal captured with a longitudinal transducer at the peak frequency of 1.78 MHz: (a) time domain; (b) Frequency domain (FFT).

To generate the maximum ultrasonic energy, the transducers must be excited at their peak frequencies.

6.10 Ultrasonic function generator and digitiser

A function generator is a device that generates a desired waveform. These waveforms are then sent to the ultrasonic transducers to generate waveforms and propagate the ultrasonic waves into a medium. One of the most common function generators is a Picoscope, as shown in Figure 6.9. Some of the common waveforms generated by a function generator are square and sinusoidal (sin) waveforms. The current study aims to generate ultrasonic waves with a single frequency and generate higher frequencies in a medium or contact of the solids. Therefore, a sinusoidal waveform is used. In addition to the waveform, the number of cycles or waveform duration is important. In tone burst cycle mode, a finite number of cycles are generated. When the number of tone burst cycles increases, more ultrasonic energy is generated in the medium. In Section 6.14.1, tone burst cycles and their effect on higher-order harmonics are discussed.

The ultrasonic signals captured with a receiver are analogue (continuous signals in time) and are required to be converted to digital signals (discrete-time signals) [103].

Figure 6.9: A Picoscope that works as a function generator and a digitiser.

The Picoscope (shown in Figure 6.9) is also an analogue-to-digital converter.

6.11 Power amplifier

The maximum amplitude of the waveform that the Picoscope, used in the current study (shown in Figure 6.9), can generate is 4 V peak-to-peak. This amplitude is not sufficiently large to generate higher-order harmonics (material or contact non-linearity). The generated signals are required to be amplified using a high-power amplifier, as shown in Figure 6.10. The amplifier is equipped with a function generator; therefore, in the current experiment, the Picoscope was used only as a digitiser.

Figure 6.10: High-power amplifier used in the current study to amplify ultrasonic waves.

6.12 Laser Doppler vibrometer

The output of the ultrasonic transducers is in a voltage unit. As is seen in Sections 7.3, 7.4, 8.2 and 11.2 the voltage is required to convert to a metre unit. In the current study, a laser Doppler vibrometer (shown in Figure 6.11) is used to perform this conversion. A laser beam incident a vibrating surface of a solid medium. The

Figure 6.11: Laser Doppler vibrometer.

reflected laser is captured by the head of the laser. The phase shift of the captured and incident laser beam is digitised by a Picoscope. These captured signals measure the velocity of the vibrating surface. A numerical integral of the velocity is used to measure the displacement of the surface. The maximum frequency that can be measured with the laser Doppler vibrometer is almost 4 MHz.

6.13 Ultrasonic instrumentation

6.13.1 Ultrasonic transducers

As seen in Chapter 5, the ultrasonic waves reflected from the interface are distorted. This distortion is presented as high-order frequencies. The higher the amplitude of the incident wave, the more nonlinear the contact is, and the greater the number of high-order harmonics. The high-order harmonics are integer multiples of the fundamental frequency (excitation frequency). For example, if the fundamental frequency is $f_1 = f_0$, then the second and third order harmonics are $f_2 = 2f_0$ and $f_3 = 3f_0$, respectively. There are two procedures to capture these high-order harmonics. The first method uses the pulse-echo method, in which a single transducer is used as the emitter and receiver (Figure 6.7a). In this method, the transducer bandwidth should be large enough to capture second-order harmonics with an amplitude reduction of not less than -6 dB. Making these transducers is a challenge to manufacture. The second method is to use either pitch-catch through transmission (used by [53, 49]) or pith-catch through reflection which is used in this study. Figure 6.12 shows the pitch-catch mode and a sample measurement from the interface.

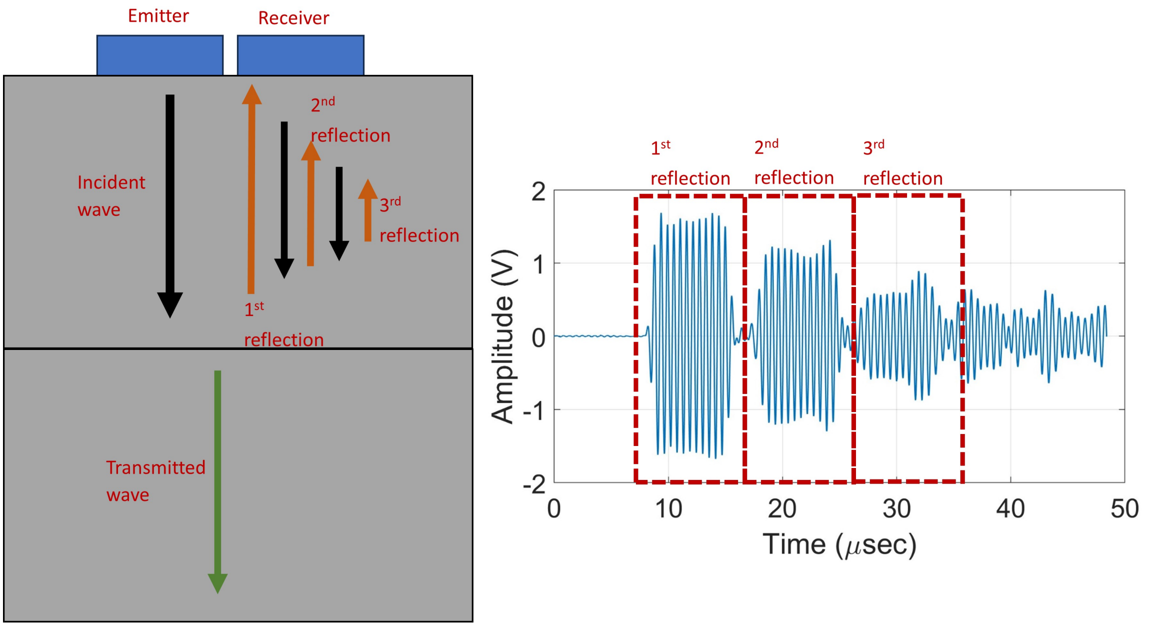

Figure 6.12: Reflections from an imperfect interface: (a) schematic diagram; (b) signals in time domain.

When ultrasonic waves are incident on the interface, they are partly reflected and transmitted because of factors such as the percentage of the real contact area and acoustic impedance mismatch of the mating surfaces at the interface. The first reflection is captured by the receiver, as shown with an orange arrow in Figure 6.12a and the first window in Figure 6.12b. This reflection contains the most reflected ultrasonic energy and is used for the analysis of the current study. When the first reflection incident on the top face of the boundary, part of the ultrasonic wave reflected and propagated back towards the interface. The waves are reflected back from the interface and captured with the receiver. They are the second reflection, shown as an orange arrow in Figure 6.12a and the second red window in Figure 6.12b. The amplitude of ultrasound of these waves is attenuated and becomes smaller. In addition, they interfere with other reflections in the medium and from the interface; therefore, the information they provide might not purely contain the contact condition.

The only concern is the receiver's centre frequency, which must be within the frequency bandwidth of the fundamental frequency (emitter's frequency). In this study, the centre frequency of the emitter was selected to be 1.78 MHz and the receiver had a centre frequency of 5 MHz. As shown in Section 5.2.4, this is the appropriate frequency range for the CAN with the dimension of the samples used here.

6.13.2 Ultrasonic transducer placement and layout

Figure 6.13 shows an ultrasonic transducer and a spacer placed on the black face of the samples. A couplant gel was used to transfer the maximum ultrasonic energy from the transducer to the specimen and also the reflected wave from the specimen to the transducer. The transducer must be subjected to constant contact pressure

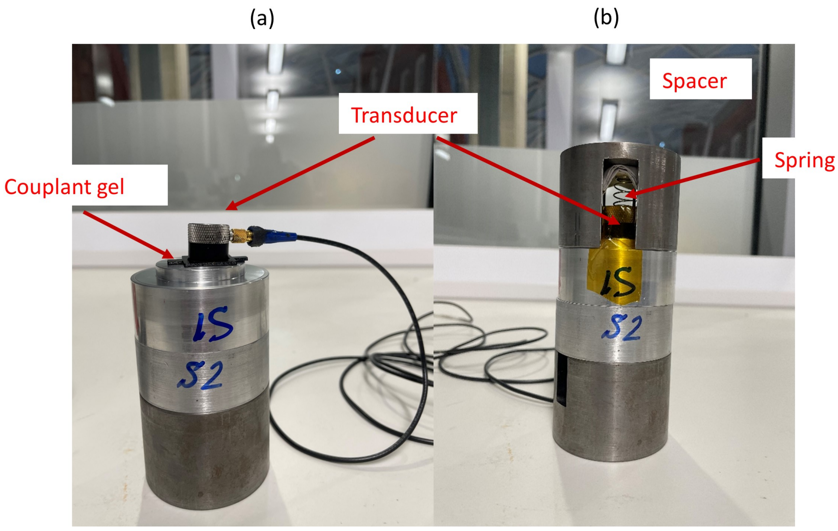

Figure 6.13: Ultrasonic transducer setup.

for steady and uniform contact between the specimen and the transducer. Therefore, a spring is placed between the spacer and the transducer. The schematic diagram of the experimental setup was shown in Figure 6.14.

The position of the receiver and its distance from the emitter affect the amplitude of ultrasound reflected from the interface. To study the effect of the separation distance, the pitch-catch through reflection was used with a zero separation distance (Figure 6.15a). Then, the separation distance between the transducers increased, and the reflected signals from the solid-air interface were captured. Figure 6.15b shows the variation of the reflected signals as a function of the separation distance. It is seen that the maximum reflected signal was captured when the ultrasonic waves were

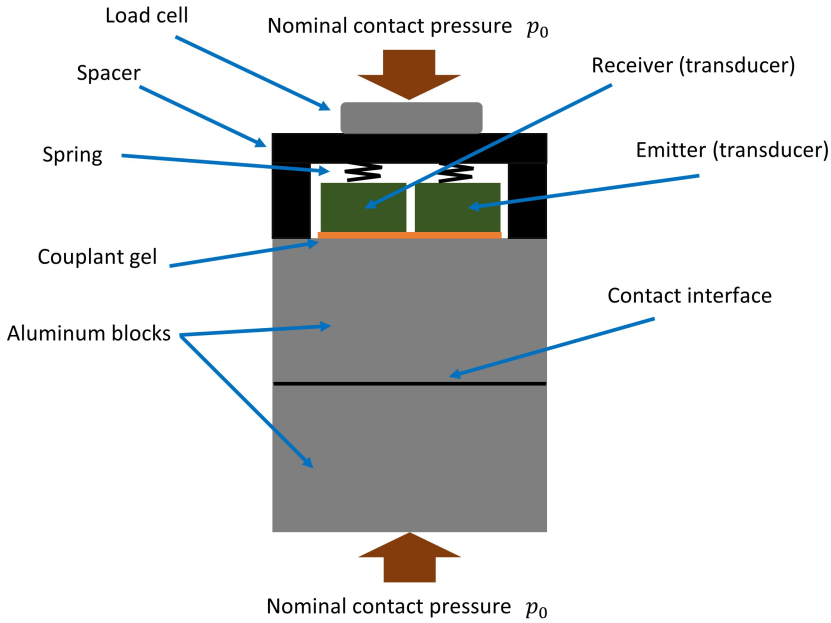

Figure 6.14: Schematic diagram of the pitch-catch through reflection mode used for CAN adapted from [2].

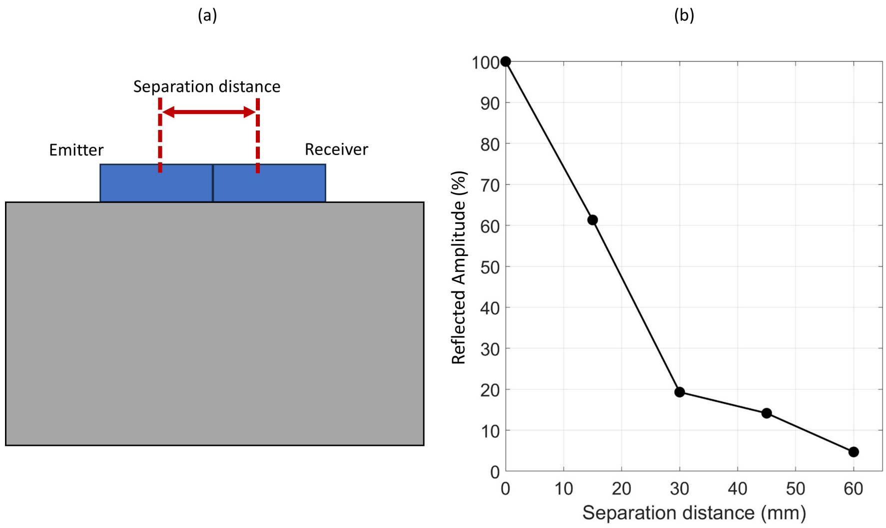

Figure 6.15: The effect of separation distance between the emitter and receiver on the reflected amplitude: (a) schematic diagram; (b) reflected amplitude.

incident perpendicular to the interface. The amplitude decreased as the separation between the transducers increased. Consider the reflected waves as a reference when the transducers are placed with zero separation, so 100% of the ultrasonic waves were reflected. As the transducers were separated further, the reflected waves by the receiver were reduced. For example, when the separation distance was 60 mm, the receiver captured less than 10% of the reflected waves. In this study, the transducers were placed at the closest possible distance to each other.

6.13.3 High-power amplifier

The transducers use electrical power to generate ultrasonic waves. If the input power is low, the output voltage of the transducers is also low; therefore, the displacement of the particles is insufficient to generate CAN. A high-power amplifier is used to amplify the input voltage of the transducer, and subsequently, the amplitude of the output voltage increases to create contact nonlinearity. Figure 6.16 shows the FFT of the reflected ultrasonic waves from an imperfect interface using a high-power amplifier (RITEC RAM-5000) at different excitation amplitudes. Contact nonlinearity

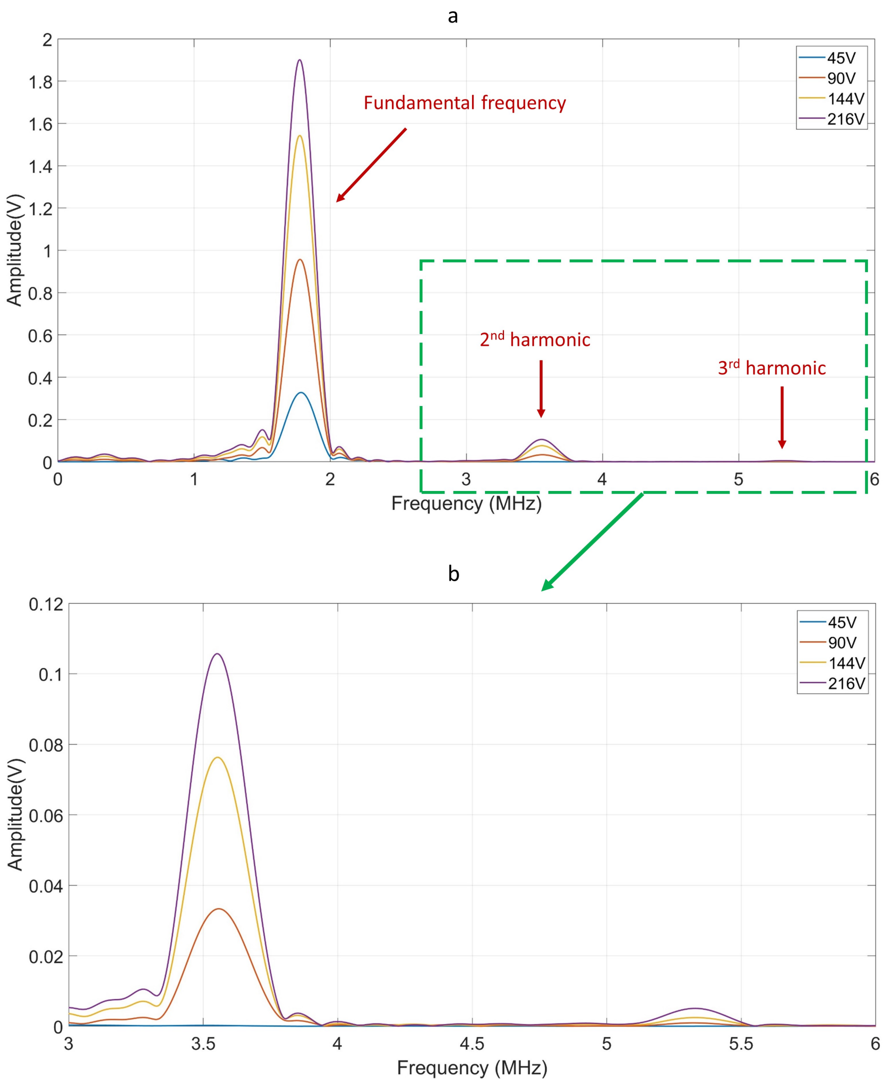

Figure 6.16: The effect of amplified excitation amplitude on CAN: (a) frequency domain; (b) zoomed-in to show the second- and third-order harmonics.

(higher-order harmonics) was not generated for the excitation amplitude below 45 V. However, as the input voltage of the transducers was increased, the amplitude of higher-order harmonics increased.

6.13.4 Couplant gel and its effect on CAN

Figure 6.6 shows that the air gap between the transducer and a medium reflects the ultrasonic energy of the transducer-medium interface. Couplant gels are used to transfer the highest possible ultrasonic energy to the medium. Here, the effect of the couplants on the signals is studied on the basis of three different approaches.

1. waveform
2. transferred energy
3. their effects on nonlinearity.

Figure 6.17 shows the real-time reflected ultrasonic waves from a solid-air interface without using any couplant and with distilled water, PAO100 and a shear gel SWC-2 as couplants. Figure 6.17a shows that the ultrasound cannot be adequately trans-

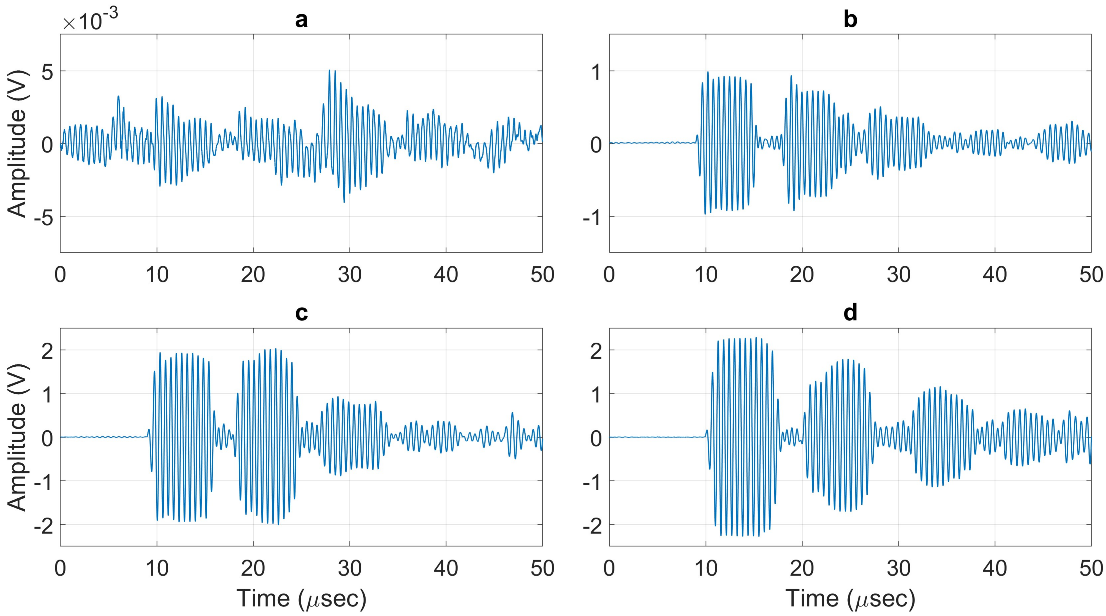

Figure 6.17: Reflected signals from different couplants: (a) without couplant gel; (b) distilled water; (c) PAO100; (d) shear gel SWC-2.

ferred to the medium. Although the waveform was more stable when distilled water and PAO100 were used, the most steady reflection occurs for the shear gel SWC-2

(Figures 6.17b-d). The term steady in the waveform means that the consecutive cycles of the tone burst do not have fluctuations. The other factor for using a couplant is the amount of energy that they transfer. Figure 6.18 shows the FFT of the reflection from a solid-air with and without using the couplants. The amplitude of the fundamental frequency A_1 is a measure to show the amount of reflected ultrasonic waves. It is seen in Figure 6.19a that the shear gel SWC-2 transfers the maximum energy

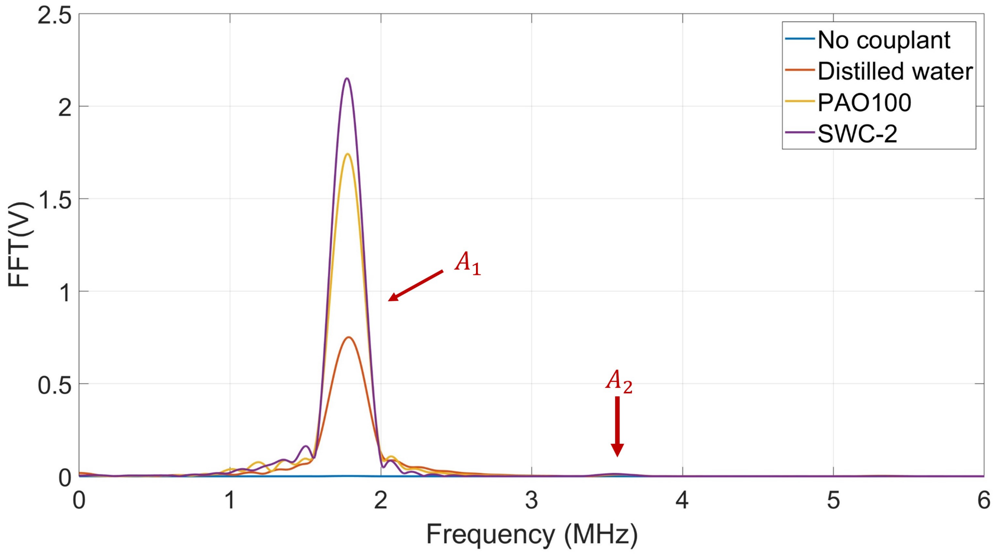

Figure 6.18: FFT of reflection from a solid-air contact with and without using the couplants.

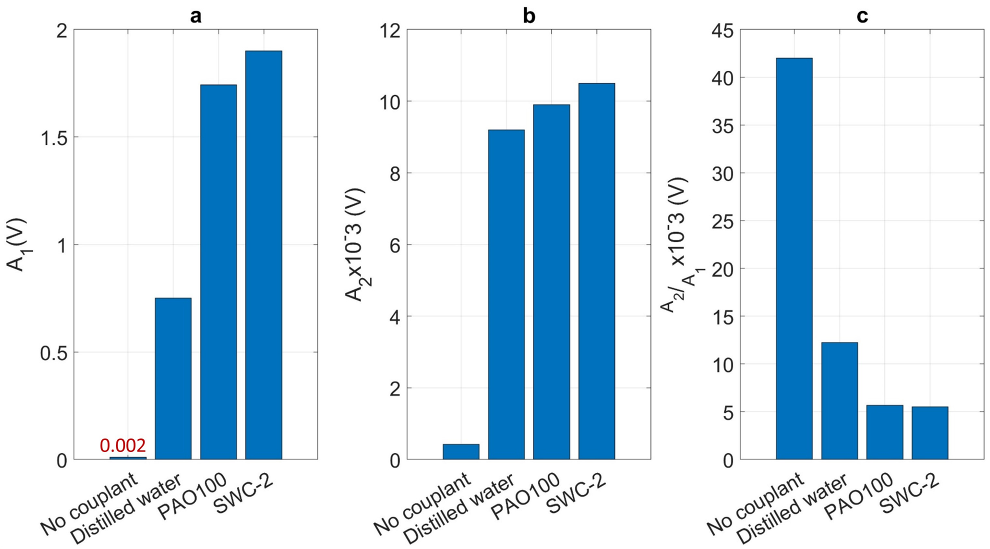

Figure 6.19: The effect of couplant on the: (a) amplitude of fundamental frequency A_1; (b) amplitude of the second-order harmonic A_2; (c) the ratio of A_2/A_1.

compared to the couplants. There is also a second-order harmonic in the frequency domain (Figure 6.18), which indicates the couplants generate nonlinearity (Figure 6.19b). Maximum nonlinearity was generated when the shear gel SWC-2 was used. The best couplant can transfer the maximum ultrasonic energy (A_1) and generate the minimum possible nonlinearity (A_2). In order to decide the best couplant, the ratio A_2/A_1 is used. It is seen from Figure 6.19c both PAO100 and shear gel SWC-2 have the minimum A_2/A_1. In the current study, the shear gel SWC-2 wave was used as it is a non-toxic material and provides a sticky condition between the transducer and the sample.

6.14 Data acquisition and processing

In CAN and material nonlinearity in solids and liquid lubricants (Chapters 9-11), the number of tone burst cycles and the windows of captured waves are required to be determined.

6.14.1 Number of tone burst cycles

The number of tone burst cycles is required to be determined to optimise the number of cycles such that sufficient ultrasonic energy is transferred to the medium to generate nonlinearity. Figure 6.20 shows the FFT of the reflected waves from an imperfect contact with a centre frequency of 1.78 MHz and an excitation amplitude of 216 V. The number of tone burst cycles varied at 2, 8 and 11. The more tone burst cycles,

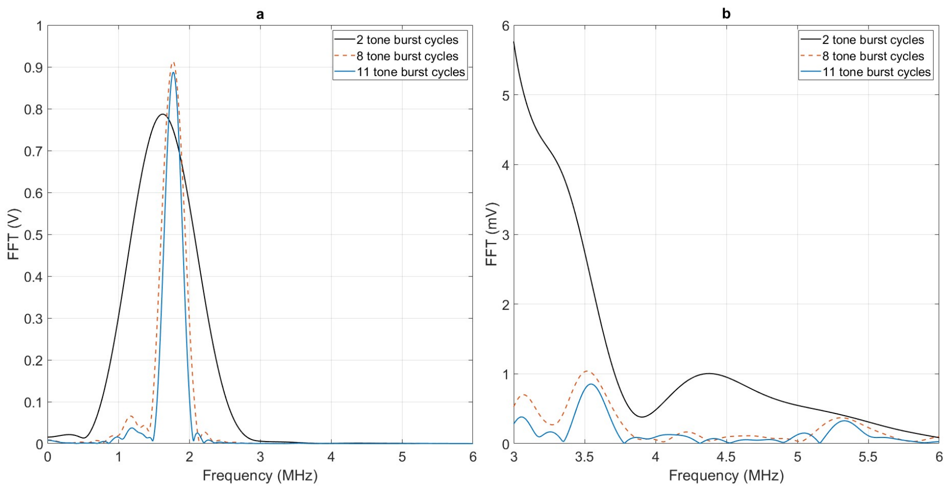

Figure 6.20: The effect of the number of tone burst cycles on the ultrasonic energy and CAN: (a) frequency domain up to 6 MHz; (b) zoomed-in to show the second-order harmonic.

the more ultrasonic energy is generated. Figure 6.20 shows that the amplitude of the reflected wave generated with the eight- and eleven-tone burst cycles was 142% and 152%, respectively, compared to the two-tone burst cycle. As a result, CAN is seen when using eight- and eleven-tone burst cycles, while the energy generated by a two-tone burst cycle is not sufficiently large (Figure 6.20b). Therefore, for CAN, not only the amplitude of excitation but also the number of tone burst cycles are important for generating the maximum ultrasonic energy. It should be noted that the sampling frequency (the number of generated data points in a unit of time) here was 125 MHz. This is significantly higher than the peak frequency of the ultrasonic waves, which ensures the avoidance of aliasing.

6.14.2 Number of captured windows

The ultrasonic tone burst cycles are generated as a series of signals with a delay. In other words, the first tone burst cycles are generated and propagated in a medium, and after a delay, the second tone burst cycles are generated. This process is continued over the experiment (here, a 10 μsec delay was used as this time is sufficient for the waves not to interfere). When ultrasonic waves are captured, there are a number of reflected waves from consecutive triggers, which can be called windows. It is essential to study how many of these windows should be considered. To do this, the reflected waves from a solid-air interface ran for a few seconds, and a total of 4600 windows were captured (4600 triggers). Figure 6.21 shows the FFT of the mean reflected waves of an imperfect contact with different captured windows of 1, 500, 1000 and 3000. The

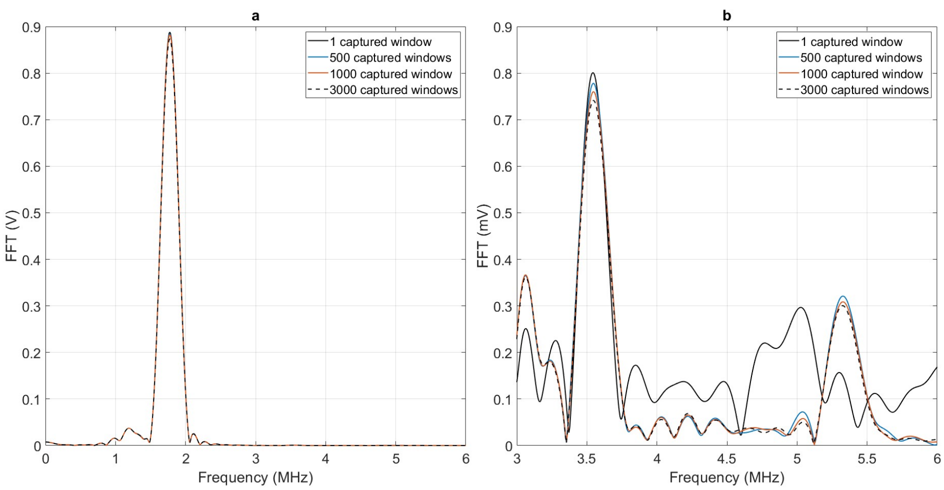

Figure 6.21: The effect of captured windows on the FFT of reflected waves: (a) frequency domain between 0 and 6 MHz; (b) zoomed-in frequency domain to show the higher-order harmonics.

amplitude of the mean varies as the number of captured windows increases. In fact, during the experiment, some factors, such as noise, can affect the results; therefore, the mean value of the captured windows can reduce the uncertainty. In Figure 6.22, it is seen that there is an error of almost 10% between 1 window capturing and the total windows, while this error is almost 1.5% error when 3000 windows were averaged. Although the more windows captured, the more accurate the results are, for the large size of data, it might be significantly time-consuming. For the current study, due to the insignificant size of the windows, all windows were averaged.

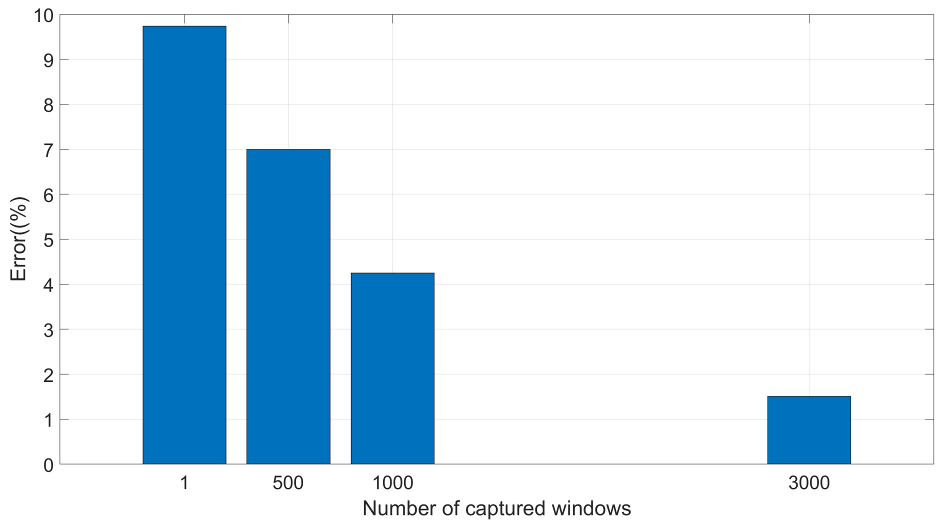

Figure 6.22: Percentage error on the number of captured windows compared to all windows.

6.15 Signal processing

The procedure for signal processing used in this study follows the concepts presented in Ref [45]. The captured ultrasonic waves are time-domain signals. There is no unique procedure for signal and data processing and is taken according to the nature of the data and the type of information it aims to provide. However, the main procedure can be summarised as follows:

1. importing the real-time data captured by the transducer
2. storing the data
3. averaging the desired number of captured windows (Section 6.14.2)
4. truncating the target signals

5. windowing and zero padding the data

6. using FFT to transfer the captured ultrasonic signals from the time domain to the frequency domain

The data were first imported and stored by coding programmes (in the current study MATLAB was used). The signals in the time domain contain different reflections, as shown in Figure 6.23a. First, the target signal must be truncated. The target signal

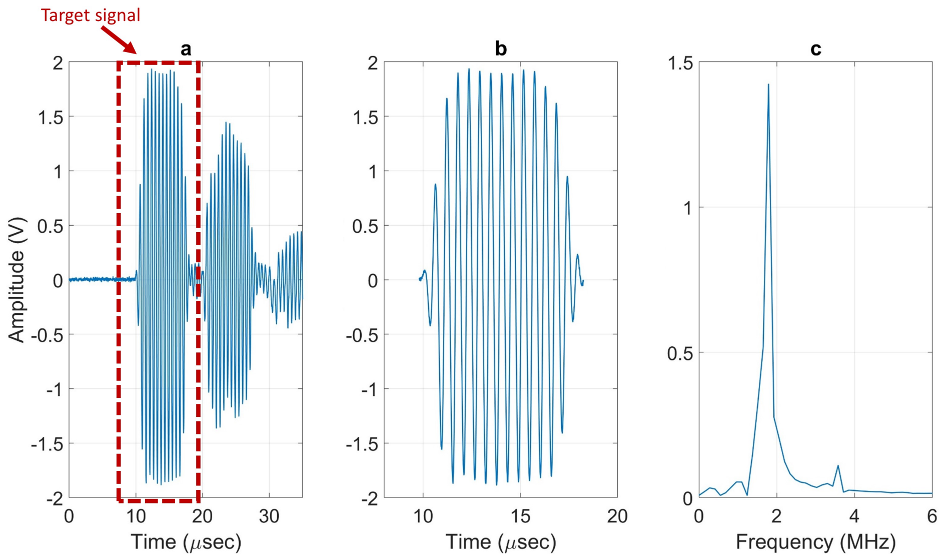

Figure 6.23: Signal processing on the time domain of reflected waves: (a) all reflections; (b) truncation of the target signal.

of CAN is the first reflection, as it contains a higher energy compared to the other reflections, and it gives the information of the first incident, while the consecutive reflections may also contain information such as the internal interference. (To study this, the first two reflections of the interface are investigated in Section 7.5). Figure 6.23b shows the truncated window of the first reflection. The time domain signal does not indicate the existence of higher-order harmonics and values at each frequency. Therefore, the time domain is required to transfer to the frequency domain. To do this, FFT is employed. In Figure 6.23c, the value of the reflected waves from the interface is seen at each frequency.

6.15.1 Effect of windowing and zero padding

The resolution of the FFT of the target signal was poor, as shown in Figure 6.23c. To increase the resolutions, a window and zero padding function were required before the

FFT. There are different window functions, such as Hanning, Hamming and Rectangular. Among them, the Hanning window reduces side lobes more efficiently [103] and the higher-order harmonics can be easily distinguished. The Hanning window creates an envelope around the truncated waves and closes both ends of the signals. This reduces the amplitude of the side lobes in the frequency domain. Figure 6.24b shows the target signal with an applied Hanning window. Figure 6.24c shows that although the resolution of the FFT is increased after using the Hanning window, it is insufficient. A zero padding function adds zeroes at the end or on both sides of the

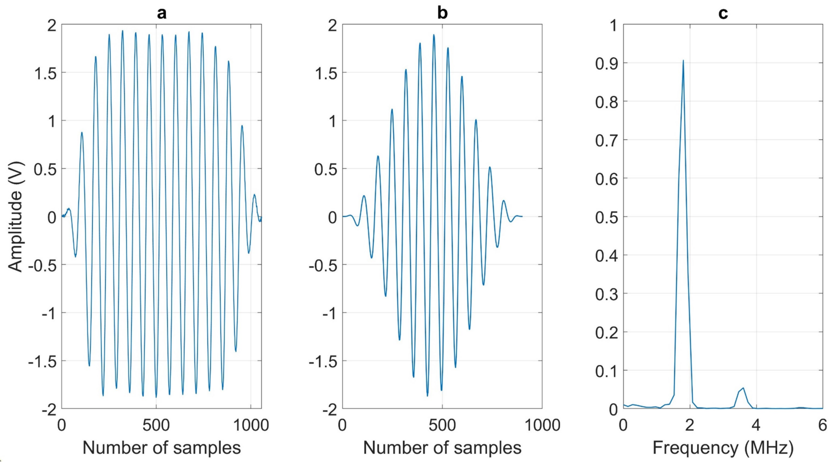

Figure 6.24: The effect of Hanning window on the resolution of FFT: (a) target signal; (b) target signal after applying the Hanning window; (c) frequency domain.

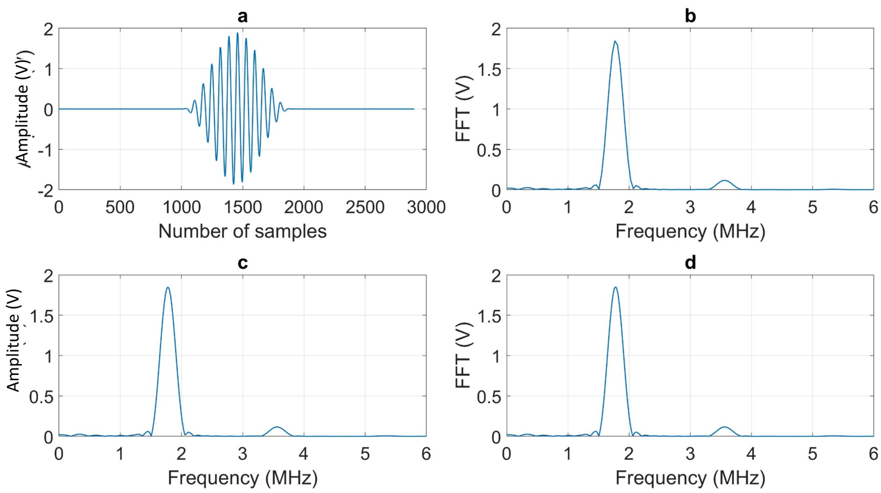

Figure 6.25: The effect of zero padding on: (a) 2000 zeros add on both sides of the Hanning window; (b-d) and the resolution of the FFT with: (b) 2000 zeros; (c) 5000 zeros; (d) 20000 zeroes.

Hanning window. These zeros do not influence the results of the FFT but increase the resolutions. Figure 6.25a shows a zero padding function at both ends of the Hanning window with 2000 zeros. Figure 6.25b shows that the resolution of FFT, while using 2000 zeros, is significantly improved from the FFT one without using any zero padding (Figure 6.24c). Despite increasing the number of zeros, the result of FFT does not change and only the computational time increases. It should be noted that the number of zeros varies with the different datasets, and there is not a general rule for it.

6.16 Laser Doppler Vibrometer: voltage-to-length unit conversion

Reflected ultrasonic waves captured by the receiver are in units of voltage. To measure the second-order nonlinear parameter, second-order nonlinear normal interfacial stiffness (Chapters 7 and 8) and nonlinear coefficient (Chapters 10 and 11), it is necessary to have the amplitudes in units of length. An approach for this conversion is to use a laser Doppler vibrometer [45, 104]. Figure 6.26 shows the laser Doppler configuration (Polytec with laser sensor head OFV 354 and vibrometer controller OFV 2500), where a laser beam is emitted from the laser head. The laser beam is then incident to the surface of the sample and reflected. The reflected beam is again captured by the laser head. If the sample surface is stationary without any vibration, the reflected beam shows zero surface displacement. However, when the sample vibrates (for example, at the frequency of the transducer), the Doppler effect of the reflected beam is captured by the laser head and appears as displacement (velocity or acceleration) in the reflected beam. When the laser head and the sample are set up, the

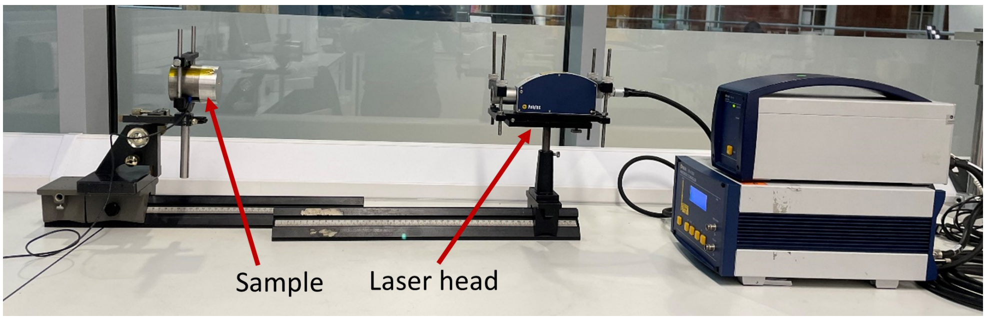

Figure 6.26: Laser Doppler vibrometer setup.

distance between them must be in focus. If this distance is less than or larger than the optimal length, the quality of the reflected beam is poor, and the signal-to-noise ratio is significantly low. Figure 6.27 shows the quality bar on the laser controller when the sample and the laser head are in and out of the focal length. The other condition is that the laser beam must also be incidentally normal to the surface, such that the laser head captures the reflected beam.

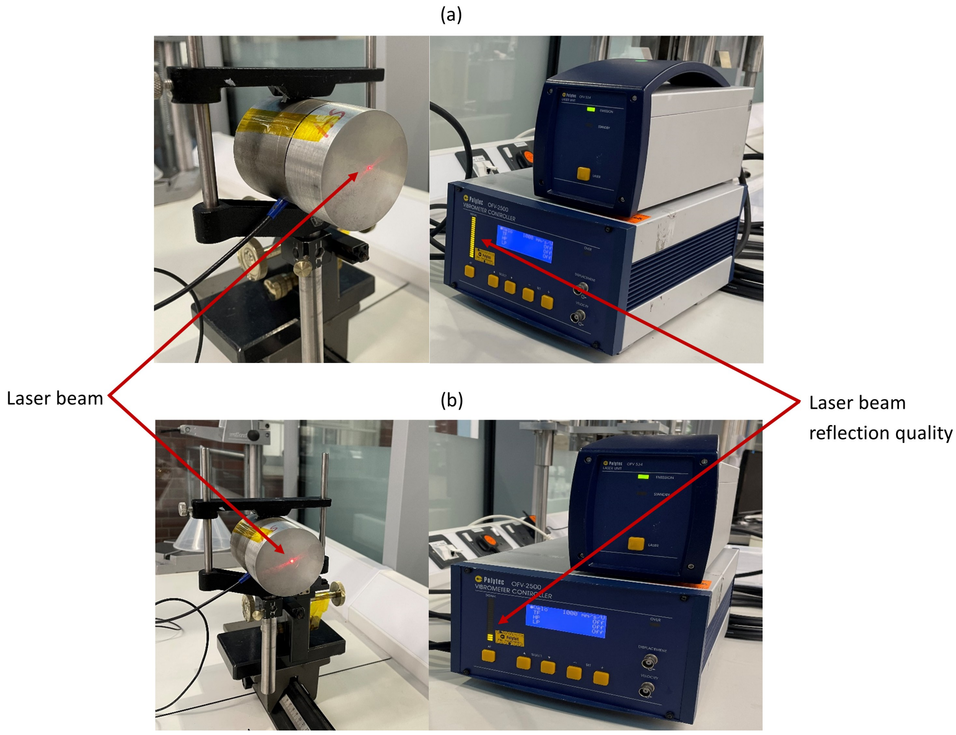

Figure 6.27: Quality of the laser beam: (a) in focal length; (b) out of focal length.

Figure 6.28 shows the schematic diagram of the conversion of the voltage to the length unit. This measurement was taken in two steps. **step 1:** the emitter was placed on the back face of the upper body and the receiver on the front face, as shown in Figure 6.28a. The ultrasonic waves were generated by the emitter (with peak frequencies of 1.78 MHz and 3.56 MHz) at different excitation peak-to-peak voltages of 4.5 V to 288 V in 16 increments and captured with the receiver. **step 2:** as shown in Figure 6.28b, a laser beam was emitted to the face of the upper body to capture the ultrasonic waves generated by the emitter. In other words, the laser Doppler vibrometer was used as a receiver that can measure the velocity and displacement of the surface motion. The laser Doppler vibrometer was capable of capturing frequencies up to 4 MHz. The frequencies of 1.78 MHz and 3.56 MHz are equal to the fundamental frequency and second-order harmonics for CAN in the solid-solid contact when subjected to the 1.78 MHz ultrasonic waves.

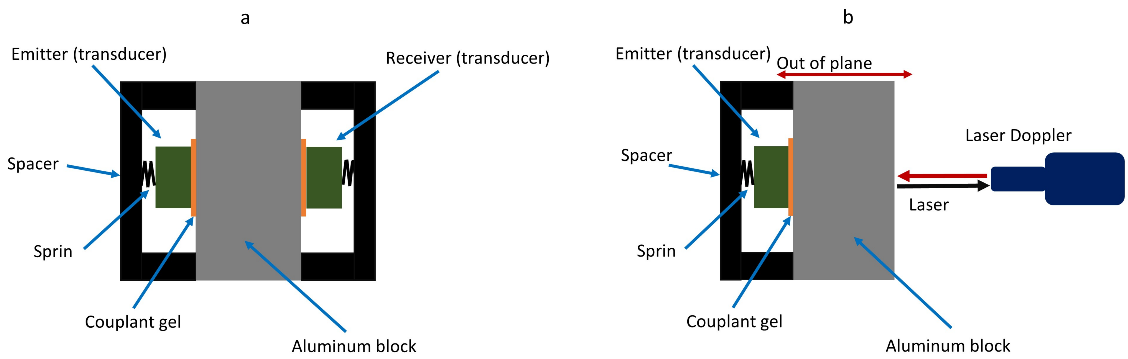

Figure 6.28: Schematic diagram of amplitude calibration apparatus: (a) ultrasonic measurement; (b) laser measurement.

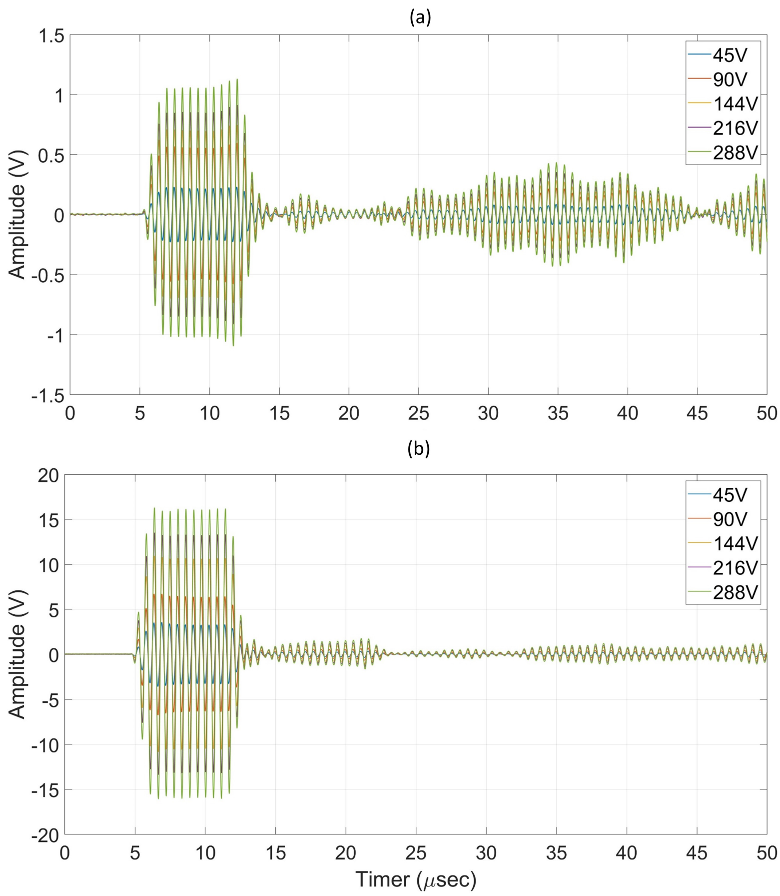

Figure 6.29: Time domain reflection captured by: (a) laser Doppler vibrometer; (b) ultrasonic transducers.

Figure 6.29 shows the waves reflected from the surface of the sample captured by the receiver (step 1) and the corresponding reflection captured by the laser head (step 2). The reflection captured by the laser head is the velocity of the particle on the surface (Figure 6.30a). It is converted to displacement using a numerical integral

(Cumtrapz function in MATLAB), as shown in Figure 6.30b. The FFT of the reflected

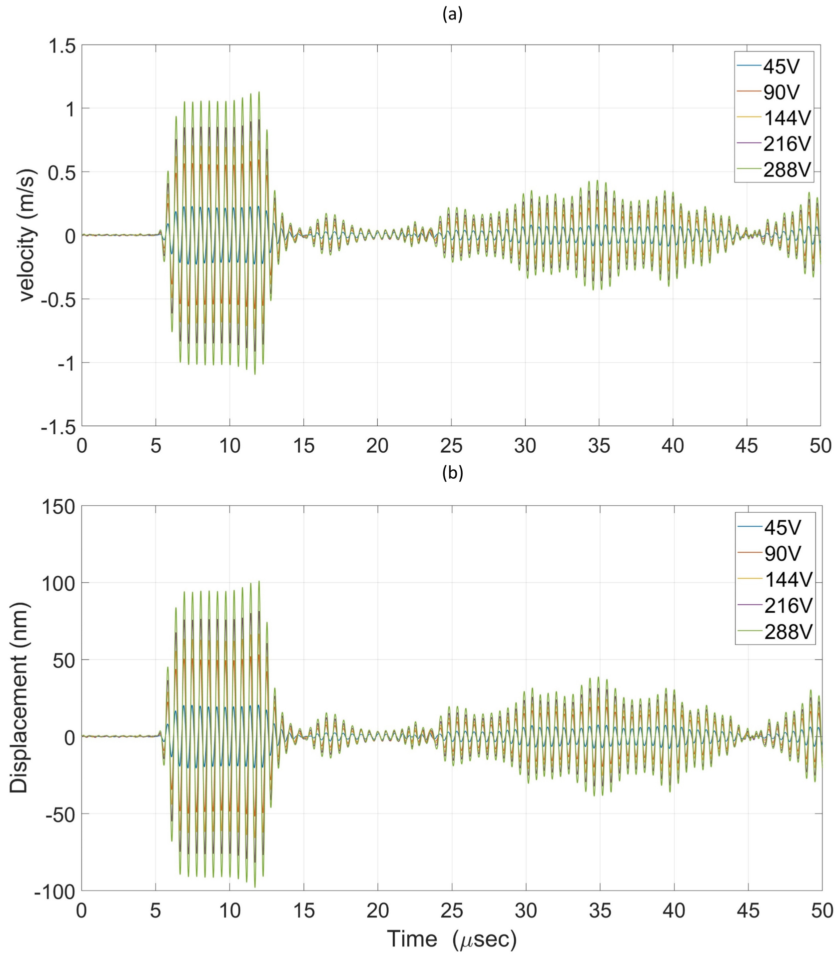

Figure 6.30: Time domain reflection : (a) velocity; (b) displacement.

waves captured by the laser head and the ultrasound transducers is determined to find their values at the fundamental frequency and the higher-order harmonic (Figure 6.31). For each excitation amplitude, the displacement of the particles was plotted against the corresponding ultrasound values to derive the unit conversion voltage to length, as shown in Figure 6.32. The slope of the best-fit lines gives the voltage-to-length unit conversion [2, 45].

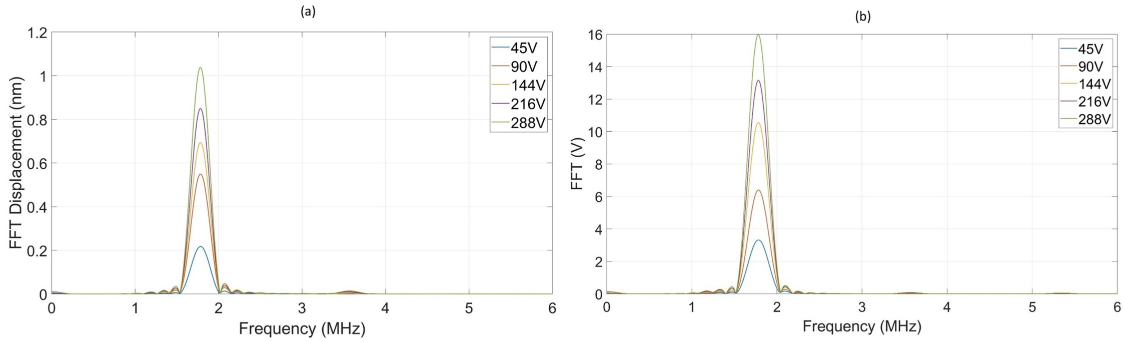

Figure 6.31: The frequency domain of reflections captured by: (a) laser Doppler vibrometer; (b) ultrasonic transducers.

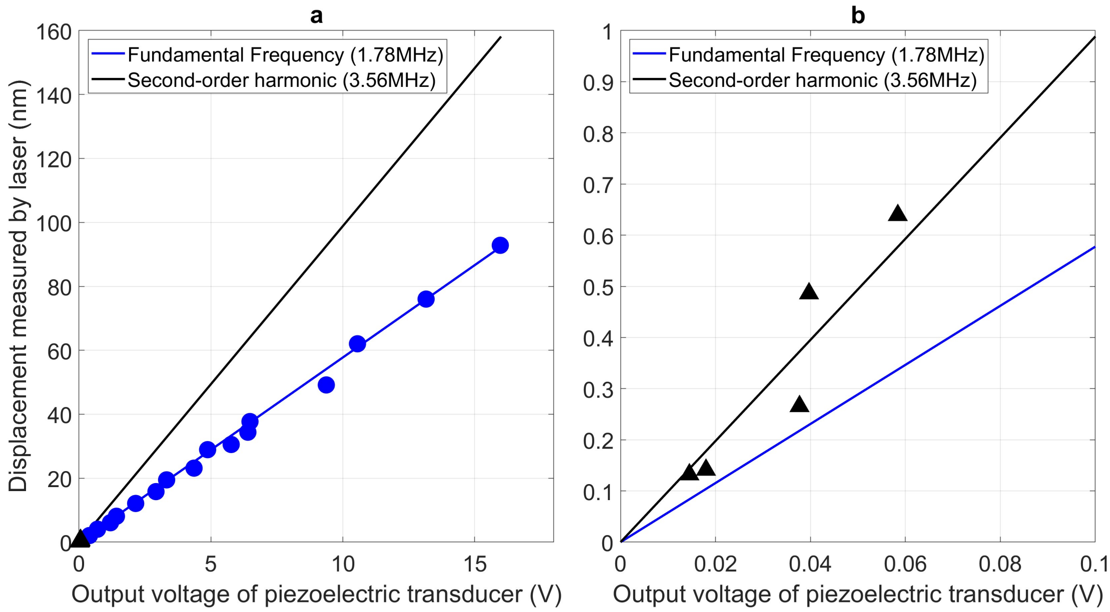

Figure 6.32: The voltage-to-length unit conversion with frequencies 1.78 MHz and 3.56 MHz at ultrasonic incident peak-to-peak amplitude of 4.5 V to 288 V: (a) actual length; (b) zoomed-in view to show the second-order harmonic data points.

6.17 Conclusion

In this chapter, the experimental setup and signal processing required for CAN were presented. The loading apparatus, samples and their surface topography and roughness before the first loading were shown. It was seen that more of the amplitude of ultrasound is captured when the transducer (emitter and receiver) is placed as close as possible. The effect of the couplant gel on the amplitude of the ultrasonic waves and nonlinearity was also studied. It was shown that the shear gel SWC-2 is suitable to use as it generates less nonlinearity and transmits more ultrasonic energy than distilled water and PAO100.

Data acquisition was explained to investigate the number of tone burst cycles and captured windows for averaging. As the number of cycles increased, more ultrasonic energy was seen to be generated. The ultrasound amplitude was 142% and 152% for 8 and 11 cycles compared to 2 cycles. The effect of the Hanning window and the zero padding function was presented for signal processing. It was seen that using both the Hanning window and a higher number of zeroes in the zero padding increased the resolution of reflected waves in the frequency domain.

The reflected ultrasonic waves with the transducers are in units of voltage. Since the equation to detect the second-order nonlinear normal interfacial stiffness is in units of metres, the ultrasonic waves must be converted to metres. Therefore, a laser Doppler vibrometer was used at the fundamental frequency and higher-order harmonics. This gave a coefficient that converts voltage to metres, which was then used in Chapters 7 and 8 to determine the second-order nonlinear normal interfacial stiffness.

Chapter 7

Linear and Nonlinear Normal Interfacial Stiffness in Dry Contacts

This chapter covers the linear and nonlinear normal interfacial stiffness measured using reflected ultrasonic waves. The analytical method for ultrasonic waves discussed in Chapter 5 is used to derive the linear and nonlinear normal interfacial stiffness. This model was proposed by Biwa. et al., [53]. In the current study, the author of this thesis proposed two nonlinear differential equations based on linear and second-order nonlinear normal interfacial stiffnesses [2]. The solutions of these equations were used to validate the proposed model by [53].

7.1 Theoretical approach

7.1.1 Ultrasound

The main theoretical approach is outlined in Ref [2, 53]. Two linear elastic media with rough surfaces subjected to a one-dimensional elastic longitudinal ultrasonic wave are considered in contact, as shown in Figure 7.1. Ultrasonic waves are propagated through the thickness of the medium defined as the x-axis. The origin of the x-axis is defined as the point where the asperities of the surfaces are in the first contact. The roughness mean lines of the upper and lower bodies of the interface are located at X_- and X_+, respectively, as shown in Figure 7.1a. When only external pressure is applied (in the absence of ultrasonic waves), the contact is in static equilibrium and the surface separation is h_0 (Figure 7.1c). To simplify the analysis, the upper body is assumed to be flat and rigid, and the deformation of the lower body is considered as an elastic material. When ultrasonic waves are generated, the contact pressure is the sum of ultrasonic waves $p_{ultrasound}$ and external pressure p_0. In this condition, the surface separation $h(t)$ varies from the equilibrium separation h_0. The difference between surface separation and equilibrium separation is represented by the relative surface approach $Y(t)$ (the approach of the contact surfaces when the ultrasonic waves are incident at the interface). The relative surface approach is zero under only external pressure p_0 (no ultrasound). The contact can be modelled as a distributed spring [43, 12].

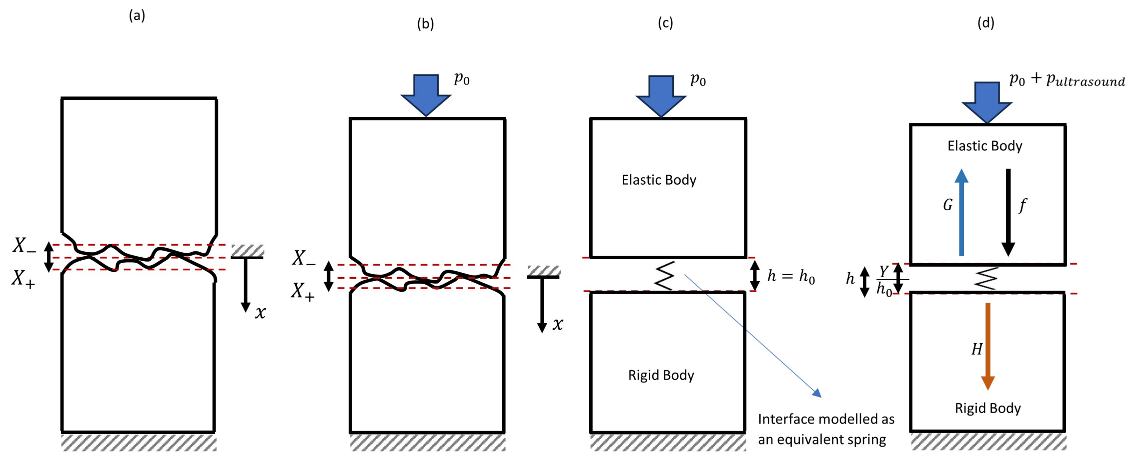

Figure 7.1: Schematic diagram of the imperfect contact and ultrasonic wave propagation through elastic media adapted from Ref [2]: (a) elastic media and asperity junctions in the absence of normal load and ultrasonic pressure; (b) origin of contact; (c) mating surfaces under the normal load only under static equilibrium contact; (d) surface separation and approach caused by ultrasound.

The stiffness of an interface can be modelled as a series of springs created by the individual asperity contacts [13, 43]. The series of springs is then equivalent to a single distributed spring with an equivalent stiffness (expressed per unit area) [29]:

$$K = -\frac{dp_0}{dh} \tag{7.1}$$

The spring is nonlinear for practical rough surface contacts since the relation between the applied pressure and surface separation is not directly proportional. As the contact pressure increases, asperity contact occurs, and the interface stiffens. If the deflection is small (and less than the elastic limit of the spring material [105]) the nonlinearity can be neglected. The pressure–separation relationship and the resulting nonlinear stiffness must be considered for large deflections. One of the approaches to deal with the nonlinear contact pressure-relative surface approach of the interface (boundary or contact nonlinearity) is to express it as a series of polynomial terms in a Taylor series around $h = h_0$ [53].

$$p(h) = p(h_0 + Y) = p_0 - K_1 Y + K_2 Y^2 \tag{7.2}$$

where K_1 and K_2 are the linear and second-order nonlinear normal interfacial stiffness and p_0 is the nominal contact pressure at h_0. The linear K_1 and K_2 nonlinear terms of the interfacial stiffness are then defined by:

$$K_1 = -\frac{dp}{dY} \quad or \quad K_1 = -\frac{dp}{dh} \quad ; \quad h = h_0 \tag{7.3}$$

$$K_2 = \frac{1}{2}\frac{d^2p}{dY^2} \quad or \quad K_2 = \frac{1}{2}\frac{d^2p}{dh^2} \quad ; \quad h = h_0 \tag{7.4}$$

Differentiation of Eq. 5.18 with respect to the argument of the function at the interface $x = X_-$ results in:

$$\frac{\partial f(X_- ct)}{\partial (X_- ct)} = A\omega \; sin\omega t \tag{7.5}$$

Substituting Eqs. 7.2-7.5 into Eq. 5.14 gives:

$$\dot{Y} + \frac{2K_1}{\rho c}Y - \frac{2K_2}{\rho c}Y^2 = 2A\omega \; sin\omega t \tag{7.6}$$

which is a first-order nonlinear differential equation. An approximate solution, such as the homotopy perturbation method (HPM) [106], is required to derive the particular solution of the relative approach of the contacting surfaces. To do this, the solution of the differential equation is defined as the sum of the linearised equations of the differential equation which is known as a perturbation series [106]:

$$Y = Y_0 + \alpha Y_1 + \alpha^2 Y_2 + \alpha^3 Y_3 \tag{7.7}$$

where Y_0, Y_1, Y_2 and Y_3 are the first, second, third and fourth terms of the perturbation series and α is an embedding parameter that is assumed to be 1 to derive the particular solution of the differential equation. As α approaches 1, Eq. 7.7 gives an approximate solution to the nonlinear differential equation Eq. 7.6 [106]. In order to solve the nonlinear differential equation (Eq. 7.6), the differentiation of Eq. 7.7 with respect to time is substituted into Eq. 7.6. A series of differential equations in terms of only Y_0, Y_1, Y_2 and Y_3 are derived. The differential equations containing Y_0 and Y_2 are in a transient state (homogeneous differential equations). The initial surface approach is zero, subsequently $Y_0 = Y_2 = 0$. Therefore, the transient behaviour of the differential equation was ignored, and only the steady-state behaviour was considered. It should be noted that the ultrasonic waves used in the current study contain a ten-tone burst cycle. This number of tone burst cycles makes steady-state behaviour compared to ultrasonic waves with a four-tone burst cycle.

$$Y_1 = \frac{2A}{\sqrt{1+(2K_1/\rho c\omega)^2}} sin(\omega t - \delta_1) \tag{7.8}$$

$$Y_3 = \frac{2K_2A^2}{K_1(1+(2K_1/\rho c\omega)^2} \left\{ 1 - \frac{sin(2\omega t - 2\delta_1 + \delta_2)}{\sqrt{1+(K_1/\rho c\omega)^2}} \right\} \tag{7.9}$$

Substituting Eqs. 7.8 and 7.9 into Eq. 7.7 gives the relative surface approach $Y(t)$:

$$Y(t) = \frac{2A}{\sqrt{1+(K_1/\rho c\omega)^2}} sin(\omega t - \delta_1) + \frac{2K_2A^2}{K_1(1+(2K_1/\rho c\omega)^2} \left\{ 1 - \frac{sin(2\omega t - 2\delta_1 + \delta_2)}{\sqrt{1+(K_1/\rho c\omega)^2}} \right\} \tag{7.10}$$

where $\delta_1 = tan^{-1}(\rho c\omega/2K_1)$ and $\delta_2 = tan^{-1}(K_1/\rho c\omega)$. Substituting Eq. 7.10 into Eq. 5.17 results in an analytical equation for the reflected waves:

$$G(x+ct) = -\frac{K_2A^2}{K_1\{1+(2K_1/\rho c\omega)^2\}} - \frac{A}{\sqrt{1+(2K_1/\rho c\omega)^2}} sin\{\omega t + \frac{\omega}{c}(x - X_-) - \delta_1\} + \frac{K_2A^2}{\rho c\omega\sqrt{1+(K_1/\rho c\omega)^2}} sin\{2\omega t + \frac{2\omega}{c}(x - X_-) - 2\delta_1 + \delta_2\} \tag{7.11}$$

The terms in this equation with a frequency ω and 2ω represent the fundamental and second-order harmonics, respectively. So, the coefficient of terms containing ω (which is $\frac{A}{\sqrt{1+(2K_1/\rho c\omega)^2}}$) and 2ω (which is $\frac{K_2A^2}{\rho c\omega\sqrt{1+(K_1/\rho c\omega)^2}}$) is the amplitude of the fundamental frequency A_1 and second-order harmonic A_2, respectively. The reflection coefficient R is defined as the ratio of the amplitude of the reflected pulse from the interface to the amplitude of the incident wave [29]. The reflection coefficient R at an imperfect contact is dependent on the interfacial stiffness per unit area of the interface (where the wavelength of an elastic wave is larger compared to the air gap). The reflection coefficient of the fundamental frequency is given by [12]:

$$R = \left| \frac{A_1}{A} \right| \tag{7.12}$$

$$R = \frac{1}{\sqrt{1+(2K-1/\rho c\omega)^2}} \tag{7.13}$$

where A_1 is the amplitude of the fundamental frequency of the reflected signals from the contact interface and A is the amplitude of the incident wave. In practice, A_1 can be found in the experimental pulses from the amplitude of FFT of the fundamental frequency. Rearranging Eq. 7.12 gives the linear interfacial stiffness K_1 in terms of the reflection coefficient:

$$K_1 = \frac{\rho c \omega}{2} \frac{\sqrt{1 - R^2}}{R} \tag{7.14}$$

Eq. 7.14 is the same as the spring model. The second-order nonlinear parameter for the reflected ultrasound from the interface γ (derived from Eq. 7.11) is defined by [53]:

$$\gamma = \left| \frac{A_2}{A_1^2} \right| \tag{7.15}$$

$$\gamma = \frac{K_2}{\rho c \omega \sqrt{1 + (K_1/\rho c \omega)^2}} \tag{7.16}$$

where A_2 is the amplitude of the second-order harmonic of the reflected wave. In the analytical approach (Eq. 7.15), A_2 is the coefficient of the $2\omega t$ term. Again, experimentally, A_2 can be obtained from the amplitude of the second-order harmonics obtained using FFT.

K_2 is the second-order nonlinear normal interfacial stiffness. The second-order nonlinear parameter for reflected ultrasound can be measured by the experiment with the values of A_1 and A_2. In order to derive the nonlinear stiffness per unit area of the interface K_2, Eq. 7.16 is rearranged:

$$K_2 = \gamma \rho c \omega \sqrt{1 + (K_1/\rho c \omega)^2} \tag{7.17}$$

The nonlinear nominal contact pressure relationship (Eq. 7.2 can then be defined at any nominal contact pressure p_0 with the corresponding linear and nonlinear normal interfacial stiffness, K_1 and K_2 from Eqs. 7.14 and 7.17.

7.2 Experimental approach

The experimental setup was presented in Chapter 6. The samples S1, S2, S9 and S10, make the imperfect contact pair of S1S2 and S9S10. As shown in Figure 7.2, the emitter and receiver with peak frequencies of 1.78 MHz and 3.56 MHz were attached to the upper face of the upper aluminium block using the shear coupling gel SWC-2. A ten-tone burst cycle longitudinal ultrasonic waves with sinusoidal waveform were generated and impulsed at different peak-to-peak excitation amplitudes of 144 V, 216 V and 288 V using a high-power amplifier (RITEC RAM-5000). The power generated at these voltages was large enough to generate higher harmonics in reflected pulses from the interface. In this experiment, higher harmonics were observed when the incident wave had a voltage greater than 60 V peak-to-peak. The reflected pulses

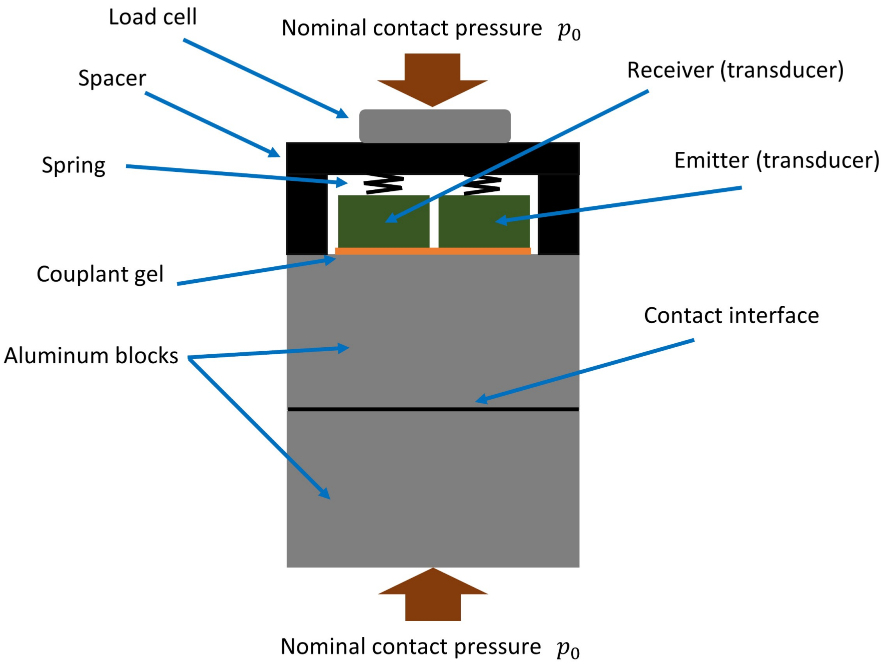

Figure 7.2: Schematic diagram of a pitch-catch through reflection measuring apparatus adapted from Ref [2].

from the contact interface were captured with the receiver and stored using a digital oscilloscope. A reference signal was captured from a solid–air contact to eliminate the inherent effect of the materials and consider only the influence of the interface. A PC running LabVIEW was used to trigger the pulsing and receive the digitised reflection data.

7.2.1 Signal processing: removing nonlinearity of other sources than CAN

Figures. 7.3a and 7.3d show the time domain of the reflected signals from the interface. The generated ultrasonic waves by the emitter are incident on the imperfect contact, and part of it reflects and is captured by the receiver which is placed next to the emitter. Figure 7.3a shows the reference signal (solid-air interface) and Figure 7.3d shows the solid-solid contact at the nominal contact pressure 2 MPa. The first reflected the time domain was truncated, followed by a Hanning window and a zero pad function, as shown in Figures 7.3b and 7.3e. These functions increase the resolution of the signals. The time-domain signals contain multiple higher frequencies and noise. Therefore, they are required to convert from the time domain to the frequency domain. This is done by FFT as shown in Figures. 7.3c and 7.3f. It should be noted

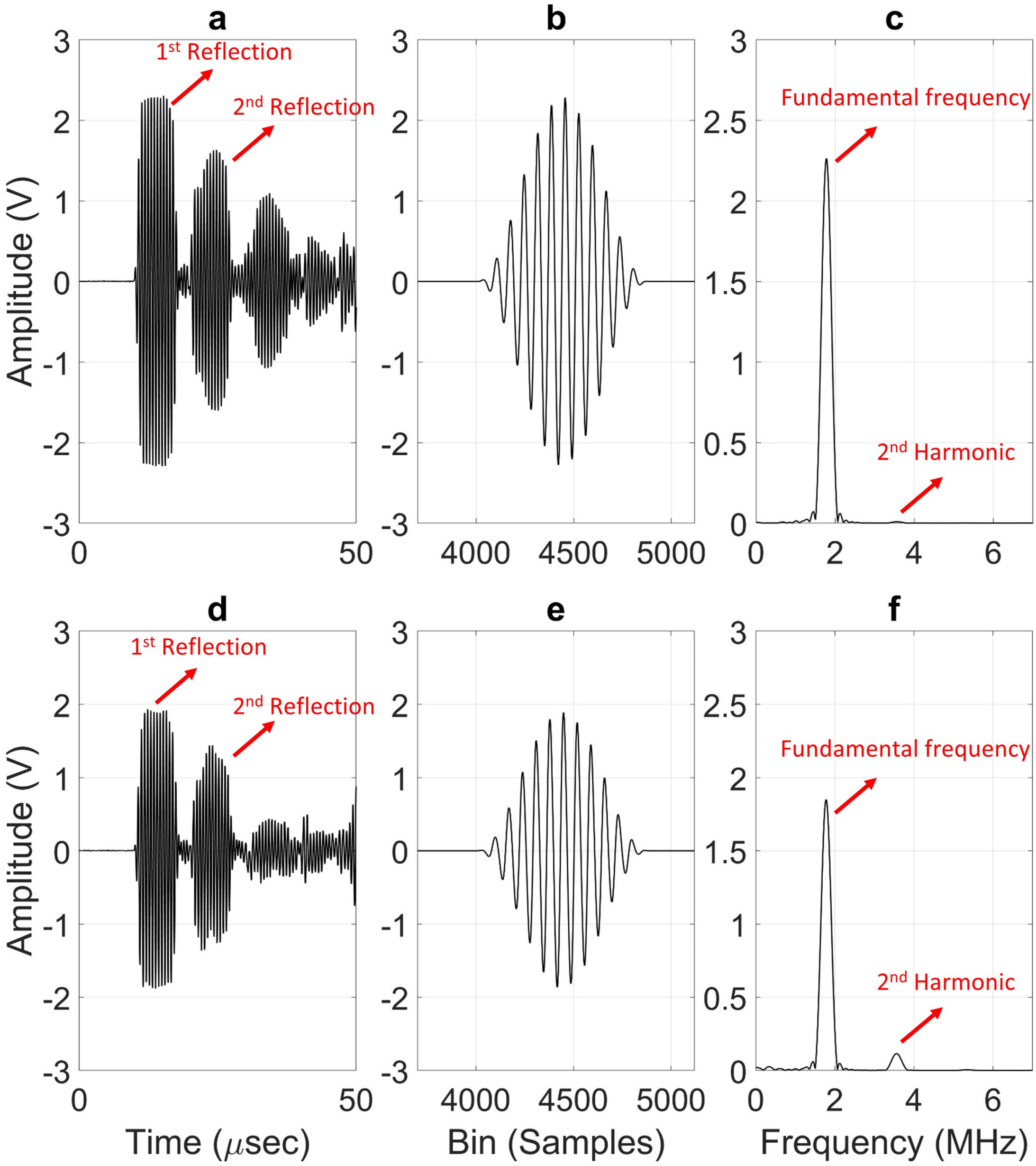

Figure 7.3: Signal processing of reflected ultrasonic waves from the pair S9S10 using 216 V excitation with incident frequency 1.78 MHz: (a-c) reflected waves from solid-air interface (reference signal); (d-f) solid-solid interface at 2 MPa nominal contact pressure; (a,d) time domain; (b,e) Hanning window and zero pad results of the first reflected waves; (c,f) frequency domain.

that the contact is not the only source of nonlinearity. The other sources of nonlinearity are [2, 45]: **(1)** material nonlinearity in all media through which high-power ultrasonic waves propagate, such as the couplant gel and aluminium blockes, and **(2)** electrical sources such as an amplifier and transducers. Figure. 7.3c shows that the amplitude of the second-order harmonic in the solid-air interface is insignificant, indicating that all materials, amplifiers and transducers generate low nonlinearity. The nonlinearity of the other sources apart from the contact is eliminated by subtracting the second-order nonlinear parameters at any applied load from the reflection at the solid-air interface. Eqs. 7.15 and 7.16 are rewritten as [2, 107]:

$$\gamma = \left| \frac{A_2}{A_1^2} - \frac{A_{2\,ref}}{A_{1\,ref}^2} \right| \tag{7.18}$$

where $A_{1\,ref}$ and $A_{2\,ref}$ are the amplitudes of fundamental frequency and second-order harmonics from the reference signal (solid-air interface), respectively.

7.2.2 Calibration: voltage-to-length unit conversion

Figure 7.4 shows the displacement measured by the laser Doppler vibrometer and the amplitude of ultrasound at the corresponding amplitude of excitation for the fundamental and second-order harmonic (as shown in Section 6.16). An excitation amplitude greater than 60 V was sufficient to generate a second-order harmonic. The slope of the best-fit lines gives the voltage-to-length unit conversions (Figure

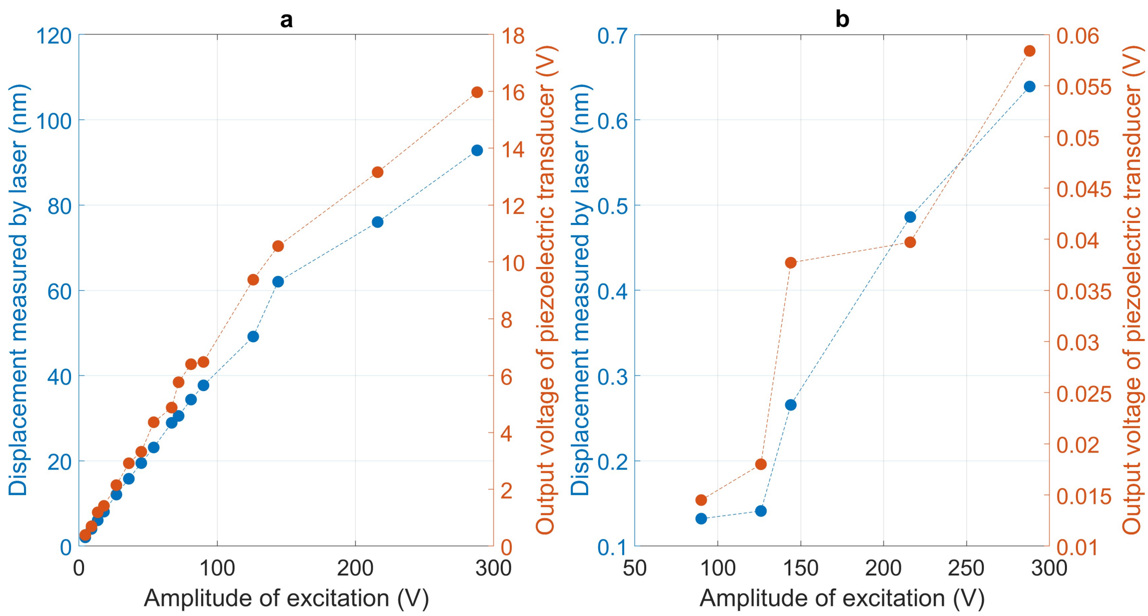

Figure 7.4: Displacement of the particle at the free surface measured by the laser Doppler vibrometer and the amplitude of ultrasound at the corresponding amplitude of excitation for the: (a) fundamental frequency; (b) second-order harmonic.

7.4). Multiplying these conversions by the amplitude of fundamental frequency and second-order harmonics in units of voltage gives [2, 45]:

$$\gamma(m^{-1}) = \frac{\delta_2}{{\delta_1}^2}\gamma(V^{-1}) \tag{7.19}$$

where δ_1 and δ_2 are the slopes of the displacement measured by the laser Doppler vibrometer to the output voltage captured by transducers from the fundamental frequency and second-order harmonics, respectively. δ_1 and δ_2 are in units of $m.V^{-1}$.

7.2.3 Finite element (FE) model for the real contact

When an external load is applied to the contacting bodies, the surfaces are pushed against each other and the asperities deform. Figure 7.5 shows a schematic diagram of the contacting surfaces before loading and as the external load increases. An FE

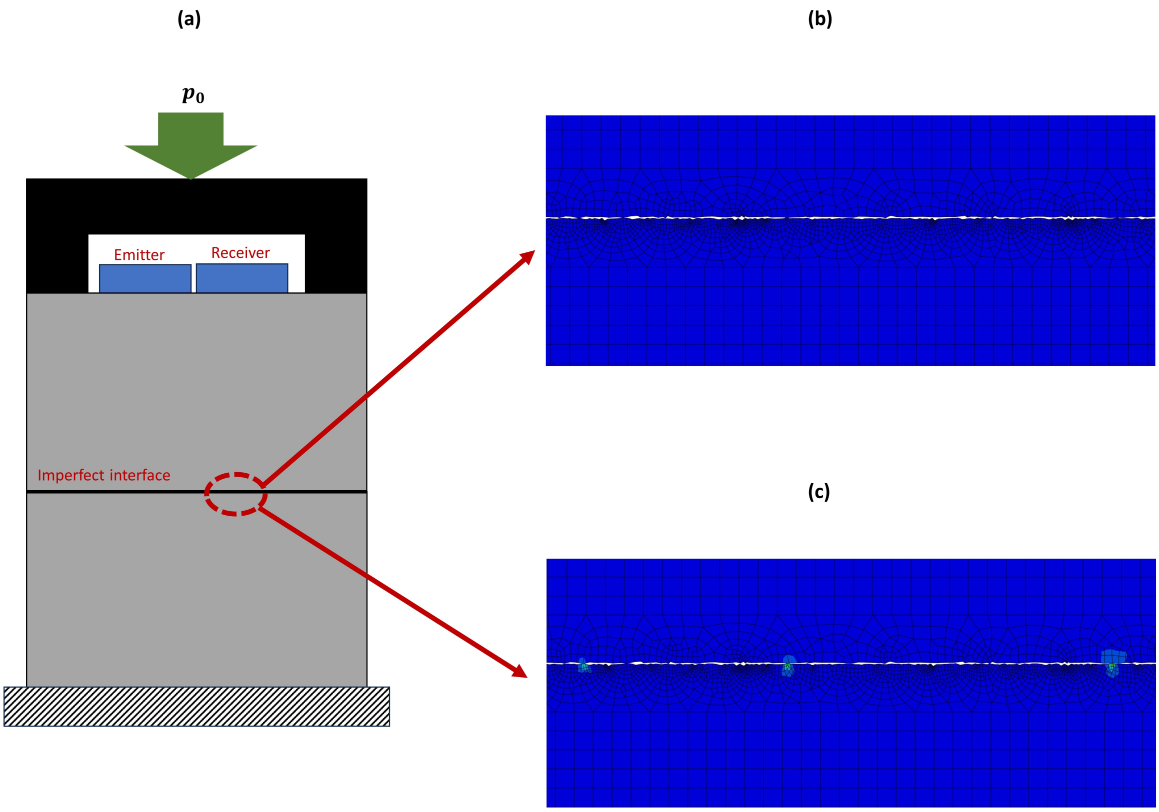

Figure 7.5: Asperity deformation as the load increases: (a) schematic diagram; (b) FE analysis before applying external load; (c) FE analysis at nominal contact pressure 100 MPa.

model was created to show the real contact area when the flat surfaces come into contact. Two linear elastic blocks with the material properties listed in Table 5.1 were made with ABAQUS/Standard. The static analysis was defined to simulate the static load applied on the contacting surfaces. The lower face of the lower block was fixed using the ENCASTRE boundary condition. The real surface area of pair S1S2 was scanned (using Alicona Infinite SL), and the surface topography was imported into ABAQUS using Python. The surfaces were then pushed against each other up to 100 MPa in static equilibrium. It is seen from Figure 7.5b that the surface is in contact with some asperities. When the applied load increases, the asperities deform and more asperities come into contact (Figure 7.5c). The real contact area, which takes place at the peak of asperities in contact, is seen to be significantly smaller than the nominal contact area.

7.3 Results and discussion

7.3.1 Amplitude of fundamental frequency and higher-order harmonics

To determine A_1 and A_2, the receiver (transducer) captured the reflected ultrasonic waves at every applied load. The signal processing explained in Section 7.2.1 was used for these reflections. Then, the amplitude of the fundamental frequency A_1 and the second-order harmonic A_2 was determined for all load increases, as shown in Figure 7.3. A_1 andA_2 were plotted against the nominal contact pressure, as shown in Figure 7.6.

Figure 7.6 shows the amplitude of the fundamental frequency A_1 and second-order harmonics A_2 as the nominal contact pressure increases at the amplitude of excitation 216 V of the pair S9S10. To determine A_1 and A_2, the receiver (transducer) captured the reflected ultrasonic waves as the load increased. The signal processing explained in Section 7.2.1 was used for these reflections. Then, the amplitude of the fundamental frequency A_1 and second-order harmonic A_2 on all load increments were determined, as shown in Figure 7.3. The A_1 and A_2 were then plotted against the nominal contact pressure, as shown in Figure 7.6. When the surfaces are pushed against each other, the asperities deform, and more asperities come into contact. This makes the real contact area larger and more capable of transferring ultrasonic energy. Therefore, the amplitude of the fundamental frequency decreased monotonically (Figure 7.6a). As seen in Figure 7.6b, the amplitude of the second-order harmonic A_2 initially increased as the nominal contact pressure increased until the normal stress generated by the ultrasound became equal to the nominal contact pressure (for the perfect contact). For an imperfect contact, the peak was related to the real contact pressure. When

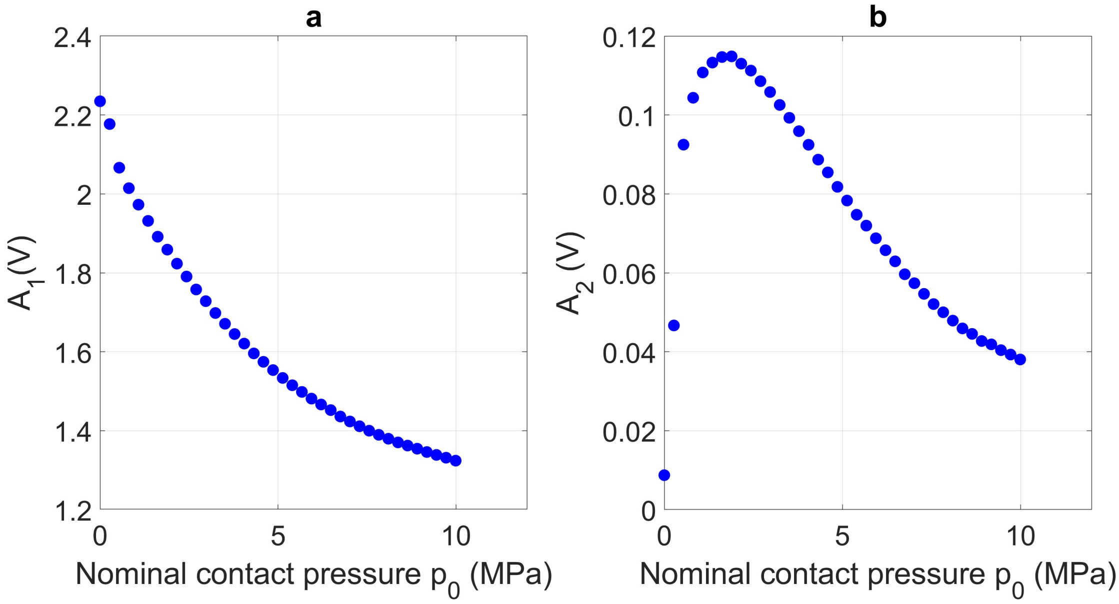

Figure 7.6: The effect of nominal contact pressure p_o of the pair S9S10 at excitation amplitude of 216 V on the amplitude of: (a) fundamental frequency A_1; (b) second-order harmonic A_2.

the nominal contact pressure increased and became larger than the normal stress generated by ultrasound, the amplitude of the contact nonlinearity decreased. In other words, the normal stress generated by ultrasound after the peak was not sufficient to open and close the gap at the interface.

The amplitude of the fundamental frequency A_1 and the reference signal (solid-air interface) were substituted into Eq. 7.12 to determine the reflection coefficient R as shown in Figure 7.7a. The reflection coefficient was substituted into Eq.7.14 to determine the linear interfacial stiffness (Figure 7.7b). It is seen that as the nominal contact pressure increased, the contact became stiffer.

The second-order nonlinear parameter γ was determined by Eq. 7.15 (Figure 7.8). It was measured in units of voltage. It is required to be converted to the length unit. Therefore, γ (V^{-1}) was substituted in Eq. 7.19. In addition, as shown in Figure 7.3c, there were other sources of nonlinearity rather than the contact which must be removed, so the second-order nonlinear parameter (in length unit) was substituted in Eq. 7.18 shown in Figure 7.9a. As explained in Section 5.2.4, the maximum amplitude of the second-order harmonic was where the nominal contact pressure and the ultrasound pressure were equal. The ultrasound pressure opened and closed the interface from zero to this contact pressure. This increased the nonlinearity (amplitude of A_2) from zero to the contact pressure as the contact pressure increased.

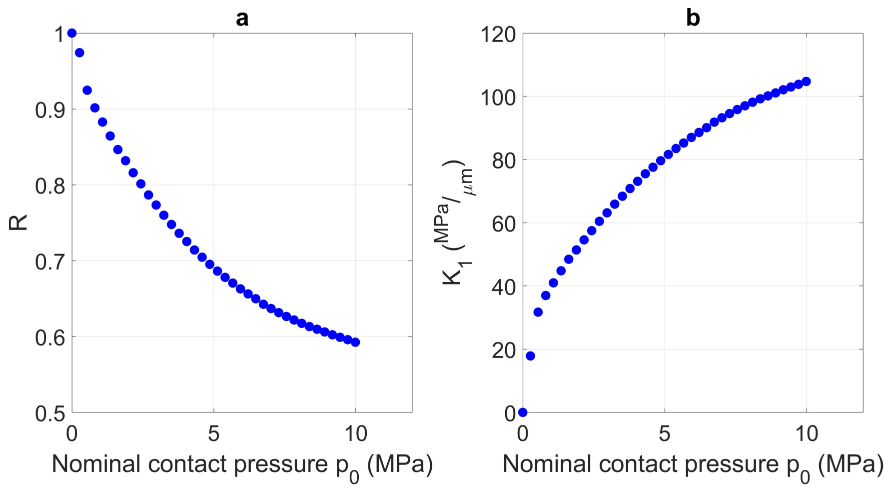

Figure 7.7: The effect of nominal contact pressure p_o of the pair S9S10 on: (a) Reflection coefficient R ; (b) linear interfacial stiffness K_1.

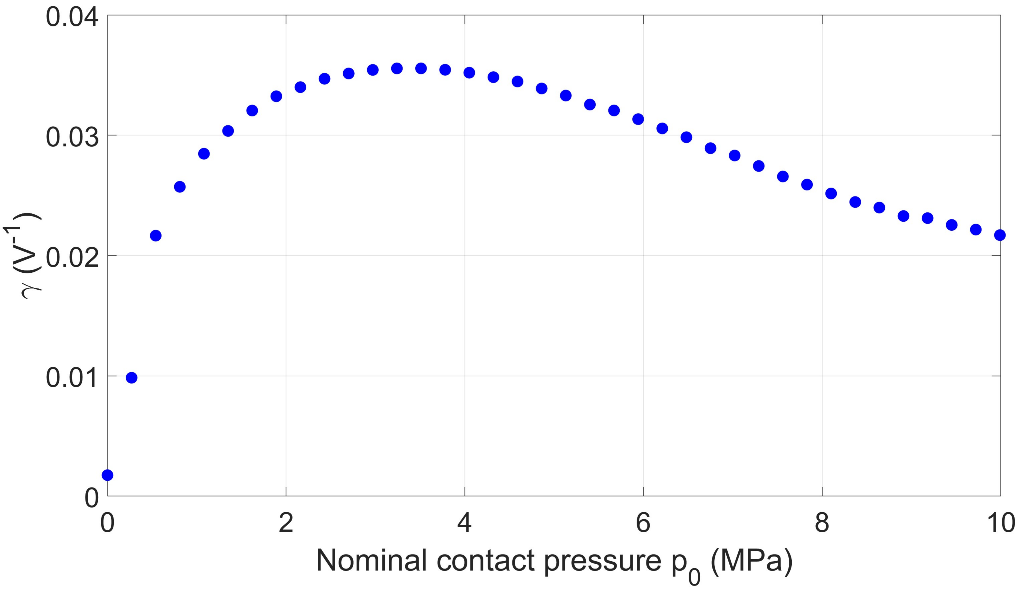

Figure 7.8: The second-order nonlinear parameter γ in units of voltage.

From this contact pressure and beyond, the ultrasound pressure was unable to keep the interface open for the same period as it was below the peak. This reduced the acoustic nonlinearity as the contact pressure increased, as shown in Figure 7.9a. This was also true for second-order nonlinear normal interfacial stiffness. The maximum nonlinear stiffness occurred when the maximum nonlinearity was generated. When the interface was opened and closed, the interfacial stiffness varied nonlinearly. As the contact pressure increased (after the peak), the contact remained closed longer

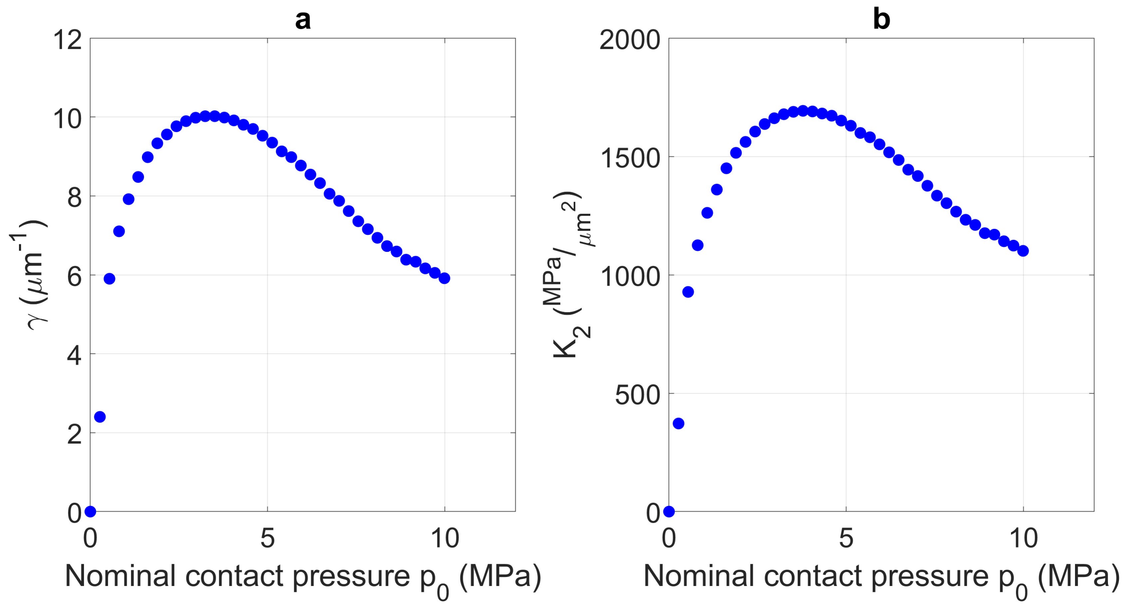

Figure 7.9: The effect of nominal contact pressure p_o of the pair S9S10 on the: (a) second-order nonlinear parameter γ ; (b) second-order nonlinear normal interfacial stiffness K_2.

and the contact nonlinearity decreased, making the surface less nonlinearly stiffer.

7.3.2 The Effect of incident amplitude

The amplitude of the fundamental frequency and second-order harmonic as a function of nominal contact pressure is shown in Figure 7.10. The higher the excitation amplitude, the higher the amplitude of the fundamental frequency. As shown in the numerical results (Chapter 5, Figure 5.11a), the peak of the second-order harmonic A_2 occurred at the point where the normal stress generated by ultrasound was equal to the nominal contact pressure. However, as the contact was imperfect (unlike the numerical analysis), the peak occurred at the real contact stress equal to the normal stress generated by the ultrasound. The real contact pressure was higher with a higher incident amplitude for the same contact topography (pair S9S10 and the same loading cycle). Therefore, the peak of A_2 for the incident amplitude of 144 V, 216 V and 288 V occurred at nominal contact pressure 4.6 MPa, 4.86 MPa and 5.12 MPa, respectively. Figures. 7.11a and 7.11b show the reflection coefficient and linear interfacial stiffness measured at an incident amplitude of 144 V, 216 V and 288 V. Figure 7.4a shows that as the incident amplitude of excitation increased, the particle displacement at the fundamental frequency (and second-order harmonic) increased.

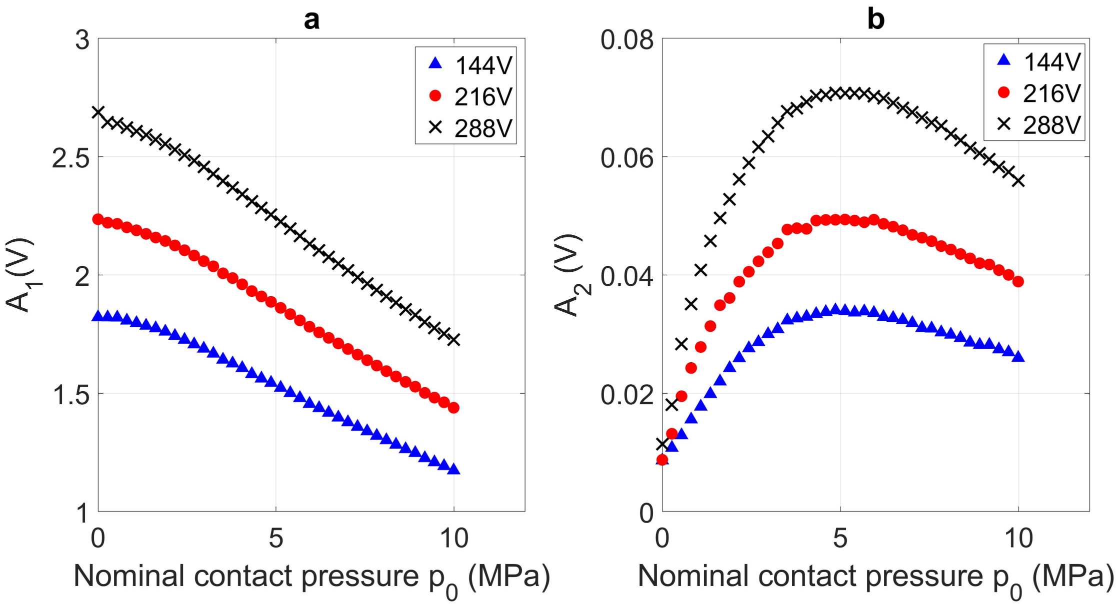

Figure 7.10: The effect of excitation amplitude on the amplitude of the: (a) fundamental frequency A_1; (b) second-order harmonic A_2.

For example, at the excitation amplitudes of 144 V, 216 V and 288 V, the displacement of the particle on the free surface was 62 nm, 76 nm and 93 nm, respectively. The normal stress generated by ultrasound at the fundamental frequency was given by [28, 108]:

$$\sigma = \rho c \omega_1 A_1 \tag{7.20}$$

This indicates that the ultrasonic waves at the amplitudes of excitation 144 V, 216 V and 288 V generated normal stresses of 9.55 MPa, 11.704 MPa and 14.32 MPa, respectively. Therefore, at every nominal contact pressure p_0, the higher the amplitude of excitation, the more contacting surfaces were pushed. This results in more asperity deformation in contact, and, subsequently, the reflection became smaller (Figure 7.11a). As a result, the contact for the higher amplitude of excitation became stiffer (Figure 7.11b). Figure 7.12 shows the effect of the amplitude of excitation on the second-order nonlinear parameter and second-order nonlinear normal interfacial stiffness K_2. Figure 7.12a shows that as the amplitude of the incident increased, the second-order nonlinear parameter γ increased, indicating the effect of the amplitude of the incident on the nonlinearity of the contact. As a result, the asperity deformed more due to the higher normal stress generated by ultrasound, and the contact became stiffer.

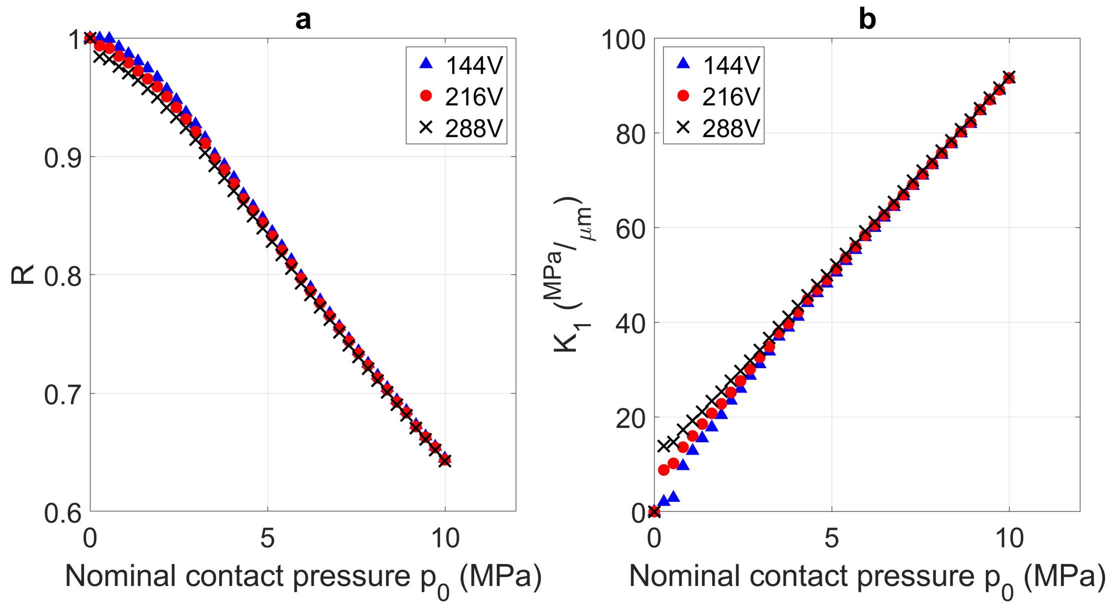

Figure 7.11: The effect of excitation amplitude on the: (a) reflection coefficient R; (b) linear interfacial stiffness K_1.

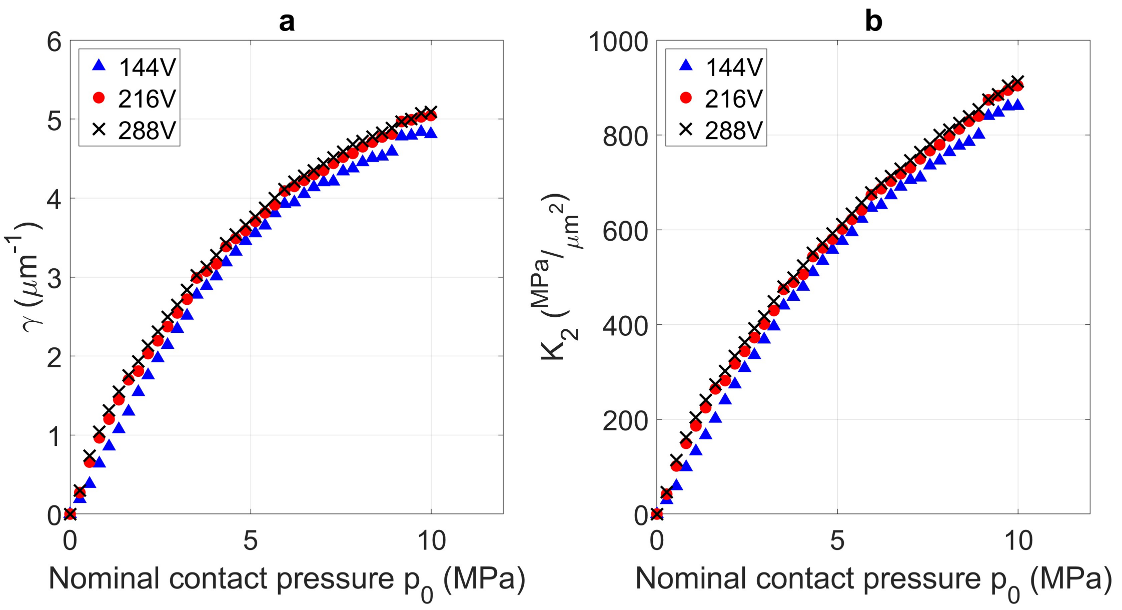

Figure 7.12: The effect of excitation amplitude on the: (a) second-order nonlinear parameter γ; (b) second-order nonlinear normal interfacial stiffness K_2.

7.4 Validation of nonlinear normal interfacial stiffness

There is no other method to validate the second-order interfacial stiffness generated by ultrasound. Therefore, one of the methods the author of the current study used for validation is presented here. This study has been published in [2]. The best-fit curve to the linear interfacial stiffness shown in Figure 7.13a for the pair S9S10 was given by a fourth-order polynomial expression (agrees with [2] for the peak frequency of 2 MHz and [6] with the peak frequency of 5 MHz):

$$K_1(p_0) = \sum_{n=0}^{4} a_n p_0^n \tag{7.21}$$

where a_n is a constant coefficient. This coefficient is dependent on the surface topography and the elastoplastic deformation of the contacts. The nominal contact

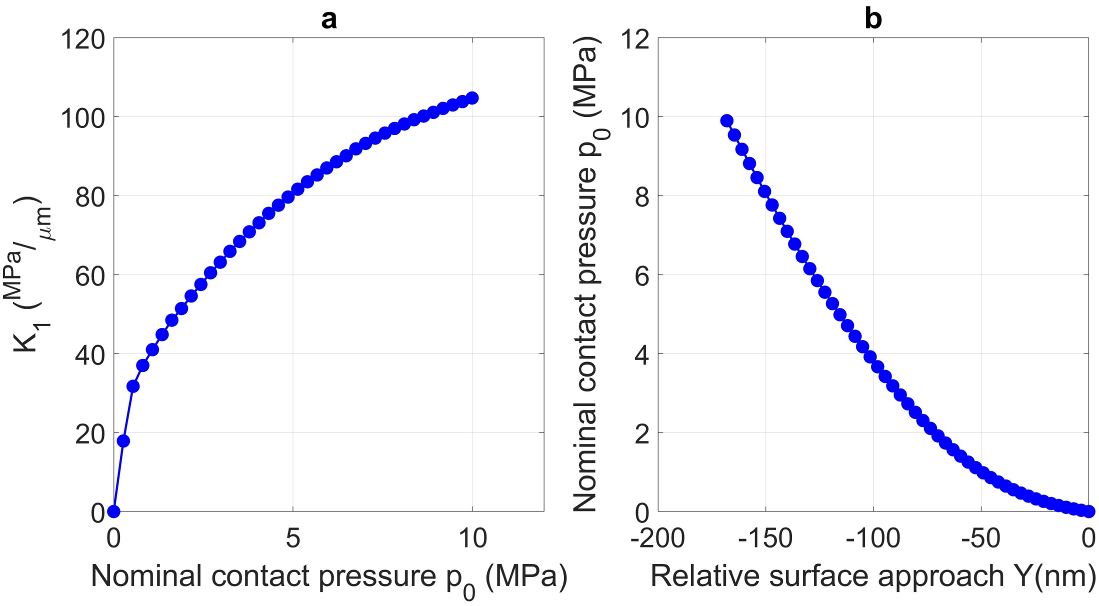

Figure 7.13: (a) The best-fit line of linear interfacial stiffness K_1 (Eq. 7.22); (b) nominal contact pressure against relative surface approach determined by Eq. 7.23.

pressure p_0 can be presented in terms of the relative surface approach Y of the contacting surfaces. To do this, the linear interfacial stiffness K_1 (Eq. 7.21) is substituted into Eq. 7.3 defining a first order nonlinear homogeneous differential equation:

$$\frac{dp}{dY} + K_1(p_0) = 0 \quad , \quad p(0) = 0 \tag{7.22}$$

The initial condition indicates that there is no elastic wave (ultrasound) at time zero. The Runge-Kutta method was employed to solve Eq. 7.22 with respect to the relative surface approach:

$$p_0(Y) = \sum_{n=0}^{2} b_n Y^n \tag{7.23}$$

where b_n is a constant coefficient. This coefficient, like a_n, was also dependent on surface asperity and material properties. A numerical differential equation (ode45 function in MATLAB [109]) of the data in Figure 7.13a according to Eq. 7.22 was used to determine the relationship between the nominal contact pressure and the relative surface approach, as shown in Figure 7.13b.

The shape of the nonlinear nominal contact pressure-relative surface approach curve demonstrated the stiffening behaviour of the interfacial spring under increasing contact pressure. In other words, increasing the nominal contact pressure reduced the gap, resulting in more solid contact and a stiffer interface. In the absence of an elastic wave, the relative surface approach was zero ($Y = 0$) under the nominal contact pressure $p_0 = 0$ MPa (the nominal contact pressure generated by the weight of the upper body is negligible). The negative sign of the relative surface approach Y indicates the reduction of interface separation (a greater deflection in the asperities). The gradient of the curve increased with an increase in the nominal contact pressure, demonstrating stiffer interfacial contact.

A best-fit curve to the second-order nonlinear normal interfacial stiffness K_2 shown in Figure 7.14a is a third-order polynomial expression (agrees with [2] for the peak frequency of 2 MHz and [6] with the peak frequency of 5 MHz):

$$K_2(p_0) = \sum_{n=0}^{3} c_n p_0^n \tag{7.24}$$

where c_n is a constant coefficient. This coefficient depends on some factors such as surface topography and elastoplastic deformation of the asperities in contact. However, further studies are required. As before, the nominal contact pressure p_0 is expressed in terms of the relative surface approach Y of the contacting surfaces. To do this, the nonlinear normal interfacial stiffness K_2 (Eq. 7.14) was substituted into Eq. 7.4 creating a second-order nonlinear homogeneous differential equation:

$$\frac{1}{2}\frac{d^2p}{dY^2} - K_2(p_0) = 0 \quad , \quad \frac{dp}{dY} = 0 \quad , \quad p(0) = 0 \tag{7.25}$$

The initial conditions indicate that in the absence of an elastic wave (ultrasound), there is zero relative surface approach and linear interfacial stiffness. The Runge-Kutta method was again employed to solve Eq. 7.25 with respect to the relative surface approach. A numerical differential equation (ode45 function in MATLAB [109]) of the data in Figure 7.14a according to Eq. 7.25 was used to determine the nominal contact pressure-relative surface approach relationship, as shown in Figure 7.14b. The result was the same as in Eq. 7.23.

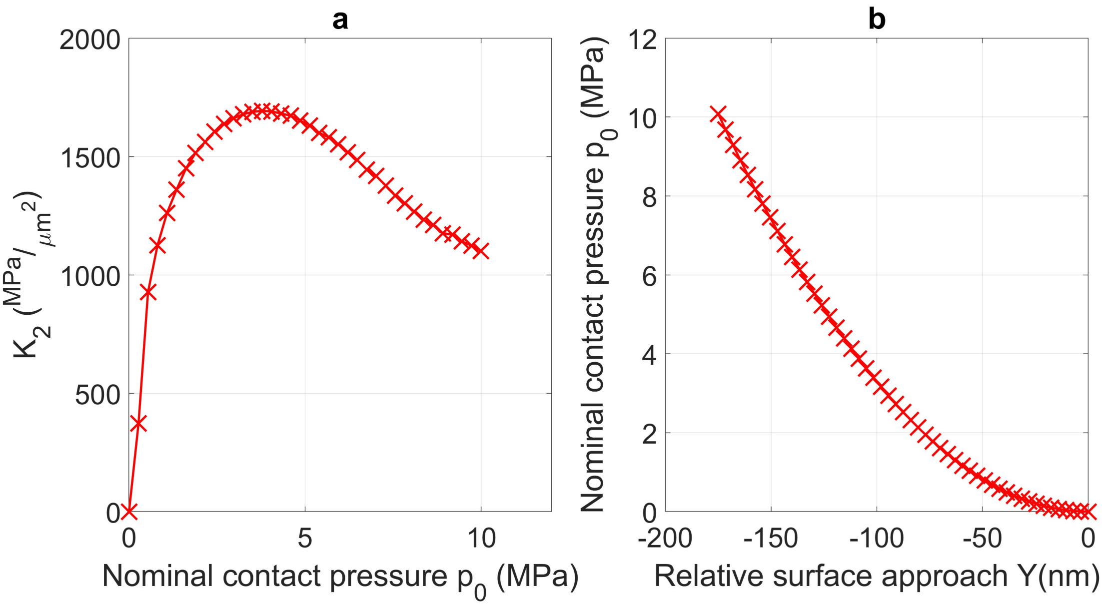

Figure 7.14: (a) The best-fit line of nonlinear normal interfacial stiffness K_2 (Eq. 7.24); (b) nominal contact pressure against relative surface approach determined by Eq. 7.25.

The comparison between the pressure-relative surface approach derived from linear and nonlinear normal interfacial stiffness is presented in Figure 7.15. Figure 7.15a shows the pressure-relative surface approach derived from the experimental data. Figure 7.15b is included for comparison at the peak frequency of excitation with 5 MHz and shows the pressure-relative surface derived from the experimental data [6]. It should be noted that the experiment presented in [6] was through transmission, while the current paper considered a reflected signal. Both approaches yield a similar relationship.

It is seen that the pressure-approach relationship derived from the linear stiffness K_1 and second-order nonlinear stiffness K_2 are very similar. As expected, the pressure-approach response should not depend on whether it was determined from either linear or nonlinear stiffness-measured data. This shows the precision of the proposed model for the linear and second-order nonlinear normal interfacial stiffnesses. The interfacial spring can be modelled with a stiffness described by a Taylor expression with first and second-order components (Eq. 7.2). Further, an experimental measurement of either one of those components, using ultrasonic reflection, is sufficient to deduce the other and, hence, characterise the spring stiffness.

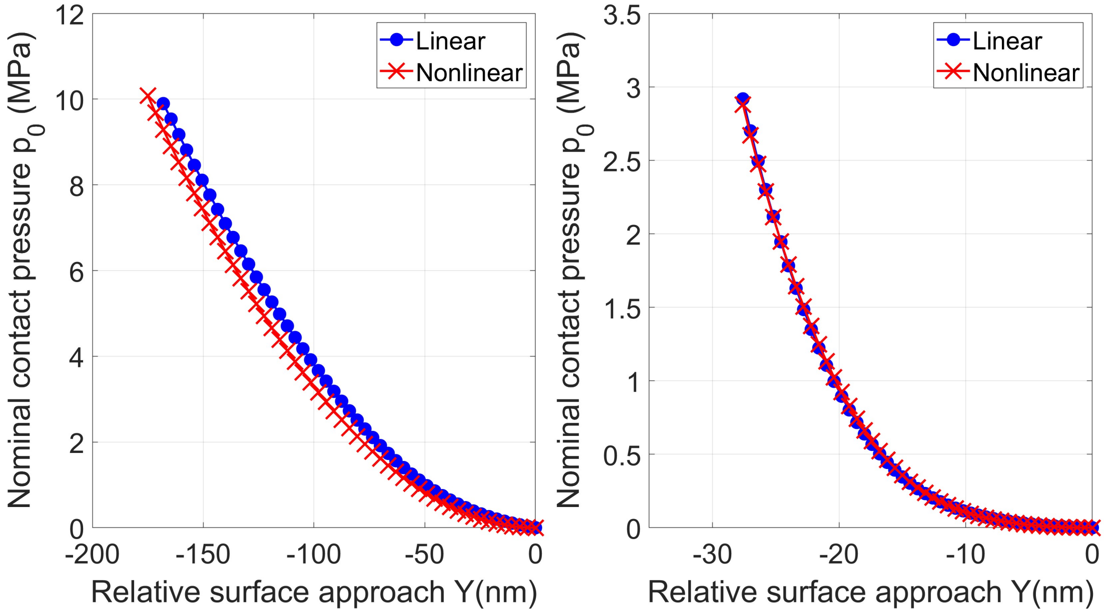

Figure 7.15: Pressure-relative surface approach derived from the linear and nonlinear normal interfacial stiffness: (a) experimental data of the current study at incident excitation of 216 V and peak frequency of 1.78 MHz; (b) experimental data from [6] at incident amplitude of excitation of 347 V and peak frequency of 5 MHz.

7.5 Finite element model for reflected ultrasonic waves

To study the behaviour of the first and second reflections of the interface, a finite element model was created with ABAQUS/Explicit, as shown in Figure 7.16. Two elastic bodies with material properties listed in Table 5.1 were created in 2D. The solver was defined as dynamic explicit, which is more accurate for the nonlinear contact problems. The size of the mesh element was defined as $0.2mm$. This element size is 10% of the wavelength of ultrasound wave propagation in the medium. The contact interface was defined as the surface-to-surface mode. The emitter was defined on the top face of the upper body, similar to the experiment. To generate ultrasonic waves, a ten-tone burst cycle with the sinusoidal waveform pressure and a centre frequency of 1.78 MHz was applied to the nodes allocated for the emitter. The waves were incident at the interface and reflected. These reflections were captured with the same transducer as shown in Figures 7.16a and 7.16b. When waves were propagated, they were not reflected from other boundaries. Therefore, the first reflection was captured by the receiver without interference from other reflections, as shown in Figure 7.16c. However, when the ultrasonic waves were reflected from the interface,

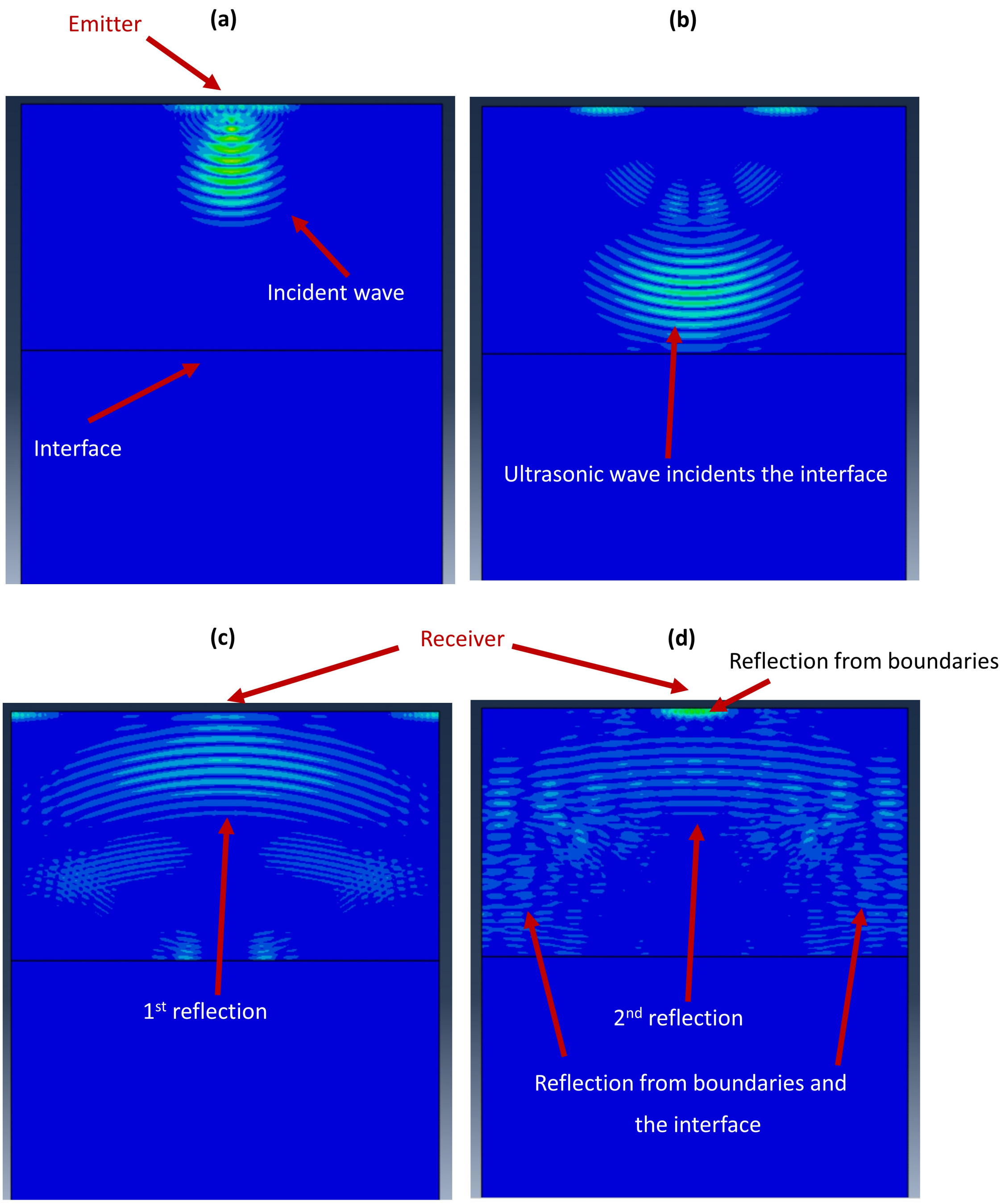

Figure 7.16: Illustration of the multiple reflections with ABAQUS: (a) incident wave; (b) ultrasonic waves were incident on the interface; (c) first reflection from the interface; (d) second reflection from the interface.

they interfered with the other reflected waves from the boundaries and contact (Figure 7.16d). This interference affected the amplitude of the second reflections.

7.6 Linear and nonlinear normal interfacial stiffness using the second reflection

So far, the amplitude of the fundamental frequency and the second harmonic of the first reflection from the interface have been used to determine the reflection coefficient, second-order nonlinear parameter, and subsequently, the linear and second-order nonlinear normal interfacial stiffness. It is required to study how these parameters vary when the second reflection is considered. Figure 7.17 shows the schematic diagram and the corresponding time-domain signals of consecutive reflections from an imperfect interface. Figure 7.18 compares the reflection coefficient and the linear interfacial

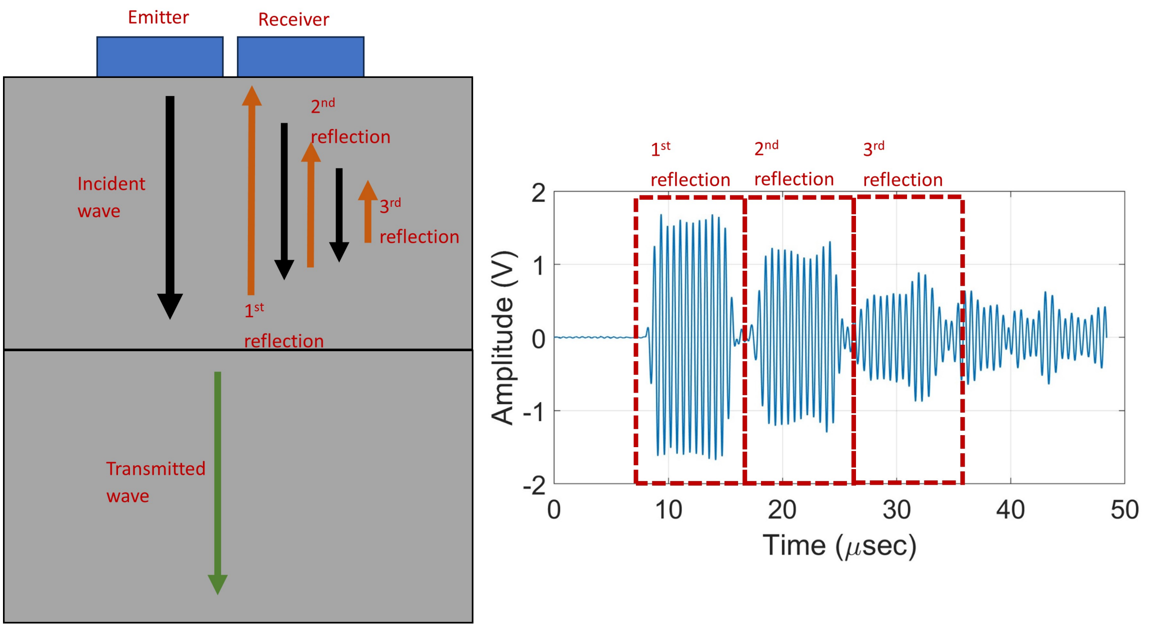

Figure 7.17: Reflections from an imperfect interface: (a) schematic diagram; (b) time domain signals.

stiffness of the first and second reflections. Similar signal processing was applied for the second reflection. It is seen in Figure 7.18a that the reflection coefficient of the second reflection is larger than that of the first reflection. As expected, when the nominal contact pressure increased, the asperities deformed more and less ultrasonic energy was reflected; therefore, the reflection coefficient decreased monotonically. However, the ultrasonic energy of the second reflection remained constant as the nominal contact pressure increased to more than 2 MPa.

Figure 7.18b compares the linear interfacial stiffness K_1 determined by the first and second reflections against the nominal contact pressure. As expected, the contact became stiffer when the nominal contact pressure increases. The second reflection

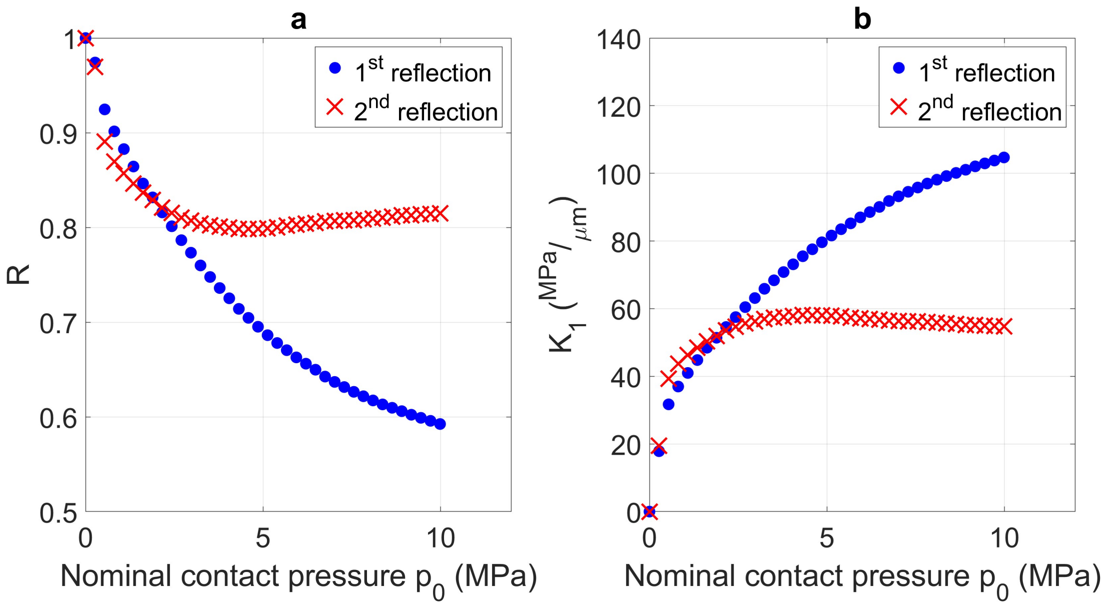

Figure 7.18: Comparison of the first and second reflections: (a) reflection coefficient R; (b) linear interfacial stiffness K_1.

shows that the stiffness of the contact did not vary with higher contact pressure. This is also due to the interference of the reflections from the boundaries and the contact. Figure 7.19a shows the second-order nonlinear parameter γ for the first and second reflections. It is seen that the nonlinear parameter for the second reflection was larger than the first reflection for all applied loads due to the interference of other reflections with the second reflection. The peak of the second-order nonlinear parameter γ for the second reflection occurred at a nominal contact pressure higher than that of the first reflection, which indicates that the ultrasonic energy was larger due to interference. As a result, the second-order nonlinear normal interfacial stiffness determined by the second reflection shows stiffer contact compared to the first reflection (Figure 7.19b).

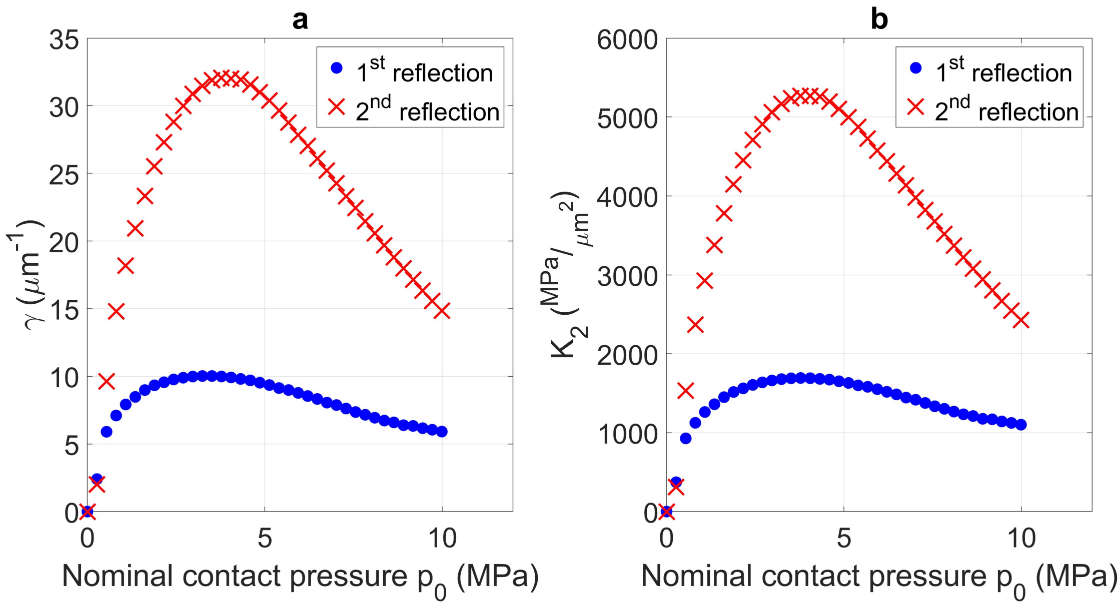

Figure 7.19: Comparison of the first and second reflections: (a) second-order nonlinear parameter γ; (b) second-order nonlinear normal interfacial stiffness K_2.

7.7 Conclusion

In this study, a second-order nonlinear normal interfacial stiffness was experimentally measured. The amplitudes of the fundamental frequency and second-order harmonic were determined. These amplitudes were then used to measure the reflection coefficient R, the second-order nonlinear parameter γ, and the linear and second-order nonlinear normal interfacial stiffness. It was also shown that the amplitude of the incident wave affected the reflected waves. The higher the amplitude of the incident wave, the higher the amplitude of the reflected waves. The amplitude of the fundamental frequency and the second-order harmonic were dependent on the amplitude of the incident wave. However, the ratio R, γ and $A_2/{A_1}^2$ were shown to be independent of the amplitude of excitation. Therefore, the interfacial stiffness measured with ultrasound was independent of the amplitude of excitation, which agrees with the concept of contact stiffness.

As there is no method other than ultrasound to measure second-order nonlinear normal interfacial stiffness, in this study, the first and second-order nonlinear homogeneous differential equations were defined based on the best-fit curves of the linear and nonlinear normal interfacial stiffness. These equations were solved using a numerical method (the Rungue-Kutta method) to derive the pressure-surface approach relationship. The results showed that the pressure-surface approach determined from the linear and nonlinear equations agrees, which indicates the method's accuracy. In addition, the same validation method was used for a different experiment carried out by [6], where they used ultrasonic waves with a peak frequency of 5 MHz of pitch-catch through transmission mode. Their results also proved the validation.

All the results used the first reflection of ultrasonic waves from the interface. Therefore, the last part of the chapter was devoted to studying the effect of second reflections from the interface and its effect on the reflection coefficient, second-order nonlinear parameter and linear and nonlinear normal interfacial stiffnesses. A finite element analysis with ABAQUS/Explicit was used to illustrate the consecutive reflections from the interface and boundaries. It was seen that no reflection from other boundaries affects the first reflection from the interface. Therefore, as the nominal contact pressure increased, the asperities deformed more, and the contact became stiffer. However, reflection from the boundaries and contact interfere with the second reflection from the interface, making the contact stiffer than in the first reflection.

Chapter 8

Asperity Deformation and its Influence on Nonlinear Normal Interfacial Stiffness

This chapter aims to study the effect of asperity deformation on the second-order nonlinear parameter and second-order nonlinear normal interfacial stiffness. Two pairs with different surface roughnesses are used during several loading/unloading cycles to determine the normal interfacial stiffness using ultrasound and study how the surface topography and elastic-plastic deformation affect the contact stiffness. It is also shown that the second-order nonlinear parameter is a function of the real contact area.

8.1 Introduction

The experimental setup was presented in Sections 7.2-7.6. To study the effect of asperity deformation on the second-order nonlinear parameter γ and second-order nonlinear normal interfacial stiffness K_2, pairs S1S2 and S9S10 (with different surface roughness presented in Table 6.1) were placed in the loading machine (Tinius Olsen 25ST). The pairs S1S2 and S9S10 are here called rough and smooth contacts, respectively. The samples were first loaded from 0 MPa to 10 MPa with an increase of 0.25 MPa. The pairs were then unloaded to make the first loading/unloading cycle. At each increment in nominal contact pressure, an ultrasonic wave with incident amplitude of 144 V, 216 V and 288 V was emitted. The loading/unloading cycles were repeated for up to 10 cycles.

8.2 Elastic-plastic asperity deformation

The elastic-plastic asperity deformation is studied here in two separate sections: **(i)** a finite element model and **(ii)** experimental results.

8.2.1 Finite element model

To study the elastic and plastic deformation of the asperities in contact, a finite element analysis with ABAQUS/Explicit was modelled. Surface roughness was considered as a series of asperities with the shape of identical hemispheres with a radius of 3 μm (this value is the average of a radius of surface roughness measured with the Alicona Infinite SL). The yield stress and plasticity of the samples were defined for the contact surfaces to consider the plastic deformation of the contact according to [110]. Since the loading and unloading were under a quasi-static state, the explicit solver was used to consider the contact nonlinearity. The mesh was created with a free pattern and with a higher density at the tip of the asperities to give more accurate results. The mesh element type was defined as CPS4R, which is a 4-node, bilinear, plane stress quadrilateral with reduced integration and hourglass control. To decide the size of the mesh element of the asperities, a mesh convergence process was taken from the element size of 10 μm to 0.25 μm , as shown in Figure 8.1. The size of the

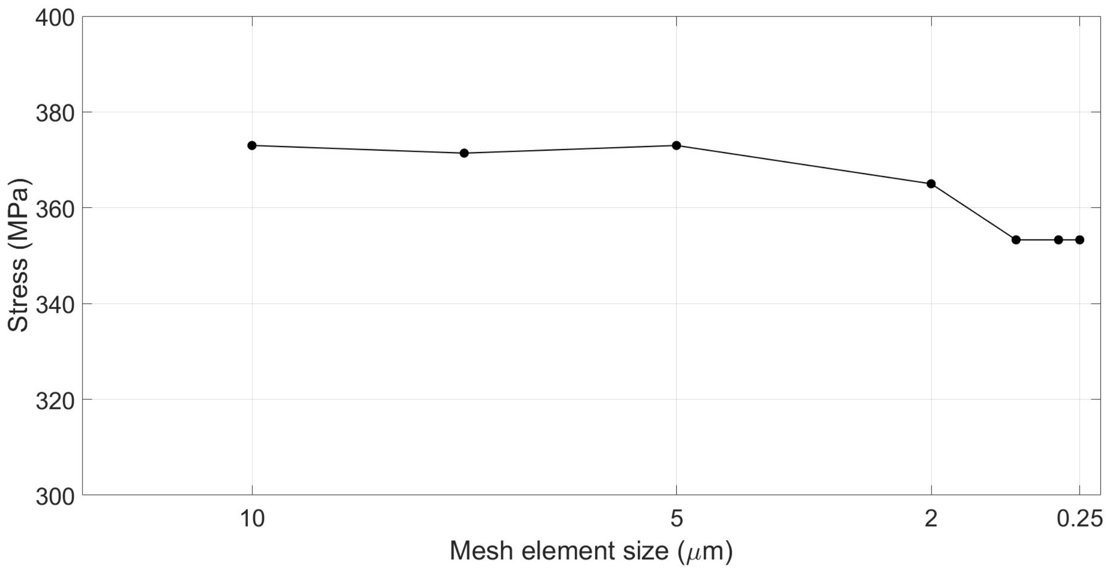

Figure 8.1: The mesh convergence of the FE model.

mesh element of 1 μm was used for this model. The lower face of the lower body was restricted with a fixed boundary condition (ENCASTRE). The contacting pair was loaded and unloaded, as shown in Figure 8.2. The contact stress at the loading of the asperities was 353 MPa, as shown in Figure 8.2c. This is greater than the yield strength of aluminium. Therefore, plastic deformation occurred (Figures 8.2d and e).

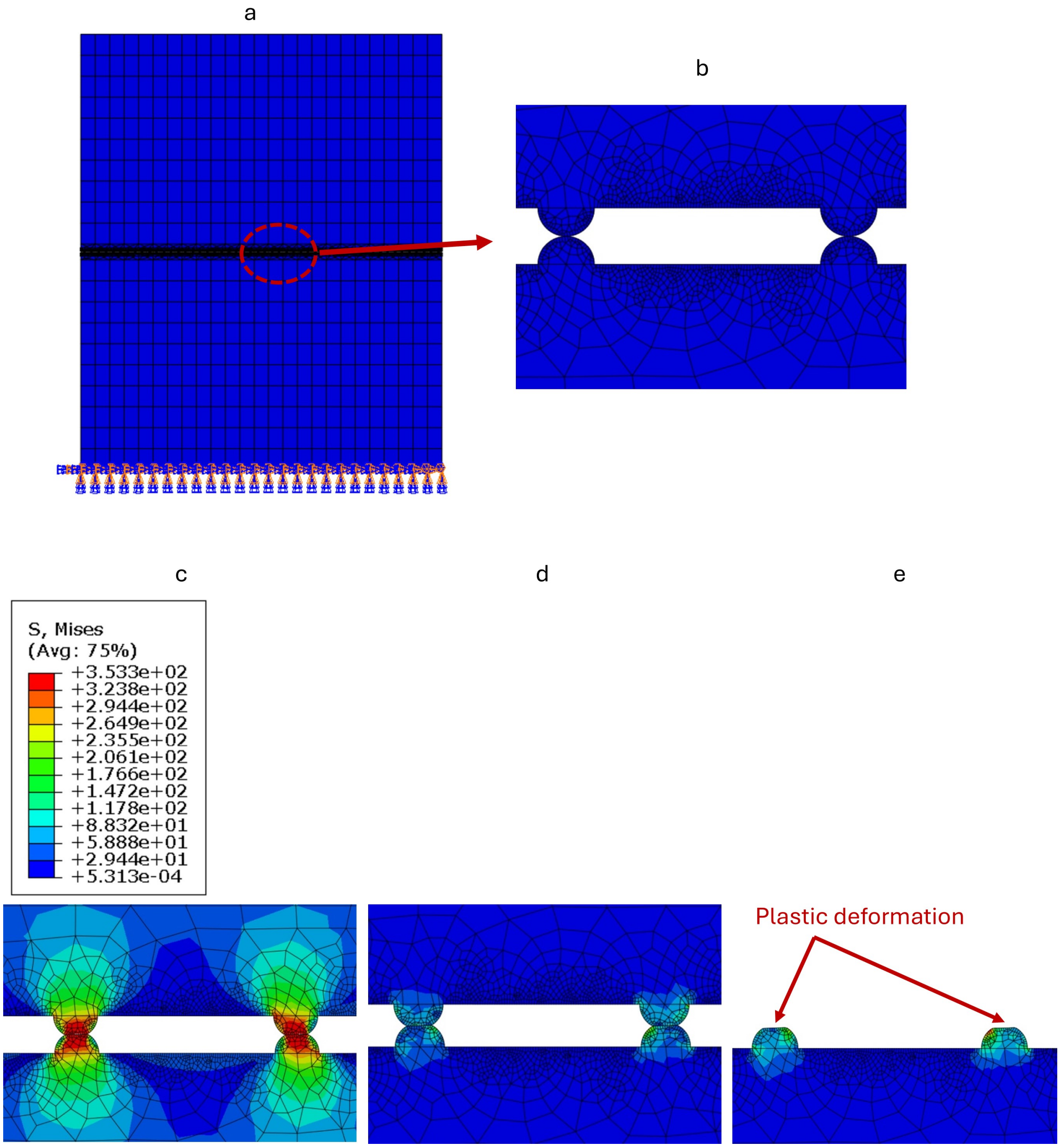

Figure 8.2: The effect of elastic-plastic deformation of the asperities on: (a-b) before loading R; (c) 1^{st} loading; (d) 1^{st} unloading; (e) plastic deformation.

8.2.2 Experimental results

This section was presented by the author of this thesis in [83]. Figure 8.3 shows the surface topography of the samples S1, S2, S9 and S10 before the 1^{st} loading and after the 10^{th} loading/unloading cycles. It should be noted that surface topography could not be measured after every loading/unloading cycle. If the surfaces are put back after they are taken for measuring the surface topography, the new contact between the aspects is created. Therefore, the surface topography was measured before the 1^{st} loading and after all the loading and unloading cycles. In Figure 8.3, it is seen

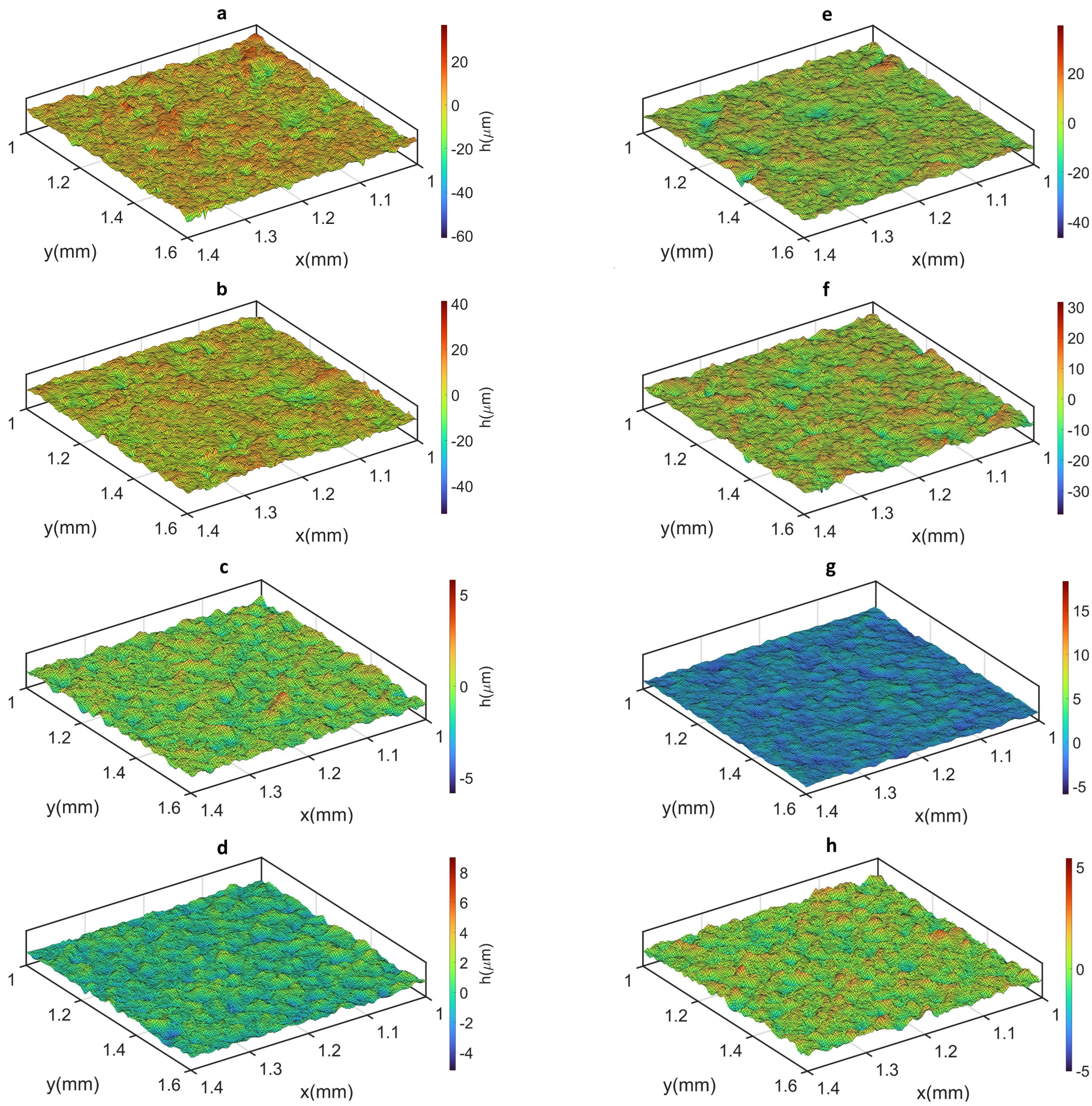

Figure 8.3: Comparison of the 3D surface topography of the samples: (a-d) before the 1^{st} loading; (e-h) after the 10^{th} loading/unloading cycle; (a, e) S1; (b, f) S2; (c, g) S9; (d, h) S10.

that the asperity heights of the samples decreased after the 10^{th} loading/unloading cycles. These topographies were used to measure the surface roughness of the contact pairs, as shown in Table 8.1. Figure 8.4 shows the reflection coefficient R and linear interfacial stiffness K_1 of the pairs S1S2 and S9S10 during the 1^{st}, 2^{nd} and 10^{th} loading/unloading cycles against the nominal contact pressure. As the nominal contact pressure increased, the asperities deformed, making the contact stiffer; therefore, the

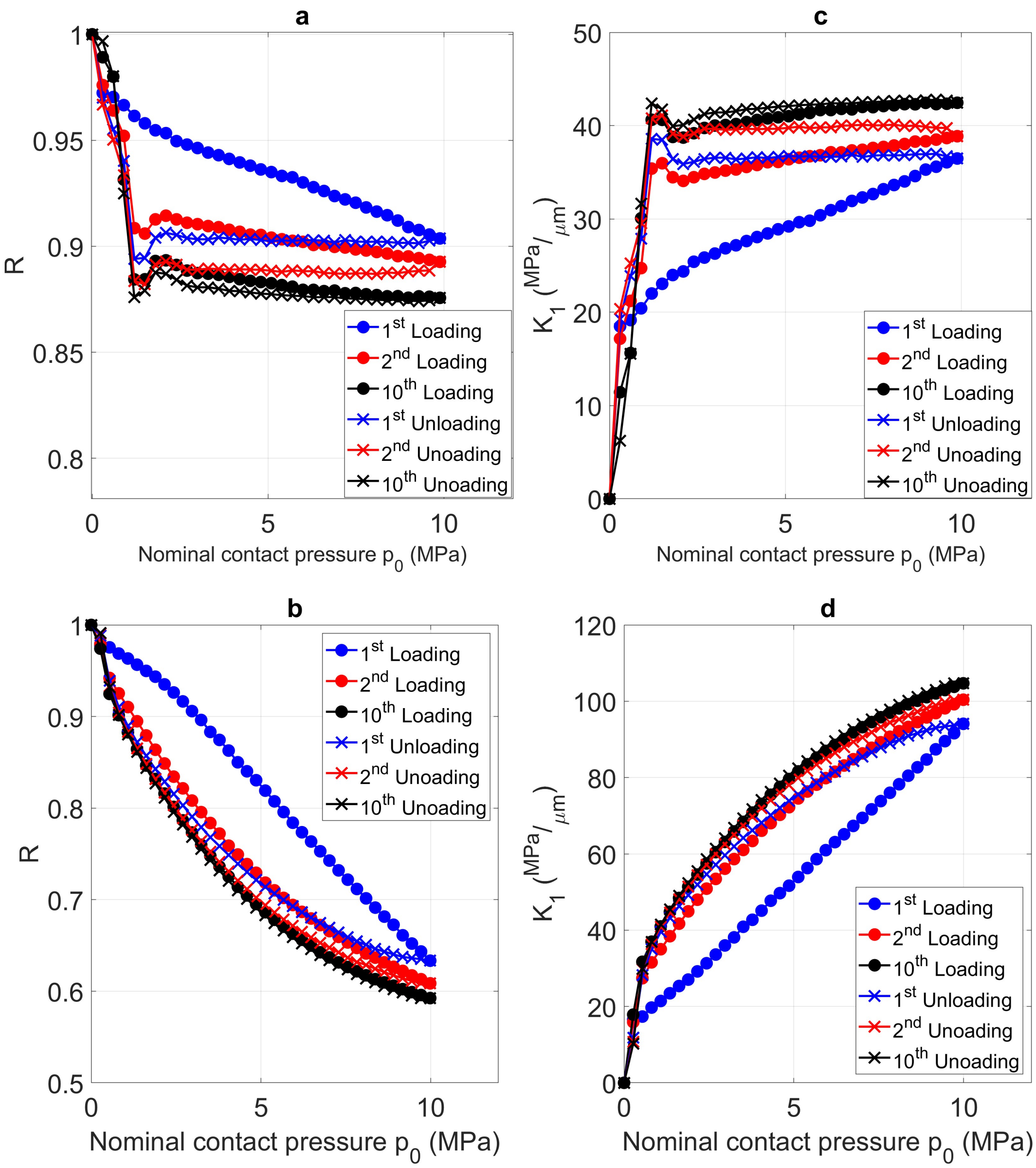

Figure 8.4: The effect of elastic-plastic deformation of the asperities on: (a-b) reflection coefficient R; (c-d) linear interfacial stiffness K_1; (a,c) pair S1S2 (rough); (b,d) pair S9S10 (smooth).

Table 8.1: Surface roughness of the samples before the 1^{st} loading and after the 10^{th} loading/unloading cycles.

	Sample	$R_a(\mu m)$	$R_q(\mu m)$	$R_z(\mu m)$
Before 1^{st} loading	S_1	3.707	5.000	34.711
	S_2	4.063	6.047	35.672
	S_9	0.455	0.588	3.148
	S_{10}	0.495	0.640	3.453
After 10^{th} loading/ unloading cycle	S_1	3.499	4.691	29.985
	S_2	3.175	4.124	23.842
	S_9	0.406	0.509	2.618
	S_{10}	0.451	0.559	2.706

reflection coefficient decreased, meaning that more ultrasonic energy was transferred to the lower body. During the 1^{st} loading, the real contact area was small since a few asperities were in contact. This led to a significantly high contact pressure beyond the bulk yield stress of aluminium $Al6082$-$T6$, and the asperities were plastically deformed [8]. There is a hysteresis in the 1^{st} loading/unloading cycle shown in Figures 8.4a and b. During the 1^{st} unloading cycle, only the asperities in the elastic limits were recovered, and those under plastic deformation were still in contact. This made the contact area larger during the unloading than during the loading in the 1^{st} cycle. Therefore, the contact became stiffer [8], as shown in Figures 8.4c and d. The contact was stiffer during the 2^{nd} loading cycles. This is because the plastic deformation of those asperities in contact during the 1^{st} loading allowed the new asperities to touch. Therefore, the real contact area increased, and the contact pressure decreased compared to the 1^{st} loading. This made the contact stiffer and reduced the plastic flow in asperities. Although the hysteresis in the 2^{nd} loading/unloading cycle is less compared to the 1^{st} loading/unloading cycle, it indicates the plastic flow of the asperities that were either newly in contact or not fully deformed during the previous loading/unloading. From Figure. 8.4, it is seen that the 1^{st} unloading curve and the 2^{nd} loading curve intersect. According to Dwyer-Joyce et al.[8], these intersections irreversibly indicate both plastic flow and contact. Hysteresis almost disappeared after the 10^{th} loading/unloading cycles. The comparison between the roughness of the upper and lower bodies showed that the roughness before the 1^{st} loading cycle and after the 10^{th} loading/unloading cycles decreased, as shown in Table 8.1. It could be concluded that after several loadings/unloadings, the asperities were more elastic. Figure 8.5 shows the second-order nonlinear parameter γ and second-order nonlinear

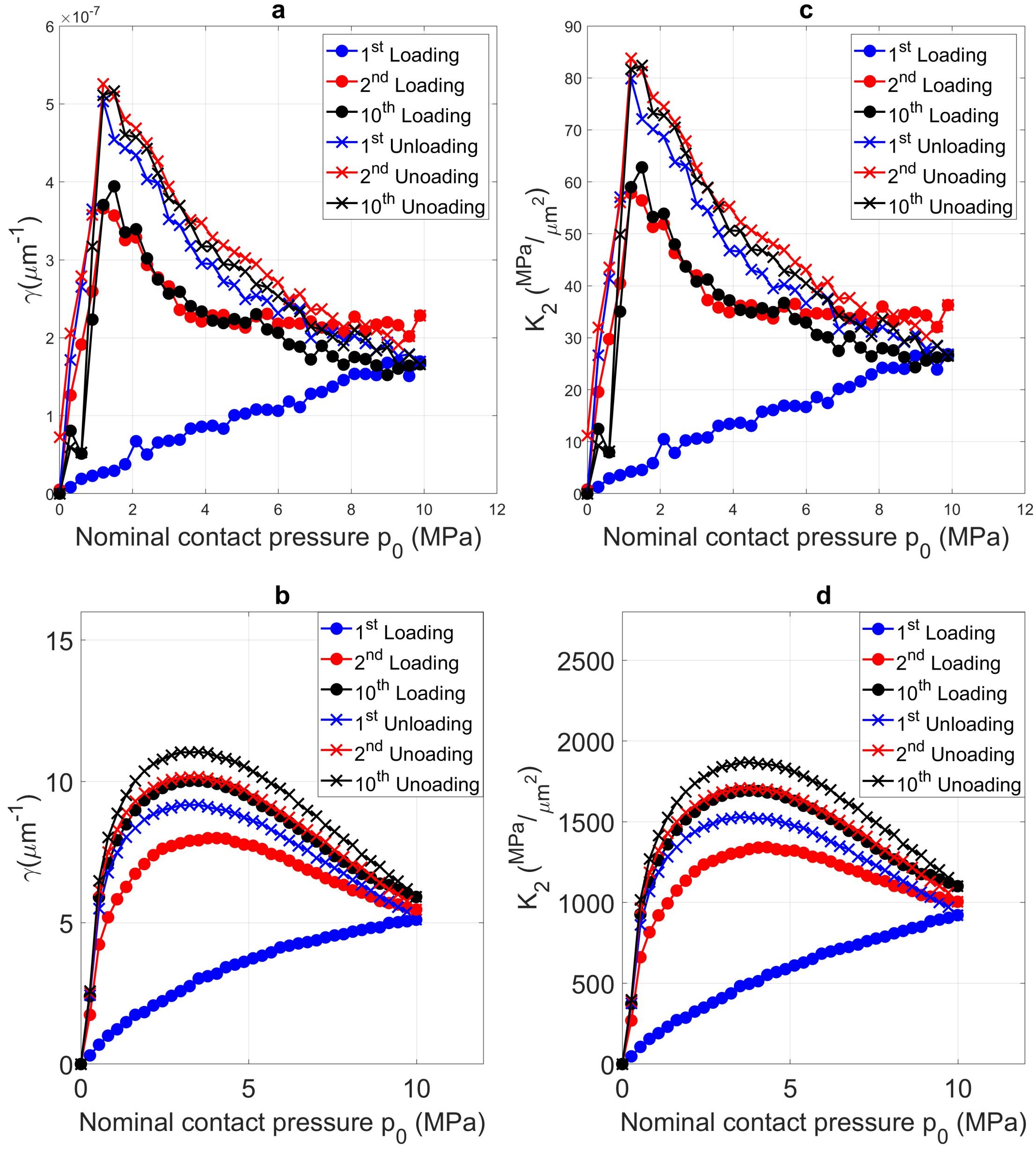

Figure 8.5: The effect of elastic-plastic deformation of the asperities on: (a-b) second-order nonlinear parameter γ; (c-d) second-order nonlinear normal interfacial stiffness K_2; (a,c) pair S1S2 (rough); (b,d) pair S9S10 (smooth).

normal interfacial stiffness K_2 of the pairs S1S2 and S9S10 during the 1^{st}, 2^{nd} and 10^{th} loading/unloading cycles as a function of the nominal contact pressure [83]. The second-order nonlinear parameters γ were measured using the ratio of the amplitude of FFT of the second-order harmonic A_2 to the square of the amplitude of the fundamental frequency A_1 at any nominal contact pressure (Eq. 7.15). Then, γ was substituted into Eq. 7.19 to convert the unit from voltage to length.

Like the reflection coefficient and linear interfacial stiffness, there is a hysteresis in the loading/unloading cycles for the second-order nonlinear parameter and second-order nonlinear normal interfacial stiffness. Only the asperities in elastic limits were recovered during the unloading, making more junctions compared to the loading. Subsequently, the second-order nonlinear normal interfacial stiffness was larger during unloading. This hysteresis became smaller for consecutive loading/unloading cycles. After the 2^{nd} loading cycles, the second-order nonlinear normal interfacial stiffness decreased after the peak. However, the contact became stiffer as the linear interfacial stiffness increased. A comparison between the hysteresis of the linear and second-order nonlinear normal interfacial stiffness shows the greater value of nonlinear stiffness. This can be a valuable observation that indicates the existence of imperfect irreversible contact.

8.2.3 The effect of surface topography

It is required to investigate the effect of surface topography on the linear and second-order nonlinear normal interfacial stiffnesses. Figure 8.6 shows the probability density function of the asperity height pairs S1S2 and S9S10. The percentage of the peaks of asperities greater than R_q of samples S1 and S2 (19.6% and 17.7%, respectively) was less than the samples S9 and S10 (27.9% and 25.1%, respectively). This indicates that more asperities were in contact for the pair S9S10 than for the pair S1S2. This makes the contact of pair S9S10 stiffer than that of pair S1S2.

Figure 8.7 shows the linear and second-order nonlinear normal interfacial stiffness of the pairs S1S2 and S9S10 during the loading/unloading cycles. In Figure 8.7, it is seen that the rough pair S1S2 was less stiff than the smooth pairs S9S10 during the 1^{st}, 2^{nd} and 10^{th} loading/unloading cycles.

As discussed in Section 5.2, the second-order nonlinear parameter γ is a function of the applied normal load and the normal stress generated by ultrasound when the contact is assumed to be perfect (without roughness and waviness) and frictionless. The peak of the second-order nonlinear parameter was shown to occur when the normal stress generated by ultrasound is the same as the nominal contact pressure. Figures 8.8a-c show that the peak γ of the pair S1S2 was at a lower nominal contact pressure compared to the pair S9S10. This is because the real contact area of the pair S1S2 was less than that of the pair S9S10. This made the real contact pressure of the pair S1S2 higher than that of the pair S9S10 at the corresponding nominal

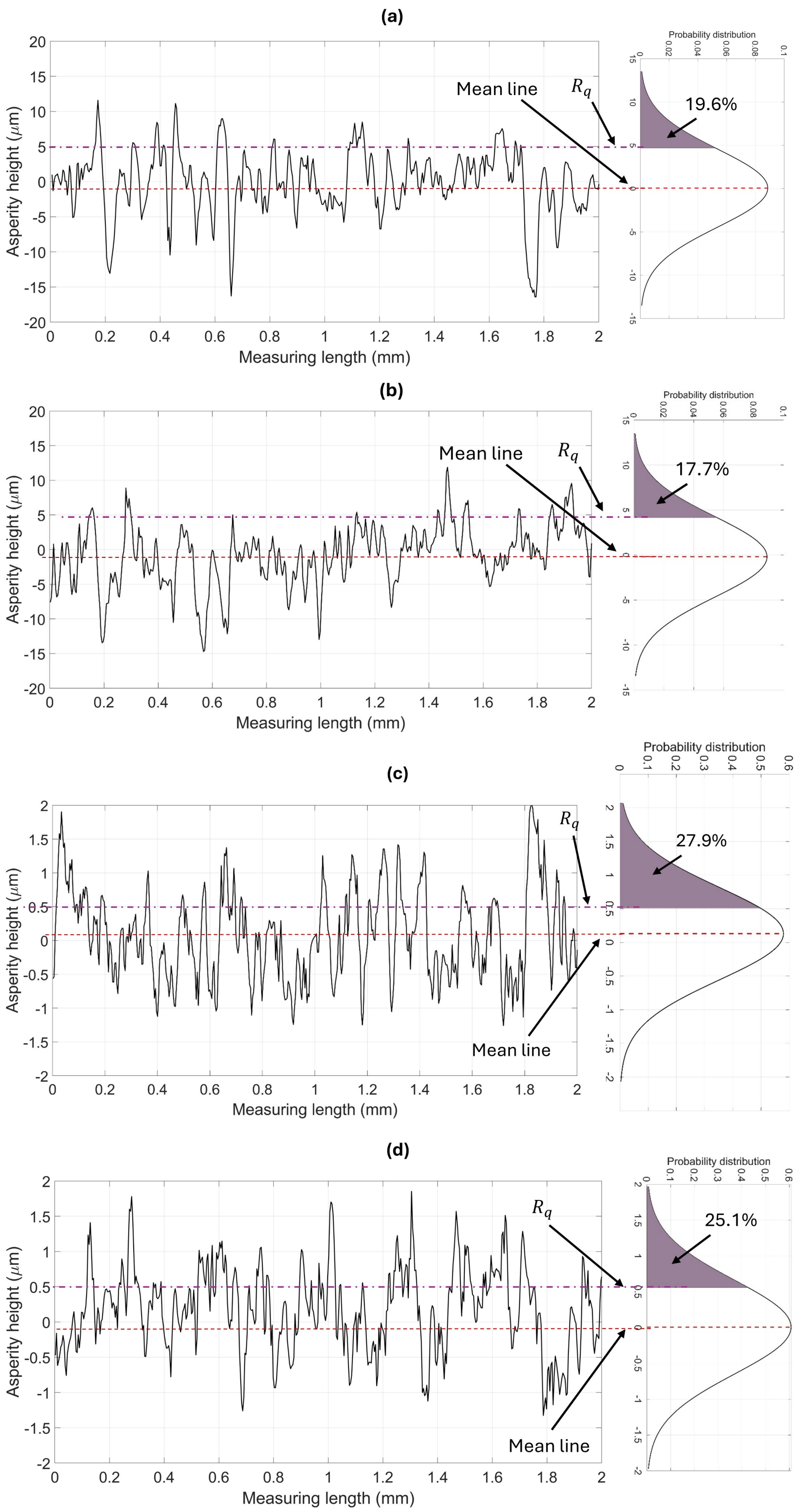

Figure 8.6: Probability density function of the asperity height of the pairs S1S2 and S9S10 after the 10^{th} loading/unloading cycle.

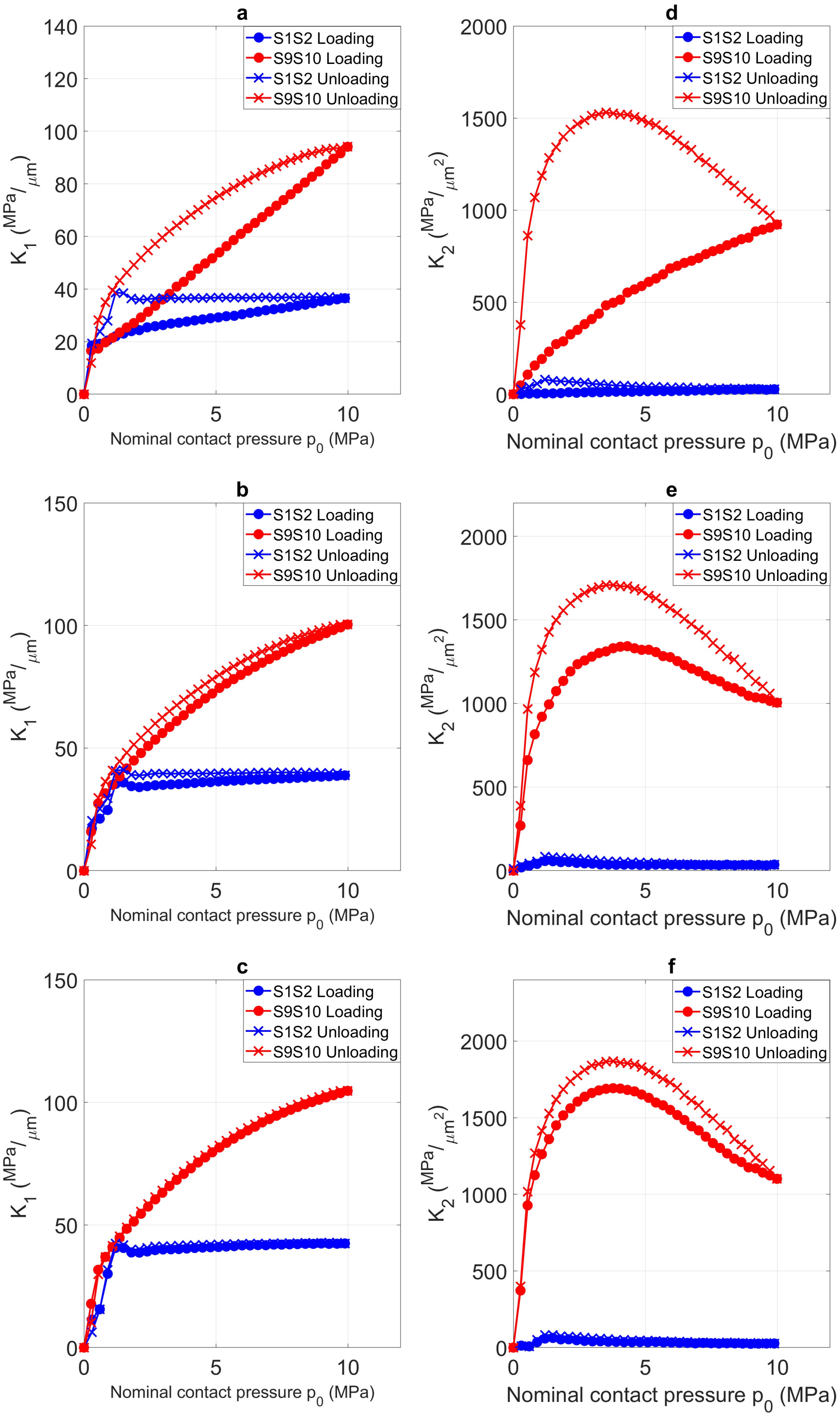

Figure 8.7: The effect of elastic-plastic deformation of the asperities on: (a-b) linear interfacial stiffness K_1; (d-f) second-order nonlinear interfacial stiffness K_2; (a,d) 1^{st} loading/unloading cycle; (b,e) 2^{nd} loading/unloading cycle; (c,f) 10^{th} loading/unloading cycle

contact pressure. However, more studies are required to explain why γ increases monotonically for the 1^{st} loading (Figure 8.8a).

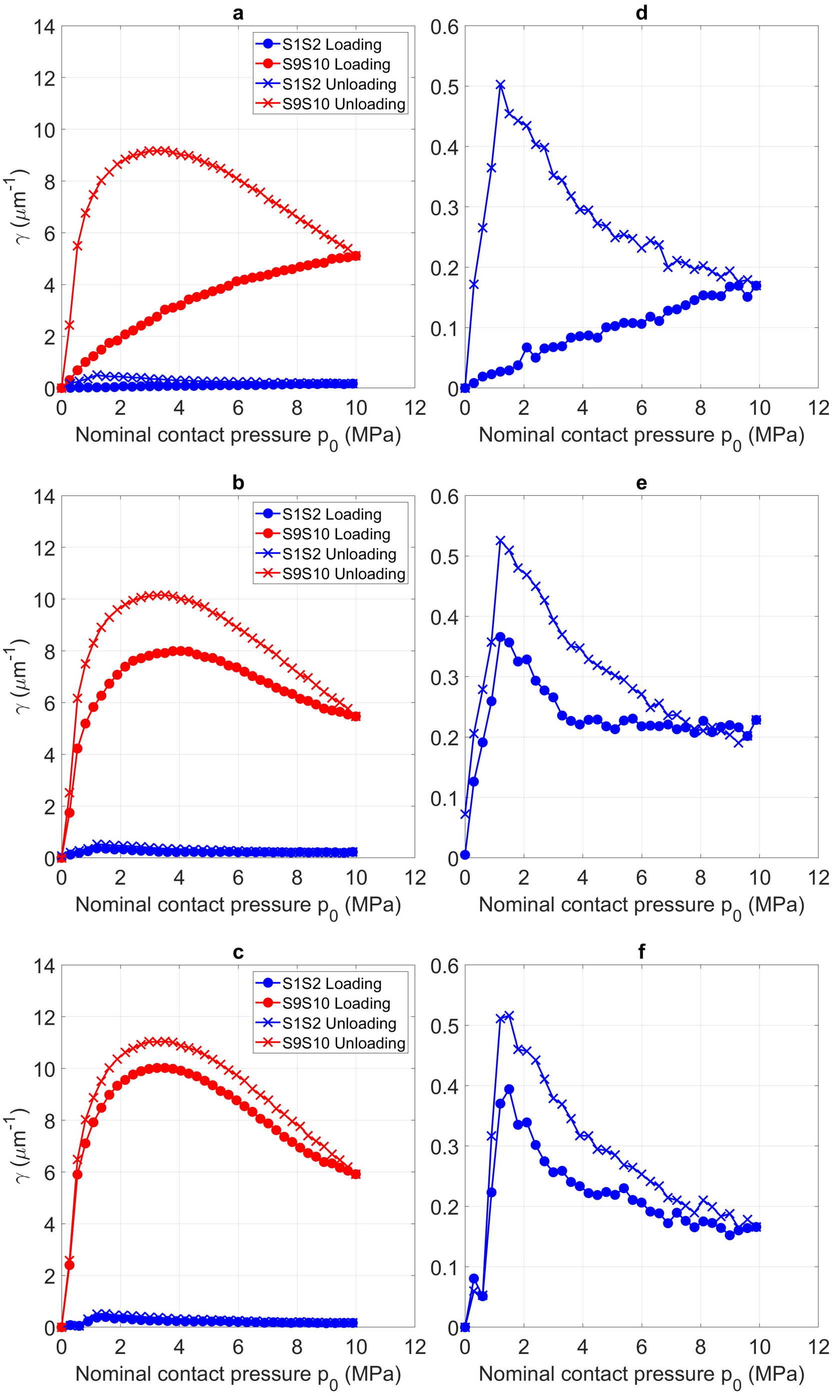

Figure 8.8: The effect of real contact pressure on the second-order nonlinear parameter γ of the pairs S1S2 and S9S10: (a) 1^{st} loading/unloading; (b) 2^{nd} loading/unloading; (c) 10^{th} loading/unloading; (d-f) zoomed-in view of S1S2.

8.3 Conclusion

The real contact is placed at the peak of the asperities. Before the first loading, this contact is significantly smaller than the nominal contact area. During the first loading/unloading cycles, the contact pressure created plastic flow in the asperities as the contact area was small. The deformed asperities became flatter at this point, increasing the real contact area. During the consecutive loading/unloading cycles, the real contact area increased, and the contact stress did not exceed the yield strength. Therefore, the second-order nonlinear normal interfacial stiffness became stiffer. Like linear interfacial stiffness, the hysteresis in the loading/unloading cycles became smaller, indicating the plastic deformation of the asperities decreased and the contacts became more elastic.

It is seen that when the contact was rougher and the probability density function of the asperity height was higher than the root-mean-square R_q, the real contact area was smaller than the smoother contact. This reduced the second-order nonlinear parameter γ of the rougher surface compared to the smoother contact; therefore, the contact became less stiff. The other observation was that the peak of γ of the rougher contact was at the lower nominal contact pressure compared to the smoother surface. This agrees with the analytical and numerical analysis presented in Section 5.2, which indicates that the normal stress generated by ultrasound at the peak was equal to the contact pressure. Therefore, for the rougher contact with a smaller real contact area, the real contact pressure was larger than the smoother contact, and the peak of γ was at a lower nominal contact pressure. However, more studies are required to determine the real contact area and the contact pressure using γ.

In this chapter, a finite element model with ABAQUS/Explicit was created to show the effect of consecutive loading/unloading on the asperities of the contact. The asperities were modelled as the hemisphere with the same radius of curvature as scanned from the real surfaces. The mesh convergence was used, and it was found that the mesh size of 1 μm was suitable for this study. The asperities were seen to be plastically deformed during the first loading as the contact area was small. The following loading/unloading cycles showed the elastic deformation of the asperities. This agrees with the experimental results.

Chapter 9

Analytical Analysis of Nonlinear Behaviour of Ultrasound in Liquid Lubricants

In this chapter, the mechanism of nonlinear ultrasound in liquid lubricants is investigated. An analytical approach is used to derive the nonlinear coefficient. Different factors and parameters are used to study their effects on the nonlinear behaviour of ultrasound.

9.1 Nonlinear ultrasound mechanism

When a longitudinal ultrasonic wave propagates in the medium, the particles oscillate around their equilibrium position, as explained in Section 3.1. The direction of particle oscillation is along the direction of wave propagation. A longitudinal ultrasonic wave consists of two parts: compression and rarefaction parts. When low-power ultrasonic waves propagate in a Newtonian (for example, a mineral oil) or non-Newtonian liquid lubricant (for example, a multigrade engine oil), the sound pressure generated by compression and rarefaction parts is equal. So, the sound speed c_0 of the particles of the medium is constant throughout the wave, as shown in Figure 9.1a. In this condition, the waves propagate without distortion and have the same frequency as the incident frequency generated by the ultrasonic source (a piezoelectric transducer). However, when high-power ultrasonic waves propagate in Newtonian or a non-Newtonian liquid lubricant, the waves can distort, as shown in Figure 9.1b. There are two causes of this distortion: (1) nonlinearity due to the convection effect; (2) nonlinearity of the medium [28, 108]. In terms of the convection effect, the sound pressures in the rarefaction and compression parts of high-power ultrasonic waves are

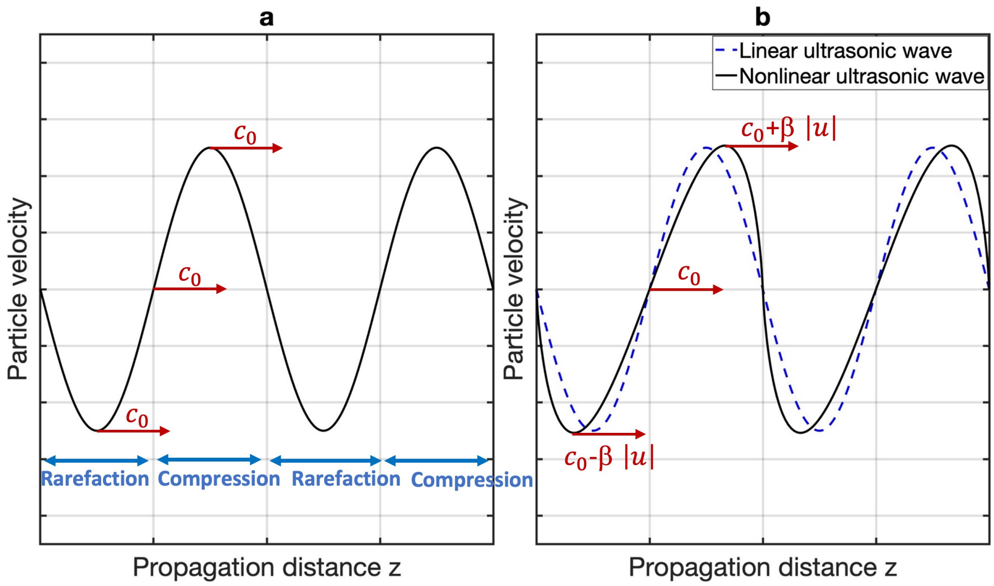

Figure 9.1: Schematic diagram of particle velocity generated by longitudinal ultrasonic waves: **(a)** linear behaviour of ultrasonic waves due to low-power excitation amplitude; **(b)** nonlinear behaviour of ultrasonic waves due to high-power excitation amplitude.

different. Therefore, the velocity of the particles varies throughout the wave, which distorts the waveform, as shown in Figure 9.1b [108]. As the sound pressure generated by high-power waves increases, the bulk modulus and stiffness of the liquid in the compression part increase [28, 108]. The sound speed of the particles is the sum of the speed of sound, particle velocity and a coefficient of nonlinearity β [28]. The peak of the compression part travels at $c_0 + \beta|u|$ faster than the trough at $c_0 - \beta|u|$ [28]. This distortion generates higher-order harmonics even in Newtonian liquids such as distilled water [27]. In contrast, the absorption caused by highly viscous liquids dissipates the energy. Even using high-power waves in a highly viscous liquid leads to lower the amplitudes of the fundamental frequency and high-order harmonics [108]. β contains both the effect of convection and the nonlinearity of the medium.

9.2 Theoretical approach

The region in the path of an ultrasonic source (a piezoelectric transducer) is divided into near-field and far-field regions, as shown in Figure 9.2. For distances close to the ultrasonic source in the near-field region, the wavefronts are planar [28]. This

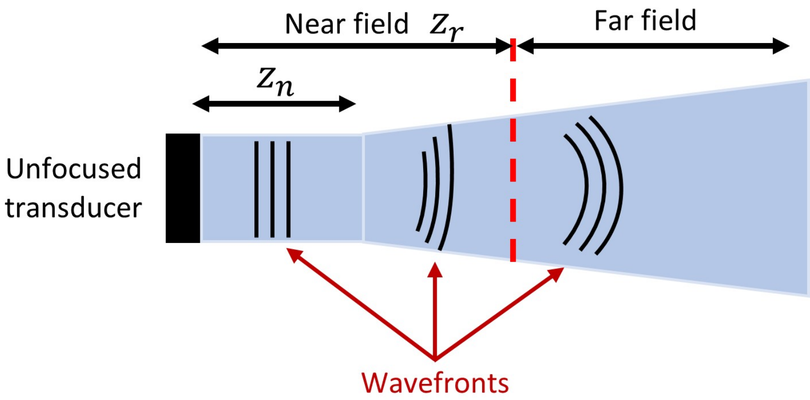

Figure 9.2: Schematic diagram of the near-field and far-field regions.

distance is given by [28]:

$$Z_n = \frac{\omega_0 a^2}{2\pi c_0} \tag{9.1}$$

where ω_0 is the angular frequency of the generated ultrasonic wave, a is the radius of the piezoelectric transducer and c_0 is the linear (also called small-signal) sound speed of the medium at ambient pressure. As the waves propagate further from the source and approach the end of the near-field, the wavefronts become quasi-planar [28]. This is due to the diffraction effect caused by the finite size of the source. The distance from the piezoelectric source to the end of the near-field is called the Rayleigh distance [28]:

$$Z_r = \frac{\omega_0 a^2}{2c_0} \tag{9.2}$$

The end of the Rayleigh distance is a transition between the near-field and far-field regions [28]. When the waves propagate further and reach the far-field region, the wavefronts become spherical [28].

A second-order wave equation can model the nonlinear behaviour of ultrasound in lossless and lossy liquid lubricants. The two main equations are the Burgers equation and the Khokhlov-Zabolotskaya-Kuznetsov (KZK) equation. The Burgers equation describes the effect of absorption and nonlinearity of ultrasound in a fluid [96]. This equation is valid in the near-field zone close to the ultrasonic source (Z_n distance) where the wavefronts are planar [28]. However, these solutions are unable to model the nonlinear behaviour of ultrasound for distances larger than Z_n. The KZK equation is one of the most accurate equations that considers the effect of absorption, nonlinearity and diffraction of ultrasound in a fluid [97, 98, 111]. There are few analytical solutions to the KZK equation [112], and it is mainly solved numerically as presented in [113–115]. The KZK equation in two dimensions is given as [28, 111]:

$$\frac{\partial^2 p}{\partial z \partial \tau} = \frac{c_0}{2}\left(\frac{\partial^2 p}{\partial r^2} + \frac{1}{r}\frac{\partial p}{\partial r}\right) + \frac{\delta}{2c_0^3}\frac{\partial^3 p}{\partial \tau^3} + \frac{\beta p}{\rho_0 c_0^3}\frac{\partial^2 p}{\partial \tau^2} \tag{9.3}$$

where ρ_0 is the ambient density (unperturbed density) of the liquid, δ is sound diffusivity, β is the nonlinear coefficient, z is propagation direction, $\tau = t - \frac{z}{c_0}$ is the retarded time, r is cylindrical coordinate variable from the centre of the ultrasound source and p is the total pressure (pressure generated by ultrasound and the ambient pressure). Eq. 9.3 is in polar coordinates, which allows the first term of the right-hand side to consider the beam spreading (diffraction) as the ultrasonic waves propagate in fluid. For plane waves, this term is ignored, and Eq. 9.3 is used for one-dimension propagation and becomes Eq. 9.5 [28]. Appendix C shows the derivation of Eq. 9.3. Sound diffusivity is defined as [116]:

$$\delta = \frac{1}{\rho_0}\left(\frac{4}{3}\mu + \mu_B\right) + \frac{\kappa}{\rho_0}\left(\frac{1}{c_v} - \frac{1}{c_p}\right) \tag{9.4}$$

where μ shear viscosity, μ_B is bulk viscosity, κ is the thermal conductivity, c_v and c_p are the specific-heat coefficients at constant volume and pressure, respectively. In the sound diffusivity equation, the term representing the thermal conductivity κ due to ultrasound is ignored as it has an insignificant effect. The first term on the right-hand side of Eq. 9.3 considers diffraction, the second term represents absorption and the third term considers nonlinearity. Ultrasonic transducers (ultrasonic sources) are finite in size. Therefore, the emitted ultrasonic waves are diffracted as they propagate further from the source [117]. This diffraction is significantly small near the ultrasonic source (the distance of Z_n) and the wavefronts are planar. The shear and bulk viscosities of lubricants absorb the ultrasonic energy as the waves propagate. For linear ultrasound, where the amplitude of excitation is low, there is no nonlinearity, and only diffraction and absorption affect the waves. Ignoring the diffraction and absorption terms (first and second term on the right-hand side) of Eq. 9.3 followed by integration with respect τ, simplifies the KZK equation to the lossless Burgers equation [96]:

$$\frac{\partial p}{\partial z} = \frac{\beta p}{\rho_0 c_0^3}\frac{\partial p}{\partial \tau} \tag{9.5}$$

There are different solutions for the Burgers equation such as the Fubini [28, 118], Fay [28, 119] and Blackstock [28, 120] solutions, that can be used depending on the values of the nonlinear coefficient, frequency and sound diffusivity. In this study, an approximate solution of Eq. 9.5 can be derived using the homotopy perturbation method (HPM) [106] to present a unique and simplified solution:

$$H(Y,\alpha) = (1-\alpha)[L(Y) - L(p(0,\tau))] + \alpha[L(Y) + N(Y) - f(r)] = 0 \tag{9.6}$$

where L is the linear part, N is the nonlinear part and $f(r)$ is the known analytical function of the differential equation, which is zero for the lossless Burger equation (Eq. 9.5). The particular solution of Eq. 9.5 is the sum of linearised equations known as a perturbation series:

$$p = Y = Y_0 + \alpha Y_1 + \alpha^2 Y_2 + ... \tag{9.7}$$

where α is an embedding parameter Y_0, Y_1 and Y_2 are the first, second and third terms of the perturbation methods, respectively. α is an embedded parameter, for $\alpha = 1$, Eq. 9.7 gives an approximate solution to the partial differential equation (Eq. 9.5). Since only the fundamental frequency and the second-order harmonic are sufficient in this study, Eq. 9.7 is considered up to the second term (to derive the third harmonics, the term Y_2 also needs to be used). The homotopy perturbation formula is constructed by substituting Eqs. 9.5 and 9.7 into Eq. 9.6:

$$\begin{aligned} H(Y,\alpha) =& (1-\alpha)\left[\frac{\partial(Y_0+\alpha Y_1)}{\partial z} - \frac{\partial p(0,\tau)}{\partial z}\right] + \\ & \alpha\left[\frac{\partial(Y_0+\alpha Y_1)}{\partial z} - \frac{\beta(Y_0+\alpha Y_1)}{\rho_0 c_0^3}\frac{\partial(Y_0+\alpha Y_1)}{\partial \tau}\right] = 0 \end{aligned} \tag{9.8}$$

Expanding Eq. 9.8 gives:

$$\begin{aligned} H(Y,\alpha) =& \frac{\partial Y_0}{\partial z} - \frac{\partial p(0,\tau)}{\partial z} + \alpha\left[\frac{\partial Y_1}{\partial z} + \frac{\partial p(0,\tau)}{\partial z} - \frac{\beta Y_0}{\rho_0 c_0^3}\frac{\partial Y_0}{\partial \tau}\right] - \\ & \alpha^2\left[\frac{\beta Y_0}{\rho_0 c_0^3}\frac{\partial Y_1}{\partial \tau} + \frac{\beta Y_1}{\rho_0 c_0^3}\frac{\partial Y_0}{\partial \tau}\right] = 0 \end{aligned} \tag{9.9}$$

A mono-frequency sinusoidal ultrasonic wave with pressure amplitude p_0 is generated by a transducer at $z = 0$:

$$p(0,\tau) = p_0\, e^{-(\tau/T_0)^2}\, sin(\omega_0 \tau) \tag{9.10}$$

where T_0 is the time duration of the source waveform. Eq. 9.10 is substituted into Eq. 9.9 to derive the following linear equations:

$$\alpha^0 : \quad \frac{\partial Y_0}{\partial z} = \frac{\partial p(0,\tau)}{\partial z} \tag{9.11}$$

Integration of Eq. 9.11 with respect to z gives:

$$Y_0 = p(0,\tau) = p_0\, e^{-(\tau/T_0)^2}\, sin(\omega_0 \tau) \tag{9.12}$$

In Eq. 9.9, the coefficients of α are solved to give Y_1:

$$\alpha: \quad \frac{\partial Y_1}{\partial z} + \frac{\partial p(0,\tau)}{\partial z} - \frac{\beta Y_0}{\rho_0 c_0^3}\frac{\partial Y_0}{\partial \tau} = 0 \tag{9.13}$$

Integration of Eq. 9.13 concerning z gives:

$$Y_1 = \frac{z\beta\omega_0}{2\rho_0 c_0^3}\, p_0^2\, e^{-2(\tau/T_0)^2}\, sin(2\omega_0 t) \tag{9.14}$$

The particular solution of Eq. 9.5 in the distance of Z_n of the near-field region is given by substituting Eqs. 9.12 and 9.14 into Eq. 9.7:

$$p = p_0\, e^{-(\tau/T_0)^2}\, sin(\omega_0\tau) + \frac{z\beta\omega_0}{2\rho_0 c_0^3}\, p_0^2\, e^{-2(\tau/T_0)^2}\, sin(2\omega_0\tau) \tag{9.15}$$

if p_1 is defined as the amplitude of fundamental frequency (coefficient of the first term of Eq. 9.15) and p_2 is defined as the amplitude of second-order harmonic (coefficient of the second term of Eq. 9.15):

$$p_1 = p_0 \tag{9.16}$$

$$p_2 = \frac{z\beta\omega_0}{2\rho_0 c_0^3}\, p_0^2 \tag{9.17}$$

As mentioned earlier, wavefronts in the distance Z_n of the near-field region are planar due to the absence of the attenuation effect. Dividing p_2 by square of p_1 gives:

$$\frac{p_2}{p_1^2} = \frac{z\beta\omega_0}{2\rho_0 c_0^3} \tag{9.18}$$

The square of p_1 makes Eq. 9.18 independent of the amplitude of the excitation p_0. The linear relationship between the sound pressure and particle displacement for the fundamental frequency and second-order harmonic is given as [28, 108]:

$$p_1 = \rho_0 c_0 \omega_1 A_1 \quad ; \quad p_2 = \rho_0 c_0 \omega_2 A_2 \tag{9.19}$$

where ω_1 and ω_2 are the angular frequency of the fundamental frequency and second-order harmonic, A_1 and A_2 amplitude of particle displacement of the fundamental frequency and second-order harmonic. The fundamental angular frequency is the same as the angular frequency of the ultrasonic wave $\omega_1 = \omega_0$, and so $\omega_2 = 2\omega_0$. Eq.

9.19 is substituted into Eq. 9.18 to convert sound pressure to particle displacement. The nonlinear coefficient is non-dimensional and given by:

$$\beta = \frac{4c_0^2}{\omega_1^2 z}\frac{A_2}{A_1^2} \tag{9.20}$$

Eq. 9.18 and Eq. 9.20 agree with [121]. The values of A_1 and A_2 are measured experimentally (see Sections 11.1 and 11.2) and substituted in Eq. 9.20 to measure the nonlinear coefficient of the liquid lubricants.

9.2.1 Effect of absorption

To investigate the effect of absorption on ultrasonic wave propagation, the term absorption of Eq. 9.3 is considered as:

$$\frac{\partial p}{\partial z} = \frac{\delta}{2c_0^3}\frac{\partial^2 p}{\partial \tau^2} \tag{9.21}$$

This is a simple parabolic partial differential equation which can be solved using Fourier Transform [117]. For the source condition given by [117, 122]:

$$p(z = 0, \tau) = p_0\, f(\tau) \tag{9.22}$$

The solution is given by [122]:

$$p = \frac{p_0}{\sqrt{2\pi\delta z/c_0^3}} \int_{-\infty}^{\infty} f(\psi) exp\left[-\frac{(\tau-\psi)^2}{2\delta z/c_0^3}\right] d\psi \tag{9.23}$$

where ψ is a convolution variable. For the source given by Eq. 9.10, the sound pressure in the liquid is given by [114, 117]:

$$p = \frac{p_0}{\sqrt{1+\alpha_1 z}} exp(-\frac{\alpha_0 z}{1+\alpha_1 z}) e^{-(\tau/T)^2} sin(\omega_c \tau) \tag{9.24}$$

where T is pulse duration, ω_c is the centre frequency, α_0 and α_1 are the attenuation coefficients:

$$T(z) = T_0\sqrt{1+\alpha_1 z} \tag{9.25}$$

$$\omega_c(z) = \frac{\omega_0}{1+\alpha_1 z} \tag{9.26}$$

$$\alpha_0 = \frac{\delta\omega_0^2}{2c_0^3} \tag{9.27}$$

$$\alpha_1 = \frac{2\delta}{c_0^3 T_0^2} \tag{9.28}$$

Table 9.1: Properties of the liquid lubricant and ultrasonic wave.

Parameters and Properties	Values
Waveform	sin-Gaussian wave
Density ρ	850 kg/m^3
Shear rate γ	1000 s^{-1}
Speed of sound c	1484 m/s
Shear viscosity μ	0.85 Pa.s
Nonlinear coefficient β	6.21
Frequency of excitation f_0	1.02 MHz
Amplitude of excitation p_0	28 MPa (1 MPa of FFT)
Bulk viscosity μ_B (2.67*μ)	$2.67 * 10^{-3}$ Pa.s
Time duration of the source waveform T_0	2 μsec

The bulk viscosity is almost 2.67 times the shear viscosity at the temperature 22^0C of distilled water [123, 124]. In the current study, this relation is used for the liquid lubricants. The ultrasonic wave propagation in a lubricant (PAO40) with the properties shown in Table 9.1. Figure 9.3 shows the excitation and propagation waves at the separation distances (propagation distance of the ultrasonic wave from the source) 30 mm, 60 mm, 100 mm and their FFTs. As the ultrasonic waves propagated further from the source, they attenuated (Figures 9.3a-d). However, the FFT shows that they contained only the fundamental frequency (1.02 MHz), and there was no nonlinearity (no higher-order harmonics).

Figure 9.4a shows the variation in the fundamental frequency of the liquid as a function of separation distance for three different liquid lubricants of PAO40, SAE 10W-30 Cat DEO-ULS and SAE 5W-30 Shell Helix Ultra with shear viscosity of 0.85 Pa.s, 0.158 Pa.s and 0.1 Pa.s, respectively, at shear of 1000 s^{-1}. As expected, the higher the viscose lubricant (PAO40), the higher the absorption. This variation was more linear for less viscose lubricant (SAE 5W-30 Shell Helix Ultra) and became nonlinear as viscosity increased. Figure 9.4b shows the variation in the amplitude of the fundamental frequency with the separation distance of PAO40 at different shear rates 50 Pa.s, 1000 Pa.s and 8000 s^{-1} with a shear viscosity of 0.88 Pa.s, 0.85 Pa.s and 0.57 Pa.s, respectively. It is seen that for the same lubricant with shear viscosity at different shear rates, the absorption was lower for lower viscosity.

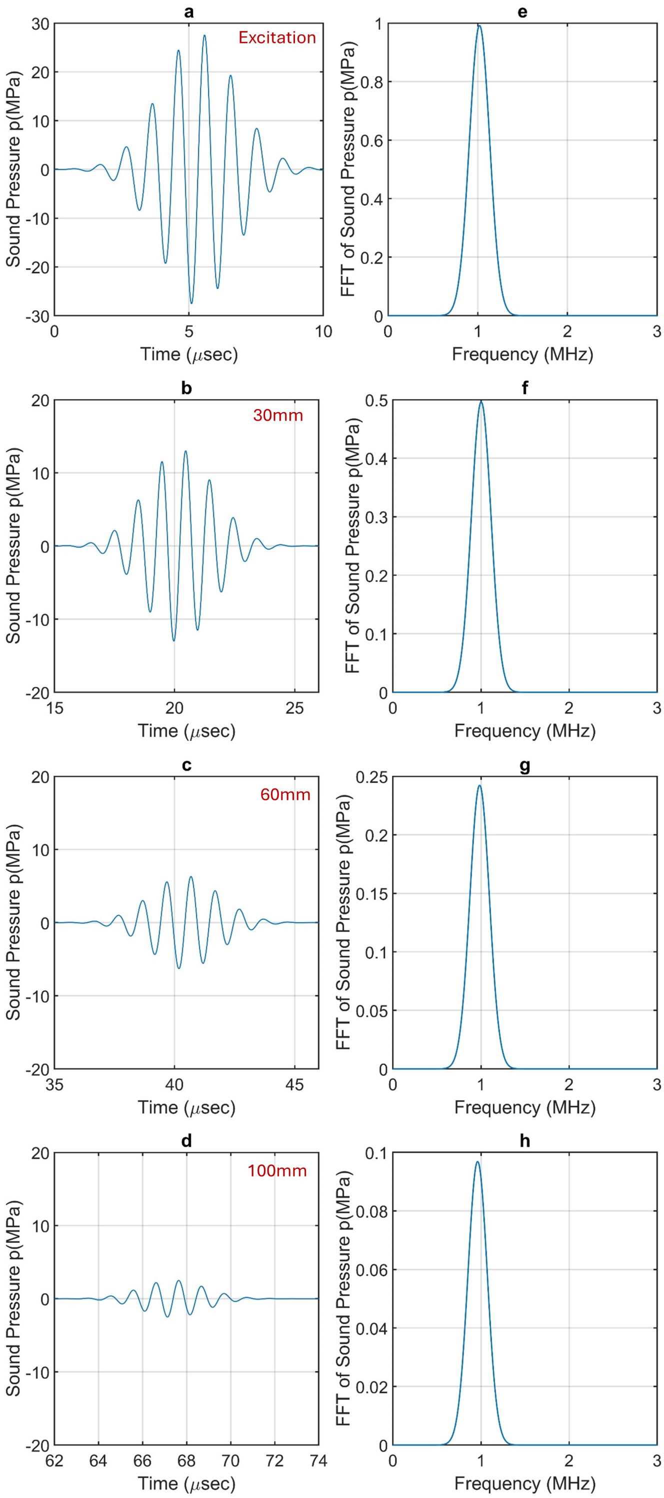

Figure 9.3: Ultrasonic waves generated and propagated in PAO40 considering the effect of absorption: (a-d) time domain; (e-h) frequency domain; (a,e) incident wave; (b,f) 30 mm; (c,g) 60 mm; (d,h) 100 mm away from the source.

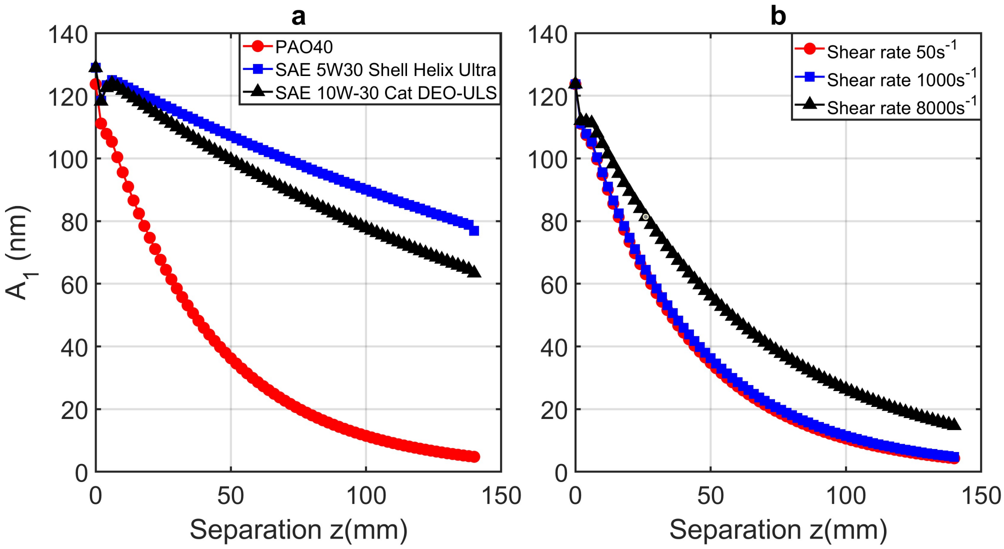

Figure 9.4: Variation of the ultrasonic wave as a function of separation distance considering the effect of absorption: (a) at the shear rate of 1000 s^{-1} for PAO40, SAE 10W-30 Cat DEO-ULS and SAE 5W-30 Shell Helix Ultra; (b) different shear rate of 50 s^{-1}, 1000 s^{-1} and 8000 s^{-1} for PAO40.

9.2.2 Effect of nonlinearity

To investigate the effect of the separation distance on the nonlinearity of ultrasound, the properties listed in Table 9.1 are substituted into Eq. 9.15. The same excitation wave was generated as shown in Figures 9.3a and e. The excitation was a mono-frequency wave that contained only the fundamental frequency (Figure 9.5 e). As the high-power ultrasonic wave propagated further in the liquid lubricant, the waves were distorted, as shown in Figures 9.5a-c. This distortion appeared as a higher-order harmonic in the frequency domain, which is the second-order harmonic (Figure 9.5d-f). Figure 9.6 illustrates the amplitude of the fundamental frequency A_1, second-order harmonic A_2 and the ratio of A_2/A_1^2 of PAO40, SAE 10W-30 Cat DEO-ULS and SAE 5W-30 Shell Helix Ultra as a function of separation distance with the nonlinear coefficient β of 6.21, 7.30, 6.79, respectively (the nonlinear coefficient β was measured experimentally, as shown in Table 11.1). It is seen from Figure 9.6 that in the absence of absorption and diffraction, the amplitude of the fundamental frequency A_1 of all lubricants was constant. However, the amplitude of the second-order harmonic A_2 increased as the ultrasonic waves propagated further. Therefore, as z approached ∞, the amplitude of the second-order harmonic A_2 approached ∞. The amplitude of the second-order harmonic A_2 was zero at the separation distance 0, indicating that there was no nonlinearity. However, the nonlinearity increased significantly over a distance

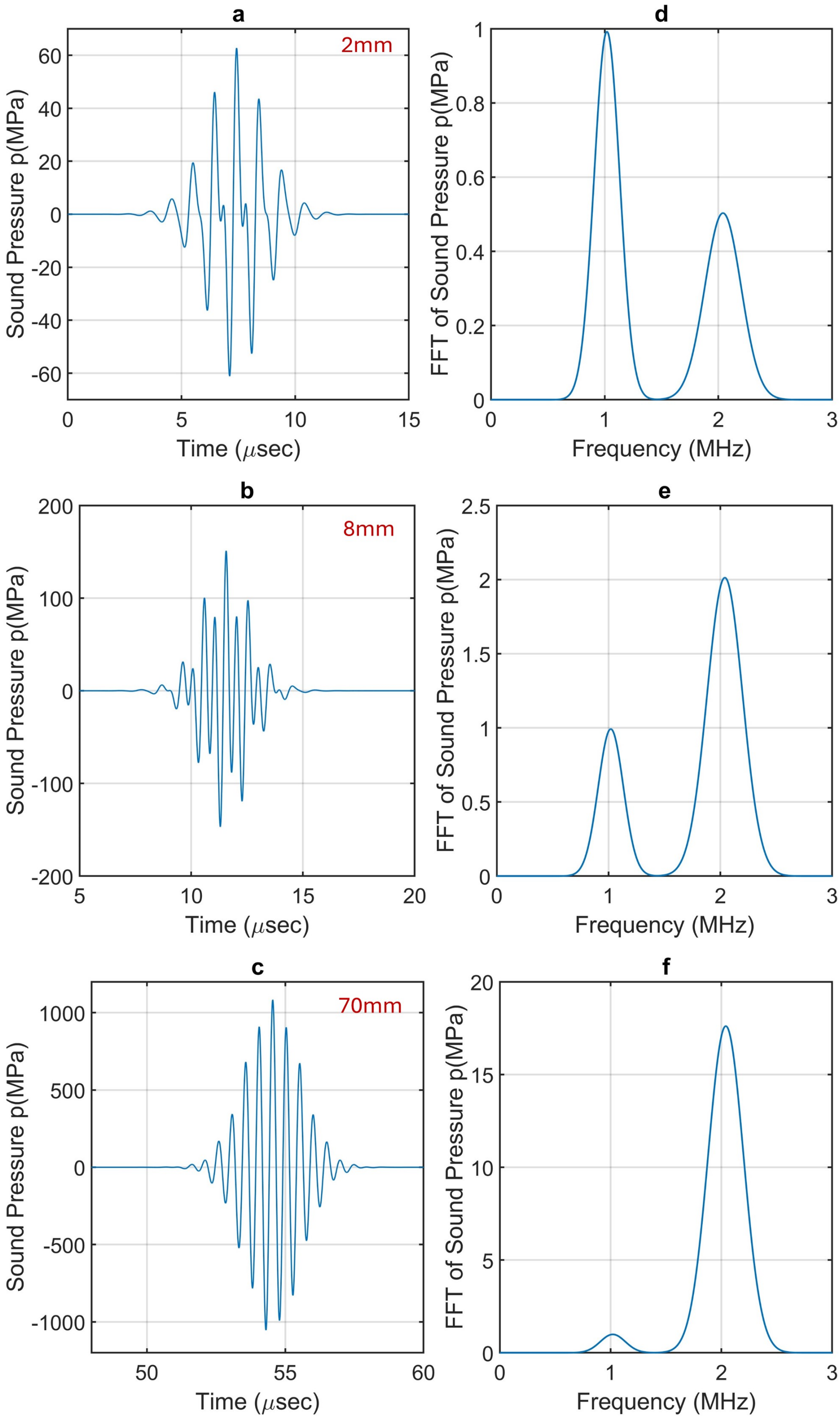

Figure 9.5: Ultrasonic waves propagated in PAO40 considering the effect of nonlinearity: (a-c) time domain; (d-f) frequency domain; (a,e) 2 mm; (c,g) 8 mm; (d,h) 70 mm away from the source.

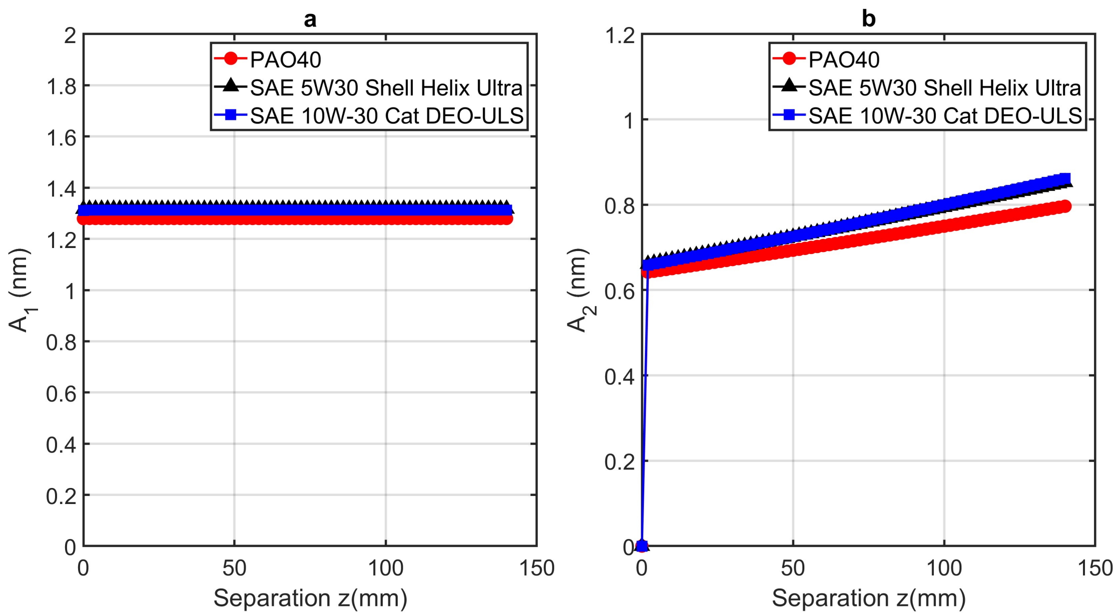

Figure 9.6: Variation of the ultrasonic wave as a function of separation distance considering the effect of nonlinearity: (a) amplitude of fundamental frequency A_1; (b) amplitude of second-order harmonic A_2.

of 2 mm.

9.2.3 Effect of diffraction

The KZK equation (Eq. 9.3) with the effect of diffraction is given by:

$$\frac{\partial^2 p}{\partial z \partial \tau} = \frac{c_0}{2}\left(\frac{\partial^2 p}{\partial r^2} + \frac{1}{r}\frac{\partial p}{\partial r}\right) \tag{9.29}$$

Integration of Eq. 9.29 with respect to retarded time τ gives [117]:

$$\frac{\partial p}{\partial z} = \frac{c_0}{2}\int_{-\infty}^{\tau}\left(\frac{\partial^2 p}{\partial r^2} + \frac{1}{r}\frac{\partial p}{\partial r}\right) d\psi \tag{9.30}$$

For an unfocused circular uniform source with radius a at $z = 0$ is given by [117]:

$$p = \begin{cases} p_0 f(t) & \text{for} \quad r < a \\ \\ 0 & \text{for} \quad r > a \end{cases} \tag{9.31}$$

where $f(t)$ is an arbitrary function of time. Substituting Eq. 9.31 into Eq. 9.30 gives a general solution for the centre of the ultrasonic beam at $r = 0$ as [114]:

$$p = p_0\left(f(\tau) - f(\tau - \frac{a^2}{2c_0 z})\right) \tag{9.32}$$

For the arbitrary function of:

$$f(\tau) = e^{-(\tau/T_0)^2}\, sin(\omega_0 \tau) \tag{9.33}$$

the excitation becomes the same as Eq. 9.10. Substituting Eq. 9.33 into Eq. 9.32 gives the ultrasonic propagation waves in a lubricant with the effect of diffraction only:

$$p = p_0 e^{-(\tau/T_0)^2}\, sin(\omega_0 \tau) - e^{-((\tau - \frac{a^2}{2c_0 z})/T_0)^2}\, sin(\omega_0(\tau - \frac{a^2}{2c_0 z})) \tag{9.34}$$

Figure 9.7 shows the amplitude of the fundamental frequency A_1 as a function of

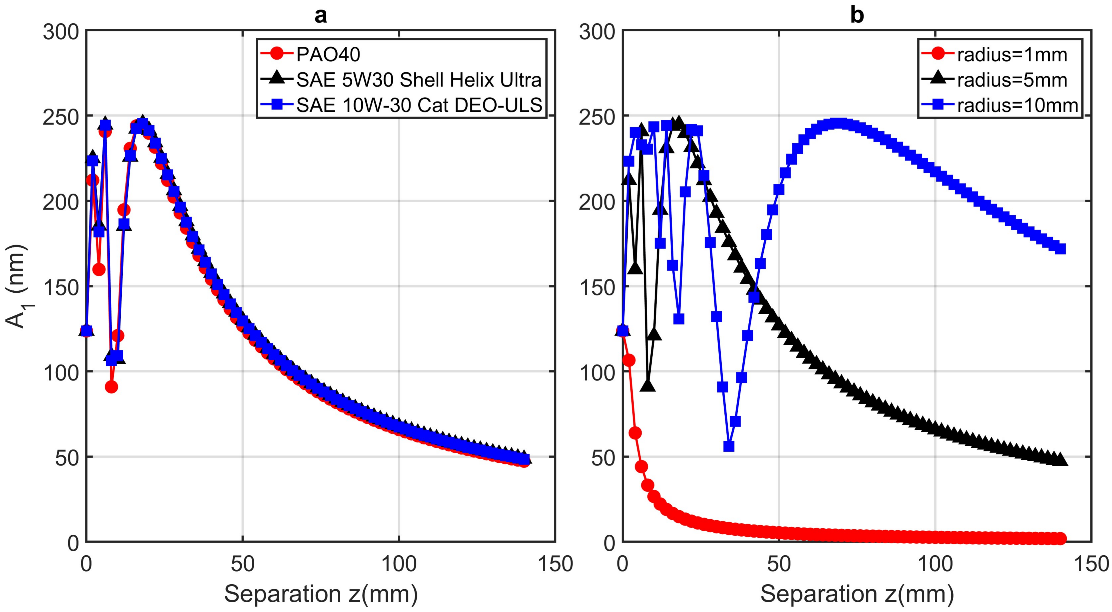

Figure 9.7: Variation of the ultrasonic wave as a function of separation distance considering the effect of diffraction: (a) at the shear rate of 1000 s^{-1} for PAO40, SAE 10W-30 Cat DEO-ULS and SAE 5W-30 Shell Helix Ultra; (b) different radius of the source.

the separation distance by considering the effect of diffraction using Eq. 9.34 with the excitation frequency of 1.02 MHz. In Figure 9.7a a fluctuation is seen up to a distance of Z_n for PAO40, SAE 10W-30 Cat DEO-ULS and SAE 5W-30 Shell Helix Ultra (see Table 10.1).

This distance for PAO40 with the centre frequency of 1.02 MHz and the radius of transducer of 5 mm is 17.8 mm. As the wave propagated further from the source, there was fluctuation. This fluctuation indicates an unsteady sound beam. This fluctuation depends on the speed of the sound in the lubricant, the peak frequency of the excitation, the amplitude of the excitation and the radius of the ultrasonic transducer. As the radius of the transducer increased, the distance of Z_n increased; therefore, the fluctuation of the ultrasonic beam appeared over a longer distance (Figure 9.7b). Although the transducer with the smaller radius generated a more steady sound beam over the distance of Z_n, the energy generated with this transducer might not be sufficiently large for wave propagation over the distance of 50 mm.

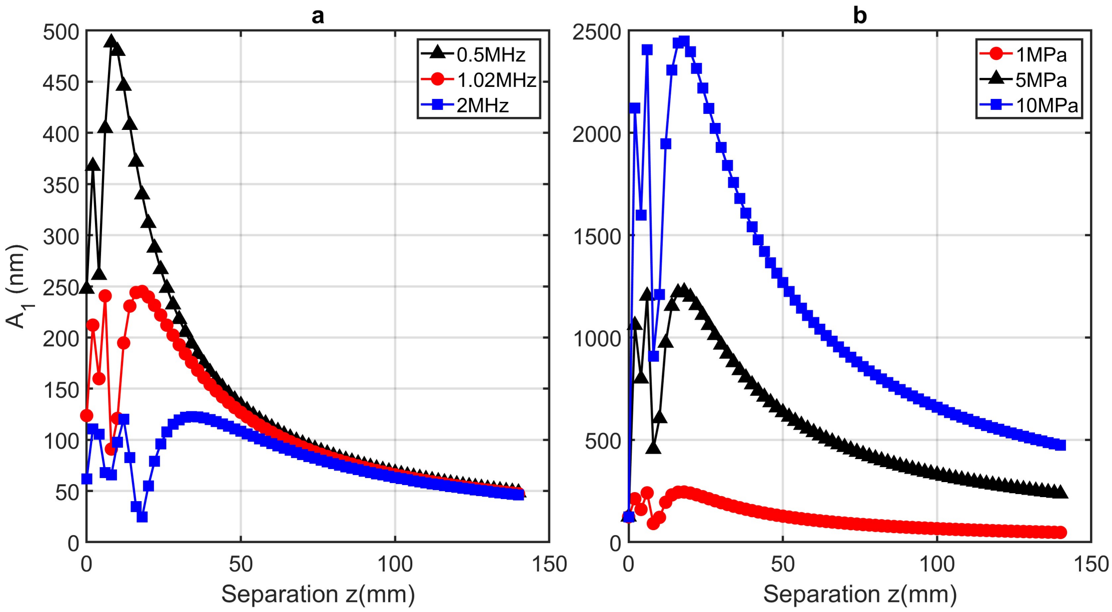

Figure 9.8: Variation of the ultrasonic wave as a function of separation distance considering the effect of diffraction: (a) different excitation frequency; (b) different excitation amplitude.

Figure 9.8a shows the variation in the amplitude of the fundamental frequency A_1 versus the separation distance of PAO40 with a peak frequency of 0.5 MHz, 1.02 MHz and 2 MHz, the excitation amplitude of 1 MPa and the transducer radius of 5 mm. The distance Z_n is determined using Eq. 9.1, which was 8.42 mm, 17.18 mm, and 33.69 mm for 0.5 MHz, 1.02 MHz and 2 MHz, respectively. The higher the excitation frequency, the longer the Z_n distance and the longer propagation distance required for the waves to become steady.

Figure 9.8b shows the effect of the excitation amplitude on the amplitude of the fundamental frequency A_1, considering only the diffraction. The distance Z_n was independent of the amplitude of excitation, and the waves became steady at the end of the distance of Z_n.

9.2.4 Effect of absorption and nonlinearity

There are a few analytical solutions to solve the KZK equation, which they neglect the term diffraction or absorption to be able to solve it, which is mainly solved numerically. In the correct study, an analytical solution for the KZK equation was used for its simplicity and accuracy compared to the numerical models. The Burgers equation is the KZK equation (Eq. 9.3) neglecting the diffraction term and its integration with respect to the retarded time τ [28, 96]:

$$\frac{\partial p}{\partial z} = \frac{\delta}{2c_0^3}\frac{\partial^2 p}{\partial \tau^2} + \frac{\beta p}{\rho_0 c_0^3}\frac{\partial p}{\partial \tau} \tag{9.35}$$

For a mono-frequency sinusoidal excitation given by:

$$p(0,t) = p_0 \, sin(\omega_0 t) \tag{9.36}$$

In the sake of simplicity, the following dimensionless variables are defined [28]:

$$\Phi = \frac{p}{p_0} \quad ; \quad \sigma = \frac{\beta \omega_0 p_0}{\rho_0 c_0^3} z \quad ; \quad \theta = \omega_0 \tau \quad ; \quad \Gamma = \frac{2\beta p_0}{\rho_0 \omega_0 \delta} \tag{9.37}$$

where Γ is the Gol'dberg number. Substituting of the dimensionless variables Eq. 9.37 into Eq. 9.35 gives [28]:

$$\frac{\partial \Phi}{\partial \sigma} - \frac{1}{\Gamma}\frac{\partial^2 \Phi}{\partial \theta^2} = \Phi \frac{\partial \Phi}{\partial \theta} \tag{9.38}$$

The general solution of Eq. 9.38 gives [28]:

$$\Phi(\sigma,\theta) = \frac{2}{\Gamma}\frac{\zeta_\theta}{\zeta} \tag{9.39}$$

where ζ_θ and ζ are defined by [28]:

$$\zeta_\theta = \frac{\partial \zeta}{\partial \theta} \tag{9.40}$$

$$\zeta(0,\theta) = \left(\frac{\Gamma}{4\pi\sigma}\right)^{\frac{1}{2}} \int_{-\infty}^{\infty} \zeta(0,\theta') exp\left[\frac{\Gamma(\theta-\theta')^2}{4\sigma}\right] d\theta' \tag{9.41}$$

$$\zeta(\sigma,\theta') = exp\left[\frac{\Gamma}{2}\int_{-\infty}^{\theta'} \Phi(0,\theta'')d\theta''\right] \tag{9.42}$$

using the dimensionless parameter Φ (Eq. 9.37) into the source (Eq. 9.36) [28]:

$$\Phi(0,t) = sin\theta \tag{9.43}$$

In order to derive ζ, Eq. 9.43 is substituted into Eq. 9.42 [28]:

$$\zeta(0,\theta) = exp\left[\frac{\Gamma}{2}\int_{-\infty}^{\theta'} sin\theta\right] d\theta = exp(\frac{-\Gamma}{2}cos\theta) \tag{9.44}$$

The transient effect of the ultrasonic waves disappears due to the absorption of the lubricant liquid, so the terms containing the lower limit of the integral are equal to zero [28]. Eq. 9.44 is substituted into Eq. 9.41 [28]:

$$\zeta = \left(\frac{\Gamma}{4\pi\sigma}\right)^{\frac{1}{2}} \sum_{n=-\infty}^{\infty} (-1)^n I_n(\frac{1}{2}\Gamma)e^{jn\theta} \int_{-\infty}^{\infty} exp\left[jn\theta' - \frac{\Gamma(\theta-\theta')^2}{4\sigma}\right] d\theta'$$

$where \quad I_{-n} = I_n$

$$\zeta = I_0(\frac{1}{2}\Gamma) + 2\sum_{n=1}^{\infty}(-1)^n I_n(\frac{1}{2}\Gamma)e^{-n^2\frac{\sigma}{\Gamma}}cos(n\theta) \tag{9.45}$$

where I_n is the modified Bessel function. Substituting of Eq. 9.45 into Eq. 9.39 gives [28]:

$$p = p_0\frac{4\Gamma^{-1}\sum_{n=1}^{\infty}(-1)^{n+1}nI_n(\frac{1}{2}\Gamma)e^{-n^2\frac{\sigma}{\Gamma}}sin(n\omega\tau)}{I_0(\frac{1}{2}\Gamma) + 2\sum_{n=1}^{\infty}(-1)^n I_n(\frac{1}{2}\Gamma)e^{-n^2\frac{\sigma}{\Gamma}}cos(n\omega\tau)} \tag{9.46}$$

Eq. 9.46 is an odd function of time and can be written as [28]:

$$p(z,\tau) = p_1 + p_2 + ... \tag{9.47}$$

where

$$p_1 = p_0 B_1(z)\ sin(w_0\tau) \tag{9.48}$$

$$p_2 = p_0 B_2(z)\ sin(2w_0\tau) \tag{9.49}$$

For $\Gamma < 1$, Eq. 9.46 can be expanded directly using the Taylor series (Keck-Beyer solution) [28]:

$$I_n(\frac{1}{2}\Gamma) \sim \frac{\Gamma^n}{2^{2n}n!}\left(1 + \frac{\Gamma^2}{8(2n+1)} + \frac{\Gamma^4}{64(5n+1)} + ...\right) \tag{9.50}$$

Substituting Eq. 9.50 into Eq. 9.46 gives the first two Fourier coefficients [28, 125, 126]:

$$B_1 = e^{-\alpha_1 z} - \frac{1}{32}e^{-\alpha_1 z}(1 - e^{-\alpha_2 z})^2 + O(\Gamma^4) \tag{9.51}$$

$$B_2 = \frac{1}{4}\Gamma(e^{-\alpha_2} - e^{-2\alpha_2 z}) + O(\Gamma^3) \tag{9.52}$$

where O(Γ) is error, $\alpha_1 = \frac{\delta\omega_1^2}{2c_0^3}$ and $\alpha_2 = \frac{\delta\omega_2^2}{2c_0^3}$ are the thermoviscous attenuation coefficients for the fundamental frequency and second-order harmonics [28]. Substituting the Gol'dberg number Γ (Eq. 9.32) into Eqs. 9.51 and 9.52 followed by Eqs. 9.48 and 9.49 gives:

$$p_1 = p_0 \left(e^{-\alpha_1 z} - \frac{1}{32} \left(\frac{2\beta p_0}{\rho_0 \omega_0 \delta} \right)^2 e^{-\alpha_1 z} (1 - e^{-\alpha_2 z})^2 \right) sin(w_0 \tau) \tag{9.53}$$

$$p_2 = \frac{1}{2} \frac{\beta p_0^2}{\rho_0 \omega_0 \delta} (e^{-\alpha_2 z} - e^{-2\alpha_2 z}) sin(2 w_0 \tau) \tag{9.54}$$

It should be noted that the errors are ignored for simplicity in Eqs. 9.53 and 9.54. Substituting Eqs. 9.53 and 9.54 into Eq. 9.47 gives:

$$\begin{aligned} p =& p_0 \left(e^{-\alpha_1 z} - \frac{1}{32} \left(\frac{2\beta p_0}{\rho_0 \omega_0 \delta} \right)^2 e^{-\alpha_1 z} (1 - e^{-\alpha_2 z})^2 \right) sin(w_0 \tau) + \\ & \frac{1}{2} \frac{\beta p_0^2}{\rho_0 \omega_0 \delta} (e^{-\alpha_2 z} - e^{-2\alpha_2 z}) sin(2 w_0 \tau) \end{aligned} \tag{9.55}$$

The Gol'dberg number Γ for the lubricants used in the current study (listed in Tables

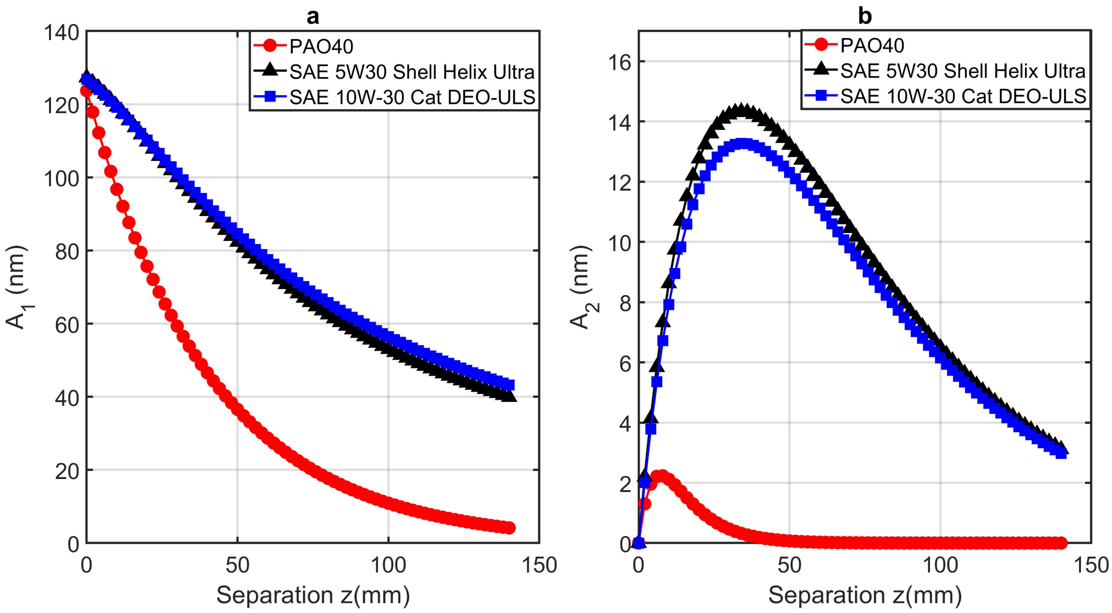

Figure 9.9: Analytical model based on the Burgers equation considering the effect of absorption and nonlinearity for PAO40, SAE 10W-30 Cat DEO-ULS and SAE 5W-30 Shell Helix Ultra: (a) amplitude of fundamental frequency A_1; (b) amplitude of second-order harmonic A_2.

10.1 and 11.1 and Figure 10.6) for the frequency of excitation greater than 100 KHz and amplitude of excitation up to 10 MPa is less than 1. Therefore, Eq. 9.55 can be used for analytical analysis. The amplitude of the fundamental frequency A_1 and the second-order harmonic A_2 for the lubricants PAO40, SAE 10W-30 Cat DEO-ULS and SAE 5W-30 Shell Helix Ultra at the peak frequency 1.02 MHz and amplitude of excitation of 1 MPa is shown in Figure 9.9.

It is seen from Figure 9.9a that the amplitude of the fundamental frequency decreased monotonically as the waves propagated further in the lubricant. This amplitude depended on the lubricants' shear viscosity, where the absorption was higher in PAO40 with a higher shear viscosity than SAE 10W-30 Cat DEO-ULS and SAE 5W-30 Shell Helix Ultra. The amplitude of the second-order harmonic A_2 initially increased due to the nonlinearity of the waves propagating from the source. However, absorption (only viscosity in the Burgers model (Eq. 9.55) overcame the nonlinearity. From the source to the distance Z_n, the amplitude of A_2 increased linearly (see Table 10.1) as the pressure term of absorption ($e^{-\alpha_2 z}$ and $e^{-2\alpha_2 z}$) was not large enough to attenuate the waves. However, as the waves propagated further from the distance Z_n, the term of sound pressure by absorption overcame the nonlinearity and A_2 decreased.

Figure 9.10 shows the effect of the excitation frequency on the wave propagation for PAO40. As the excitation frequency increased, the amplitude of the fundamental

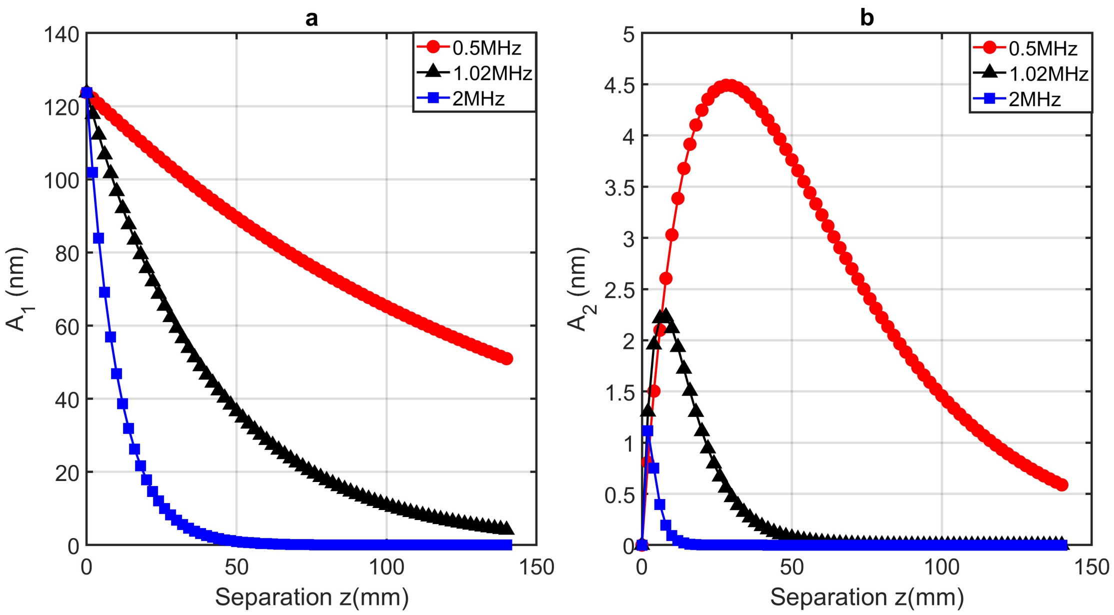

Figure 9.10: Analytical model based on the Burgers equation considering the effect of absorption and nonlinearity for PAO 40 at excitation frequencies 0.5 MHz, 1.02 MHz and 2 MHz: (a) amplitude of fundamental frequency A_1; (b) amplitude of second-order harmonic A_2.

frequency A_1 and the second-order harmonic decreased, indicating higher absorption in higher frequency.

Figure 9.11 shows the variation in the excitation amplitude in the amplitude of the fundamental frequency A_1 and the second-order harmonic A_2. As expected, the

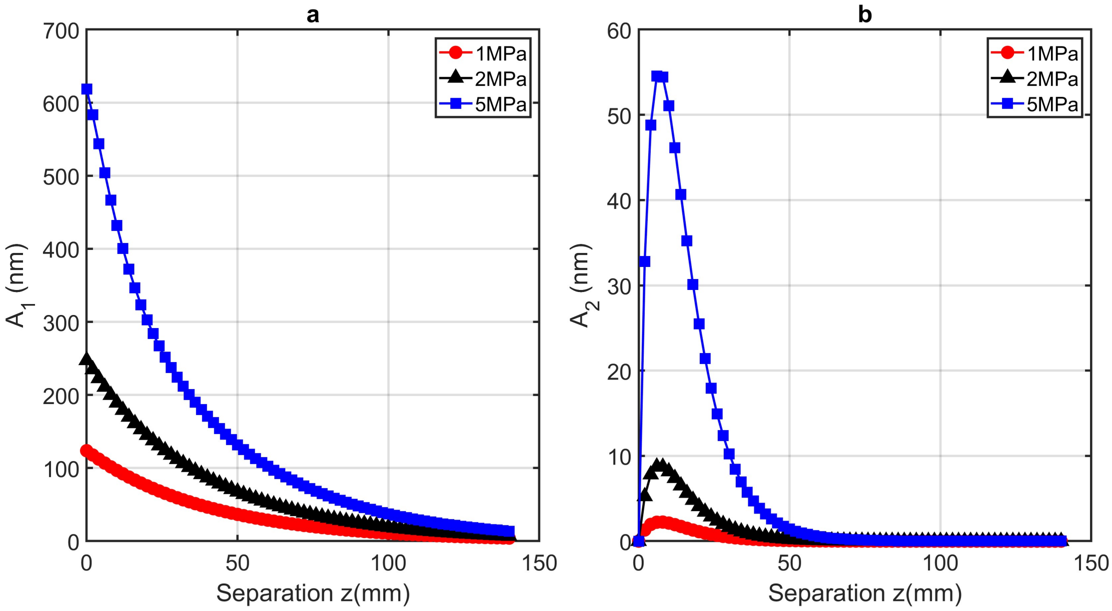

Figure 9.11: Analytical model based on the Burgers equation considering the effect of absorption and nonlinearity for PAO 40 at amplitude of excitation 1 MPa, 2 MPa and 5 MPa: (a) amplitude of fundamental frequency A_1; (b) amplitude of second-order harmonic A_2.

higher the amplitude of excitation, the higher the amplitudes of the fundamental frequency A_1 and the second-order harmonic A_2. It should be noted that the peak of A_2 was at a longer distance of 2 mm as the excitation amplitude varied.

9.3 Conclusion

In this chapter, an analytical solution of the ultrasonic waves propagating in a liquid lubricant was used. It was seen that as the high-power ultrasonic waves were propagated in liquids, the compression part travelled faster than the tensile part. This creates distortion in the ultrasonic waves, which were seen as higher-order harmonics in the frequency domain (using FFT). Three terms of the KZK equation (absorption, diffraction and nonlinearity) were considered separately to analyse their effects on ultrasonic waves. The attenuation term decreased the amplitude of the ultrasonic waves as they propagated further from the ultrasonic source in the liquid lubricants. Since only attenuation was considered, so no nonlinearity was generated. A comparison between three different lubricants showed that at the same excitation frequency and amplitude, PAO40 attenuated more than the engine oils SAE 10W-30 cat DEO-ULS and SAE 5W-30 Shell Helix Ultra. This is because the PAO40 is more viscous than the engine oils.

When only considering the effect of nonlinearity, the compression part travelled faster than the tensile part. The amplitude of the fundamental frequency was constant (as there was no attenuation), and the nonlinearity (the amplitude of the higher-order harmonic) increased. However, the amplitude increased to infinity, which is impossible in reality. Thus, the effect of attenuation was also considered. It was seen that the amplitude of fundamental frequency decreased monotonically (due to attenuation). Unlike the amplitude of fundamental frequency, the amplitude of the second-order harmonic increased as the wave propagated further from the ultrasonic source to a distance where the absorption overcame the generated ultrasonic pressure. After this distance, the amplitude of the second-order harmonic decreased and approached zero. It was seen that, at the same excitation frequency, the maximum amplitude of second-order harmonic for PAO40 at the excitation amplitudes of 1 MPa, 2 MPa and 5 MPa, the maximum amplitude of the second-order harmonic occurred at a further distance from the ultrasonic source (at 6 mm, 7 mm and 8 mm, respectively).

Then, the KZK equation was simplified to the Burgers equation by considering the effect of absorption and nonlinearity only as the analytical solution is available, and there is no need to use complicated numerical solutions. The effect of shear viscosity and excitation frequency showed a higher attenuation in the ultrasonic waves.

Chapter 10

Experimental Setup for Nonlinearity in Liquid Lubricants

This chapter describes the techniques and tools for experimentally measuring nonlinear longitudinal ultrasonic waves in liquid lubricants. Five fresh lubricants were contaminated with distilled water, iron and carbon powders, which are the most common materials in degraded oils. Similar to contact acoustic nonlinearity (CAN), a laser Doppler vibrometer was used to convert the ultrasound amplitude from voltage to length unit. However, the experimental setup was different, as the emitted laser beam could not be directly reflected from the surface of the liquid lubricants.

10.1 Introduction

Ultrasonic waves generated by an immersion transducer (emitter) have been captured by another immersion transducer using transmission, as shown in Figure 6.7c. In this technique, the emitter and receiver are placed in the lubricant, and the receiver captures the generated ultrasonic waves without reflecting from the boundaries. One of the advantages of using this method is that the captured signals contain information about the lubricant without any boundary interface.

10.2 Measuring apparatus and test lubricants

Figure 10.1 shows the experimental apparatus designed to capture transmitted signals through liquid lubricants. Figure 10.2 shows three containers with different diameters to detect ultrasonic waves in liquid lubricants. An immersion transducer (emitter) was placed at the bottom of the containers. It was sealed with a silicon paste to prevent any leakage. The second immersion transducer (receiver) was attached to a holder and

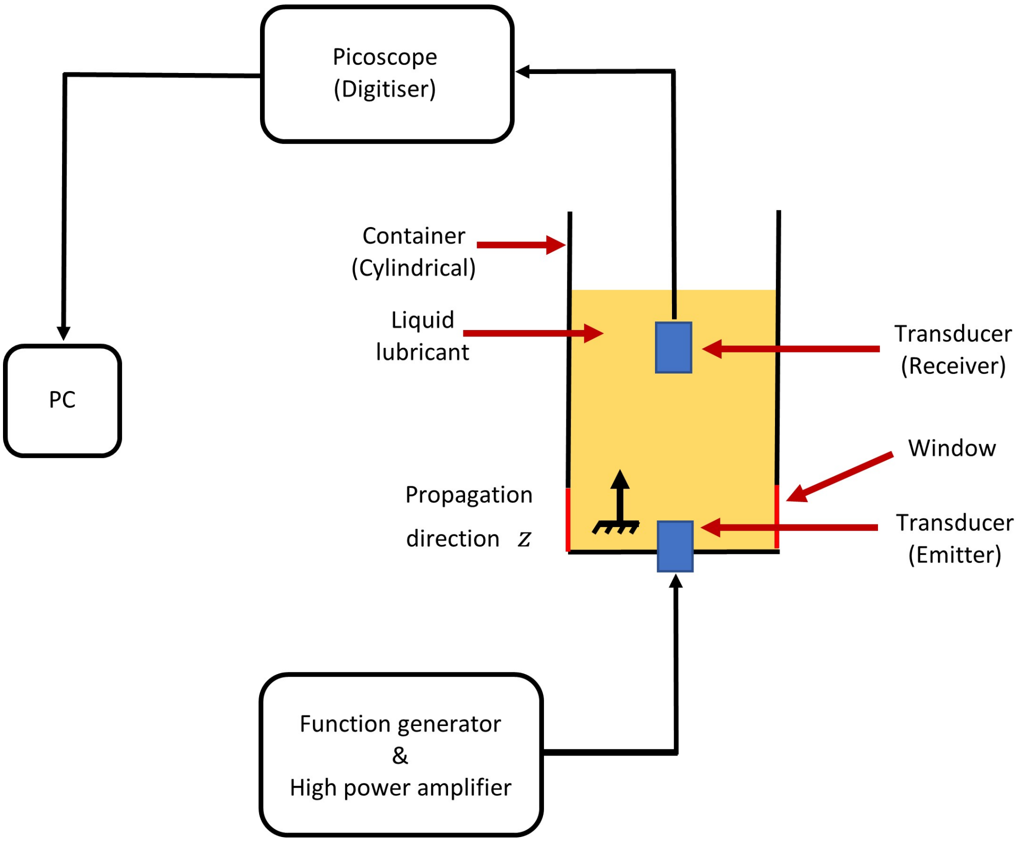

Figure 10.1: Schematic diagram of nonlinear coefficient measurement in liquid lubricant.

rod. The rod was connected to a loading mechanism to provide vertical movement for the receiver. The container was filled with liquid lubricants, and the receiver was fully immersed. The lubricants were slowly poured and remained stationary for 30 minutes to remove all air bubbles as they can be an external source of nonlinear ultrasonicity. To detect degradation and determine the nonlinearity, five fresh samples of liquid lubricants were used:

1. fresh polyalphaolefins: PAO40, PAO100 and PAO4+40 (mix of PAO4 and PAO40 by 1:1 ratio)
2. fresh SAE 5W-30 passenger car engine oil (SAE 5W-30 Shell Helix Ultra)
3. fresh SAE 10W-30 passenger car engine oil (SAE10W-30 Cat DEO-ULS)

These lubricants were used as PAO, a base oil for most engineering lubricants. SAE 5W-30 and SAE 10w-30 are common engine oils used for normal temperatures. This experiment used four artificially contaminated and degraded lubricants made of 5wt% iron powder, 5wt% distilled water and 5wt% carbon black (SAE10W-30 Cat DEO-ULS). The degraded SAE 10W-30 Cat DEO-ULS was fully degraded by real

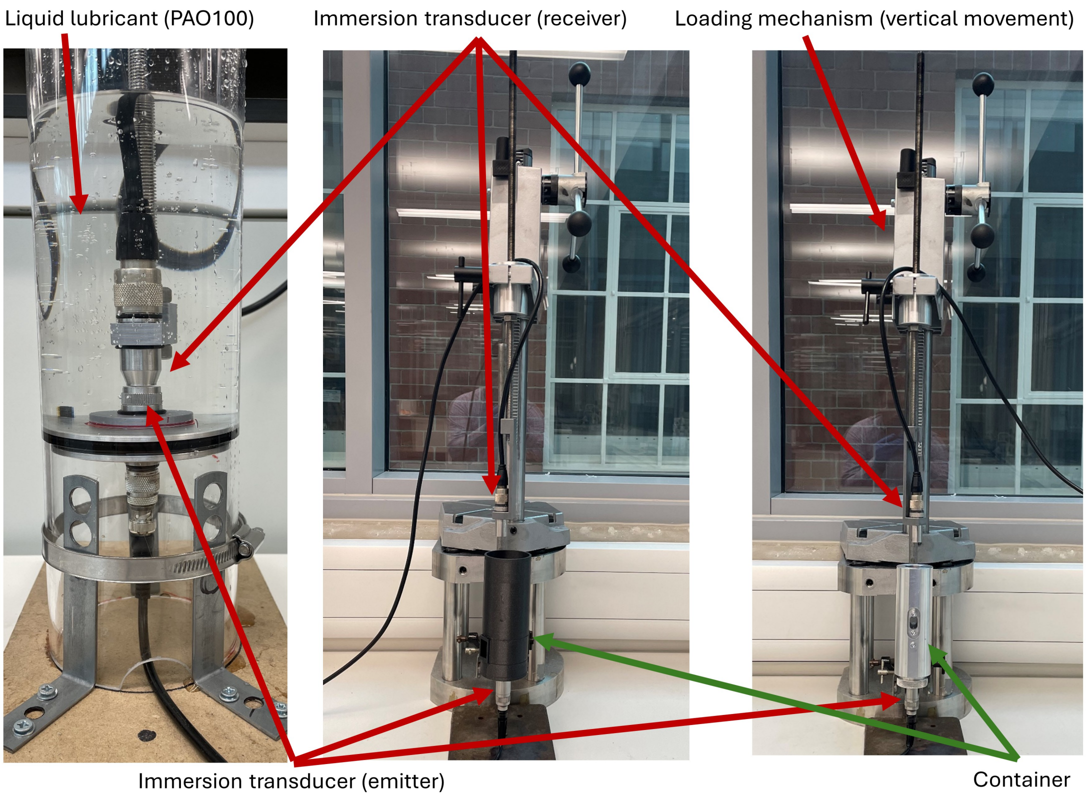

Figure 10.2: Experimental setup of the nonlinear coefficient measurement.

engine running. Figure 10.3 shows the substances used for artificially contaminated lubricants: 5wt% distilled water, iron powder with particle size 1-3 μm (supplied by Alfa Aesar with purity 98+%) and carbon black powder with particle size 4 μm (supplied by nanografi with purity 99.99%). This particle size remains in suspension

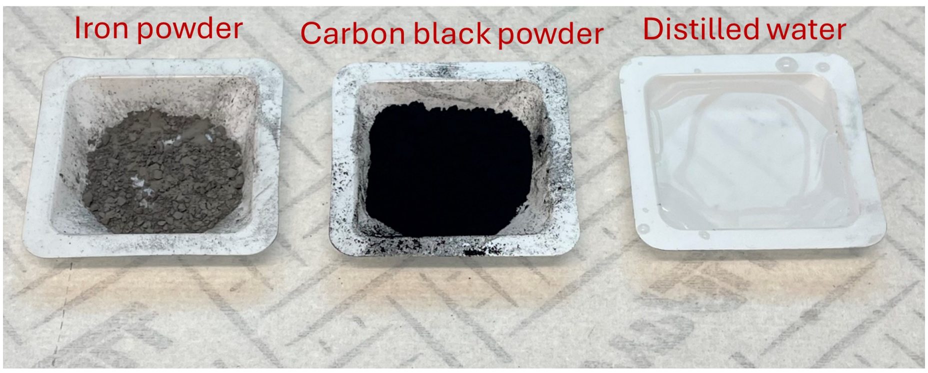

Figure 10.3: Substances used for artificial contamination.

longer than the bigger particle size so that the experiment can be carried out more accurately. A digital overhead stirrer (SciQuip Pro-40) was used at the lowest angular speed (50 rpm) for 30 minutes to make artificially contaminated lubricants, as shown in Figure 10.4. Figure 10.5 shows the fresh, degraded and artificially contaminated

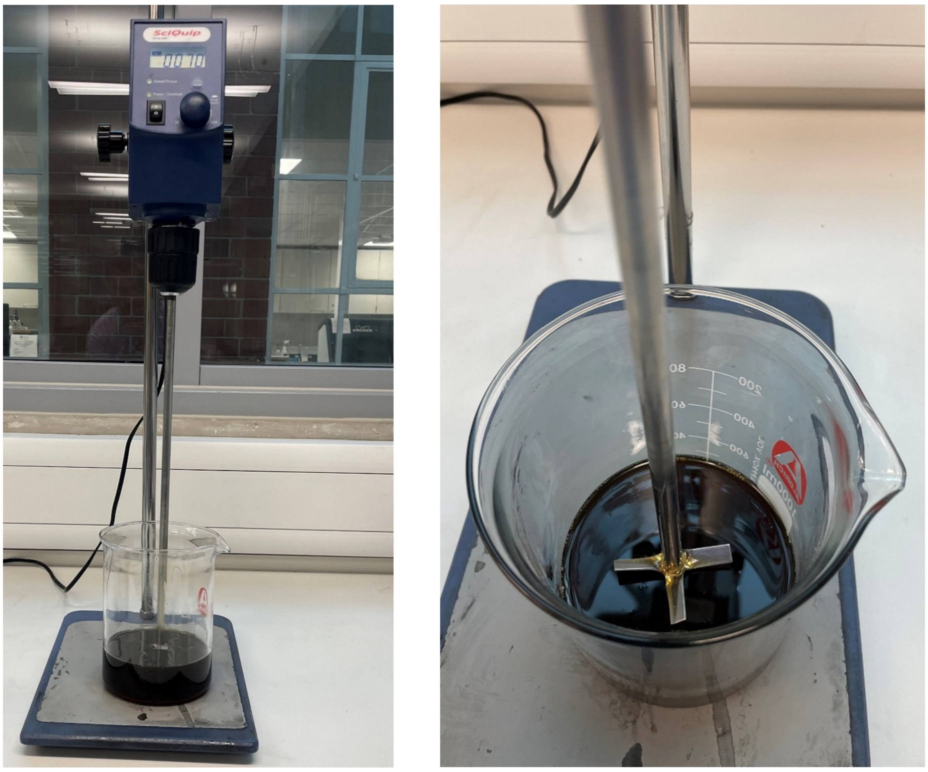

Figure 10.4: Digital overhead stirrer (SciQuip Pro-40) to make artificial degradation.

lubricants. The containers were cleaned with n-Heptane and left to dry. 250 ml of the oils was poured into the container at room temperature 23^oC. Figure 10.6 shows the shear viscosity of the lubricants on a logarithmic scale at temperature 23^oC measured using a rheometer (TA Instruments rheometer HR 10).

10.3 Instrumentation

Two piezoelectric longitudinal immersion transducers (10 mm diameter) with centre frequencies of 1 MHz and 2.25 MHz were used as the emitter and receiver (with peak frequencies of 1.02 MHz and 2.04 MHz). The bottom of the cylinder was screwed to the source transducer (emitter) to immerse the cylinder in liquid lubricant. The emitter was sealed using a silicone sealant. The second transducer was attached to a vertical translational motion. The propagation direction was the z direction. At $z = 0$, the separation between the emitter and receiver was zero. The vertical motion mechanism separates the transducers in steps of 2 mm from zero to 110 mm. This

Figure 10.5: Lubricant samples: (**a**) PAO 4+40; (**b**) PAO 40; (**c**) PAO 100 (**d**) SAE 10W-30 Cat DEO-ULS; (**e**) SAE 5W-30 Shell Helix Ultra; (**f**) degraded SAE 10W-30 Cat DEO-ULS ; (**g**) SAE 10W-30 Cat DEO-ULS contaminated by 5wt% distilled water; (**h**) SAE 10W-30 Cat DEO-ULS contaminated by 5wt% iron powder; (**i**) SAE 10W-30Cat DEO-ULS contaminated by 5wt% carbon black.

distance is almost 1.5 times larger than the Rayleigh distance Z_r to ensure that the waves do not reflect from the lubricant-air interface or interfere with the propagated signals (see Table 10.1). Four windows were placed on the sides of the cylinders to ensure that the transducers were aligned and their faces were parallel.

A 1.02 MHz longitudinal with twenty-tone burst cycles at different peak voltages of 22 V, 45 V, 67 V, 90 V and 144 V were generated and amplified using a high-power amplifier (RITEC RAM-5000). The number of cycles was large enough to generate steady state behaviour [127] and contained sufficient energy to create higher-order harmonics. In this study, the number of tone burst cycles was investigated. This

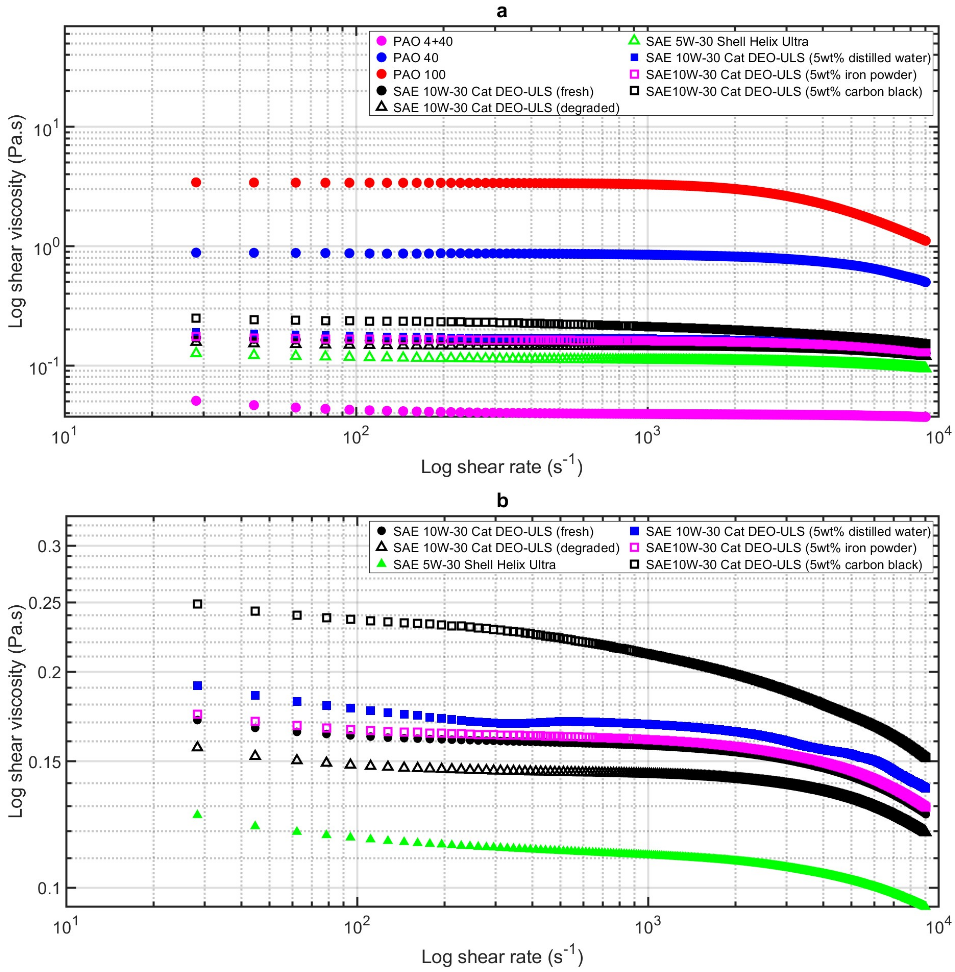

Figure 10.6: Shear viscosity of liquid lubricants at room temperature: (a) all the lubricants; (b) zoomed-in plot of (a).

number was influenced by the viscosity of the liquid lubricants. For example, for an amplitude lower than 15 V in PAO40, the least minimum number of cycles to generate higher harmonics was 10 cycles. The excitation amplitude below 3 V, even with a greater number of tone burst cycles, was not large enough for the distances further in the near-field to generate higher-order harmonics. The signals transmitted in the liquid lubricants were captured with the receiver with a peak frequency of 2.04 MHz and stored using a digital oscilloscope. A PC equipped with LabVIEW was employed to trigger the pulsing and receive the digitised transmitted signals.

The peak frequency of the transducers might be slightly different from the nominal ones. In order to maximise generated signals, they are required to excite at their peak frequencies. To do this, the function generator generated a two-tone burst cycle sinusoidal ultrasonic wave in the bandwidth of -3 dB. In this bandwidth, any frequency that generates the maximum amplitude is considered the peak frequency. The peak frequency of the transducers used in this study was 1.02 MHz for the emitter and 2.04 MHz for the receiver.

10.4 Speed of sound

The time-of-flight (TOF) of the signals for separation was measured from 0 mm to 60 mm by a step of 4 mm. The separation of each lubricant was plotted against TOF. The slope of the graphs gives the speed of sound at the ambient pressure of the lubricants, as shown in Figure 10.7.

Table 10.1 shows the speed of sound, Z_n distance and Rayleigh distance Z_r of the lubricants at room temperature measured using time of flight, Eqs. 9.1 and 9.2.

Table 10.1: Speed of sound, Z_n distance and Rayleigh distance Z_r of the lubricants at room temperature.

Lubricant	Speed of sound $c_0(m.s^{-1})$	$Z_n(mm)$	$Z_r(mm)$
PAO40	1484	17.18	53.98
PAO100	1501	16.99	53.37
PAO4+40	1429	17.84	56.06
Distilled water	1498	17.02	53.48
SAE 5W-30 Shell Helix Ultra (fresh)	1442	17.68	55.55
SAE 10W-30 Cat DEO-ULS (fresh)	1448	17.61	55.23
SAE 10W-30 Cat DEO-ULS (degraded)	1460	17.46	54.87
SAE 10W-30 Cat DEO-ULS (5wt% iron)	1442	17.68	55.55
SAE 10W-30 Cat DEO-ULS (5wt% carbon black)	1457	17.50	54.98
SAE 10W-30 Cat DEO-ULS (5wt% distilled water)	1456	17.51	55.02

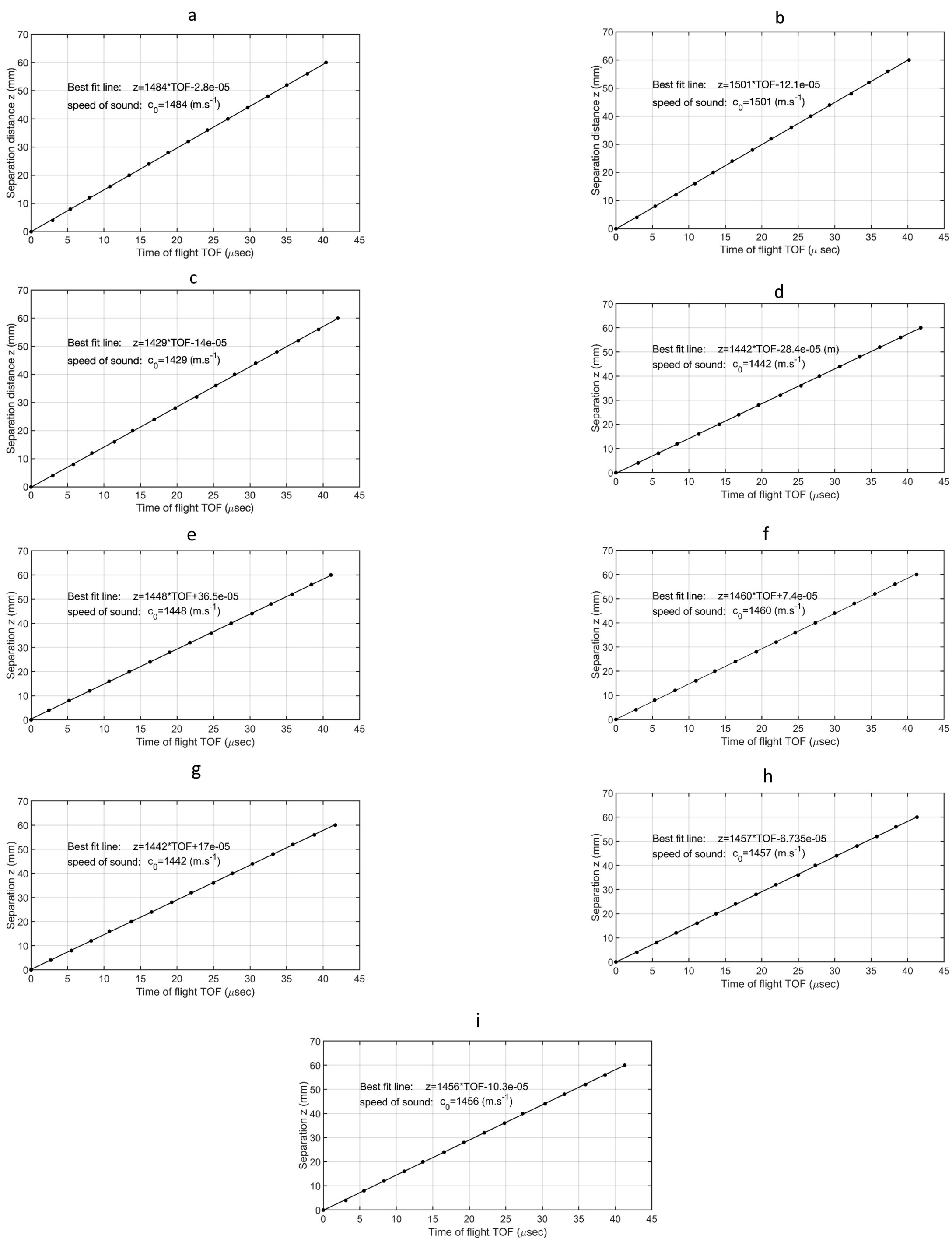

Figure 10.7: Speed of sound in: (a) PAO 40; (b) PAO 100; (c) PAO4+40; (d) SAE 5W-30 Shell Helix Ultra (fresh); (e) SAE 10W-30 Cat DEO-ULS (fresh); (f) SAE 10 W-30 Cat DEO-ULS (degraded); (g) SAE 10W-30 Cat DEO-ULS (5Wt% iron); (h) SAE 10W-30 Cat DEO-ULS (5Wt% carbon black); (i) SAE 10W-30 Cat DEO-ULS (5Wt% distilled water).

10.5 Laser Doppler vibrometer: voltage-to-length unit conversion

Similar to CAN (Section 6.16), the nonlinear coefficient β is required a voltage-to-length unit conversion. Figure 10.8 shows the setup of the laser Doppler vibrometer for the conversion. The laser head had to be placed vertically to emit the beam along the ultrasonic propagation direction. The laser beam did not reflect from the surface of the liquid lubricant (Figure 10.8a). Therefore, a thin shiny solid film (steel) with a thickness of 50 μm was placed on the surface of the lubricant to move freely (Figure 10.8c). The reflected laser beam was captured by the laser head. Figure 10.9

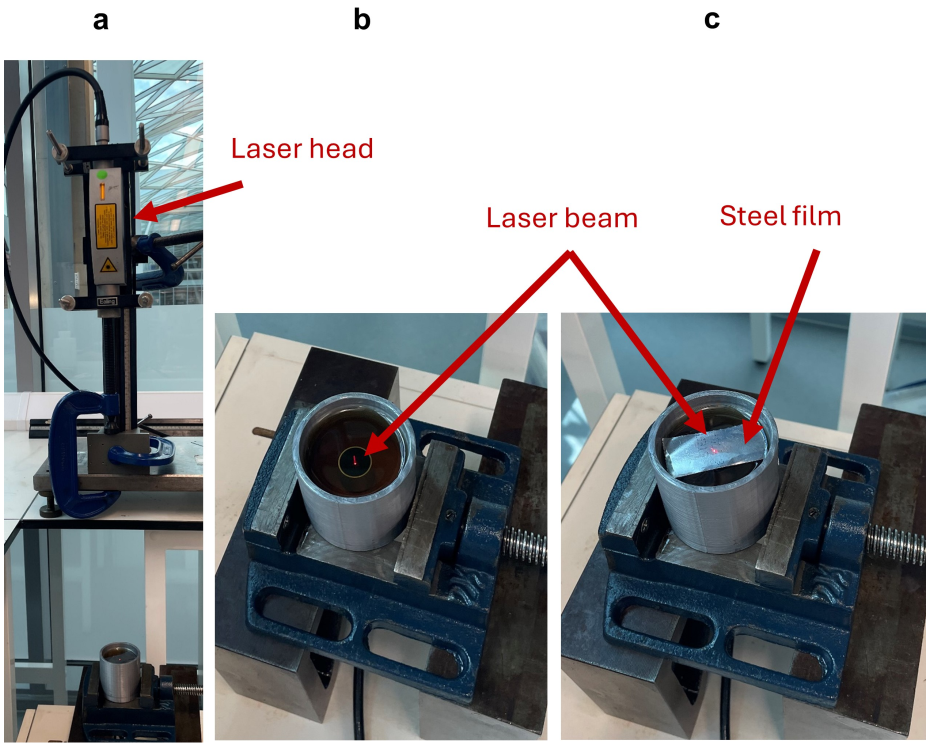

Figure 10.8: Laser Doppler vibrometer setup.

shows a schematic diagram of the laser Doppler vibrometer for conversion. First, ultrasonic waves at excitation voltages 22 V to 216 V in 6 equal increments at peak frequency 1.02 MHz were propagated in the liquid lubricant and captured by the receiver at different separation distances (as shown in Figure 10.9a). Although ultrasonic waves were generated at the same separation distances, excitation voltages and peak frequency, a laser beam was incident on the steel film. It reflected from the steel film to capture the displacement generated by the emitter (as shown in Figure 10.9b). The waves captured with the laser at each excitation voltage contained both

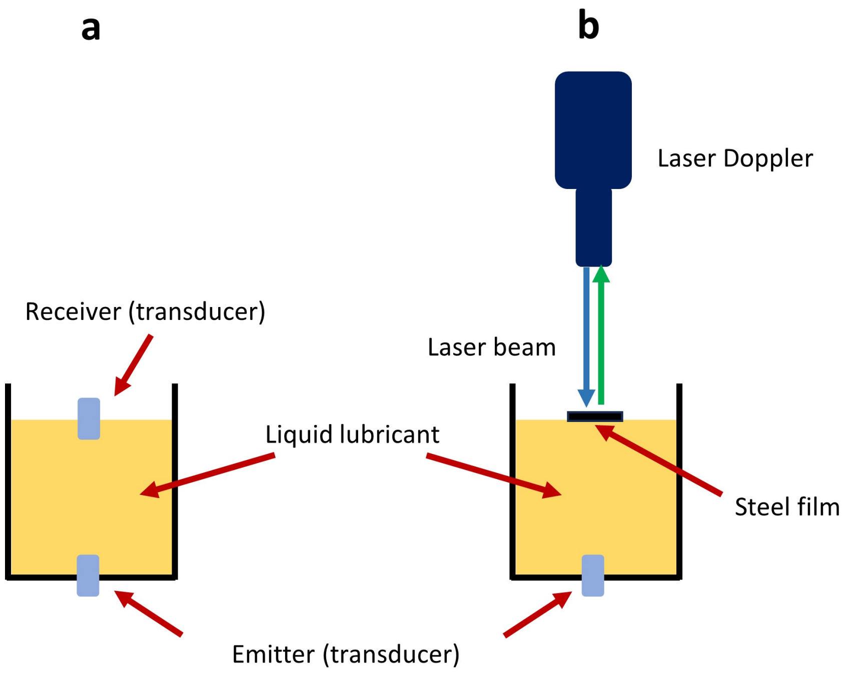

Figure 10.9: Schematic diagram of voltage-to-meter conversion apparatus: (a) ultrasound; (b) laser Doppler vibrometer.

the fundamental frequency and the second-order harmonic. These amplitudes were plotted against the amplitude of the corresponding frequencies captured by the ultrasonic receiver, as shown in Figure 10.10. The slope of the curves of the fundamental

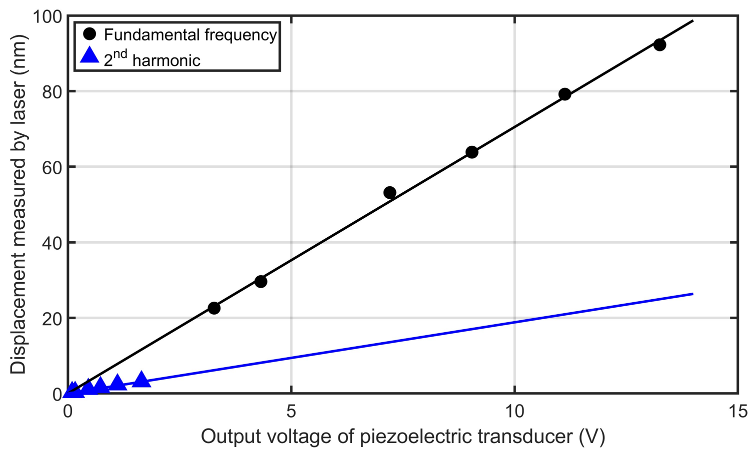

Figure 10.10: Voltage-to-meter conversion at ultrasonic incident amplitude 22 V to 216 V.

frequency and second-order harmonic give voltage-to-meter conversions:

$$\frac{A_2}{A_1^2}(m^{-1}) = \frac{\delta_2}{\delta_1^2}\frac{A_2}{A_1^2}(V^{-1}) \tag{10.1}$$

where δ_1 and δ_2 are the conversion for the fundamental frequency and second-order harmonic, respectively. Eq. 10.1 is substituted into Eq. 9.20 to give the nonlinear coefficient β.

10.6 Conclusion

In this chapter, the experimental setup required for the nonlinear coefficient of liquid lubricants is presented. Different liquid lubricants were used and artificially contaminated with water, iron and carbon powder. These are the main sources of lubricant degradation. The viscosity of the liquid lubricants was measured at a temperature of 23^{o}C using a rheometer (TA Instruments rheometer HR 10). The speed of sound in all lubricants was measured to determine the near-field distance and the nonlinear coefficient in Chapter 11. In addition, as the ratio $A_2/{A_1}^2$ is in metre units, the laser Doppler vibrometer was used to determine the reflected ultrasonic waves.

Chapter 11

Oil Degradation and Contamination Detection using Nonlinear Behaviour of Ultrasound

This chapter describes the techniques and tools to measure nonlinear longitudinal ultrasonic waves in liquid lubricants experimentally. Five fresh lubricants were contaminated with distilled water, iron and carbon powders. These substances are the most common materials in degraded oils. Different parameters were investigated, such as the amplitude of excitation, the viscosity of the lubricants, and the effect of the distance between the ultrasonic source and the receiver. Similar to contact acoustic nonlinearity (CAN), a laser Doppler vibrometer was used to convert the ultrasound amplitude from voltage to length unit. However, the experimental setup was different, as the emitted laser beam could not be directly reflected from the surface of the liquid lubricants. A similar signal processing principle and procedure used for CAN was also applied here.

11.1 Signal Processing

The same principle and procedure of signal processing used for CAN (Section 6.15) was applied here. Figure 11.1 shows the signals captured by the receiver at separations 0 mm and 40 mm in fresh SAE 10W-30 Cat DEO-ULS at the temperature of 23^oC. Figures 11.1a and 11.1d show the signals in the time domain (the average of the first 1000 transmitted signals). When the separation distance between the emitter and receiver was less than the distance equivalent to the multiple of wavelength and the number of tone burst cycles of the ultrasonic waves, some of the waves reflected from the receiver and interfered with the upcoming waves (Figure 11.1a). As the

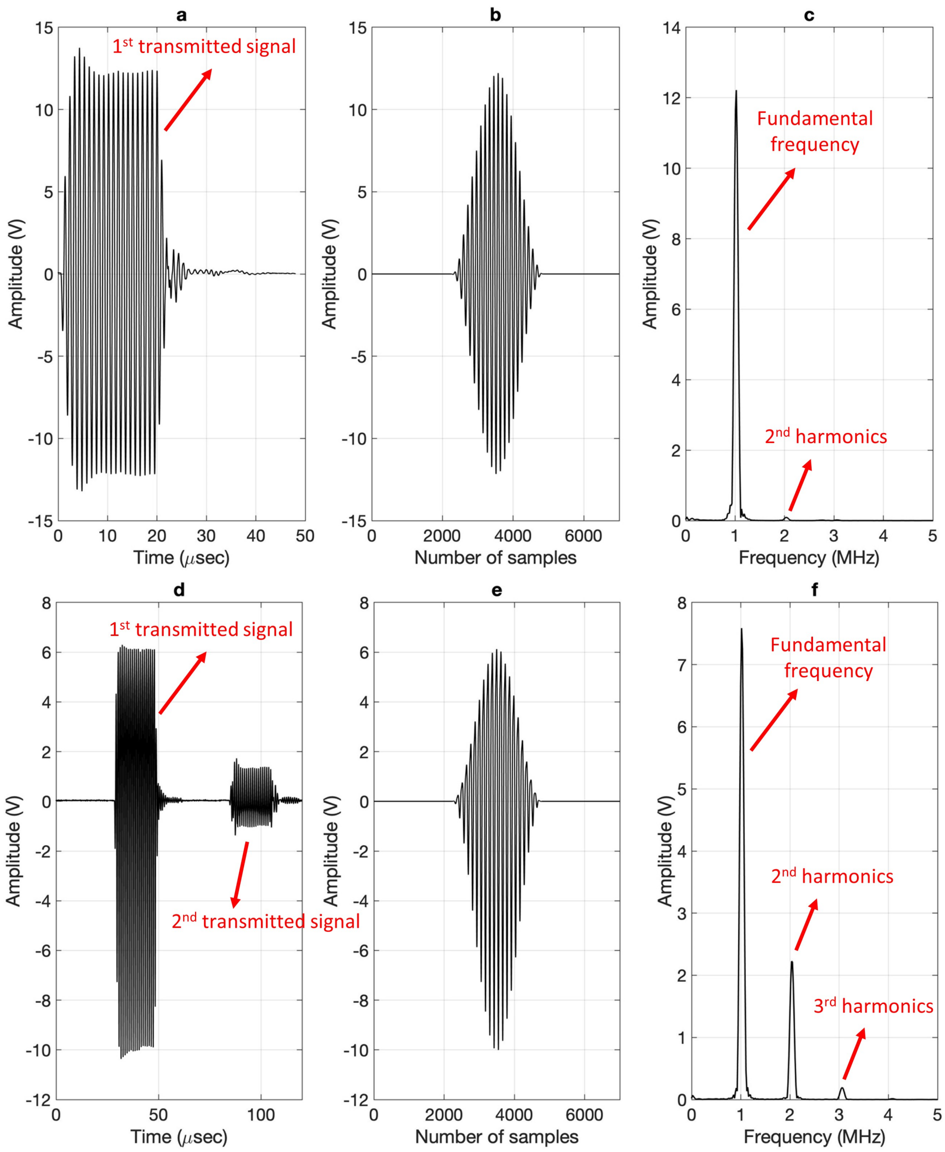

Figure 11.1: Signal processing of the transmitted pulses in fresh SAE 5W-30 Shell Helix Ultra using a 90 V excitation amplitude and frequency 1.02 MHz: (a-c) separation 0 mm (the emitter and receiver are in touch and there is no separation between them); (d-f) separation 40 mm; (a,d) time domain of transmitted signals; (b,e) Hanning window and zero pad results of the transmitted signals; (c,f) FFT of the transmitted signals.

transducers separated further, the reflected waves of the receiver did not influence the propagating waves, as shown in Figure 11.1d. Only the first signal was considered as it contains more valuable information about the lubricants. This signal was then extracted, and a Hanning window function and a zero pad function were applied to increase the resolution of the pulses (Figures 11.1b and 11.1e). To extract data at each frequency, FFT was used to convert the time domain to the frequency domain (Figures 11.1c and 11.1f). The peaks indicates the amplitude of the fundamental frequency A_1 and higher-order harmonics (A_2, A_3 and etc.). It should be noted that the separation was the distance between the emitter and the receiver. This distance began from zero (when the emitter and receiver were in touch) and increased in steps of 2 mm. Figure 11.1c shows the preface of a very small second-order harmonic at the separation 0 mm (without lubricant). This was due to the nonlinearity of other sources in addition to the liquid lubricant, such as transducers and amplifier circuitry [2, 128, 45]. The amplitude of the second-order harmonic was less than -40 dB of the fundamental frequency. This was sufficiently small to allow the nonlinearity generated by all other sources to be ignored [128]. The amplitude of the fundamental frequency A_1 and the second-order harmonic A_2 were substituted into Eq. 9.20 to determine the nonlinear coefficient β [121]. It should be noted that A_1 and A_2 shown in Figure 11.1 were in units of voltage, while they were in units of Pa or metre in Eqs. 9.18 and 9.20, respectively.

11.2 Effect of near- and far-field zones on the nonlinearity in liquid lubricants

To investigate how ultrasonic nonlinearity varies as the waves propagate in the liquid lubricants, the receiver was separated from the emitter with a distance increment size of 2 mm, as shown in Figure 11.2. In the time-domain signals (Figures 11.2a-d), as the wave propagated in the liquid lubricant further from the ultrasonic source (emitter), the distortion increased. This distortion appeared as higher-order harmonics in the frequency domain, as shown in Figures 11.2e-h. When the ultrasonic waves propagated a distance of 16 mm from the emitter, a third-order harmonic was generated (Figure 11.2a). However, for the propagation of 40 mm, 54 mm and 100 mm, up to the fifth-order harmonic was generated, which indicates the increase of nonlinearity in the ultrasonic waves. In addition, the amplitude of the higher-order harmonic increased up to 54 mm and then decreased, while the amplitude of the fundamental frequency decreased as the wave propagated further in the lubricants. The decrease in the amplitude of fundamental and higher-order harmonics was due to the effect of attenuation.

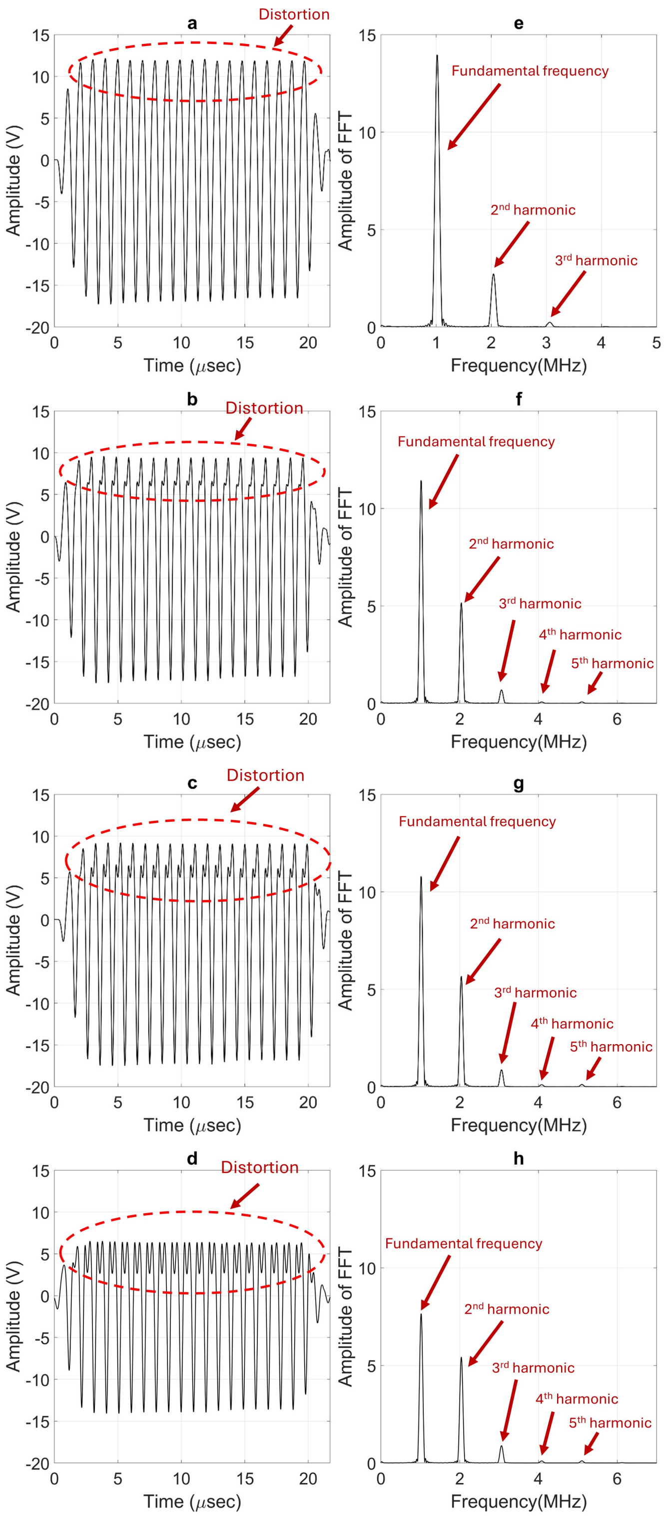

Figure 11.2: The propagation distance effect on the nonlinearity of ultrasonic wave in PAO40: (a-d) time domain; (e-h) FFT; (a,e) 16 mm; (b, f) 40 mm; (c, g) 50 mm; (d, h) 100 mm separation.

11.3 Effect of viscosity on linear and nonlinear ultrasound

Figure 11.3 shows A_1 and A_2 for PAO40 and PAO100 against the separation distance at excitation amplitude 144 V. The amplitude of fundamental frequency A_1 for both PAO40 and PAO100 decreased monotonically as the separation distance from the receiver and the ultrasonic source increased (as shown in Figure 11.3a). This attenuation was due to the effect of the viscosity of the lubricants [28]. The shear viscosity of PAO100 is higher than that of PAO40 (PAO100 attenuates more than PAO40). Therefore, A_1 of PAO100 was less than PAO40. It can be seen in Figure

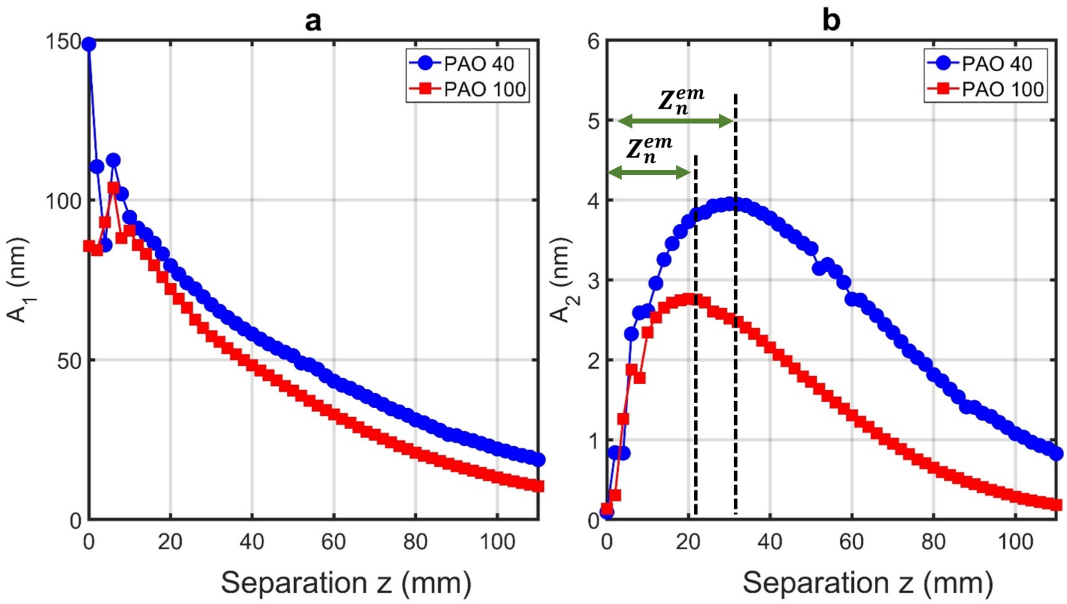

Figure 11.3: The effect of nonlinearity, absorption and diffraction in the near- and far-field regions for PAO40 and PAO100 on the: (a) amplitude of fundamental frequency A_1; (b) amplitude of the second-order harmonic A_2.

11.3b that the behaviour of A_2 is different from that of A_1. Let us introduce Z_n^{em}, which is defined as the distance from the ultrasonic source to the peak of A_2. When ultrasonic waves propagated from the ultrasonic source to Z_n^{em}, the distortion of the wave increased exponentially until it reached the maximum value. The ultrasonic energy overcame the effect of attenuation (viscosity). Therefore, the distortion of A_2 increased exponentially. If the lubricants were inviscid, the amplitude of A_2 would increase to infinity, as shown in Section 9.2.2. However, it is impossible for A_2 to increase to infinity [118, 121]. From distance Z_n^{em} onwards, A_2 decreased as the effect of attenuation was large enough to dissipate ultrasonic energy. According to Figure

10.6, PAO100 is more viscous than PAO40. Therefore, A_2 for the same excitation amplitude in PAO100 was less than in PAO40.

11.4 Effect of excitation amplitude

Figure 11.4 shows the captured signals at the peak frequency of 1.02 MHz and excitation amplitudes of 22 V, 45 V, 67 V, 90 V and 144 V in PAO40 and PAO100. In Figures 11.4a, 11.4b, 11.4d and 11.4e, it is seen that the amplitude of the fundamental frequency A_1 and the second-order harmonic A_2 increased as the excitation amplitude increased. The higher the viscosity of the lubricants, the greater the attenuation of the waves. The minimum excitation amplitude to generate the second-order harmonic depends on the viscosity of the lubricants, diameter and the peak frequency of the emitter. For example, the second-order harmonic was detectable at excitation amplitude 22 V up to a distance of 105 mm in PAO40, while this distance for PAO100 was 90 mm. PAO40 and PAO100 were measured separately. So, any noise and changes in electrical circuits might affect the levels of A_1 and A_2. This can be improved by measuring the ratio A_2/A_1^2. Figure 11.4c and 11.4d show the variation of the ratio A_2/A_1^2 against the separation. It is seen that this ratio was independent of the amplitude of the excitation. Therefore, regardless of the excitation amplitude, the ratio A_2/A_1^2 was unique for the lubricants at a specific frequency and temperature. There was a fluctuation in A_1 and A_2 in the distance close to the source, as shown in Figure 11.3. This fluctuation was due to the diffraction effect, as shown in Section 9.2.3.

11.5 Validation of the method

Pantea et al. [121] used a piezoelement transducer to emit ultrasound and captured it with a hydrophone as a receiver to measure the sound pressure and nonlinear coefficient in distilled water. In the current study, a second piezoelement transducer was used. Since the output was in voltage, it was converted to units of metres to determine sound pressure, particle displacement and nonlinear coefficient. To validate the configuration, the nonlinear coefficient of distilled water was determined, which was measured by a hydrophone. Figure 11.5 shows the ratio A_2/A_1^2 at room temperature over a separation distance of 110 mm. The slope of the best-fit line in the distance of Z_n is substituted into Eq. 9.20. The nonlinear coefficient was determined to be 3.5, which agrees with [28, 121].

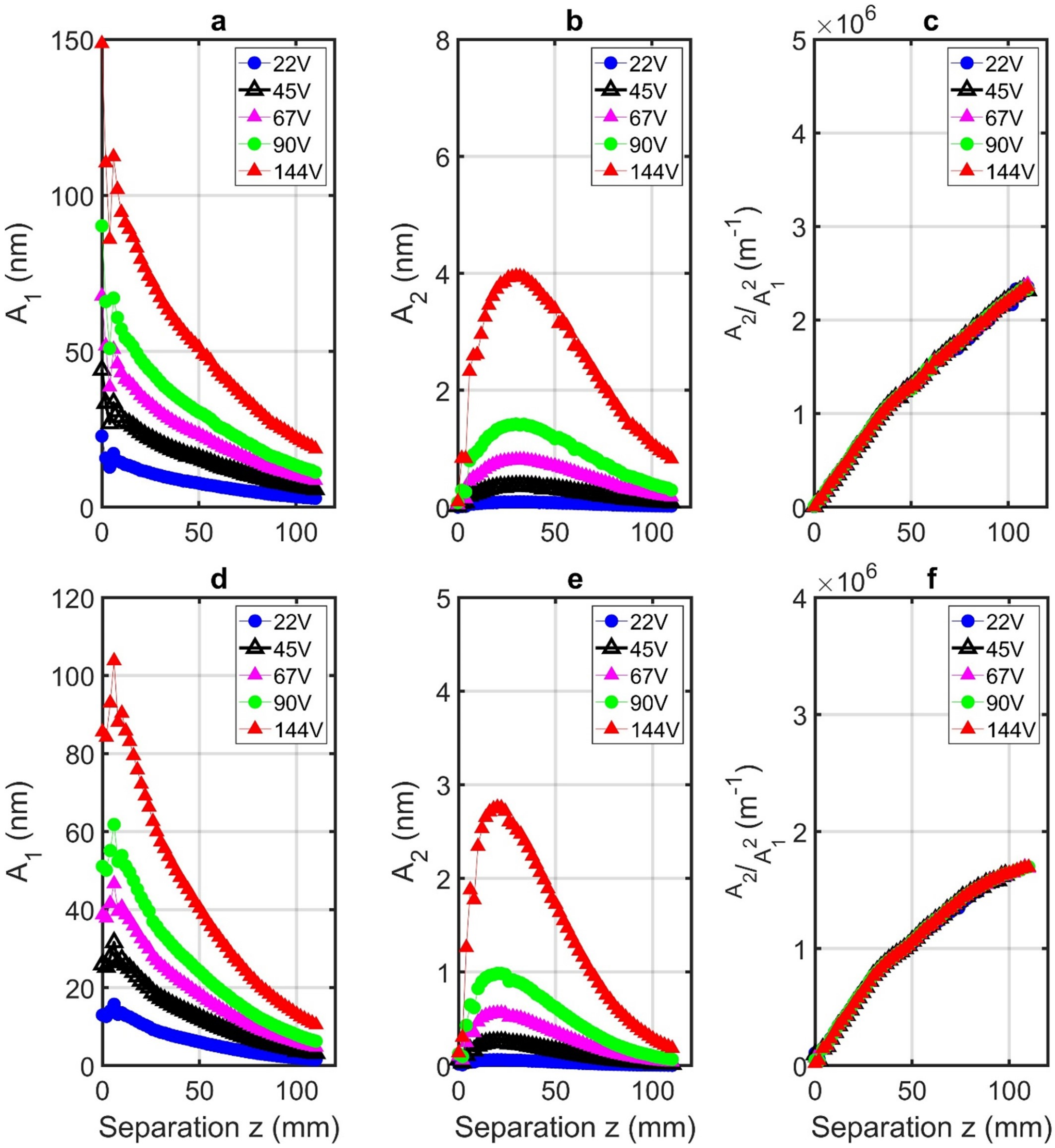

Figure 11.4: Amplitude of the fundamental frequency A_1, the second-order harmonic A_2 and the ratio A_2/A_1^2 against separation distance z: (a-c) PAO40; (d-f) PAO100; (a,d) amplitude of fundamental frequency A_1; (b,e) amplitude of the second-order harmonic A_2; (c,f) the ratio A_2/A_1^2.

11.6 Nonlinear coefficient measurement

The nonlinear coefficient of some of the liquid lubricants used in this thesis was presented by the author of this thesis in Ref [129]. Figures 11.6a and b show how the ratio A_2/A_1^2 varied in the near- and far-field regions for PAO40 and PAO100. From Eq. 9.1, the distance Z_n of the near-field is the distance where the wavefronts are

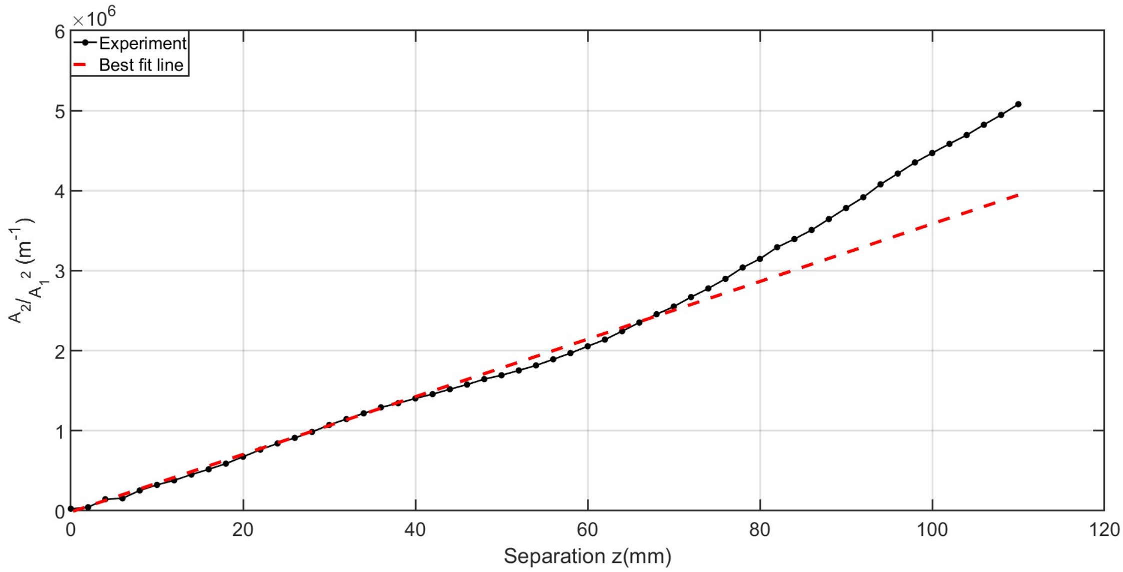

Figure 11.5: Variation of A_2/A_1^2 against separation distance of distilled water.

planar. This distance is a function of the excitation angular frequency, the radius of the piezoelectric transducer and the speed of sound of the medium in which the ultrasound is propagated. In this equation, the effect of absorption as a result of viscosity is not considered. Therefore, as seen in Table 10.1, for lubricants with approximately similar speed of sound, the distance Z_n is almost equal. This distance

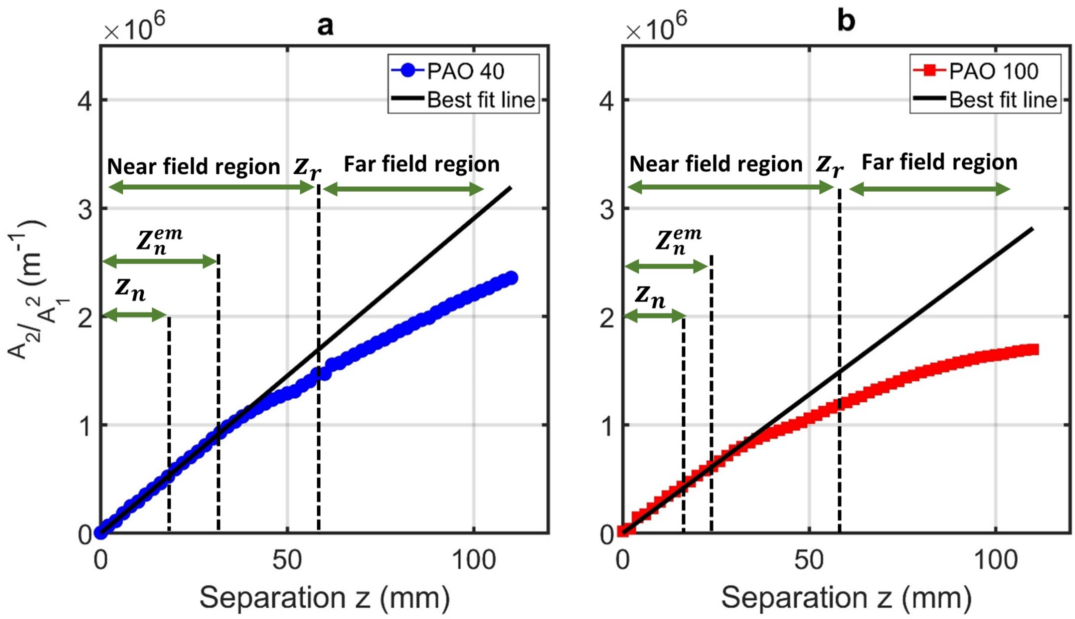

Figure 11.6: The effect of the near- and far-field regions on A_2/A_1^2 for: (a) PAO40; (b) PAO100.

is important because Eqs. 9.18 and 9.20 are valid at this distance. Eq. 9.20 indicates A_2/A_1^2 varies linearly; therefore, Z_n is required to measure this separation distance. Figure 10.6 shows that the linear variation of A_2/A_1^2 was longer than predicted by Z_n. However, the proposed distance Z_n^{em}, which is an empirical distance, shows the distance where A_2/A_1^2 had a linear behaviour. Eq. 9.20 indicates that from the ultrasonic source to the separation distance Z_n^{em}, the effect of attenuation of A_1 and A_2 for the ratio A_2/A_1^2 was insignificant; therefore, at this distance, A_2/A_1^2 varied linearly as the separation distance increased. However, as ultrasonic waves propagated further the distance Z_n^{em}, the ratio A_2/A_1^{em} was a function of the attenuation of both A_1 and A_2 and varied exponentially and deviated from linearity. The slope of the best-fit lines shown in Figure 11.7 was depended on the nonlinear coefficient, incident frequency and the speed of sound of the lubricants. Figure 11.7 shows the ratio A_2/A_1^2

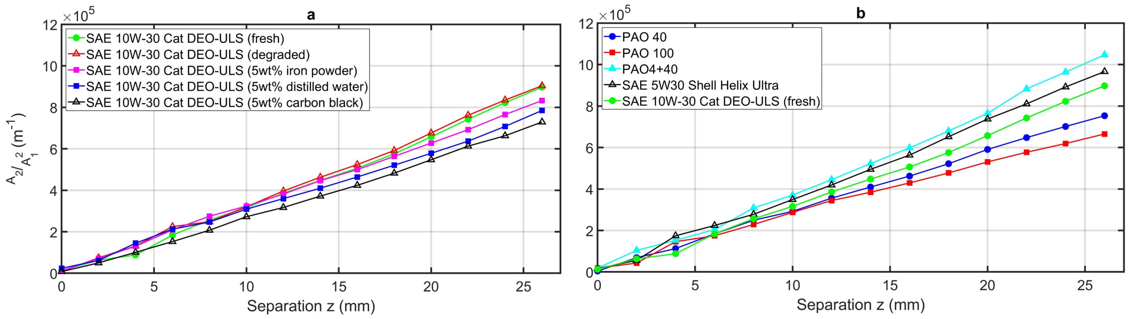

Figure 11.7: Variation of A_2/A_1^2 of the lubricant in the distance Z_n^{em} of the near-field region.

of the fresh and contaminated lubricants at the distance Z_n^{em} of the near-field and their best-fit lines. The slopes of these best-fit lines were substituted into Eq. 9.20 to determine the nonlinear coefficient of the lubricants as shown in Table 11.1.

Figure 11.8 illustrates the effect of viscosity on the nonlinear coefficient. It shows that the fresh SAE 10W-30 Cat DEO-ULS lubricant and its contamination had different nonlinear coefficients β. The real degraded SAE 10W-30 Cat DEO-ULS has a larger β than the fresh one, while its shear viscosity was the lowest. As shown in Figure 10.6b, artificially contaminated SAE 10W-30 Cat DEO-ULS lubricants with iron powder, distilled water and carbon black affect their shear viscosity. From 11.8a, these contaminated lubricants are seen, and the real degradation had a unique β. As β decreased, the shear viscosity of the lubricants increased. Likewise, Figure 11.8b shows that β was inversely proportional to shear viscosity. PAO 4+40 had the highest β with the lowest shear viscosity. PAO100 was the thickest lubricant with a minimum

Table 11.1: Nonlinear coefficient of the liquid lubricants.

Lubricant	Nonlinear coefficient β
PAO 40	6.21
PAO 100	5.61
PAO4+40	7.58
SAE 5W-30 Shell Helix Ultra (fresh)	7.30
SAE 10W-30 Cat DEO-ULS (fresh)	6.79
SAE 10W-30 Cat DEO-ULS (degraded)	6.94
SAE 10W-30 Cat DEO-ULS (5wt% iron)	6.21
SAE 10W-30 Cat DEO-ULS (5wt% carbon black)	5.67
SAE 10W-30 Cat DEO-ULS (5wt% distilled water)	5.71

of β. It is also observed that β was measurable for Newtonian and non-Newtonian lubricants. The lubricants in this study are all non-Newtonian (as shown in Figure 10.6) and Pantea. et al. [121] measured β for distilled water; therefore, unlike some online lubricant degradation monitoring, β can be used for Newtonian and non-Newtonian lubricants.

The Burgers equation (Eq. 9.5) contains no viscosity parameter. However, as seen in Figure 11.8, β varies as the viscosity changes. Therefore, the Burgers equation implicitly considers the effect of viscosity in the distance Z_n^{em} of the near-field.

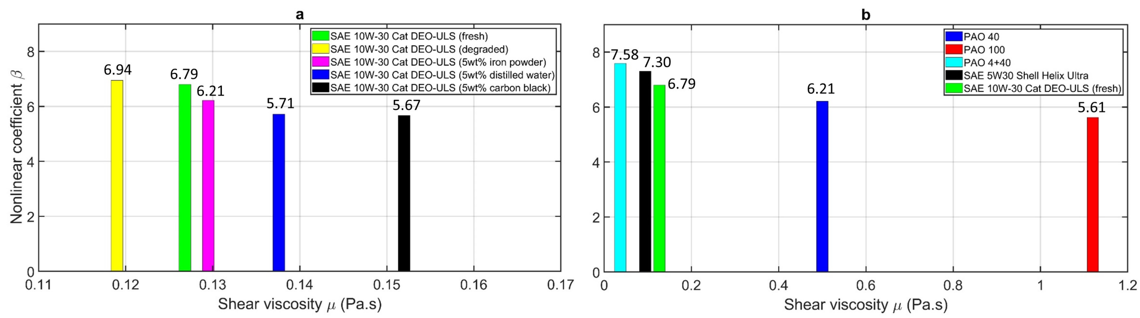

Figure 11.8: Variation of nonlinear coefficient β with shear viscosity: (a) fresh, artificially contaminated and read degraded SAE 10W30 Cat DEO-ULS; (b) fresh lubricants.

Figure 11.8 also illustrates that the viscosity of SAE 10W-30 increased as it was contaminated by 5wt% iron powder, distilled water and carbon black. Lubricants with higher intermolecular forces are more viscous. The iron powder contains Fe elements, increasing the number of intermolecular interactions of the lubricant. Subsequently, the viscosity of the lubricant increases compared to the fresh lubricant, as shown in Figure 10.6b. This intermolecular force is less than the interaction between distilled water and carbon black powder with the lubricants. As a result, the viscosity of SAE 10W-30 contaminated with carbon black powder is greater than that contaminated with distilled water and iron powder.

11.7 Conclusion

In this chapter, the nonlinear behaviour of longitudinal ultrasonic waves was used for online lubricant degradation and contamination monitoring. The effect of excitation amplitude on the amplitude of the fundamental frequency and second-order harmonic was investigated experimentally. It was seen that as the amplitude of excitation increased, the amplitude of the fundamental frequency and second-order harmonic were increased, and the ratio ${A_2}/{A_1}^2$ was independent of the excitation amplitude, which was in agreement with the analytical results presented in Chapter 9.

The ratio ${A_2}/{A_1}^2$ was linearly increased from the source until the end of the distance Z_n. The slope of the curves was used to determine the nonlinear coefficient of the lubricants. To validate the measurement method, distilled water was used and the nonlinear coefficient was measured. The nonlinear coefficient was 3.5 and was in agreement with the value presented by the other researchers.

It was also observed that β is inversely proportional to the viscosity of the liquid lubricants. In this study, it was seen that β could be measured for non-Newtonian liquids. An empirical value was also presented to correct the theoretical value of Z_n of the near-field region where the nonlinear coefficient was determined.

Another outcome of this study was the effect of different types of contamination on the same liquid lubricant. The results show that SAE 10W-30 artificially contaminated by 5wt% iron powder was less viscous than artificially contaminated by 5wt% distilled water, and artificially contaminated by 5wt% distilled water was less viscous than artificially contaminated by 5wt% carbon black. This is because the intermolecular interaction of SAE artificially contaminated with iron powder is less than that of the one degraded by distilled water and carbon black. The fact that lubricants with higher intermolecular forces are more viscous confirms this result.

The nonlinear coefficient can be used for the online detection and monitoring of lubricant degradation and contamination because it is a unique number for each lubricant under a specified condition.

Chapter 12

Conclusion

This thesis presents the nonlinear behaviour of ultrasound in solid-solid contact and in a liquid lubricant. In this chapter, a summary of the findings is presented using different lubricants and surface roughness for solid-solid contact.

12.1 Limitations of contact acoustic nonlinearity (CAN)

The analytical and numerical methods used to predict and simulate CAN are based on the assumptions of frictionless and perfect contact. In other words, the surface roughness and waviness of the contacts are ignored. When the perfect surfaces (no surface roughness and waviness) come into contact, the nominal and real contact pressure become the same. This makes them significantly stiffer than the real ones.

Researchers have also shown that interfacial stiffness measured by ultrasound is 2-10 times stiffer than that of analytical and statistical models such as the Greenwood and Williamson (GW) model. However, it requires more study as the GW model simplified the contacts by assuming the asperities are treated as a distribution of hemispherical capped peaks and neglecting the effect of deformation of neighbour peaks.

12.2 Limitations of liquid degradation and contamination

One of the limitations of nonlinear ultrasound in liquid lubricants is the analytical models for the KZK equation. The available solutions mainly ignore the effect of diffraction, which makes the solution less accurate.

In terms of the experimental detection of the degradation of the liquid lubricants, air bubbles in the lubricants affect the nonlinear coefficient. Therefore, the liquid is required to be stationary for a longer time to allow the air bubbles to disappear.

12.3 Contact acoustic nonlinearity (CAN)

The ultrasonic waves reflected from perfect contact were simulated analytically and numerically using the available methods. It was shown that as the amplitude of excitation increased, the nonlinearity in the reflected waves also increased. The main limitations of the analytical and numerical analyses were that the contact was assumed to be perfect and frictionless without any surface roughness. In reality, these assumptions are impractical as engineering surfaces are imperfect, containing roughness, waviness and lay. In addition, common engineering surfaces have a static coefficient of friction of 0.05-0.5.

In this thesis, the pitch-catch through reflection method was used to measure the second-order nonlinear interfacial stiffness on two pairs of imperfect contacts. This method is important as in most engineering contacts, only one side of the contact is accessible. To validate the model presented with the other researchers, as there are no other methods to measure the second-order nonlinear normal interfacial stiffness other than ultrasound, the nonlinear differential equation was defined for the linear and second-order nonlinear normal interfacial stiffness. These equations were solved numerically, and the results gave the nominal contact pressure as a function of relative surface approach. The results showed the accuracy of the method. To ensure the accuracy of this method, a set of experimental data presented by other researchers was fed into the proposed nonlinear differential equations. The results proved the accuracy of the method.

Another achievement of this thesis was studying the effect of elastic-plastic deformations of asperities on the second-order nonlinear normal interfacial stiffness. It was seen that in the 1^{st} loading/unloading cycle, the hysteresis in the interfacial stiffness was larger due to the plastic deformation of the asperities. This hysteresis decreased during the 2^{nd} loading/unloading cycles, indicating that the real contact area increased and that some of the asperities were within the elastic limit. At the 10^{th} loading/unloading cycle, that hysteresis became relatively small. The two pairs used in this study had different surface roughnesses from smooth to rough contact. It was seen that even for a rough surface contact with R_a almost 4.5 μm, nonlinearity was generated in the contact. As surface roughness increased, the second-order nonlinear interfacial stiffness decreased, and the surface became less stiff.

12.4 Lubricant degradation and contamination monitoring

The KZK equation was used to model the propagation of ultrasonic waves in nine liquid lubricants. This equation considers the effect of absorption, diffraction and nonlinearity. As there is no analytical solution to the KZK equation, it is solved numerically. To be able to solve it analytically, the effects of absorption, diffraction and nonlinearity were considered separately for the lubricants. It was seen that as the viscosity increased, the attenuation of the ultrasonic waves increased. The Burgers equation is a simplified equation of the KZK equation as it ignores the effect of diffraction. This equation was used to analytically simulate the effect of absorption and nonlinearity. The amplitude of the fundamental frequency and second-order harmonic against the separation distance at different excitation frequency, shear viscosity and amplitude was investigated. Higher attenuation was observed at higher excitation frequencies and the shear viscosity of the lubricants.

Different fresh liquid lubricants were contaminated by 5%wt distilled water, carbon powder and black iron. They are the main sources of degradation and contamination in lubricants. The nonlinear coefficient of these lubricants was then measured. It was found that any lubricant at a specific temperature has a unique nonlinear coefficient that can be used as a means of lubricant degradation. This number was independent of the amplitude of excitation and frequency.

12.5 Future works

Further developments are listed below:

- Improve analytical and numerical (FDM) models to consider the effect of friction and surface roughness.
- Import surface roughness into ABAQUS (FEA) to simulate the reflection and transmission of ultrasonic waves to determine the second-order nonlinear normal interfacial stiffness.
- Measure kinematic and shear viscosities using nonlinear coefficients of lubricants.
- Detecting the nature of the contamination of lubricants using nonlinear coefficients.
- Measurement of nonlinear coefficients at different temperatures.

12.6 List of Publications during PhD Study

Peer-reviewed journal paper:

1. **S. Taghizadeh**, R.S. Dwyer-Joyce, "Linear and Nonlinear Normal Interface Stiffness in Dry Rough Surface Contact Measured using Longitudinal Ultrasonic Waves", Appl. Sci. June 2021, 11(12), 5720.

Conference presentations:

1. **S. Taghizadeh**, R.S. Dwyer-Joyce, "Application of the Non-linear Behaviour of Longitudinal Ultrasonic Waves in Lubricants Monitoring", 23rd International Colloquium Tribology", 25-27 Jan 2022.

2. **S. Taghizadeh**, R.S. Dwyer-Joyce, "Influence of Asperity Deformation on Linear and Nonlinear Normal Interfacial Stiffness in Dry Rough Surface Contact", 15th International Conference on Advances in Experimental Mechanics (BSSM),2021.

Appendix A

MATLAB script for solid-air contact in linear elastic media

```
clear; close all; clc;
%%
E = 70E9; % Elastic modulus
rho = 2700;% Density
c = sqrt(E/rho); % speed of sound
f0 = 2E6; % frequency of excitation
p = 0:0.15:10;
p0 = -p(2)*10ˆ6; % applied load
disp([’Applied prerssure is : ’, num2str(p0*10ˆ-6)])
n = 5; %number of tone burst cycles
A0 =0.127; % (0.127 equal to 5nm, 0.1905 equal to 7.5nm, 0.254 equal to 10nm amplitude)
L=32E-3; % length of specimen
t1 = L/c;
tf=20e-6; % end time
dx=6E-5; % space increment
dt=6E-9; % time increment
N˙x=round(L/dx); % number of space nodes
N˙t=round(tf/dt); % number of time nodes
t˙hit = 2*L/c;
N˙hit = round(t˙hit/dt);


CFL=c*dt/dx; % stability
```

```
if CFL ¡ 1
Lambda=CFL;
else
fprintf('CFL stability is not satisfied. Input dx and dt such that CFL becomes less
than 1')
end
%%
x = linspace(0,L,N˙x+1);
t = linspace(0,tf,N˙t+1);
u = zeros(N˙x+1,N˙t+1);
% zero matrix for displacemeN˙t
sigma = zeros(N˙x+1,N˙t+1); % zeros matrix for normal stress

F = zeros(N˙t+1,1);
N˙exc=round(n/(f0*dt)+1); % number of elements of excitation

F(1:N˙exc)=A0*sin(2*pi*f0*t(1:N˙exc));
Gaussian=gausswin(N˙exc); % Gaussian window
F(1:N˙exc)=F(1:N˙exc).*Gaussian;

   %% Initial condition, boundary condition and propagation
u(1,2)= u(1,1) + 0.5*Lambda*(-3*u(1,1)+4*u(2,1)-u(3,1))+2*F(1)*dt;
sigma(2:N˙x,1)=E*(u(3:N˙x+1,1)-u(1:N˙x-1,1))/(2*dx);
sigma(N˙x+1,1)=E*(3*u(N˙x+1,1)-4*u(N˙x,1)+u(N˙x-1,1))/(2*dx);
sigma(1,1)=E*(-3*u(1,1)+4*u(2,1)-u(3,1))/(2*dx);
u(2:N˙x-1,2) = 0.5*(Lambdaˆ2*u(3:N˙x,1)+(2-2*Lambdaˆ2)*u(2:N˙x-1,1)+Lambdaˆ2*u(1:N˙x-
2,1));

for j=2:N˙t
u(1,j+1) = u(1,j) + 0.5*Lambda*(-3*u(1,j)+4*u(2,j)-u(3,j))+2*F(j)*dt;
u(2:N˙x-1,j+1)=Lambdaˆ2*(u(3:N˙x,j)-2*u(2:N˙x-1,j)+u(1:N˙x-2,j))+2*u(2:N˙x-1,j)-u(2:N˙x-
1,j-1);
u(N˙x,j+1)= Lambdaˆ2*(u(N˙x+1,j)-2*u(N˙x,j)+u(N˙x-1,j))+2*u(N˙x,j)-u(N˙x,j-1);
sigma(2:N˙x,j)=E*(u(3:N˙x+1,j)-u(1:N˙x-1,j))/(2*dx);
sigma(1,j)=E*(-3*u(1,j)+4*u(2,j)-u(3,j))/(2*dx);
sigma(N˙x+1,j) = E*(-4*u(N˙x,j)+u(N˙x-1,j)+3*u(N˙x+1,j))/(2*dx);
```

end

Appendix B

MATLAB script for solid-solid interface in linear elastic media

```
%%
E = 70E9; % Elastic modulus
rho = 2700;% Density
c = sqrt(E/rho); % speed of sound
f0 = 2E6; % frequency of excitation
p = 0:0.15:10;
p0 = -p(2)*10ˆ6; % applied load
disp(['Applied prerssure is : ', num2str(p0*10ˆ-6)])
n = 5; %number of tone burst cycles
A0 =0.127; % (0.127 equal to 5nm, 0.1905 equal to 7.5nm, 0.254 equal to 10nm am-
plitude)
L=32E-3; % length of specimen
t1 = L/c;
tf=20e-6; % end time
dx=6E-5; % space increment
dt=6E-9; % time increment
N˙x=round(L/dx); % number of space nodes
N˙t=round(tf/dt); % number of time nodes
t˙hit = 2*L/c;
N˙hit = round(t˙hit/dt);


CFL=c*dt/dx; % stability
if CFL ¡ 1
```

```
Lambda=CFL;
else
fprintf('CFL stability is not satisfied. Input dx and dt such that CFL becomes less than 1')
end
%%
x = linspace(0,L,N˙x+1);
t = linspace(0,tf,N˙t+1);
u = zeros(N˙x+1,N˙t+1);
% zero matrix for displacemeN˙t
sigma = zeros(N˙x+1,N˙t+1); % zeros matrix for normal stress

F = zeros(N˙t+1,1);
N˙exc=round(n/(f0*dt)+1); % number of elements of excitation

F(1:N˙exc)=A0*sin(2*pi*f0*t(1:N˙exc));
Gaussian=gausswin(N˙exc); % Gaussian window
F(1:N˙exc)=F(1:N˙exc).*Gaussian;

    u(1,2)= u(1,1) + 0.5*Lambda*(-3*u(1,1)+4*u(2,1)-u(3,1))+2*F(1)*dt;
sigma(2:N˙x,1)=E*(u(3:N˙x+1,1)-u(1:N˙x-1,1))/(2*dx);
sigma(N˙x+1,1)=E*(3*u(N˙x+1,1)-4*u(N˙x,1)+u(N˙x-1,1))/(2*dx);
sigma(1,1)=E*(-3*u(1,1)+4*u(2,1)-u(3,1))/(2*dx);
u(2:N˙x-1,2) = 0.5*(Lambdaˆ2*u(3:N˙x,1)+(2-2*Lambdaˆ2)*u(2:N˙x-1,1)+Lambdaˆ2*u(1:N˙x-2,1));

    for j=2:N˙t
u(1,j+1) = u(1,j) + 0.5*Lambda*(-3*u(1,j)+4*u(2,j)-u(3,j))+2*F(j)*dt;
u(2:N˙x-1,j+1)=Lambdaˆ2*(u(3:N˙x,j)-2*u(2:N˙x-1,j)+u(1:N˙x-2,j))+2*u(2:N˙x-1,j)-u(2:N˙x-1,j-1);
u(N˙x,j+1)= Lambdaˆ2*(u(N˙x+1,j)-2*u(N˙x,j)+u(N˙x-1,j))+2*u(N˙x,j)-u(N˙x,j-1);
sigma(2:N˙x,j)=E*(u(3:N˙x+1,j)-u(1:N˙x-1,j))/(2*dx);
sigma(1,j)=E*(-3*u(1,j)+4*u(2,j)-u(3,j))/(2*dx);
sigma(N˙x+1,j) = E*(-4*u(N˙x,j)+u(N˙x-1,j)+3*u(N˙x+1,j))/(2*dx);
if sigma(N˙x+1,j) + p0 ¡ 0
u(N˙x+1,j) = 0;
```

```
u(N˙x,j+1)=Lambdaˆ2*u(N˙x+1,j)+(2-2*Lambdaˆ2)*u(N˙x,j)+Lambdaˆ2*u(N˙x-1,j)-
u(N˙x,j-1);
else
u(N˙x+1,j) = ((-2*dx*p0/E)+4*u(N˙x,j)-u(N˙x-1,j))/3;
u(N˙x,j+1)= Lambdaˆ2*(u(N˙x+1,j)-2*u(N˙x,j)+u(N˙x-1,j))+2*u(N˙x,j)-u(N˙x,j-1);
sigma(N˙x+1,j) = E*(-4*u(N˙x,j)+u(N˙x-1,j)+3*u(N˙x+1,j))/(2*dx);
end
end
```

Appendix C

Derivation of Khokhlov-Zabolotskaya-Kuznetsov (KZK) equation

The nonlinear behaviour of ultrasound in a homogeneous lossy liquid lubricant (considering the effect of viscosity and thermal conductivity) is defined by mass conservation, momentum conservation, entropy equation and equation of state [28]. These equations are required to be written in terms of quantities affected by ultrasound such as pressure and density and be written as a single equation as follows.

C.1 Mass Conservation

The mass conservation is given by [28]:

$$\frac{\partial \rho}{\partial t} + \boldsymbol{u}.\nabla\rho + \rho\nabla.\boldsymbol{u} = 0 \tag{C.1}$$

where ρ is the density of the liquid and $\boldsymbol{u}$ is the liquid particle velocity vector generated by propagating ultrasonic waves. When ultrasonic waves propagate in the liquid lubricant, the density of the liquid is defined by:

$$\rho = \rho_0 + \rho' \tag{C.2}$$

where ρ' is the density fluctuated by ultrasound of liquid as the ultrasonic wave propagates and ρ_0 is the liquid density in the absence of ultrasonic wave. Then Eq. C.1 can be represented in terms of density fluctuated by ultrasound [28]:

$$\frac{\partial \rho'}{\partial t} + \rho_0\nabla.\boldsymbol{u} = -\rho'\nabla.\boldsymbol{u} - \boldsymbol{u}.\nabla\rho' \tag{C.3}$$

C.2 Momentum Conservation

The momentum conservation is presented by [28]:

$$\rho\frac{\partial \boldsymbol{u}}{\partial t} + \rho\boldsymbol{u}\nabla.\boldsymbol{u} + \nabla P = \mu\nabla^2\boldsymbol{u} + (\mu_B + \frac{1}{3}\mu)\nabla(\nabla.\boldsymbol{u}) \tag{C.4}$$

where P is the total pressure of the liquid, $\nabla.$ is divergence operator, ∇ is gradient operator, ∇^2 is Laplacian operator, μ is the shear viscosity and μ_B is the bulk viscosity of the liquid. When ultrasonic waves propagate in the liquid lubricant, the total pressure of the liquid is defined as:

$$P = P_0 + p \tag{C.5}$$

where p is the sound pressure in liquid as the ultrasonic wave propagates and P_0 is the liquid pressure in the absence of an ultrasonic wave. Then Eq.C.4 can be represented in terms of sound pressure [28]:

$$\rho_0\frac{\partial \boldsymbol{u}}{\partial t}+\nabla p = (\mu_B+\frac{4}{3}\mu)\nabla^2\boldsymbol{u}-\frac{1}{2}\rho_0\nabla u^2-\rho'\frac{\partial \boldsymbol{u}}{\partial t}+(\mu_B+\frac{1}{3}\mu)\nabla\times\nabla\times\boldsymbol{u}+\rho_0\boldsymbol{u}\times\nabla\times\boldsymbol{u} \tag{C.6}$$

The terms containing $\nabla \times \boldsymbol{u}$ are small in comparison to the other terms, therefore, they are ignored and the momentum equation (Eq.C.6) is rewritten as [28]:

$$\rho_0\frac{\partial \boldsymbol{u}}{\partial t} + \nabla p = (\mu_B + \frac{4}{3}\mu)\nabla^2\boldsymbol{u} - \frac{1}{2}\rho_0\nabla u^2 - \rho'\frac{\partial \boldsymbol{u}}{\partial t} \tag{C.7}$$

C.3 Equation of State

Equation of state is used to define the pressure-density relationship of liquid as ultrasonic waves propagate. Taylor series expansion of the equation of state up to terms of second order can be presented by [28]:

$$p = \left(\frac{\partial P}{\partial \rho}\right)_{s,0}(\rho - \rho_0) + \frac{1}{2!}\left(\frac{\partial^2 P}{\partial \rho^2}\right)_{s,0}(\rho - \rho_0)^2 + \left(\frac{\partial P}{\partial s}\right)_{\rho,0}s' \tag{C.8}$$

where s is the specific entropy and s' is the acoustic fluctuation in the specific entropy of the liquid. The first and second terms of Eq. C.8 can be defined as [28]:

$$A = \rho_0\left(\frac{\partial P}{\partial \rho}\right)_{s,0} = \rho_o{c_0}^2 \quad , or \quad c_0^2 = \frac{P_o}{\rho_0} \tag{C.9}$$

The coefficient A is called the bulk modulus of the liquid lubricant at ambient pressure and density (unperturbed liquid).

$$B = \rho_0^2\left(\frac{\partial^2 P}{\partial \rho^2}\right)_{s,0} \tag{C.10}$$

Substituting of Eq. C.9 and Eq. C.10 into the equation of state (Eq. C.8) gives:

$$p = {c_0}^2\rho' + \frac{c_0^2}{\rho_0}\frac{B}{2A}\rho'^2 + \left(\frac{\partial P}{\partial s}\right)_{\rho,0} s' \tag{C.11}$$

According to the Boyl's law and its derivative with respect to time [28]:

$$\frac{p}{P_0} = \frac{\rho'}{\rho_0} \tag{C.12}$$

$$\frac{\partial \rho'}{\partial t} = \frac{\rho_0}{P_0}\frac{\partial p}{\partial t} \tag{C.13}$$

By substituting Eq. C.9 and Eq. C.12, the equation of state (Eq. C.11) can be written as the acoustic fluctuation in density ρ' becomes the subject [28]:

$$\rho' = \frac{p}{c_0^2} - \frac{1}{\rho_0 c_0^4}\frac{B}{2A}p^2 - \frac{1}{c_0^2}\left(\frac{\partial P}{\partial s}\right)_{\rho,0} s' \tag{C.14}$$

C.4 Entropy Equation

The entropy equation is the third equation required to explain the nonlinear behaviour of ultrasound in a liquid lubricant [28]. By ignoring the terms containing small variables compared to the other terms and considering the effect of sound speed on the specific entropy, the entropy equation is written as follow[28]:

$$\rho_0 T_0 \frac{\partial s'}{\partial t} = \kappa \nabla^2 T' \tag{C.15}$$

where s' is the acoustic fluctuation in specific entropy, T_0 ambient temperature, T' is acoustic fluctuation in temperature and κ is thermal conductivity.

C.5 Equation of State without Temperature and Entropy

Measuring entropy in liquid lubricant as the ultrasonic waves propagate is difficult. Therefore, it is convenient to eliminate entropy from the equation of state (Eq. C.14). The assumption of a lossless and linear wave equation makes a substitution $\nabla^2 T' = \frac{1}{c_0^2}\frac{\partial^2 T'}{\partial t^2}$ that can be used in Eq. C.12 [28]:

$$\rho_0 T_0 \frac{\partial s'}{\partial t} = \frac{\kappa}{c_0^2}\frac{\partial^2 T'}{\partial t^2} \tag{C.16}$$

This assumption might affect the accuracy of the solution but it may be the only way to remove $\nabla^2 T'$ from Eq. C.15. An integral with respect to time of Eq. C.14 gives [28]:

$$\rho_0 T_0 s' = \frac{\kappa}{c_0^2}\frac{\partial T'}{\partial t} \tag{C.17}$$

Substituting Eq. C.17 into the equation of state (Eq. C.14) gives [28]:

$$\rho' = \frac{p}{c_0^2} - \frac{1}{\rho_0 c_0^4}\frac{B}{2A}p^2 - \frac{\kappa}{\rho_0 T_0 c_0^4}\frac{\partial T'}{\partial t}\left(\frac{\partial P}{\partial s}\right)_{\rho,0} \tag{C.18}$$

In order to remove temperature from Eq. C.18, a substitution for T' and its derivative with respect to time is used [28]:

$$T' = \rho'\left(\frac{\partial T}{\partial \rho}\right)_{s,0} \tag{C.19}$$

$$\frac{\partial T'}{\partial t} = \frac{\partial \rho'}{\partial t}\left(\frac{\partial T}{\partial \rho}\right)_{s,0} \tag{C.20}$$

Substituting Eq. C.20 and Eq. C.13 into Eq. C.18 gives:

$$\rho' = \frac{p}{c_0^2} - \frac{1}{\rho_0 c_0^4}\frac{B}{2A}p^2 - \frac{\kappa}{\rho_0 T_0 c_0^4}\frac{\partial \rho'}{\partial t}\left(\frac{\partial T}{\partial \rho}\right)_{s,0}\left(\frac{\partial P}{\partial s}\right)_{\rho,0} \tag{C.21}$$

The thermodynamic relations between pressure-entropy and temperature-density are required to remove from Eq. C.21 [28]:

$$\left(\frac{\partial p}{\partial s}\right)_{\rho} = \rho_0^2\left(\frac{\partial T}{\partial \rho}\right)_{s} \tag{C.22}$$

$$\left(\frac{\partial T}{\partial \rho}\right)_{\rho}^{2} = (\frac{1}{c_\nu} - \frac{1}{c_p})\frac{T_0 c_0^2}{\rho_0^2} \tag{C.23}$$

Substitution of Eq. C.9 and Eqs. C.22 and C.23 into Eq. C.21 gives the equation of state without temperature and entropy [28]:

$$\rho' = \frac{p}{c_0^2} - \frac{1}{\rho_0 c_0^4}\frac{B}{2A}p^2 - \frac{\kappa}{\rho_0 c_0^4}(\frac{1}{c_\nu} - \frac{1}{c_p})\frac{\partial p}{\partial t} \tag{C.24}$$

C.6 Second-Order Wave Equation

The nonlinear behaviour of acoustics in liquid lubricants has an approximate solution to the second order of a small ordering parameter $\tilde{\varepsilon}$ [28]. Defending the approximate analytical solutions for any sources is more straightforward than the exact solution

[28]. This ordering parameter is the smallest of both the acoustic Mach number ε and parameter η [28]:

$$\varepsilon = \frac{|u|}{c_0} \tag{C.25}$$

$$\eta = \frac{\mu\omega}{\rho_0 c_0^2} \tag{C.26}$$

where $|u|$ is the amplitude of particle velocity and ω is the angular frequency of ultrasonic wave. η is a quantity to measure the effect of viscose stress generated by the sound pressure by progressive plane waves [28]. These two ordering parameters are very small in liquid lubricant ($\varepsilon << 1, \eta << 1$) [28], thus the approximate solution for orders higher than two is neglected. When plane ultrasonic waves propagate in a liquid lubricant, sound pressure and particle velocity are linearly dependent as given by [28]:

$$p = \rho_0 c_0 u \tag{C.27}$$

According to Eq. C.12 and Eqs. C.25-C.27 all the terms in Eq. C.3, Eq. C.7 and Eq. C.24 are up to the second order of small ordering parameter $\tilde{\varepsilon}$.

The mass conservation (Eq. C.3), momentum conservation (Eq. C.7) and equation of state without the terms containing entropy and temperature (Eq. C.24) are required to be written as a single equation [28]. First, the gradient of vector particle velocity is eliminated. Using substitutions for the terms on the right-hand side of the mass conservation and momentum conservation, Eq. C.3 and Eq. C.7 become [28]:

$$\frac{\partial \rho'}{\partial t} + \rho_0 \nabla.\boldsymbol{u} = \frac{1}{\rho_0 c_0^4}\frac{\partial p^2}{\partial t} + \frac{1}{c_0^2}\frac{\partial L}{\partial t} \tag{C.28}$$

$$\rho_0 \frac{\partial \boldsymbol{u}}{\partial t} + \nabla p = -\frac{1}{\rho_0 c_o^2}(\mu_B + \frac{4}{3}\mu)\nabla\frac{\partial p}{\partial t} - \nabla L \tag{C.29}$$

where L is called the second order Lagrangian density [28]:

$$L = \frac{1}{2}\rho_0 u^2 - \frac{p^2}{2\rho_0 c_0^2} \tag{C.30}$$

For the plane ultrasonic waves, the second order Lagrangian density becomes zero $L = 0$ [28] (substituting Eq. C.27 in Eq. C.30). Finally, to derive a single equation that describes the nonlinear behaviour of ultrasound in liquid lubricant, a time derivative of Eq. C.28 is subtracted from the divergence of Eq. C.29 followed by substitution of Eq. C.24 [28]:

$$\nabla^2 p - \frac{1}{c_0^2}\frac{\partial^2 p}{\partial t^2} + \frac{\delta}{c_0^4}\frac{\partial^3 p}{\partial t^3} = -\frac{\beta}{\rho_0 c_0^4}\frac{\partial^2 p^2}{\partial t^2} \tag{C.31}$$

where $\beta = 1 + \frac{B}{2A}$ is the nonlinear coefficient and δ is the diffusivity of sound [116]:

$$\delta = \frac{1}{\rho_0}\left(\frac{4}{3}\mu + \mu_B\right) + \frac{\kappa}{\rho_0}\left(\frac{1}{c_\nu} - \frac{1}{c_p}\right) \tag{C.32}$$

Let us define new variables as $x_1 = \tilde{\varepsilon}^{\frac{1}{2}}x$, $y_1 = \tilde{\varepsilon}^{\frac{1}{2}}y$, $z_1 = \tilde{\varepsilon}z$ and $\tau = t - z/c_0$ [28]. Substituting the variables into Eq. C.31 gives the KZK equation [28]:

$$\frac{\partial^2 p}{\partial z \partial \tau} = \frac{c_0}{2}\left(\frac{\partial^2 p}{\partial r^2} + \frac{1}{r}\frac{\partial p}{\partial r}\right) + \frac{\delta}{2c_0^3}\frac{\partial^3 p}{\partial \tau^3} + \frac{\beta p}{\rho_0 c_0^3}\frac{\partial^2 p}{\partial \tau^2} \tag{C.33}$$

It should be noted that as $\tilde{\varepsilon}$ is almost 1.

References

[1] Y. A. Cengel and J. M. Cimbala, *Fluid Mechanics: Fundamentals And Applications.* Tata McGraw Hill Education Private Limited, third ed., 2014.

[2] S. Taghizadeh and R. S. Dwyer-Joyce, “Linear and nonlinear normal interface stiffness in dry rough surface contact measured using longitudinal ultrasonic waves,” *Applied Sciences*, vol. 11, p. 5720, 2021.

[3] K. Y. Jhang, “Nonlinear ultrasonic techniques for nondestructive assessment of micro damage in material: A review,” *Int. J. Precis. Eng. Manuf.*, vol. 10, pp. 123–135, 2009.

[4] X. Li and R. S. Dwyer-Joyce, “Measuring friction at an interface using ultrasonic response,” *Proceedings of the Royal Society A*, vol. 476, pp. 1–21, 2020.

[5] “Evident, Transducer construction. Available at: https://www.olympus-ims.com/en/ndt-tutorials /thicknessgauge/transducers/construction/.”

[6] S. Biwa, S. Hiraiwa, and E. Matsumoto, “Experimental and theoretical study of harmonic generation at contacting interface,” *Ultrasonics*, vol. 44, pp. 1319–1322, 2006.

[7] G. W. Stachowiak and A. W. Batchelor, *Engineering Tribology.* Elsevier Butterworth-Heinemann, fourth ed., 2014.

[8] R. S. Dwyer-Joyce, B. W. Drinkwater, and A. M. Quinn, “The use of ultrasound in the investigation of rough surface interfaces,” *J. Tribol.*, vol. 123, pp. 8–16, 2001.

[9] M. Schirru, R. Mills, R. Dwyer-Joyce, O. Smith, and M. Sutton, “Viscosity measurement in a lubricant film using an ultrasonically resonating matching layer,” *Tribology Letters*, vol. 60, pp. 1–11, 2015.

[10] B. Drinkwater, R. Dwyer-Joyce, and P. Cawley, “A study of the transmission of ultrasound across real rough solid-solid interfaces,” *Proc. R. Soc. Lond. A*, vol. 452, pp. 2613–2628, 1996.

[11] D. M. Mulvihill, H. Brunskill, M. E. Kartal, R. S. Dwyer-Joyce, and D. Nowell, “A comparison of contact stiffness measurements obtained by the digital image correlation and ultrasound techniques,” *Exp. Mech.*, vol. 53, pp. 1245–1263, 2013.

[12] H. G. Tattersall, “The ultrasonic pulse-echo technique as applied to adhesion testing.,” *Appl. Phys D Appl Phys*, vol. 6(7), pp. 819–832, 1973.

[13] J.-M. Baik and R. B. Thompson, “Ultrasonic scattering from imperfect interfaces: a quasi-static model,” *Journal of Nondestructive Evaluation*, vol. 4, pp. 177–196, 1984.

[14] R. S. Dwyer-Joyce, “The application of ultrasonic NDT techniques in tribology,” *Proceedings of the Institution of Mechanical Engineers, Part J: Journal of Engineering Tribology*, vol. 219, pp. 347–366, 2005.

[15] S. Biwa, A. Suzuki, and N. Ohno, “Evaluation of interface wave velocity, reflection coefficients and interfacial stiffnesses of contacting surfaces,” *Ultrasonics*, vol. 43, pp. 495–502, 2005.

[16] M. Gonzalez-Valadez, A. Baltazar, and R. S. Dwyer-Joyce, “Study of interfacial stiffness ratio of a rough surface in contact using a spring model,” *Wear*, vol. 268, pp. 373–379, 2010.

[17] S. Biwa, S. Hiraiwa, and E. Matsumoto, “Pressure-dependent stiffnesses and nonlinear ultrasonic response of contacting surfaces,” *J. Solid Mech. Mater. Eng.*, vol. 3, pp. 10–21, 2009.

[18] A. Baltazar, S. I. Rokhlin, and C. Pecorari, “On the relationship between ultrasonic and micromechanical properties of contacting rough surfaces,” *J. Mech. Phys. Solids*, vol. 50, pp. 1397–1416, 2002.

[19] B. Bhushan, *Modern tribology handbook, two volume set.* CRC press, 2000.

[20] J. D. Achenbach, *Wave propagation in elastic solids.* Elsevier, 2012.

[21] A. D. Pierce, *Acoustics: an introduction to its physical principles and applications.* Springer, 2019.

[22] D. Ensminger and L. J. Bond, *Ultrasonics: fundamentals, technologies, and applications.* CRC press, 2024.

[23] L. E. Kinsler, A. R. Frey, A. B. Coppens, and J. V. Sanders, *Fundamentals of acoustics.* John Wiley & sons, 2000.

[24] J. D. N. Cheeke, *Fundamentals and applications of ultrasonic waves.* CRC press Taylor and Francis Group, second ed., 2012.

[25] J. Krautkramer and H. Krautkramer, *Ultradonic Testing of Mterials.* Springer-Verlag Berlin Heidelberg, fourth ed., 1990.

[26] M. D. C. Moles, C. R. Bird, P. Herzog, T. Armitt, P. Ciorau, R. Roberts, and M. Davis, *Introduction to Phased Array Ultrasonic Technology Applications*, vol. 1. Evident, 2024.

[27] T. D. Rossing, *Springer handbook of acoustics.* Springer, second ed., 2014.

[28] M. F. Hamilton and D. T. Blackstock, *Nonlinear acoustics*, vol. 237. Academic press San Diego, 1998.

[29] T. R. Thomas and R. S. Sayles, "Stiffness of machine tool joints. a random process approach," *J. Manuf. Sci. Eng. Trans. ASME*, vol. 99, pp. 250–256, 1977.

[30] R. D. Mindlin, "Compliance of elastic bodies in contact," *Appl Mech AME*, vol. 16, pp. 259–268, 1949.

[31] J. A. Greenwood and J. B. Williamson, "Contact of nominally flat surfaces," *Proc. R. Soc. Lond. Ser.*, vol. 295, pp. 300–319, 1966.

[32] R. A. Onions and J. F. Archard, "The contact of surfaces having a random structure," *Journal of Physics D: Applied Physics*, vol. 6, pp. 289–304, 1973.

[33] D. J. Whitehouse and J. F. Archard, "The properties of random surfaces of significance in their contact," *Proceedings of the Royal Society of London. A. Mathematical and Physical Sciences*, vol. 316, pp. 97–121, 1970.

[34] A. W. Bush, R. D. Gibson, and T. R. Thomas, "The elastic contact of a rough surface," *Wear*, vol. 35, pp. 87–111, 1975.

[35] C. Campañá, B. N. J. Persson, and M. H. Müser, "Transverse and normal interfacial stiffness of solids with randomly rough surfaces," *J. Phys. Condens. Matter*, vol. 23, 2011.

[36] M. E. Kartal, D. M. Mulvihill, D. Nowell, and D. A. Hills, "Determination of the frictional properties of titanium and nickel alloys using the digital image correlation method," *Exp. Mech.*, vol. 51, pp. 359–371, 2011.

[37] J. de Crevoisier, N. Swiergiel, L. Champaney, and F. Hild, "Identification of in situ frictional properties of bolted assemblies with digital image correlation," *Exp. Mech.*, vol. 52, pp. 561–572, 2012.

[38] P. P. Chikate and S. K. Basu, "Contact stiffness of machine tool joints," *Tribol. Int.*, vol. 8, pp. 9–14, 1975.

[39] Z. Handzel-Powierza, T. Klimczak, and A. Polijaniuk, "On the experimental verification of the greenwood-williamson model for the contact of rough surfaces," *Wear*, vol. 154, pp. 115–124, 1992.

[40] J. Królikowski and J. Szczepek, "Prediction of contact parameters using ultrasonic method," *Wear*, vol. 148, pp. 181–195, 1991.

[41] H. A. Sherif and S. S. Kossa, "Relationship between normal and tangential contact stiffness of nominally flat surfaces," *Wear*, vol. 151, pp. 49–62, 1991.

[42] Y. Sun, H. Xiao, and J. Xu, "Investigation into the interfacial stiffness ratio of stationary contacts between rough surfaces using an equivalent thin layer," *Int. J. Mech. Sci.*, vol. 163, 2019.

[43] K. Kendall and D. Tabor, "An ultrasonic study of the area of contact between stationary and sliding surfaces," *Proc. R. Soc. London. A. Math. Phys. Sci.*, vol. 323, pp. 321–340, 1971.

[44] J. Królikowski, J. Szczepek, and Z. Witczak, "Ultrasonic investigation of contact between solids under high hydrostatic pressure," *Ultrasonics*, vol. 27, pp. 45–49, 1989.

[45] D. Yan, B. W. Drinkwater, and S. A. Neild, "Measurement of the ultrasonic nonlinearity of kissing bonds in adhesive joints," *NDT and E Int.*, vol. 42, pp. 459–466, 2009.

[46] S. I. Rokhlin and Y. J. Wana, "Analysis of boundary conditions for elastic wave interaction with an interface between two solids," *J. Acoust. Soc. Am.*, vol. 89, pp. 503–515, 1991.

[47] F. Du, J. Hong, and Y. Xu, "An acoustic model for stiffness measurement of tribological interface using ultrasound," *Tribol. Int.*, vol. 73, pp. 70–77, 2014.

[48] H. Xiao and Y. Sun, "An improved virtual material based acoustic model for contact stiffness measurement of rough interface using ultrasound technique," *Int. J. Solids Struct.*, vol. 155, pp. 240–247, 2018.

[49] O. Buck, W. L. Morris, and J. M. Richardson, "Acoustic harmonic generation at unbonded interfaces and fatigue cracks," *Applied Physics Letters*, vol. 33, pp. 371–373, 1978.

[50] F. M. Severin and I. Y. Solodov, "Experimental observation of acoustic demodulation in reflection from a solid-solid interface," *Phys. Acoust.*, vol. 35, pp. 447–448, 1989.

[51] K. S. Len, "Experimental observation of the influence of contact nonlinearity on the reflection of bulk acoustic waves and the propagation of surface acoustic waves," *Sov. Phys. Acoust.*, vol. 37, pp. 610–612, 1991.

[52] J. M. Richardson, "Harmonic generation at an unbonded interface-i. planar interface between semi-infinite elastic media," *Int. J. Eng. Sci.*, vol. 17, pp. 73–85, 1979.

[53] S. Biwa, S. Nakajima, and N. Ohno, "On the acoustic nonlinearity of solid-solid contact with pressure-dependent interface stiffness," *ASME. J. Appl. Mech.*, vol. 71, pp. 508–515, 2004.

[54] N. K. Myshkin and L. V. Markova, *On-line condition monitoring in industrial lubrication and tribology*, vol. 8. Springer, 2018.

[55] J. Zhu, D. He, and E. Bechhoefer, "Survey of lubrication oil condition monitoring, diagnostics, and prognostics techniques and systems," *Journal of chemical science and technology*, vol. 2, pp. 100–115, 2013.

[56] L. Guan, X. L. Feng, G. Xiong, and J. A. Xie, "Application of dielectric spectroscopy for engine lubricating oil degradation monitoring," *Sensors and Actuators A: Physical*, vol. 168, pp. 22–29, 2011.

[57] M. D. Brouwer, L. A. Gupta, F. Sadeghi, D. Peroulis, and D. Adams, "High temperature dynamic viscosity sensor for engine oil applications," *Sensors and Actuators A: Physical*, vol. 173, pp. 102–107, 2012.

[58] X. Zhu, C. Zhong, and J. Zhe, "Lubricating oil conditioning sensors for online machine health monitoring – a review," *Tribology International*, vol. 109, pp. 473–484, 2017.

[59] S.-I. Moon, K.-K. Paek, Y.-H. Lee, J.-K. Kim, S.-W. Kim, and B.-K. Ju, "Multiwall carbon nanotube sensor for monitoring engine oil degradation," *Electrochemical and solid-state letters*, vol. 9, pp. H78–H80, 2006.

[60] A. Basu, C. Buelna, J. Campbell, K. Ismail, Y. Lin, L. Rodrieguez, and S. Wang, "Smart sensing of oil degradation in gasoline engines," *SAE technical Paper Series No.200-01-1366*, 2002.

[61] H.-S. Lee, S. S. Wang, D. J. Smolenski, M. B. Viola, and E. E. Klusendorf, "In situ monitoring of high-temperature degraded engine oil condition with microsensors," *Sensors and Actuators B*, vol. 20, pp. 49–54, 1994.

[62] J. D. Turner and L. Austin, "Electrical techniques for monitoring the condition of lubrication oil," *Measurement science and technology*, vol. 14, pp. 1794–1800, 2003.

[63] L. V. Markova, N. K. Myshkin, M. S. Semenyuk, V. M. Makarenko, A. V. Kolesnikov, H. Kong, H. G. Han, and E. S. Yoon, "Methods and instruments for condition monitoring of lubricants," *Journal Of Friction and Wear*, vol. 24, pp. 50–59, 2003.

[64] M. Tomita, H. Kamo, Y. Nomura, M. Nozawa, S. Yamaguti, and Y. Toda, "Study on deterioration of engine oil and its sensing," *JSAE review*, vol. 16, pp. 283–285, 1995.

[65] S. Kumar, P. S. Mukherjee, and N. M. Mishra, "Online condition monitoring of engine oil," *Industrial lubrication and tribology*, vol. 57, pp. 260–267, 2005.

[66] S. Raadnui and S. Kleesuwan, "Low-cost condition monitoring sensor for used oil analysis," *Wear*, vol. 259, pp. 1502–1506, 2005.

[67] J. Cho and S. Park, "Capacitive sensor for automotive engine oil degradation using wireless network," *2010 International Symposium on Advanced Packaging Materials: Microtech (APM)*, pp. 88–91, 2010.

[68] J. P. Coates and L. C. Setti, "Condition monitoring of crankcase oils using computer aided infrared spectroscopy," *SAE Technical Paper 831681, 1983*, pp. 37–50, 1983.

[69] J. P. Coates and L. C. Setti, "Infrared spectroscopy as a tool for monitoring oil degradation," *Aspects of Lubricant Oxidation*, pp. 57–78, 1986.

[70] F. R. van de Voort, J. Sedman, R. A. Cocciardi, and D. Pinchuk, "FTIR condition monitoring of in-service lubricants: ongoing developments and future perspectives," *Tribology Transactions*, vol. 49, pp. 410–418, 2006.

[71] H. M. Shinde and A. K. Bewoor, "Evaluating petrol engine oil deterioration through oxidation and nitration parameters by low-cost IR sensor," *Applied Petrochemical Research*, vol. 10, pp. 83–94, 2020.

[72] A. Wolak, W. Krasodomski, and G. Zajac, "Ftir analysis and monitoring of used synthetic oils operated under similar driving conditions," *Friction*, vol. 8, pp. 995–1006, 2020.

[73] Y. Takezawa, Y. Ito, and J. Katagiri, "Automobile oil deterioration diagnosing apparatus," 2002.

[74] W. G. Kim, K. H. Oh, K. W. Chung, and Y.-W. Kim, "Method and system for measuring engine oil deterioration," 2014.

[75] N. Belmiloud, I. Dufour, A. Colin, and L. Nicu, "Rheological behavior probed by vibrating microcantilevers," *Applied Physics Letters*, vol. 92, pp. 041907–041909, 2008.

[76] B. Jakoby, R. Beigelbeck, F. Keplinger, F. Lucklum, A. Niedermayer, E. K. Reichel, C. Riesch, T. Voglhuber-Brunnmaier, and B. Weiss, "Miniaturized sensors for the viscosity and density of liquids-performance and issues," *IEEE transactions on ultrasonics, ferroelectrics, and frequency control*, vol. 57, pp. 111–120, 2010.

[77] T. Brenchley, "Viscosity measurements using a multiple frequency matching layer viscometer," PhD thesis, 2021.

[78] J. M. Hammond, R. M. Lec, X. J. Zhang, D. G. Libby, and L. A. Prager, "An acoustic automotive engine oil quality sensor," *IEEE International Frequency Control Symposium*, pp. 72–80, 1997.

[79] A. Agoston, C. Ötsch, and B. Jakoby, "Viscosity sensors for engine oil condition monitoring—application and interpretation of results," *Sensors and Actuators A: Physical*, vol. 121, pp. 327–332, 2005.

[80] H. S. Ju, E. J. Gottlieb, D. R. Augenstein, G. J. Brown, and B. R. Tittmann, "An empirical method to estimate the viscosity of mineral oil by means of ultrasonic attenuation," *IEEE transactions on ultrasonics, ferroelectrics, and frequency control*, vol. 57, pp. 1612–1620, 2010.

[81] M. M. Schirru, R. S. Mills, O. Smith, R. S. Dwyer-Joyce, and M. Sutton, "In situ measurement of journal bearing lubricant viscosity by means of a novel ultrasonic measurement technique using matching layer," *Tribology Transactions*, vol. 61, pp. 157–167, 2018.

[82] A. S. Dukhin and P. J. Goetz, "Bulk viscosity and compressibility measurement using acoustic spectroscopy," *The Journal of chemical physics*, vol. 130, p. 124519, 2009.

[83] S. Taghizadeh and R. S. Dwyer-Joyce, "Influence of asperity deformation on linear and nonlinear interfacial stiffness in dry rough surface contact," *British Society for Strain Measurement, 15th International Conference on Advances in Experimental Mechanics (BSSM)*, 2021.

[84] R. S. Dwyer-Joyce, T. Reddyhoff, and J. Zhu, "Ultrasonic measurement for film thickness and solid contact in elastohydrodynamic lubrication," *Journal of Tribology*, vol. 133, pp. 1–11, 2011.

[85] R. Mills and R. Dwyer-Joyce, "Ultrasound for the non-invasive measurement of ic engine piston skirt lubricant films," *Proceedings of the Institution of Mechanical Engineers, Part J: Journal of Engineering Tribology*, vol. 228, pp. 1330–1340, 2014.

[86] R. S. Dwyer-Joyce, B. W. Drinkwater, and C. J. Donohoe, “The measurement of lubricant–film thickness using ultrasound,” *Proceedings of the Royal Society of London. Series A: Mathematical, Physical and Engineering Sciences*, vol. 459, pp. 957–976, 2003.

[87] R. S. Dwyer-Joyce, P. Harper, and B. W. Drinkwater, “A method for the measurement of hydrodynamic oil films using ultrasonic reflection,” *Tribology Letters*, vol. 17, pp. 337–348, 2004.

[88] J. Rooke, H. Brunskill, X. Li, S. Taghizadeh, A. Hunter, S. He, X. Lu, and R. S. Dwyer-Joyce, “Piston ring oil film thickness measurements in a four-stroke diesel engine during steady-state, start-up and shut-down,” *International Journal of Engine Research*, vol. 24, pp. 1499–1514, 2023.

[89] G. Manson, “A forward-looking approach to nonlinear systems,” pp. 2697–2708, International Conference on Noise and Vibration Engineering, 2016.

[90] W. P. Mason, W. O. Baker, H. J. McSkimin, and J. H. Heiss, “Measurement of shear elasticity and viscosity of liquids at ultrasonic frequencies,” *Physical Review*, vol. 75, pp. 936–946, 1949.

[91] W. Roth and S. R. Rich, “A new method for continuous viscosity measurement. general theory of the ultra-viscoson,” *Journal of Applied Physics*, vol. 24, pp. 940–950, 1953.

[92] F. Cohen-Tenoudji, W. J. Pardee, B. R. Tittmann, L. A. Ahlberg, and R. K. Elsley, “A shear wave rheology sensor,” *IEEE transactions on ultrasonics, ferroelectrics, and frequency control*, vol. 34, pp. 263–269, 1987.

[93] I. Alig, D. Lellinger, J. Sulimma, and S. Tadjbakhsch, “Ultrasonic shear wave reflection method for measurements of the viscoelastic properties of polymer films,” *Review of Scientific Instruments*, vol. 68, pp. 1536–1542, 1997.

[94] M. S. Greenwood and J. A. Bamberger, “Measurement of viscosity and shear wave velocity of a liquid or slurry for on-line process control,” *Ultrasonics*, vol. 39, pp. 623–630, 2002.

[95] R. Saggin and J. N. Coupland, “Oil viscosity measurement by ultrasonic reflectance,” *Journal of the American Oil Chemists’ Society*, vol. 78, pp. 509–511, 2001.

[96] J. M. Burgers, *A mathematical model illustrating the theory of turbulence*, vol. 1. Academic Press, 1948.

[97] E. A. Zabolotskaya and R. V. Khokholv, “Quasi-plane waves in the nonlinear acoustics of confined beams,” *Sov. Phys. Acoust.*, vol. 15, pp. 35–40, 1969.

[98] V. P. Kuznetsov, “Equations of nonlinear acoustics,” *Sov. Phys. Acoust.*, vol. 16, pp. 467–470, 1971.

[99] S. Hirose, “2-d scattering by a crack with contact-boundary conditions,” *Wave Motion*, vol. 19, pp. 37–49, 1994.

[100] P. Blanloeuil, L. R. F. Rose, M. Veidt, and C. H. Wang, “Time reversal invariance for a one-dimensional model of contact acoustic nonlinearity,” *Journal of Sound and Vibration*, vol. 394, pp. 515–526, 2017.

[101] R. Courant, “On the partial difference equations of mathematical physics,” *Mathematische annalen*, vol. 100, pp. 32–74, 1928.

[102] C.-K. Soh and Y. Y. Lim, “Fatigue damage diagnosis and prognosis using electromechanical impedance technique,” *Structural Health Monitoring (SHM) in Aerospace Structures*, pp. 429–446, 2016.

[103] R. G. Lyons, *Understanding digital signal processing.* Pearson Education India, 2011.

[104] S. Biwa, S. Yamaji, and E. Matsumoto, “Quantitative evaluation of harmonic generation at contacting interface,” *AIP Conf. Proc.*, vol. 1022, pp. 505–508, 2008.

[105] R. G. Budynas and J. K. Nisbet, *Shigley’s Mechanical Engineering.* Desing McGraw-Hill, USA, tenth ed., 2011.

[106] J. He, “Homotopy perturbation method: a new nonlinear analytical technique,” *Applied Mathematics and Computation*, vol. 135, pp. 73–79, 2 2003.

[107] P. Blanloeuil, A. J. Croxford, and A. Meziane, “Numerical and experimental study of the nonlinear interaction between a shear wave and a frictional interface,” *J. Acoust. Soc. Am.*, vol. 135, pp. 1709–1716, 2014.

[108] T. G. Leighton, “What is ultrasound?,” *Progress in biophysics and molecular biology*, vol. 93, pp. 3–83, 2007.

[109] L. F. Shampine and M. W. Reichelt, “The matlab ode suite,” *SIAM J. Sci. Comput.*, vol. 18, pp. 1–22, 1997.

[110] Y. Chen, X. Zhang, P. Zhang, and C. Liu, “Lubricant film thickness measurement using fiber-optic michelson interferometer and fiber-optic displacement sensor,” pp. 951–956, IEEE International Conference on Information and Automation, 2009.

[111] N. S. Bakhvalov, Y. M. Zhileikin, and E. A. Zabolotskaya, *Nonlinear theory of sound beams*. American Institute of Physics, 1987.

[112] S. S. Ray, “New analytical exact solutions of time fractional kdv–kzk equation by kudryashov methods,” *Chinese Physics B*, vol. 25, p. 40204, 2016.

[113] Y. Lee and M. F. Hamilton, “Time-domain modeling of pulsed finite-amplitude sound beams,” *The Journal of the Acoustical Society of America*, vol. 97, pp. 906–917, 1995.

[114] K. Frøysa, J. N. Tjøtta, and S. Tjøtta, “Linear propagation of a pulsed sound beam from a plane or focusing source,” *The Journal of the Acoustical Society of America*, vol. 93, pp. 80–92, 1993.

[115] M. A. Averkiou, Y. Lee, and M. F. Hamilton, “Self-demodulation of amplitude- and frequency-modulated pulses in a thermoviscous fluid,” *The Journal of the Acoustical Society of America*, vol. 94, pp. 2876–2883, 1993.

[116] M. J. Lighthill, *Waves in fluids*. Cambridge university press, 1978.

[117] Y.-S. Lee, “Numerical solution of the kzk equation for pulsed finite amplitude sound beams in thermoviscous fluids,” 1993.

[118] E. Fubini-Ghiron, “Anomalie nella propagazione di onde acustiche di grande ampiezza,” *Alta Frequenza*, vol. 4, pp. 530–581, 1935. English translation: Beyer(1984), pp.118-177.

[119] D. T. Blackstock, “On plane, spherical, and cylindrical sound waves of finite amplitude in lossless fluids,” *The Journal of the Acoustical Society of America*, vol. 36, pp. 217–219, 1964.

[120] D. T. Blackstock, “Connection between the fay and fubini solutions for plane sound waves of finite amplitude,” *The journal of the Acoustical Society of America*, vol. 39, pp. 1019–1026, 1966.

[121] C. Pantea, C. F. Osterhoudt, and D. N. Sinha, "Determination of acoustical nonlinear parameter β of water using the finite amplitude method," *Ultrasonics*, vol. 53, pp. 1012–1019, 3 2013.

[122] L. D. Landau and E. M. Lifshitz, *Fluid Mechanics*. Pergamon Press, 1984.

[123] M. J. Holmes, N. G. Parker, and M. J. W. Povey, "Temperature dependence of bulk viscosity in water using acoustic spectroscopy," vol. 269, pp. 012011–012017, Journal of Physics: Conference Series, 2011.

[124] N. Taşköprülü, A. J. Barlow, and J. Lamb, "Ultrasonic and visco-elastic relaxation in a lubricating oil," *The Journal of the Acoustical Society of America*, vol. 33, pp. 278–285, 1961.

[125] D. T. Blackstock, "Convergence of the keck-beyer perturbation solution for plane waves of finite amplitude in a viscous fluid," *The Journal of the Acoustical Society of America*, vol. 39, pp. 411–413, 1966.

[126] W. Keck and R. T. Beyer, "Frequency spectrum of finite amplitude ultrasonic waves in liquids," *The Physics of Fluids*, vol. 3, pp. 346–352, 1960.

[127] K.-Y. Jhang, C. J. Lissenden, I. Solodov, Y. Ohara, and V. Gusev, *Measurement of nonlinear ultrasonic characteristics*. Springer, first ed., 2020.

[128] W. N. Cobb, "Finite amplitude method for the determination of the acoustic nonlinearity parameter B/A," *The Journal of the Acoustical Society of America*, vol. 73, pp. 1525–1531, 1983.

[129] S. Taghizadeh and R. S. Dwyer-Joyce, "Application of the non-linear behaviour of longitudinal ultrasonic waves in lubricants monitoring," *23rd International Colloquium Tribology: Industrial and Automotive Lubrication*, pp. 351–352, 2022.